INFLUENCE OF SUBMERGED CHANNEL OBSTRUCTIONS ON FLOW PATTERNS, TURBULENCE, AND BED MORPHOLOGY UNDER ICE COVER - EXPERIMENTAL STUDY AND NUMERICAL SIMULATION

by

Guowei Li

B.Eng., Chang'an University, China, 2019
M.L.W.S., University of British Columbia, 2020

DISSERTATION SUBMITTED IN PARTIAL FULFILLMENT OF
THE REQUIREMENTS FOR THE DEGREE OF
DOCTOR OF PHILOSOPHY
IN
NATURAL RESOURCES AND ENVIRONMENTAL STUDIES

UNIVERSITY OF NORTHERN BRITISH COLUMBIA

October 2024

Abstract

This dissertation explores the complex interactions between submerged angled spur dikes, rigid leafless vegetation, and ice cover in cold-region rivers, focusing on understanding their effects on flow dynamics, sediment transport, and scour formation. The research addresses a significant gap in existing knowledge by examining these interactions under various flow conditions, including open channel and ice-covered scenarios, through large-scale flume experiments and advanced numerical simulations.

The study first investigates the influence of spur dike orientation, submergence level, and ice cover roughness on local scour depth and flow patterns. Results reveal that larger dike alignment angles (greater than 90°) reduce scour depth, while rough ice cover exacerbates scouring compared to smooth ice conditions. The research highlights the critical role of dike orientation and ice roughness in designing hydraulic structures to minimize erosion and protect riverbanks. Building on these findings, the second part of the study focuses on the turbulent flow structures around submerged angled spur dikes under ice cover. Quadrant analysis indicates that ice cover intensifies turbulence, mainly through increased ejection and sweep events near the dike tip, leading to more significant sediment mobilization and scour. The research emphasizes the importance of considering ice-covered flow dynamics in river engineering, especially in cold regions where ice significantly alters flow behavior. The final component of the dissertation examines the hydrodynamic characteristics within vegetated pools under ice cover representing regional obstruction to the flow field, emphasizing the role of vegetation configuration on flow modification. The study demonstrates that vegetation, particularly in staggered configurations, effectively reduces flow velocity and enhances

sediment deposition, creating favorable conditions for aquatic habitats. However, ice cover introduces additional complexity by altering the velocity profiles and turbulence distribution, with implications for river management and restoration efforts.

The findings of this research provide valuable insights into the design and implementation of river management strategies in cold climates. The study's outcomes have practical applications in optimizing spur dike configurations, enhancing the effectiveness of vegetated riverbank stabilization, and improving the resilience of river ecosystems to ice-related challenges. Future research should further explore the synergistic effects of spur dikes and vegetation, integrate more diverse vegetation models, and validate these findings in natural river systems under varying climatic conditions.

Preface

I served as the primary investigator in this research, responsible for designing the experimental plan, collecting and processing data, and interpreting the results. I also led the manuscript writing process and integrated the reviewers' feedback into the final versions of the dissertation. However, I recognize the assistance from my lab partner, Sanaz Sediqi, for her help in flume preparation, and my supervisory committee members, such as Dr. Jueyi Sui and Prof. Mauricio Dziedzic, for their role in finalizing the manuscripts, supervising the experimental design and assisting with data analysis. Due to their considerable contributions, they have been included as co-authors in some related publications.

This Ph.D. dissertation has resulted in one published manuscript for Chapter 3, with the manuscript for Chapter 4 accepted and the manuscript for Chapter 5 currently under review. This dissertation's publication status and authorships are as follows.

1) Li, G., Sui, J., Sediqi, S., & Dziedzic, M. (2023). Local scour around submerged angled spur dikes under ice cover. *International Journal of Sediment Research, 38*(6), 781–793. https://doi.org/10.1016/j.ijsrc.2023.08.003
2) Li, G., Sui, J., Sediqi, S. (2024). Turbulent flow structure around submerged angled spur dikes under ice cover. Manuscript submitted to *Journal of Hydrology and Hydromechanics* (accepted, forwarded to the publisher for copy editing and typesetting).
3) Li, G., Sui, J., Sediqi, S. (2024). Hydrodynamic characteristics in pools with leafless vegetation under ice-covered flow conditions - an experimental study and numerical simulation. Manuscript submitted to *Journal of Hydrology* (under review).

TABLE OF CONTENTS

List of Tables

List of Figures

Acknowledgment

I want to express my deepest gratitude to my supervisor, Dr. Jueyi Sui, for his unwavering support, patience, and guidance throughout my Ph.D. journey. His extensive knowledge and insightful feedback have been instrumental in refining my research and shaping the quality of this dissertation. I am truly fortunate to have had his mentorship, which extended beyond academics and helped me grow professionally and personally.

I am also sincerely grateful to my committee members, Prof. Mauricio Dziedzic, Dr. Faran Ali, and Dr. Liang Chen, for their valuable contributions. Their insightful comments and suggestions have been crucial in shaping the direction and outcome of my research. I want to express my special thanks to Prof. Mauricio Dziedzic for helping me acquire the license for the Flow-3D software and all the assistance from Dr. Nikhil P. Aravindakshan at UNBC HPC Center and Cristine Webb from Flow Science Inc.

My heartfelt thanks go to Dr. Ellen Petticrew and Dr. Phil Owens for providing the resources and facilities at the Quesnel River Research Center (QRRC), which significantly enhanced the depth and quality of my work. I am also profoundly thankful to Dr. Jason Raine and Jordan Lindgren for their kindness, support, and the time they dedicated to assisting me. I also want to acknowledge the assistance of my dear friend Sanaz Sediqi, whose continuous collaboration has been a great source of strength during my studies.

I also greatly appreciate the support from my parents and grandparents, who always comforted me during my lowest time, especially my mom. Lastly, I want to acknowledge the spiritual guidance and encouragement from God, whose presence has provided me with the strength, clarity, and perseverance needed to complete this journey.

1. CHAPTER ONE: INTRODUCTION AND LITERATURE REVIEW

This research was driven by recognizing the significant role that river restoration structures, such as spur dikes in channels and rigid leafless vegetation patches in pools and ice cover, influence flow dynamics within fluvial systems. While the effects of spur dikes in channels, vegetation patches in pools and ice cover, have been studied independently, a lack of research has explored their combined impact on flow resistance and channel bed deformation. This study aimed to fill that gap by thoroughly investigating the interplay between various structures and ice cover, such as spur dikes and rigid leafless vegetation patches. This research critically evaluates how these structures influence flow resistance and channel bed deformation by examining various configurations and arrangements of spur dikes in sandboxes and vegetation patches in an artificially constructed pool and the effects of ice cover roughness.

Understanding these combined effects is essential for the sustainable management and restoration of river systems, particularly in cold-weather environments. The insights gained from this study can guide decisions related to vegetation restoration, channel regulation, and the revitalization of river ecosystems. Furthermore, the findings contribute to developing precise assessment methods that can be applied in future restoration projects, helping to mitigate flood risks and ensure the long-term stability of river channels.

1.1 Channel Bed Deformation and Navigation Regulation

Riverbed deformation results from the interaction between water flow and the riverbed. A particular riverbed morphology and sediment composition correspond to specific flow conditions, and in turn, such flow conditions contribute to different extent of riverbed deformations. The factors influencing riverbed deformation are highly complex, some of which include (1) tectonic movements and the Earth's rotational dynamics, (2) changes in water volume and the process of runoff variation, (3) the river's sediment load, leading to significant changes in sediment composition, (4) riverbed morphology and geological conditions, (5) anthropogenic activities (van Denderen et al., 2022; Wang & Xu, 2018; Zheng et al., 2022). The equilibrium state of a river is temporary and relative; riverbed deformation is an ongoing process.

The slope is often steep, with complex topography in the upstream sections of large rivers, while downstream sections frequently flow through broad plains. Mountainous rivers feature steep bed slopes and turbulent flow, whereas rivers on plains often have unstable beds and shallow, meandering channels (Van Appledorn et al., 2019). Given the complexity of riverbed deformation and sediment transport, some of the primary objectives of river regulation are to prevent further bed deterioration, mitigate floods and droughts, and still meet ecological and societal needs by establishing reasonable flow standards and implementing appropriate regulatory structures (Boulange et al., 2021; Chen & Olden, 2017; Xu et al., 2021). Long-term river regulation generally focuses on flood prevention and runoff navigation under the joint impacts of climate change and urbanization (Li et al., 2024). In contrast, short-term and localized regulation aims to prevent bank erosion, stabilize hydraulic structures, and ensure transportation facility safety (e.g., canals and bridges) (Duró et al., 2020).

Flood management is the primary objective in managing major Canadian rivers. The persistent flooding challenges across the country in the 1970s highlighted the need for a shift from traditional methods focused solely on structural solutions and disaster aid. This shift was driven by dissatisfaction with the limitations of structural approaches, concerns over the redistribution of resources from the public to floodplain residents, evolving social values, increasing urbanization, and the continuous rise in flood damage costs despite existing control measures. In response, the federal government undertook a comprehensive evaluation of its flood management programs and policies, aiming to develop a new national strategy to address flood-related issues. This assessment incorporated input from provincial agencies, insights from joint basin study reports, and lessons from the U.S. experience managing flood losses. As a result, the Flood Damage Reduction Program was launched in 1975 (Watt, 2013, pp. 1976–1995). Regardless of the objectives of river regulation, such activities should not cause significant ecological impacts or damage to the river sections or neighboring areas. All river regulation projects must adhere to this principle to satisfy the Sustainable Development Goals (SDGs) (Widén et al., 2022).

1.1.1 Spur Dikes for River Regulation

Spur dikes, or groins, are hydraulic structures extending from riverbanks into the flow, designed to alter water currents and stabilize river channels. Primarily used in river engineering and navigation, these structures serve multiple purposes, including bank protection, sediment management, and flow direction. By deflecting strong currents away from the banks, spur dikes reduce erosion, promote sediment deposition in targeted areas, and create favorable conditions for navigation (Kumar & Ojha, 2021). The effectiveness of spur dikes depends on their length, orientation, spacing, and river flow conditions (Patel & Kumar, 2024). As integral to river regulation strategies, spur dikes are crucial for maintaining channel stability and mitigating flood risks, particularly in regions with complex hydraulic dynamics. The design and implementation of spur dikes require careful consideration of the interplay between hydraulic forces, sediment transport, and environmental impacts, making them a critical focus in the study of river engineering.

Spur dikes can be designed in various plan view shapes, including straight, L-head, T-head, hockey, inverted hockey, and curved (Alasadi et al., 2023). Among these, the straight rectangular shape is the most researched. Depending on their orientation angle relative to the flow direction, spur dikes can also be classified as attracting (oriented towards downstream), deflecting (90° alignment with the bank), or repelling (oriented towards upstream). Structurally, they can be either impermeable or permeable. A submerged spur dike is entirely underwater, while a non-submerged spur dike remains partially above the water's surface (Patel et al., 2022). The head of the spur dike can also take on different shapes, including rectangular, chamfered, and oblong (Masjedi & Foroushani, 2012). Spur dikes can be arranged individually or in groups for different design purposes (Ulu et al., 2023). However, if two spur dikes are placed at significant distances from each other along a river, they should also be referred to as individual spur dikes.

This study focuses mainly on submerged repelling spur dikes. These spur dikes are typically used in river regulation projects to improve navigability, especially in rivers with shallow channels where navigation difficulties frequently arise. In such cases, spur dikes are employed to straighten the river channel, stabilize navigation routes, and increase channel depth, thereby facilitating sedimentation (Liu et al., 2024). Given the complexities associated with sediment transport and channel morphology in regulated rivers, the orientation angle of spur dikes is particularly critical. Spur dikes oriented at angles greater than 90° (repelling) are particularly effective for bank protection, as they promote sediment deposition between them, resulting in a highly stable riverbank (Patel et al., 2022).

1.1.2 Major Hydraulic Issues of Spur Dikes

Spur dikes are widely applied in river regulation projects, making the study of their hydraulic characteristics and associated channel deformation critical for engineering purposes. The main issues include the water surface profile near the spur dike, the flow field, and the potential for scouring around the dike head (Huang et al., 2019; Li et al., 2024).

The primary effects of spur dikes under submerged conditions are to scour the riverbed, increase flow velocity to erode shallow areas or block and redirect the flow to raise water levels upstream, slowing down the flow (Huang et al., 2019). After a spur dike is constructed, the upstream flow is obstructed when water flows towards it, reducing flow velocity and lowering the water surface as water reaches the spur dike. Due to the narrowing of the channel, both flow velocity and turbulence increase. When the water flows past the spur dike, the flow gradually recovers, with velocity and turbulence decreasing and the water surface rising, eventually merging with the natural river section and returning to normal conditions (Qi et al., 2024).

Spur dikes influence the main flow in two primary ways: by affecting the overall movement of the main flow and by expanding the recirculation zones around the dike head and wake region (Huang et al., 2019). Studies have shown that spur dikes create a distinct shear layer and high-energy turbulent zone downstream (Koken & Constantinescu, 2008a). The vortex formed by the dike head is the leading cause of local scouring. This study focuses on the scouring effects and flow field alterations around spur dikes.

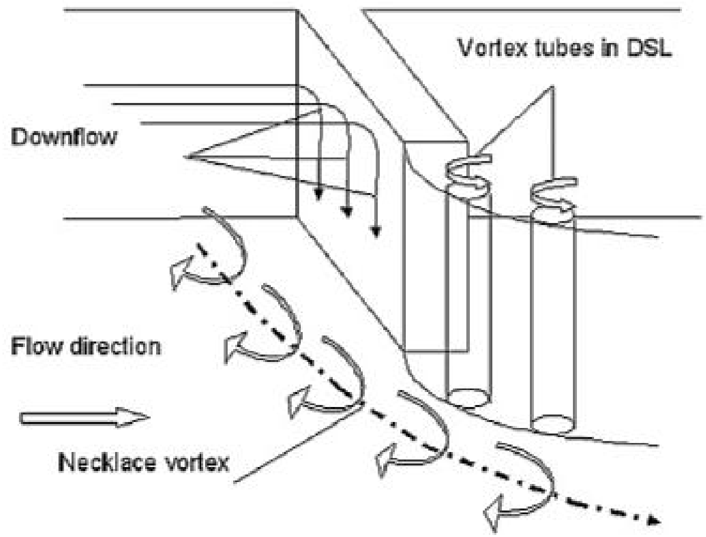

Figure 1.1. Illustration depicting the critical coherent structures and physical phenomena occurring in the flow around a solitary spur dike (source: Koken & Constantinescu, 2008a).

The study of water surface and near-field flow regions generally employs theoretical calculations, physical model experiments, and field observations (Zhang & Liu, 2023). Physical models are utilized in scientific research to study fundamental processes and their interactions under controlled conditions, in hydraulic engineering for planning and design purposes, and to assist in public decision-making by providing clear explanations and demonstrations (Mosselman, 2018). However, physical models have limitations, including scaling issues and lengthy research periods, which restrict their flexibility, adjustment, and optimization (Schweiger et al., 2020). Therefore, leveraging the latest advancements in computational fluid dynamics (CFD) and numerical simulation technologies, alongside developments in hydraulics research, offers significant academic and engineering potential for advancing river and port regulation projects.

In river regulation, numerical models are valuable in scientific research, but their field applications often cannot be fully verified or validated by strict scientific standards (Mosselman, 2018). Over the past decade, considerable effort has been dedicated to developing various CFD simulations of flow fields obstructed by spur dikes (e.g., Mulahasan et al., 2023). The reliability of simulation results has gained increasing acceptance, and the application of numerical methods in engineering projects has expanded. Incorporating these advancements, substantial researchers have conducted investigations on Canada’s natural river and navigation regulation, achieving significant outcomes (e.g., Seo & Wang, 2021). Physical modeling has become increasingly vital in hydraulic engineering, particularly in understanding hydraulic structures like spillways, energy dissipation systems, and river channels. These models are essential for ensuring the accuracy and reliability of engineering designs, which directly contribute to the success of projects and the development of new techniques in related fields (Peña & Anta, 2021).

Traditional hydraulic mass, momentum, and energy equations commonly serve as the basis for open-channel calculations (Gray & Miller, 2023). However, for natural flows in complex topographies, accurately determining parameters such as channel slope, energy loss coefficients, and adequate water surface area is challenging, often leading to significant errors in computational results (Xue et al., 2023). Due to the three-dimensional complexity of natural flows, using more refined analytical models to simulate these profiles has become a focal point in river regulation practice.

In fluid mechanics studies, physical modeling experiments face limitations due to the scale of the models, making it difficult to measure flow velocities accurately in many scenarios, especially in downstream regions (Pfister & Chanson, 2014). As a result, numerical modeling has become an essential development trend. In recent years, three-dimensional flow simulations of gas-liquid-solid multiphase flow modeling methods have been successfully applied in various fields, including hydraulic engineering, chemical engineering, structural engineering, and environmental engineering (Sun & Sakai, 2015). These methods have successfully replicated complex physical processes that are difficult to capture through physical model experiments and have provided crucial physical parameters that are challenging to measure. Such data is essential for understanding the mechanisms of physical changes and informing engineering design. Thus, numerical modeling methods have become vital in scientific research and engineering applications.

Spur dikes designed for partial submergence (non-submerged conditions) and installed in the field typically have irregular shapes. During flood events, these non-submerged spur dikes become submerged, functioning as fully submerged dikes, particularly considering the impact of increasing climate change (Gul et al., 2024; Lodhi et al., 2015). Therefore, submerged spur dike configuration is the focus of this research.

1.2 Local Scour Around Hydraulic Structures

Local scour is a natural phenomenon caused by the action of water flow on riverbeds, often leading to structure foundation erosion, such as pier and abutment scour, which can result in structure failure. The mechanisms of local scour around spur dikes resemble the bridge abutments (Kothyari & Ranga Raju, 2001). For hydraulic structures such as spur dikes and bridges, damage caused by local scour is severe. In Europe, the 2002 flood in Germany resulted in bridge and road infrastructure repair costs of €577 million, while Austria's ÖBB suffered approximately €100 million in economic losses due to the same event. In the U.K., flood events in 2009 caused the partial or complete destruction of 20 road bridges, leading to estimated financial losses of around £2 million per week. Scour risk mitigation in Europe is projected to cost €541 million annually between 2040 and 2070. In the U.S., major floods in 1964 and 1972 caused bridge and highway damages amounting to $100 million per event, and the Federal Highway Administration (FHWA) estimates that 50 to 60 bridges collapse annually due to such events. In New Zealand, scour damage costs are estimated at 36 million NZD annually. In Iran, bridge collapse financial losses totaled $562.5 million in the first decade of the 21st century, while South Africa's annual scour damage costs are around 22 million ZAR. Additionally, the 2007 floods in Bangladesh and Indonesia damaged transport infrastructure, accounting for 34% and 25% of total infrastructure costs, respectively, amounting to $363 million and $35 million (Pizarro et al., 2020).

If the design of a spur dike is not considered adequately concerning flow conditions, the shallow foundation can lead to scouring, resulting in structural instability and posing a hazard to structure safety (Patel et al., 2022). The primary locations of spur dike failure are concentrated at the dike head and foundation, where continuous water erosion weakens the structural integrity, causing the dike to lose support and eventually collapse under its weight. Additionally, the stones and materials composing the dike may become dislodged under the force of upstream water flow, leading to further structural deterioration. In the section from the confluence of the Puyang River to the Changshan sluice, over 180 spur dikes are employed for riverbank protection in China. However, strong tidal bores and turbulent flows near the dike head often result in significant sediment and rubble erosion, forming deep scour holes. This process can lead to the collapse of the dike head, hollowing and fragmentation of the protective covering, and subsequent damage to the entire structure (Pan & Li, 2022).

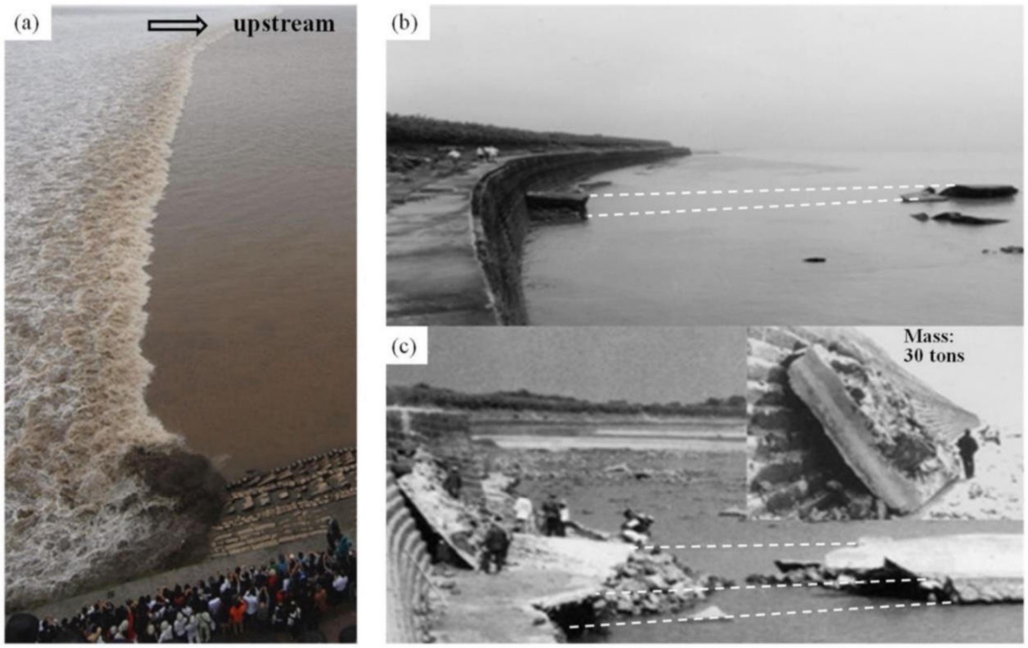

Figure 1.2 Damages to a spur dike from tidal bores include several critical impacts: (a) the upstream propagation of a tidal bore, (b) the destruction of the spur dike structure, and (c) the overturning of concrete armor, with the inset showing how the tidal bore dislodges concrete armor placed against the seawall. (source: Pan & Li, 2022)

1.2.1 Classification of Local Scour

Based on sediment transport dynamics, local scour at bridge piers can be classified into two primary types: clear-water scour and live-bed scour (Pandey et al., 2018). Clear-water scour occurs when the flow approaching the pier is devoid of sediment, typically when the flow velocity is insufficient to mobilize bed material upstream. In this scenario, the scour hole develops as the sediment is eroded from around the hydraulic structure, but no additional sediment is carried into the hole by the flow. This results in a scour depth that is generally deeper than that found in live-bed conditions, as the absence of incoming sediment allows the erosion process to continue unimpeded.

On the other hand, live-bed scour occurs when the flow carries sediment and actively transports the sediments across the riverbed. In this case, sediment is continuously supplied to the scour hole, partially filling it and limiting the maximum depth of the scour. The dynamic interaction between sediment transport and erosion in live-bed conditions often leads to a more complex and fluctuating scour profile.

Research has shown that the maximum scour depth under clear-water conditions can be approximately 10% greater than that under live-bed conditions due to the absence of sediment inflow to counteract the erosive forces (Chabert & Engelrndinger, 1956). Understanding these distinctions is critical for accurately predicting scour depth and ensuring the structural integrity of bridge piers under various hydraulic conditions.

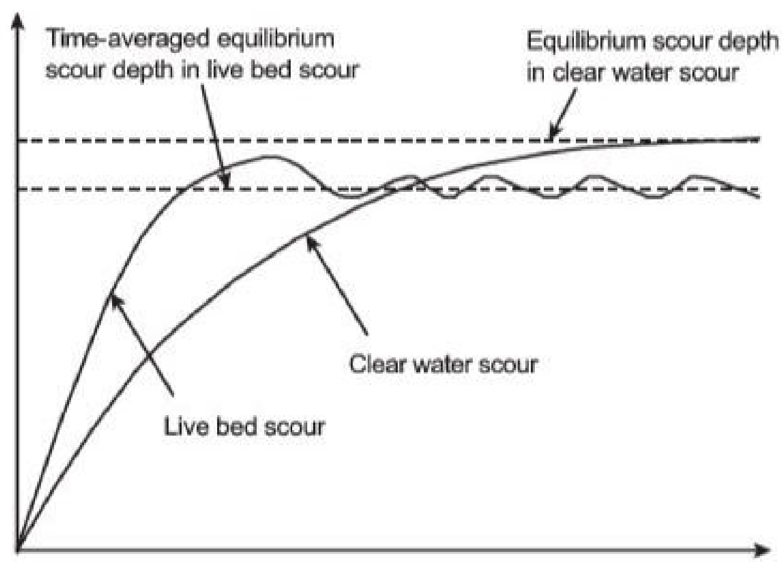

Figure 1.3 Progression of scour over time in clear-water and live-bed conditions (source: Chabert & Engelrndinger, 1956).

1.2.2 Mechanisms of Local Scour Around Hydraulic Structures

Current research on the flow structure around hydraulic structures generally focuses on downflow in front of the structure, horseshoe vortices around the foundation, flow separation at the sides, and wake vortices behind the structure. Apsilidis et al. (2010) conducted experiments using Time-Resolved Digital Particle Image Velocimetry (TR-DPIV) to measure the flow fields around cylindrical piers. The results indicated that developing three-dimensional boundary layer separation generates well-defined horseshoe vortices closely linked to the Reynolds number. Namaee et al. (2023) used flow measurements in flume experiments and numerical simulation to confirm that flow separation at the sides of bridge piers forms two counter-rotating symmetric vortices, which are then shed into the downstream flow as wake vortices. Zhang et al. (2020) applied unstructured finite-volume modeling to simulate the flow and local scour around a vertical cylinder, finding that the upstream horseshoe vortex reached maximum velocity near the pier base while wake vortices formed at the rear exhibited flow separation, aligning well with experimental observations.

The mechanisms behind local scour near the riverbed around spur dikes are complex, and experts have differing opinions. The main perspectives on the mechanisms of local scour near the riverbed around spur dikes are listed below.

1) **Horseshoe Vortex Theory**: This theory posits that the presence of the spur dike creates horseshoe vortices near the riverbed around the dike head. These vortices intensify the scouring effect by directing sediment and material downstream, deepening the scour holes (Koken & Gogus, 2015).

2) **Increased Downstream Flow Velocity Theory**: This theory suggests that the scour at the spur dike head is due to the flow obstruction by the dike, which accelerates the flow velocity around the dike head. This increase in velocity causes more sediment to be transported downstream, leading to local scour (Huang et al., 2019).

3) **Downflow Theory**: According to this theory, downflow generated by the obstruction of the spur dike creates a pressure difference around the dike head. This pressure difference forces water downwards, moving sediment away from the dike base and contributing to scour (Zhuang et al., 2023).

4) **Composite Theory**: This perspective combines elements of the previous theories, proposing that both downflow and horseshoe vortices, along with their interaction, contribute to the local scour near the spur dike (Li et al., 2024).

Based on theoretical stress analysis and experimental studies, it can be concluded that when water flows around the spur dike, the obstruction caused by the dike generates a downflow, which creates pressure differences around the dike head. Consequently, a low-pressure zone forms behind the dike. The flow undergoes deflection, creating spiral vortices that move downward, contributing to the scouring process. This downflow, interacting with the velocity gradient near the riverbed, intensifies the erosion and deepens the scour hole. As the downflow progresses, the scour hole elongates and deepens while the sediment transport rate increases, preventing material deposition within the scour hole. This process continues until the flow velocity at the strongest point of erosion decreases and the scour hole stabilizes (Koken & Constantinescu, 2008a, 2008b; Li et al., 2024; Qi et al., 2024).

1.2.3 Factors Influencing Local Scour Around Spur Dikes

The factors influencing local scour near the riverbed around spur dikes can be broadly categorized into hydrodynamic factors, sediment factors, and geometric conditions (Qi et al., 2024). Hydrodynamic factors include flow discharge Q (m^3/s), average flow velocity upstream of the scour hole U_{up}, average flow velocity at the dike head U_d, and local gravitational acceleration g (m/s²). Sediment factors involve the median particle size d_{50} (mm), sediment density ρ_s, and non-uniformity coefficient. Geometric conditions encompass channel width B (m), dike length L_d (m), dike width B_d (m), bed slope s_0, and the dike orientation angle α (°).

Early research from the 1960s indicates that sediment size affects the equilibrium depth of clear-water scour but does not influence the maximum depth of live-bed scour because, under live-bed conditions, sediment transport maintains equilibrium, with upstream sediment replenishing the material removed from the scour hole (National Academies of Sciences, 2021). Studies conducted in the 2000s found that the influence of sediment size becomes negligible when the structure size to median sediment diameter ratio exceeds 50 (Melville & Coleman, 2000). As the ratio increases, scour depth generally decreases. However, once the ratio surpasses 100, further increases in sediment size have minimal impact on reducing scour depth due to scaling effects (Lee & Sturm, 2009). The flow velocity and sediment transport dynamics near the dike also influence this relationship (Li et al., 2013). Further studies have shown that factors such as the length of the dike, its alignment with the flow, and the slope of the upstream bank all affect scour depth (Han et al., 2022; Patel & Kumar, 2024).

1.2.4 Calculation of Maximum Local Scour Depth Around Spur Dikes

Due to the complexity of local scour near spur dike heads, most calculation methods for maximum scour depth are based on empirical or semi-theoretical methods. Some researchers have begun approaching this from a numerical perspective, using CFD software or HEC-RAS to predict scour depth. However, these predictions require experimental or field data for validation.

1) $y_s = f(\ldots)H_{up}$ Type Calculation Equations

In this expression, y_s represents the maximum local scour depth at the spur dike head, and H_{up} is the average water depth upstream of the dike. The function $f(\ldots)$ represents the correction factor, which depends on various parameters such as channel width B, dike length L_d, average water depth H_0, average flow velocity U_0, sediment settling velocity U_s, local gravitational acceleration g, water density ρ, dynamic viscosity μ, sediment median particle diameter d_{50}, standard deviation of sediment size distribution σ, specific weight difference of sediment $\Delta\gamma$, dike orientation angle α, Froude number Fr, channel slope s_0, among others. Typical formulas of this type include those by Laursen (1963), Cunha & Veiga (1970), and Froehlich (1989).

2) Calculation Equations for Local Scour around Spur Dikes under Special Conditions

When calculating local scour around spur dikes under special conditions, various equations have been developed to address the complexity of these scenarios. Melville (1997) proposed specific calculation methods for compound channels that account for the unique flow dynamics present in these environments. In curved channels, the scour characteristics differ significantly, and the equation by Ahmad (1953) is typically employed to predict scour depth accurately. Permeable spur dikes, which allow water to pass through their structures, require a different approach, and Nasrollahi et al. (2008) equation can be used in these cases. For non-submerged spur dikes, where the structure remains above the water level during flow events, almost all equations for bridge abutments are applicable (Kothyari & Ranga Raju, 2001). When dealing with maximum scour depth under submerged conditions, a standard method involves calculating the equivalent clear-water scour depth for non-submerged case h_n and applying a correction factor k to account for the effects of submergence, yielding the maximum scour depth $h_s = kh_n$ (Hao et al., 2013).

3) Hydraulic Engineering Circular No. 18 (HEC-18) Framework

The HEC-18 framework, developed by the Federal Highway Administration (FHWA), is a widely recognized guideline for evaluating scour at hydraulic structures (Federal Highway Administration, 2001). The Colorado State University (CSU) equation is crucial for estimating local scour depth within this framework. The CSU equation integrates multiple factors influencing scour, including flow velocity, flow depth, sediment size, and hydraulic structures' geometry. Specifically, it accounts for the effects of flow intensity and the structure's shape, providing a detailed approach to predict the maximum scour depth around spur dikes. The equation is particularly valuable for its ability to adjust for varying hydraulic conditions and sediment characteristics. It is a robust method for engineers and researchers on bridge and river training projects. Applying the CSU equation within the HEC-18 framework helps ensure that spur dike designs are resilient against potential scour-induced failures, thereby enhancing the safety and longevity of hydraulic structures.

Table 1.1 Equilibrium Scour Predictive Equations

Reference	Equation	Notes
Ahmad (1953)	$y_s + y_1 = 0.45 K_s q_2^{2/3}$	y_s = equilibrium scour depth y_1 = approach flow depth K_s = empirical constant q_2 = local discharge intensity in contracted channel (ft^2/s)
Laursen (1963)	$\frac{a}{y_1} = 5.5\frac{y_s}{y_1}\left[\frac{\left(\frac{y_s}{11.5y_1}+1\right)^{7/6}}{\left(\frac{\tau_1}{\tau_c}\right)^{0.5}} - 1\right]$	Applies to clear-water scour. a = characteristic width τ_1 = grain roughness component of the

		bed shear τ_c = critical shear stress at the threshold of motion
Froehlich (1989)	$\frac{y_s}{a} = 0.32K_sFr^{0.2}\left(\frac{a_p}{a}\right)^{0.62}\left(\frac{a}{d_{50}}\right)^{0.08} + 1$	a_p = projected width of pier
Melville (1997)	$y_s = K_{ya}K_1K_DK_sK_\theta$ $K_{ya} = \begin{cases} 2.4\ a & \text{for } a/y_1 < 0.7 \\ 2(y_1a)^{0.5} & \text{for } 0.7 < a/y_1 < 5 \\ 4.5y_1 & \text{for } a/y_1 > 5 \end{cases}$ $K_1 = \begin{cases} \frac{V_1 - (V_{lp} - V_c)}{V_c} & \text{for } K_1 < 1.0 \\ 1 & \text{for } K_1 \geq 1.0 \end{cases}$ $K_D = \begin{cases} 0.57log_{10}\left(2.24\frac{a}{d_{50}}\right) & \text{for } \frac{a}{d_{50}} \leq 25 \\ 1 & \text{for } \frac{a}{d_{50}} > 25 \end{cases}$	V_1 = approaching velocity V_{lp} = flow velocity at the structure location under live-bed conditions V_c = critical velocity
FHWA (2001)	$y_s = 2.0K_1K_2K_3K_4a^{0.65}y_1^{0.35}Fr_1^{0.35}$	K_1 = correction factor for shape K_2 = correction factor for the attack of the flow K_3 = correction factor for bed condition K_4 = correction factor for armoring of bed material Fr_1 = Fr directly upstream of the structure
Nasrollahi et al. (2008)	$\frac{y_s}{a} = mK_fK_{yL}K_dK_RK_n$	m = empirical constant K_f = correction factor for Fr K_{yL} = correction factor for a/y_1 K_d = correction factor for d_{50} K_R = correction factor for permeability K_n = correction factor for a/B, where B = channel width.

1.2.5 Numerical Modelling of Spur Dike in a Channel

Local scour around in-stream structures has long been a predominant cause of structural damage, attracting considerable attention from scholars and engineers. Research has been conducted on the equilibrium scour depth and the extent of scour holes around spur dikes under open-flow conditions using flume experiments (e.g., Xu et al., 2023), field measurements (e.g., Pan & Li, 2022), and numerical simulations (e.g., Kuhnle et al., 2008). For one-dimensional scour analysis such as the HEC-RAS 1D model, the HEC-18 report recommends using the Colorado State University (CSU) equation (Richardson et al., 1990) for calculating scour under both live-bed and clear-water conditions. This equation is the default in HEC-RAS software. An alternative equation developed by Froehlich (1991) has also been incorporated into the local scour estimation in many applications. Although the Froehlich equation is not recommended in the HEC-18 report, it has demonstrated good agreement with observed data.

Two-dimensional (2D) scour around spur dikes with various alignment angles has also been extensively studied. In these studies, the flow and local scour patterns are assumed to be uniform across the dike's span. Research has focused on the relationship between the development of scour depth and bed shear stress under different flow conditions. Koken and Constantinescu (2008a) found that in the scour initiation stage, the highest bed shear stress in the mean flow occurs in the region of strong acceleration near the tip of the spur dike. However, elevated shear stress values are also found beneath the upstream portion of the detached shear layer. Additionally, Liao et al. (2021) used a 2D mobile-bed model incorporating a repose angle formula and a bed geometry adjustment mechanism to enhance the accuracy of simulating local scour holes around structures. Experimental studies have shown that the alignment angle influences the shape and depth of the scour hole, with a right angle (90°) leading to a more pronounced scour due to the interaction between the flow and the riverbed (Li et al., 2023). Modified or new two-dimensional numerical models have also been developed to simulate local scour around submerged spur dikes, considering factors such as sediment transport and flow turbulence. For instance, Liao et al. (2014) developed the EFA2D model, a 2D mobile-bed simulation incorporating non-equilibrium suspended sediment concentration and bedrock erosion for natural rivers. Horvat et al. (2015) introduced a 2D model coupling active layer and multiple size-class sediment transport with an improved advection algorithm, proposing a scheme that permits larger time steps. The model was validated with field data from the Danube River. These models have been validated against experimental data, demonstrating their accuracy in predicting scour patterns. The results of these studies are crucial for designing spur dikes that minimize scour risk, ensuring their stability and effectiveness in river engineering applications.

Realistically, local scour around a submerged angled spur dike occurs in a complex three-dimensional (3D) manner, where the scour process is non-uniform in any given dimension. The initiation of scour typically begins at the leading edge of the dike and propagates downstream along the dike's length, altering the local flow patterns and sediment transport dynamics (Farshad et al., 2022). Researchers have conducted physical experiments and developed 3D models to predict scour progression around spur dikes. For instance, Han et al. (2019) developed a three-dimensional numerical model. They utilized it to investigate flow dynamics and local scour in fields of grouped spur dikes with varying layout angles. Implementing the porous medium method (PMM) simplifies the process of numerical discretization and differentiation. The fully three-dimensional features are evident in the spur dikes angled at 90° and those angled downstream. The primary flow follows an S-shaped trajectory, with large-scale vortices forming a recirculation zone behind the spur dikes. This flow pattern leads to a complex distribution of suspended sediment and uneven erosion and deposition on the sandbed.

1.3 Submerged Aquatic Vegetation Patches

The evolution of river morphology is a fundamental issue in river dynamics research. Traditional research on river channel changes typically focuses only on the interactions between the channel and water flow without considering the influence of vegetation, which is widely present in river systems. With its above-ground structures like stems, vegetation acts as a resistance boundary that disturbs water flow and alters hydraulic conditions (Cui et al., 2023). This disturbance can affect bank erosion processes, riverbank stability, and changes in river morphology. Moreover, the root systems of vegetation intertwine with the soil, increasing its cohesion, particularly in the case of riparian vegetation, which plays a significant role in stabilizing riverbanks (Finotello et al., 2024). Therefore, vegetation can alter river morphology through feedback mechanisms between river hydrodynamics and bank stabilization processes, creating dynamic response mechanisms that exert significant influence.

The flow characteristics in vegetated channels are highly complex, influenced by the ever-changing river morphology, inflow conditions, and vegetation traits such as diameter, height, flexibility, submergence, and arrangement (Barahimi & Sui, 2024b; Li et al., 2018). Understanding the interactions between vegetation characteristics, channel morphology, and hydraulic properties is essential for revealing universal patterns and understanding turbulent structures in rivers, thereby enriching the emerging subject of eco-hydraulics. Research on the impact of vegetation on flow characteristics, coupled with studies on the soil stabilization effects of vegetation roots and extending to the influence of vegetation on bank stability and morphological evolution, can provide a comprehensive understanding of the role of vegetation in river system evolution.

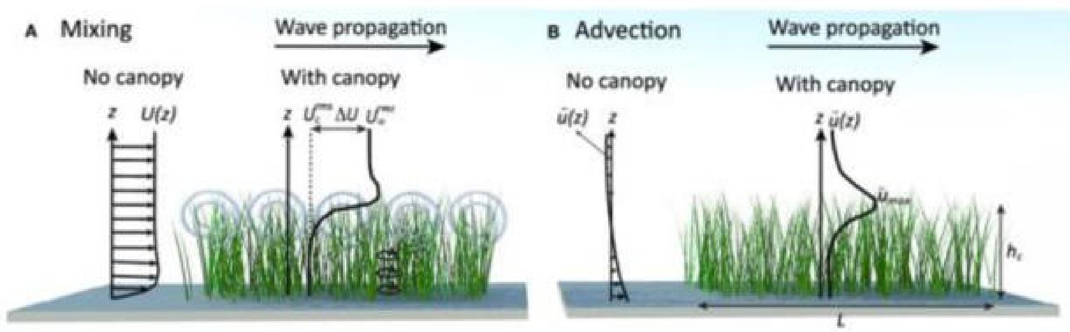

Figure 1.4 Interactive effects of wave-dominated flows over submerged canopies (A) KH-vortices generated by velocity gradients at the canopy top and (B) asymmetrical particle motion leading to a strong mean drift above the canopy (Abdolahpour et al., 2020).

1.3.1 Impact of Vegetation on Flow Resistance

Vegetation is a crucial biological factor in river ecosystems, but its presence can lead to increased water levels, greater flow resistance, and reduced flow velocity. Therefore, understanding the impact of vegetation on flow resistance is essential for ensuring the safety of flood conveyance and making reliable flood forecasts. Flow resistance in river channels is typically described by roughness coefficients, such as the Manning coefficient n and or the Darcy-Weisbach friction factor f, which are comprehensive coefficients accounting for the irregularities and roughness of the riverbed and banks (Yochum, 2018). A hydrodynamic model with a resistance term is first established to determine these roughness coefficients. Then, measured parameters such as water depth and flow velocity are substituted into the resistance equation to obtain roughness coefficients under different hydraulic conditions. However, when vegetation is present in the channel, factors such as the shape, flexibility, submergence, and distribution of vegetation complicate the determination of the roughness coefficient.

To determine the variations in roughness coefficients under different vegetative flow conditions, researchers attempted to relate the Manning coefficient n with parameters that describe flow conditions, establishing an n-vR curve, where vR is the product of average velocity and hydraulic radius (Chen et al., 2009). However, the n-vR curve primarily reflects the relationship between the Manning coefficient and the Reynolds number without capturing the essential interaction between vegetation and flow. It does not consider the influence of vegetation characteristics such as height and arrangement. Consequently, focus has also been given to the relationship between roughness coefficients and vegetation parameters, such as vegetation density, stiffness, submergence, and the proportion of the river's surface area covered by vegetation.

Since the structural characteristics of vegetation, such as stems and trunks, resemble cylindrical shapes in their interaction with water flow, when water flows past these cylindrical structures, it creates flow patterns similar to those observed in classical fluid dynamics studies of flow around a cylinder (Le Minor et al., 2021). Therefore, in addition to using roughness coefficients to reveal the impact of vegetation on flow resistance in rivers, the drag coefficient C_D can also be employed to describe the resistance effect of vegetation on water flow. Zhang et al. (2020) examined the drag coefficient C_d associated with an array of emergent flexible vegetation in a steady, nonuniform flow. Their investigation highlighted two key effects within the vegetated patch: the blockage effect, which increases the drag coefficient, and the sheltering effect, which reduces drag, particularly at the leading edge and tail of the vegetation. These opposing influences are crucial in determining the overall drag dynamics within the vegetated patch.

1.3.2 Impact of Vegetation on Bed Shear Stress

Recent studies indicate that sediment transport rates in vegetated channels are linked to bed shear stress (Conde-Frias et al., 2023; Xu et al., 2022). Therefore, understanding the distribution of bed shear stress in vegetated channels is crucial for comprehending sediment transport patterns. While there are various methods to estimate bed shear stress in non-vegetated channels, these approaches often need to be more suitable for vegetated channels due to the influence of vegetation on velocity profiles and turbulence.

In vegetated channels, the downslope force of the water due to gravity balances bed shear stress and vegetation drag. Jordanova and James (2003) attempted to estimate bed shear stress by subtracting vegetation drag from the downslope force. However, this method introduces significant uncertainty since vegetation drag and downslope force are larger than bed shear stress. In non-vegetated channels, near-bed turbulent kinetic energy (TKE) can be used to estimate bed shear stress, as turbulence is primarily generated by bed shear, establishing a relationship between the two. In vegetated channels, however, vegetation-generated turbulence constitutes most of the total turbulent energy, complicating the correlation between bed shear stress and TKE (Zhao & Nepf, 2021).

Kumar et al. (2024) used computational fluid dynamics (CFD) models to simulate bed shear stress in vegetated channels, revealing that streamwise velocity is more remarkable in non-vegetated and gap regions between vegetation stems than in areas near the vegetation. The lowest streamwise velocity and significant negative transverse velocity are observed directly behind the vegetation stems. Turbulent kinetic energy is higher behind the vegetation than the front, and turbulent kinetic energy and intensity increase as the flow moves through vegetated regions. A Reynolds stress model was used to study bed shear stress in compound channels with floodplain vegetation (Koftis & Prinos, 2018). Results indicate that shear stress at the floodplain bottom decreases while shear stress at the interface between the floodplain and the main channel increases as vegetation density increases. Their simulation results closely matched flume experimental data. Bed shear stress in vegetated experimental channels under uniform flow conditions can be estimated with existing equations, but non-uniform flow conditions are more common in actual river channels. Zhang et al. (2016) pointed out a generic pattern: bed shear stress decreases along the flow direction in decelerating flows, while bed shear stress increases along the flow direction in accelerating flows. However, the detailed variation trend of bed shear stress in vegetated channels under non-uniform flow conditions remains an area for further research.

1.3.3 Impact of Vegetation on Velocity Distribution

There is a significant difference in the vertical streamwise velocity distribution between submerged and emergent vegetation regions. In channels with emergent vegetation, the vertical velocity distribution resembles traditional open channels, with notable variations near the riverbed due to bed resistance (Maji et al., 2017). However, in channels with submerged vegetation, the velocity distribution no longer follows traditional patterns, especially near the vegetated boundary, leading to uneven velocity distribution in the vertical direction (Barahimi & Sui, 2024b). Two main views exist regarding the velocity distribution in submerged vegetated regions: the two-layer and three-layer models.

1.3.3.1 Two-Layer Model

The two-layer model divides the vertical velocity profile into vegetated and free-stream regions above the vegetation. Researchers have conducted flume experiments focusing on various lengths and velocity gradients in vegetated conditions, deriving multiple forms of velocity distribution equations. Kouwen et al. (1969) used the vegetation height H_v as the length scale and the shear velocity u_* as the velocity scale, yielding the following equation:

$$\frac{u}{u_*} = \frac{u_{hv}}{u_*} + \frac{1}{\kappa} ln\left(\frac{y}{h_v}\right) \tag{1.1}$$

where κ is the von Kármán constant, and y is the height above the riverbed. Stephan and Gutknecht (2002) used the average height of the deflected flexible vegetation h_p as the characteristic length scale for the velocity distribution above the flexible vegetation and u_* as the characteristic velocity scale. The equation for velocity distribution in the vegetated region is given as:

$$\frac{u}{u_*} = \frac{1}{\kappa} ln\left(\frac{y - h_p}{h_p}\right) + 8.5 \tag{1.2}$$

Zhang et al. (2021) used an enhanced momentum equation to derive the velocity within the vegetation layer, while the velocity in the free-surface layer incorporates both the momentum equation and the influence of wake effects. It can be observed that different characteristic length scales yield different velocity distribution equations. This variation arises from differences in vegetation type, density, flexibility, morphology, and flow conditions, which result in different flow parameter distributions. However, the trends are consistent overall, and the equations follow the expected distribution patterns.

1.3.3.2 Three-Layer Model

Compared to the two-layer model, the three-layer model is more complex, with inconsistent standards across regions and varying velocity distribution equations. The three-layer model generally divides the flow into the lower section near the bed and vegetation bottom, the middle section within the vegetation stern, and the upper section of free flow above the vegetation. El-Hakim and Salama (1992) conducted plastic model vegetation experiments, dividing the vertical flow into sections based on the average height of the deflected flexible vegetation H_{iv} and H_{v1} slightly above the vegetation. In the region of $0 < z < H_{iv}$, velocity follows a logarithmic distribution, following the first region, when $H_{iv} < z < H_{v1}$, the velocity distribution is almost linear. Lastly, various dimensionless parameters describe the velocity distributions for $H_{v1} < z < H$, where H is the approach water depth. Carollo et al. (2002) introduced Y_1 and Y_2 as dividing points for a three-layer model, where Y is defined as z/H, i.e., the ratio of vertical position to flow depth. Y_1 and Y_2 correspond to positions slightly above and below the vegetation and are used to separate the velocity profile into three distinct zones.

Selecting different dividing positions and using different dimensionless parameters to describe the velocity distribution ultimately leads to varying velocity distribution models and highlights the importance of using appropriate dimensionless parameters that account for vegetation characteristics and flow properties to derive consistent velocity distribution equations. With advances in computational fluid dynamics (CFD), numerical simulations align well with experimental results, revealing a mirrored “S” shape for velocity profiles near the top of the vegetation (Abid, 2020).

1.3.4 Impact of Vegetation on Turbulence Characteristics

In vegetated channels, the interface between the flow and the vegetated layer creates strong shear forces, leading to intense turbulence and complex three-dimensional flow variations. Researchers have conducted flume experiments and numerical simulations to explore the turbulence characteristics in vegetated channels.

1.3.4.1 Experimental Research

Nepf and Vivoni (2000) applied the tracing method to observe turbulence structure changes in arrays of cylindrical vegetation and discovered that turbulence scales are influenced by vegetation density and morphology. Sanjou (2016) used dye injection to study turbulent diffusion in submerged vegetated canopy open-channel flows. He concluded that sweep motion contributes more significantly to dye concentration transport near the vegetation edge than ejection motions. Nosrati et al. (2024), Okamoto et al. (2012), and Nezu and Onitsuka (2001) conducted flume experiments using model vegetation resembling cylinders and strips, measuring flow fields with ADV, LDV, LIF, and PIV. The results consistently showed that turbulence intensity peaks near the top of the vegetation canopy. Xu and Nepf (2020) studied plastic Typha latifolia in their experiments, focusing on the interaction between flexible vegetation and flow dynamics. Although the vegetation was arranged as emergent, it has been found that turbulent kinetic energy also reaches its maximum at the top of the vegetation layer and is vertically transferred to the riverbed, indicating that the flexibility and density of submerged vegetation significantly affect turbulence. As the canopy density increases, turbulence intensity and kinetic energy increase, with peak values occurring in this region (Barahimi & Sui, 2023). Caroppi et al. (2021) compared the flow between rigid and flexible vegetation under similar conditions. On average, the normalized shear penetration was 6–10 times higher for flexible vegetation than that observed for rigid cylinders, which leads to broader zones where significant momentum exchange occurred with the adjacent open water.

Regarding the influence of vegetation density, Souliotis and Prinos (2011) conducted flume experiments on submerged flexible vegetation, revealing that increasing vegetation density accelerates the development of flow velocity and turbulence characteristics within the vegetated patch, extending the downstream reach where these effects remain significant. Lou et al. (2022) analyzed the relationship between vertical vegetation density and turbulence intensity. They found that in unidirectional flow, a vertically varying vegetation density enhances the vertical gradient of the mean streamwise velocity, leading to increased stratification of flow velocities across different heights within the water column. Errico et al. (2019) conducted experiments using natural common reeds (*Phragmites australis*). They found similar patterns: as vegetation density increased, turbulence intensity increased, with the distribution showing greater variability at lower densities.

Additionally, other scholars have conducted experimental studies on different types of vegetation. Han et al. (2021) focused on submerged and emergent vegetation, finding that in scenarios with submerged vegetation, the gravitational current interacts with the top of the vegetation layer, effectively creating a new “wall boundary” that does not exist in emergent vegetation patches and inducing a region of negative vorticity above the vegetation canopy. Meng et al. (2021) simulated flow with various materials, such as reed, plastic sticks, grass, and chlorella, and observed that the impacts of vegetation types on the flow field cannot be ignored. Across both horizontal and vertical directions, turbulence intensity showed an “S” shape distribution pattern (Tang et al., 2023). In channels with complex flow conditions, such as meandering rivers with dense vegetation, variations in turbulence were particularly pronounced (Finotello et al., 2024). Turbulence intensity significantly increased at the intersection of the non-vegetated and vegetated zones. Still, the changes were less evident with emergent vegetation, as the vegetation obstructs the whole water depth (Han et al., 2021).

1.3.4.2 Numerical Simulation

While conducting experimental research on vegetated flows, many scholars also attempt to use numerical modeling methods to study the impact of vegetation on flow characteristics. Numerical simulations can accurately capture the flow dynamics across the entire computational domain compared to physical model tests. Based on their calculation principles, standard numerical models are classified into two main categories: Reynolds-Averaged Navier-Stokes (RANS) and Large Eddy Simulation (LES) methods (Chipongo et al., 2020). The RANS approach involves establishing Reynolds-averaged equations for specific flow conditions and then closing these equations using turbulence models such as the $k-\epsilon$ model, $k-\omega$ model, or Reynolds Stress Model (RSM). The LES method, on the other hand, solves the filtered Navier-Stokes equations directly by resolving large-scale eddies and modeling smaller ones using subgrid-scale models.

(1) Reynolds-Averaged Navier-Stokes (RANS): Two consideration levels can be incorporated when studying vegetated flows using RANS. The first is determining the momentum source terms in the dynamic equations through additional forces or momentum transfer processes, which reflect the impact of vegetation on the flow. The second approach directly models the vegetation as a series of cylindrical obstacles (Li & Yu, 2010). In terms of modifying the dynamic equations to account for the impact of vegetation, Wu et al. (2005) incorporated the drag force exerted by the vegetation into the momentum equations. They also developed a $k{-}\epsilon$ turbulence model that includes terms for turbulence generated by the vegetation, aiming to establish a depth-averaged turbulence model. Since the governing equations in the model include vegetation density, the model is particularly suitable for conditions with higher vegetation density. Zhang et al. (2013) incorporated the drag force of vegetation into the momentum and $k{-}\epsilon$ models, constructing a two-dimensional numerical model that accounts for the impact of vegetation and applying the Volume of Fluid (VOF) method to simulate the surface flow in vegetated channels. Hsieh and Shiu (2006) used a multi-porosity model, not analyzing individual vegetation elements but considering the entire vegetation patch as a porous medium. Given the complex three-dimensional flow variations in vegetated channels, three-dimensional modeling is crucial. Considering vegetation as a continuous porous medium, Lima et al. (2015) utilized the momentum and $k{-}\epsilon$ models to study the flow around square cylinder arrays under different spacing conditions. They found that as vegetation density increased, the flow dynamics in the gaps between vegetation changed significantly. Existing models need further refinement to account for the complex interactions between flow, vegetation stiffness, and morphological changes within densely vegetated channels. In summary, using the RANS method to simulate vegetated channel flow allows a macro-level understanding of the flow characteristics within vegetated channels. However, simulating the fine-scale turbulence structures in these complex flow environments presents certain challenges. Therefore, some researchers suggest applying the Large Eddy Simulation (LES) method to study vegetated flows, as it can capture more detailed turbulence characteristics within the vegetated flow (Stoesser et al., 2009).

(2) Large Eddy Simulation (LES) Method: Nadaoka and Yagi (1998) developed a two-dimensional shallow water model using LES techniques, introducing the concept of sub-depth scale turbulence. The model successfully simulated the hierarchical structure of turbulence and its effects on flow distribution, aligning well with experimental results. However, it is challenging for the model to capture changes in flow and turbulence characteristics in the horizontal direction across different depths. Su et al. (2003) also applied the three-dimensional LES model to study flow structures and eddy development in vegetated channels, finding that the LES model effectively simulated complex interactions between vegetation and turbulence. LES models can also capture the expansion and contraction of flow around vegetation and its impact on eddy formation. Yan et al. (2017) introduced an additional diffusion term into the LES model to account for the dispersion effect caused by the presence of vegetation, demonstrating its influence on turbulence. Cui and Neary (2008) used LES to capture the flow patterns around submerged vegetation, showing that the model could accurately replicate the exchange of momentum and turbulence between the vegetation and the surrounding flow. Overall, applying the Large Eddy Simulation (LES) method to the study of vegetated flow can significantly enhance the exchange of momentum and turbulence, making it a valuable tool in these studies. This method excels in simulating detailed turbulence characteristics and related interactions. However, when dealing with large computational domains or regions where fine-scale turbulent structures occupy only a small portion, LES may not be the most efficient choice for simulating overall flow characteristics in channels because LES requires finer computational grids, which increases the number of grid cells and, consequently, computational demands, leading to reduced computational efficiency (Sarkar, 2020).

1.4 Pool-Riffle Sequences

Pool-riffle sequences are among the most common geomorphic features in fluvial systems, playing a critical role in the structure and function of river channels. These alternating deep and shallow reaches are fundamental to river dynamics, sediment transport, habitat diversity, and ecological processes (Lei et al., 2023). The concept of pool-riffle sequences was first systematically studied in the early 20th century, with seminal work by Leopold and Wolman (1957), who identified these sequences as integral components of alluvial rivers. Their research established the basis for understanding the formation and maintenance of pools and riffles through balancing sediment transport and hydraulic forces. Subsequent studies expanded on this foundation, exploring these features' geomorphological and ecological significance. Pools, the deeper sections of these sequences, are especially significant due to their influence on hydraulic conditions, sediment storage, and aquatic habitats. Riffles are less likely to contain many fine sediments than pools because, during low flow periods, pools tend to collect finer materials. Consequently, riffles develop a protective layer known as armoring that is challenging for vegetation roots to penetrate (de Almeida & Rodríguez, 2011). This thesis will focus on the intricate structure of pools within pool-riffle sequences, particularly emphasizing their interaction with submerged vegetation. Submerged vegetation can significantly alter a pool's hydraulic dynamics, sediment distribution, and ecological functions. By exploring these interactions, the research aims to deepen the understanding of how vegetation influences pool formation, stability, and habitat provision within fluvial systems. This focus is essential for advancing river restoration efforts and improving the management of aquatic habitats in vegetated stream environments.

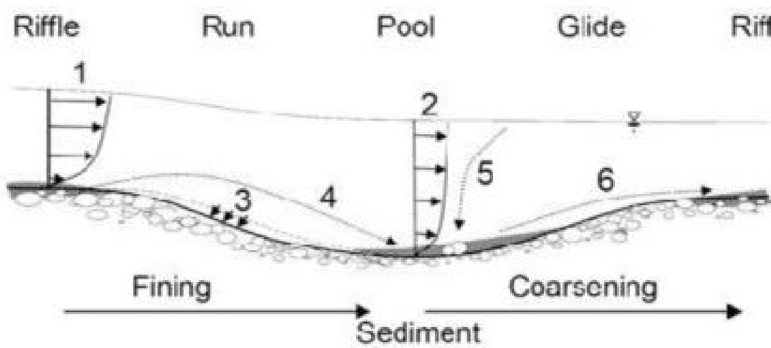

Figure 1.5 Schematic of a riffle-pool sequence at low flow, illustrating 1. flow acceleration, 2. deceleration above pools, 3. regressive run erosion, 4. pool refilling, 5. coarse grain accumulation from bank erosion, and 6. pool scouring with riffle deposition during high flows (source: Fuller, 2018).

1.4.1 Formation Mechanisms of Pools

A combination of hydraulic, sedimentary, and geomorphic factors influences the formation of pools in pool-riffle sequences. Pools are typically formed in areas of reduced flow velocity, where finer sediments are deposited. One of the primary mechanisms is flow convergence and divergence, where the convergence of flow at riffles accelerates the water, which then diverges and slows down in pools. This flow pattern contributes to the scouring of pools and the deposition of sediments in riffles (Lisle, 1986). Another significant factor is sediment sorting and transport, where the lower energy environment in pools allows for the deposition of finer particles. At the same time, riffles, with higher flow velocities, tend to winnow out finer sediments, leaving behind coarser materials (Buffington et al., 2004). Additionally, the interaction between channel geometry and bedform also plays a critical role in pool formation, with variations in channel width and curvature leading to the development of secondary currents that enhance pool scour (Thompson, 2006). Lastly, reduced turbulence and flow resistance in pools allow for settling sediments, contributing to the deepening of the pool (Dietrich & Whiting, 1989).

1.4.2 Hydraulic Dynamics of Pools

The hydraulic dynamics within pools are distinct from those in riffles, with significant implications for sediment transport, channel stability, and aquatic habitats. Flow velocities in pools are typically lower than in riffles, reducing shear stress and sediment transport capacity. The transition from riffle to pool often involves flow separation, creating zones of recirculating flow within the pool. These recirculation zones can trap sediments and organic matter, contributing to the pool's stability and ecological function (Wilcox & Wohl, 2006). Shear stress in pools is unevenly distributed, with the highest values usually found near the pool exit, where flow accelerates towards the downstream riffle. This shear stress distribution influences sediment erosion and deposition patterns within the pool. Additionally, pools often exhibit lower hydraulic roughness than riffles due to the finer sediment composition and smoother bed surface. This reduced roughness affects the flow structure and energy dissipation within the pool (Montgomery et al., 1995).

1.4.3 Sediment Dynamics in Pools

Pool sediment dynamics are closely linked to the hydraulic conditions and channel morphology. Pools act as temporary storage areas for sediments, playing a crucial role in the sediment budget of a river system. The lower flow velocities in pools favor the deposition of fine sediments, which can accumulate over time. The rate and extent of sediment deposition are influenced by factors such as flow regime, sediment supply, and channel morphology (Lisle & Hilton, 1992).

While pools are sites of sediment deposition, they also experience sediment scour, particularly during high-flow events. The balance between sediment deposition and scour determines the long-term stability of the pool (Carling, 1991). Furthermore, pools exhibit distinct sediment sorting patterns, with finer materials accumulating in the deepest parts and coarser materials deposited near the pool margins. Bedload transport through pools is typically reduced compared to riffles due to the lower shear stress and flow velocities. However, during high-flow events, pools can act as conduits for bedload transport, contributing to downstream sediment redistribution.

1.4.4 Morphological Characteristics of Pools

Pools are characterized by their depth, width, and sediment composition, which differ markedly from adjacent riffles. The depth of a pool is typically much greater than that of a riffle, with pools often being several times deeper. This depth is influenced by factors such as channel slope, sediment supply, and flow regime. Pools also tend to be wider than riffles, reflecting the lower flow velocities and the associated lateral expansion of the channel (Allan et al., 2021).

The sediment composition of pools is generally finer and more cohesive than that found in riffles due to the lower energy environment that favors the deposition of silts, clays, and fine sands. The longitudinal profile of pools often exhibits a concave shape, with the deepest point located downstream of the riffle crest (de Almeida & Rodríguez, 2011). These characteristics indicate the hydraulic conditions and reflect the geomorphic processes at play.

1.4.5 Human Impacts on Pool Dynamics

Human activities, such as river regulation, channelization, and land use changes, all impact pool dynamics, altering pool formation, maintenance, and ecological function. Flow regulation through dams and weirs can disrupt the natural processes that maintain pool-riffle sequences. Reduced flow variability can lead to the infilling of pools with sediments, while altered flow regimes can prevent the scour necessary for pool maintenance (Kondolf, 1997). River channelization, involving the straightening and deepening of channels, can eliminate pool-riffle sequences. The loss of these features reduces habitat diversity and alters sediment transport dynamics, leading to channel instability and ecological degradation (Brookes, 1987). Additionally, changes in land use, such as deforestation, agriculture, and urbanization, can alter the sediment supply to rivers. Increased sediment loads can lead to the rapid infilling of pools, while reduced sediment supply can prevent the formation of new pools (Trimble, 1997). Human activities that degrade water quality, such as pollution and nutrient loading, can impact the ecological function of pools. Poor water quality can reduce the suitability of pools as habitats for sensitive species and disrupt the natural processes that maintain pool structure (Allan, 2004).

1.4.6 Ecological Significance and Restoration of Pools

Pools are essential to the ecosystem, providing critical habitats for many aquatic organisms. Pools' physical and hydraulic characteristics create unique environmental conditions that support diverse biological communities. Pools contribute to habitat diversity within river systems by offering deep, slow-flowing environments that contrast with the shallow, fast-flowing conditions of riffles, thereby supporting a wide range of species, from benthic invertebrates to fish (Bisson et al., 1988). In addition to serving as diverse habitats, pools act as refuges for aquatic organisms during periods of low or high flow, offering protection from adverse hydraulic conditions. Pools' depth and flow structure provide stable environments where organisms can avoid predators and extreme flow velocities. Many fish species, particularly salmonids, utilize pools for spawning and rearing due to the fine sediments and stable flow conditions that provide suitable substrates for egg deposition and juvenile development (Beechie et al., 2005). Pools often exhibit lower water temperatures than riffles due to their depth and reduced exposure to solar radiation, creating thermal refugia for temperature-sensitive species, particularly during warm seasons (Ebersole et al., 2003). Moreover, pools are sites of organic matter accumulation, which provides essential food resources for aquatic organisms. The recirculating flow within pools can trap leaf litter, woody debris, and other organic materials, contributing to the overall productivity of the river system (Nakajima et al., 2006).

The restoration of pool-riffle sequences has become a key focus of river restoration efforts, particularly in systems impacted by human activities. Restoration strategies aim to recreate the natural processes that form and maintain pools, enhancing habitat diversity and ecological function. Restoring the natural flow regime, including reintroducing flow variability, is crucial for assembling and maintaining pool-riffle sequences (Schwartz et al., 2015). Managed flow releases from dams can help re-establish the dynamic processes that create and sustain pools. In addition to flow regime restoration, other strategies include reconfiguring channel morphology to promote the development of pool-riffle sequences, restoring sediment supply to balance deposition and scour processes, and improving water quality to support healthy aquatic habitats (Halket & Snelgrove, 2012; Harrison et al., 2011; Lei et al., 2023). These restoration efforts require a comprehensive understanding of the natural processes that govern pool-riffle dynamics and the specific conditions of the river system.

1.5 Formation of Ice Cover in Natural Rivers

In cold regions, rivers often form ice covers during winter. These ice formations alter the river’s surface boundary conditions, flow dynamics, and sediment transport, leading to an elevated upstream water level and potentially causing severe ice-related flooding (Sahu et al., 2024). Any obstruction in the channel, either point obstructions such as spur dikes and bridge piers or regional obstructions such as vegetation patches, will alter the river's original boundary conditions and flow conditions, including water level, average flow velocity across sections, ice transport, and sediment transport (Figure 1.6).

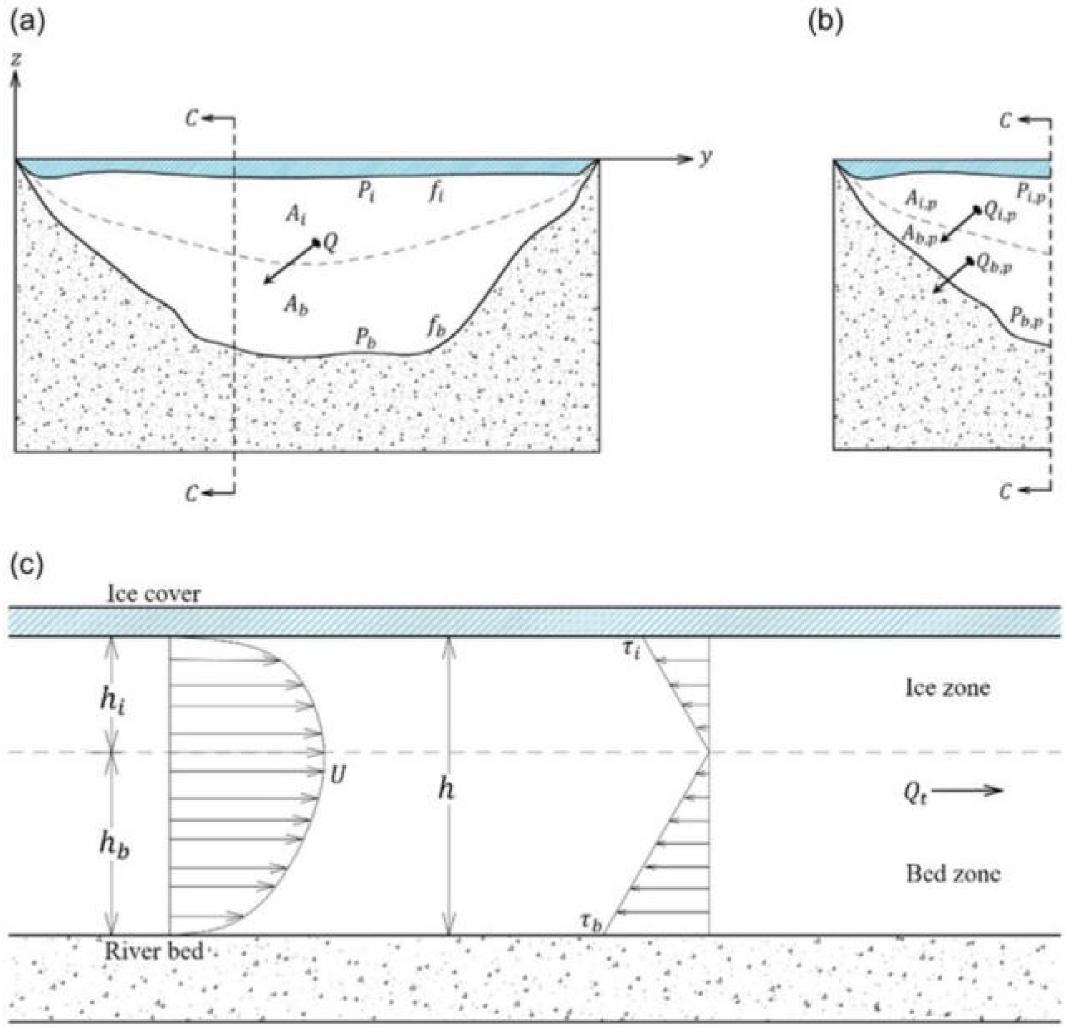

Figure 1.6 Flow characteristics in ice-covered river channels: (a) cross-sectional geometry, (b) partial cross-section view, and (c) vertical profiles of velocity and shear stress (source: J. Pan et al., 2023).

These changes significantly affect the flow fields under ice coves. The construction of hydraulic structures in cold regions must consider the impact of ice cover. In April 1987, the collapse of the Schoharie Creek Bridge on the New York State Thruway resulted in ten (10) deaths and five (5) vehicles falling into the river. The primary cause of the accident was the scouring of the bridge pier base by water flow beneath the ice cover (Hains & Zabilansky, 2012). A significant scour hole was observed upstream of the Melvin Price Lock and Dam foundation on the Mississippi River, which reappeared within a year after repairs. Researchers found through model testing that even a 100-year flood would not produce such a large scour hole. However, small flows under the ice cover were to blame for the incident, negatively impacting in-stream structures' functionality (Carr & Tuthill, 2012).

1.5.1 Local Scour Around Hydraulic Structures Under Ice Cover

Ice cover alters the flow velocity distribution, resulting in differences in local scour at hydraulic structures compared to open water conditions, such as changes in maximum scour depth and extent. Wang et al. (2008) conducted flume experiments to study the critical flow velocity for sediment movement under ice cover. They discovered that sediment transportation is more easily initiated under ice cover, indicating that local scour is more intense under ice cover conditions than in open flow. Ackermann et al. (2002) studied the effects of ice cover on local scour around cylindrical bridge piers using clear-water scour and live-bed scour. Their experimental data indicated that the maximum scour depth under ice cover increased by 25% to 35% compared to open-water conditions. Munteanu (2004) conducted experimental studies under various ice-cover conditions, including open water, complete ice cover, and partially ice-covered channel conditions. The most intense local scour around the bridge piers occurred under the partial ice cover, with the maximum local scour depth near the piers being approximately 55% greater than under open-water conditions. Hains and Zabilansky (2005) investigated the changes in local scour around cylindrical bridge piers under open-channel, fixed ice cover, and floating ice cover conditions. Their results showed that the maximum local scour depth under ice cover conditions was 21% greater than under open-water conditions. Additionally, the local scour processes under fixed and floating ice covers were similar, with an increase in ice cover roughness leading to greater local scour depths around the bridge piers.

Wu et al. (2014) conducted experimental studies on local scour around semi-circular abutments under ice cover, finding that the point of maximum scour depth occurs approximately 15 degrees upstream from the top of the abutment. Further investigation by Wu et al. (2015) was conducted on local scour around rectangular and semi-circular abutments under ice cover conditions, including the impact of protective layers formed during the scour process on local scour. They also developed an empirical relationship for predicting the maximum local scour depth:

$$\frac{y_m}{H} = A\left(\frac{U}{\sqrt{gH}}\right)^{\alpha}\left(\frac{d_{50}}{H}\right)^{\beta}\left(\frac{n_i}{n_b}\right)^{\gamma} \tag{1.3}$$

in which y_m represents the maximum local scour depth, U denotes the approaching flow velocity, H indicates the approaching water depth, d_{50} is the median grain size of the sediment, n_i is the ice cover roughness, and n_b represents the riverbed Manning roughness.

Namaee and Sui (2020) conducted experimental studies on local scour around bridge piers placed side by side under ice cover in a flume at the same cross-section. The study found that the degree of scour under ice cover is related to the strength of the horseshoe vortex and is influenced by the size of the piers and the spacing between them. Namaee and Sui (2019) also analyzed the impact of armor layers on the local scour depth of side-by-side bridge piers under ice cover conditions and the sedimentation initiation mechanism near the piers. They proposed a regression equation for side-by-side bridge piers' maximum local scour depth:

$$\frac{y_m}{y_0} = A\left(\frac{d_{50}}{y_0}\right)^{\alpha}\left(\frac{G}{D}\right)^{\beta}\left(\frac{n_i}{n_b}\right)^{\gamma} Fr^{\eta} \tag{1.4}$$

in which Fr represents the Froude number in the pier upstream, y_0 denotes the pier upstream water depth, D indicates the diameter of the piers, and G is the distance between two side-by-side piers.

The flow fields around in-stream structures are highly complex and have numerous influencing factors. Most experimental research on local scour around abutments, piers, or spur dikes under ice cover primarily involves dimensional analysis, examining factors such as spatial arrangement, hydraulic conditions, ice cover roughness, and sediment grain size. Through regression analysis, these studies have developed relationships for predicting local scour depth under ice cover within the specific range of experimental conditions. However, the resulting equations vary in form, and inputs depend on the experimental conditions. Due to limitations in flume experiments, factors considered, and the number of trials, most of these equations fit their experimental data well but do not align as closely with data from other experimental conditions.

1.5.2 Flow Fields Around Vegetation Patches Under Ice Cover

Understanding the flow fields around vegetation patches under ice cover is critical for advancing knowledge in riverine hydraulics and ecology, particularly in cold regions where ice cover significantly influences hydrodynamic processes. The interaction between flow, vegetation, and ice cover affects sediment transport, nutrient cycling, and habitat availability, essential for maintaining the ecological balance in cold-water river systems. Recent studies have focused on unraveling the complexities of these interactions, providing insights into how ice cover modifies flow patterns around vegetation patches, which in turn affects the physical and biological processes in these environments.

Flow fields around vegetation patches are inherently complex, influenced by vegetation density, morphology, and spatial arrangement. In open-channel conditions, vegetation patches act as roughness elements, altering the flow structure by creating zones of flow deceleration and acceleration, inducing turbulence, and affecting sediment deposition patterns (H. M. Nepf, 2012). The flow resistance vegetation offers is typically quantified using parameters such as drag coefficient and vegetation density (Nepf, 1999). The interaction between flow and vegetation can result in the formation of coherent structures, such as vortices and wakes, which play a significant role in sediment transport and nutrient distribution within river systems (Nikora, 2010). Ice cover introduces additional complexity to flow fields around vegetation patches. The presence of ice alters the flow structure by imposing a rigid boundary at the water surface, reducing vertical mixing and modifying the velocity profile within the water column. Under ice cover, the flow velocity near the ice-water interface is typically lower than in open-channel conditions, redistributing shear stress and turbulence within the flow (Barahimi & Sui, 2024b; Smith & Ettema, 1997). This change in flow dynamics can significantly impact the interactions between flow and vegetation, influencing sediment transport, nutrient exchange, and habitat formation.

Barahimi and Sui (2023) conducted flume experiments to investigate the flow structure around submerged flexible vegetation patches under ice-covered conditions. Their results showed that ice cover reduced the flow velocity within the vegetation patch, particularly near the bed, leading to increased sediment deposition. A field study investigated the interactions between flow, ice, and adjacent riparian floodplains in northern Canadian rivers (Prowse & Culp, 2011). The observations highlighted how seasonal ice affects the distribution of flow velocities and shear stress around vegetation patches. They addressed that river ice has been identified as a significant and often primary cause of flooding in cold-region rivers, influencing a wide range of abiotic and biotic processes within the river channel and nearby riparian floodplains.

Modifying flow fields around vegetation patches under ice cover has valuable ecological implications. Vegetation patches play a critical role in providing habitat for aquatic organisms, stabilizing riverbanks, and promoting biodiversity. The altered flow conditions under ice cover can impact the availability of these habitats, particularly during winter when flow velocities are reduced and sediment deposition increases. For instance, Prowse and Culp (2011) emphasized that ice can create microhabitats with distinct thermal and flow conditions, crucial for overwintering fish and invertebrates. Additionally, the changes in sediment transport dynamics caused by ice cover can lead to the formation of new geomorphic features, such as point bars and mid-channel islands, which further contribute to habitat diversity within river systems (Gurnell et al., 2012). However, the increased scour around vegetation patches during ice melt events can also threaten the stability of these patches, particularly in regions where ice cover is subject to frequent fluctuations.

1.6 Hypothesis

The present study hypothesizes that the interaction between obstructions, such as spur dikes and submerged vegetated patches, under ice cover leads to changes in bed deformation and flow field characteristics. The complexity of these interactions under ice-covered conditions is expected to exceed the effects observed under open-water conditions due to the additional influence of ice cover on flow dynamics and sediment transport. This study specifically focuses on the local scour around submerged angled spur dikes, flow field changes around submerged spur dikes, and the interactions with submerged vegetated patches in pools under ice cover.

1. **Local Scour Around Spur Dikes Under Ice Cover:** It is well-established that ice cover increases the severity of local scour around hydraulic structures due to the altered flow regime and reduced turbulence near the ice-water interface. The hypothesis is that the local scour depth around submerged spur dikes under ice cover will be greater than open channel conditions, primarily due to the enhanced flow constriction and ice cover, which shifts the velocity profile closer to the bed. Additionally, the geometry and orientation of the spur dike relative to the flow direction will play a critical role in determining the extent of scour, with more pronounced effects expected for spur dikes positioned at sharper angles to the flow. The presence of ice cover is hypothesized to amplify the downstream extension of the scour hole, as the restricted vertical mixing and increased flow velocity near the bed will lead to more aggressive sediment entrainment.
2. **Flow Field Changes Around Submerged Spur Dikes Under Ice Cover:** The interaction between flow and submerged spur dikes under ice cover is hypothesized to be more complex than under open channel conditions. Ice cover suppresses turbulence and reduces vertical velocity gradients, affecting the wake and vortex formation around submerged structures. The hypothesis is that ice cover will lead to a more stable and elongated wake region downstream of the submerged spur dike, with reduced turbulence intensity and altered shear stress distribution. This modification of the flow

field is expected to influence sediment transport processes, potentially leading to increased sediment deposition in the wake region and altering the scour patterns around the spur dike. Additionally, the ice cover is expected to enhance the lateral spreading of the flow around the submerged structure, potentially leading to broader zones of sediment mobilization and deposition.

3. **Influence of Ice Cover Roughness and Thickness on Scour and Deposition Patterns:** Ice cover roughness is a critical factor influencing flow dynamics under ice-covered conditions. The hypothesis is that increased ice cover roughness will enhance the redistribution of shear stress and turbulence intensity within the flow field, leading to more irregular scour and deposition patterns around spur dikes. The effect of ice cover roughness is hypothesized to create highly variable and site-specific scour and deposition patterns, with valuable implications for river management and infrastructure design in cold regions.

4. **Interaction Between Submerged Vegetated Patches in Pools Under Ice Cover:** The presence of submerged vegetated patches in pools under ice cover adds complexity to the flow field. Vegetation is known to introduce flow resistance and create zones of reduced velocity and turbulence, which can influence sediment transport and deposition patterns. The hypothesis is that the interaction between submerged vegetated patches under ice cover will result in a more heterogeneous flow field, with localized zones of high-velocity zones and turbulent kinetic energy near the boundary between vegetation and flow, and reduced flow velocities and enhanced deposition within the vegetated patches. The presence of ice cover is expected to further complicate this interaction by

suppressing vertical mixing and enhancing the lateral flow components, leading to more pronounced secondary currents. The combined effect of the vegetated patches and ice cover is hypothesized to create complex flow fields highly susceptible to ice cover roughness and thickness variations.

5. **Combined Effect of Ice Cover and Vegetation Height on Flow:** The hypothesis extends to the combined effects of ice cover and vegetation height on the overall flow structure and bed deformation. Higher vegetation is anticipated to lead to greater flow resistance and more substantial alterations to the velocity profile under ice cover, with the most significant effects observed near the bed. This increased flow resistance is expected to result in a more pronounced flow field change, with a high-velocity core forming closer to the water surface and more consistent variations within the vegetated patches. Additionally, the hypothesis suggests that the interaction between high vegetation and rough ice cover will lead to the most significant deviations from open channel flow conditions, with complex flow structures emerging that are difficult to predict using existing models.

This study hypothesizes that the interaction between local and regional obstructions under ice cover leads to complex and highly variable flow field changes and bed deformation patterns. The presence of ice cover, combined with the effects of vegetation patches and spur dike geometry, introduces significant challenges in predicting flow structure and scour processes. The study aims to comprehensively understand these interactions, with implications for designing and managing hydraulic structures in cold regions.

1.7 Objectives

The primary objective of this PhD study is to investigate the complex interactions between bed deformation and flow field changes caused by obstructions under ice cover. Specifically, the study focuses on two distinct areas: (1) the local scour and flow field changes around spur dikes under ice cover, and (2) the flow field changes around submerged vegetation patches in pools under ice cover. By understanding these interactions, this research aims to provide valuable insights into the underlying mechanisms that govern flow and sediment dynamics in ice-covered rivers, contributing to the broader knowledge required for effective river management and infrastructure design in cold regions.

1.7.1 Local Scour and Flow Field Changes Around Spur Dikes Under Ice Cover

Spur dikes are hydraulic structures designed to protect riverbanks and control flow direction. However, the local scour processes around these structures can be significantly altered under ice cover. The first objective of this study is to analyze the extent and characteristics of local scour around spur dikes under ice-covered conditions, which will involve:

1. **Evaluating the impact of ice cover on the local scour depth and pattern around spur dikes:** The study assesses how ice cover modifies the scour depth and pattern compared to open-water conditions, which includes understanding the influence of ice roughness and the positioning of the spur dike relative to the flow direction.
2. **Investigating the flow field changes induced by spur dikes under ice cover:** By analyzing the flow velocity, turbulence, and shear stress distribution around spur dikes, the study will identify the key factors that influence flow field changes under ice cover,

which includes the effect of ice-induced flow constriction and how it alters the flow structure near the spur dike.

3. **Developing predictive models for scour around spur dikes under ice cover:** The study aims to develop and validate predictive models that accurately estimate the local scour depth around spur dikes under varying ice-covered conditions. These models will consider factors including ice cover characteristics, flow conditions, and spur dike geometry.

1.7.2 Flow Field Changes Around Submerged Vegetation Patches in Pools Under Ice Cover

Submerged vegetation patches are critical in stabilizing riverbeds, enhancing habitat diversity, and influencing sediment transport. Under ice cover, the interaction between flow and vegetation becomes more complex due to the altered hydraulic conditions. The second objective of this study is to explore the flow field changes around submerged vegetation patches in pools under ice cover, which will involve:

1. **Analyzing the impact of ice cover on flow velocity and turbulence within and around submerged vegetation patches:** The study will focus on how ice cover affects the flow velocity distribution, turbulence intensity, and the formation of vortices within and around submerged vegetation patches.
2. **Evaluating the combined effects of ice cover and vegetation on the flow structure in pools:** The objective is to explore the synergistic effects of ice cover and submerged vegetation on the overall flow structure in pools, which includes analyzing how

different ice cover conditions (e.g., smooth and rough ice) interact with vegetation to create complex flow patterns that impact sediment transport and bed morphology.

1.7.3. Comparative Analysis of Open-Channel Flow, Smooth Ice-Covered, and Rough Ice-Covered Conditions

Given the distinct differences in flow behavior under open-channel, smooth ice-covered, and rough ice-covered conditions, an essential objective of this study is to conduct a comparative analysis of these scenarios:

1. **Comparing velocity profile distributions under different cover conditions:** The study will compare the distributions observed under open-channel flow, smooth ice-covered, and rough ice-covered conditions, which will provide insights into how each condition influences flow structure and the implications for sediment transport and scour around hydraulic structures and vegetation patches.
2. **Assessing the implications of different cover conditions on river management:** The findings from the comparative analysis will be used to conclude the practical implications of these flow conditions for river management, flood control, and the design of hydraulic structures in cold regions.

This PhD study aims to comprehensively understand the interactions between bed deformation and flow field changes caused by local and regional obstructions under ice cover. By focusing on the specific challenges posed by local scour around spur dikes and flow field changes around submerged vegetation patches in pools under ice cover, this research will contribute valuable knowledge to the field of cold-region hydraulics and inform the design and management of river systems in such environments.

1.8 Thesis Structure

This thesis is organized into six chapters, each building on the previous one to comprehensively understand the bed deformation and flow field changes caused by obstructions under ice cover. The chapters are structured to guide the reader from the foundational materials and methods through detailed experimental investigations and analyses, concluding with the implications and contributions of the study to the field of cold-region hydraulics.

Chapters 3 through 5 are structured to follow the chronological order of experimental dates, enabling a cohesive progression of research insights. Chapter 3 focuses on local scour around submerged angled spur dikes, investigating how design parameters, such as height, length, and alignment angle, affect scour depth and morphology. This chapter addresses structural impacts, providing foundational insights into the influence of submerged obstructions on sediment dynamics. Chapter 4 builds upon these findings by analyzing turbulent flow structures around the spur dike to elucidate the causes of observed scour patterns from Chapter 3. This analysis focuses on turbulence characteristics, including sweeps and ejections, which are critical in sediment transport processes. Together, Chapters 3 and 4 provide a comprehensive understanding of local scour mechanisms in ice-covered channels.

Chapter 5 transitions into eco-hydraulics, expanding the research from structural obstructions to vegetative impacts. Influenced by insights from cold region engineering and collaboration with Dr. Sediqi, this chapter investigates how submerged vegetation in ice-covered pools affects flow resistance, turbulent kinetic energy, and velocity profiles. This chapter reflects an integration of eco-hydraulic principles, aligning with emerging trends that emphasize sustainable and resilient river management strategies. Note that the scour pattern differed between simulated and measured results, with the simulation showing a more symmetrical pattern than observed in the field. This discrepancy may stem from minor errors in field scour measurement, such as slight inaccuracies in measuring equipment alignment or natural variability in sediment placement during tests (such as initial leveling). Due to these differences, the terrain elevation changes were not symmetrically analyzed here as they were for the localized obstruction analysis in previous chapters.

The progression across these chapters highlights a systematic exploration from structural to vegetative impacts on flow dynamics, presenting a holistic approach to understanding and managing cold-region channels.

Chapter Two: Materials, Equipment, and Experimental Design

Chapter Two serves as the foundation for the experimental work presented in this thesis. This chapter provides a detailed overview of the materials, equipment, and methodologies used throughout the study. The chapter begins by describing the characteristics of the experimental flume, including its dimensions and flow capabilities, which are critical for replicating riverine conditions under controlled laboratory settings.

Following this, the chapter elaborates on the various apparatuses used in the experiments, such as the models of submerged spur dikes and vegetated patches. The design and construction of these models are described in detail, ensuring that their relevance to real-world conditions is clearly understood. The chapter also discusses the ice cover simulation, including how different ice cover conditions (smooth and rough) were replicated within the flume. The sand used for simulating the riverbed is another critical component, and its composition, grain size distribution, and packing methods are thoroughly explained to highlight their impact on scour and sediment transport processes.

The experimental design section of this chapter outlines the procedures followed in conducting the experiments, including the setup configurations, flow conditions, and measurement techniques. The design rationale is provided to ensure that the experiments accurately reflect the dynamic interactions between flow, bed deformation, and obstruction under ice cover. This chapter is critical as it lays the groundwork for the experimental results and analyses discussed in the subsequent chapters.

Chapter Three: Local Scour Around Submerged Spur Dikes Under Ice Cover

Chapter Three delves into the investigation of local scour around submerged spur dikes with varying orientation angles under ice cover. This chapter is focused on understanding how ice cover influences the scour depth and pattern compared to open-water conditions. The study examines different orientation angles of the submerged spur dikes to assess their impact on the scour process.

The chapter begins by reviewing the existing literature on local scour around hydraulic structures, particularly under ice-covered conditions, to provide context for the experiments. The results of the experiments are then presented, highlighting the differences in scour depth and pattern due to the presence of ice cover. The findings demonstrate that ice cover significantly alters the flow velocity profile, leading to more pronounced and extensive scour around the spur dikes.

This chapter also discusses the implications of these findings for the design and placement of spur dikes in cold-region rivers. By understanding the relationship between spur dike orientation, ice cover, and local scour, this chapter provides valuable insights into mitigating scour risks and enhancing the stability of hydraulic structures in ice-affected environments.

Chapter Four: Flow Field Changes Around Submerged Spur Dikes Under Ice Cover

Building on the findings of Chapter Three, Chapter Four shifts the focus to the flow field changes induced by submerged spur dikes under ice cover. This chapter explores the flow velocity, turbulence, and shear stress distribution modifications caused by submerged spur dikes in ice-covered conditions.

The chapter begins by discussing the theoretical background of flow structures around submerged obstructions, emphasizing how ice cover alters these flow structures. The experimental results are then presented, showing how ice cover affects the wake region downstream of the spur dikes, leading to flow stability and turbulence intensity changes.

The findings reveal that ice cover increases the flow resistance and alters the flow path, which could lead to more complex sediment dynamics. This chapter is valuable in understanding the broader impacts of ice cover on riverine hydraulics, particularly in designing effective river engineering solutions.

Chapter Five: Flow Structure Changes in Vegetated Pools Under Ice Cover

Chapter Five expands the focus to examine the flow structure changes in regional obstruction in channels (vegetated pools) under ice cover. This chapter explores the interaction between submerged vegetation patches and ice cover, emphasizing how these interactions affect flow dynamics and sediment transport.

The chapter begins with a review of the role of vegetation in modifying flow structures in open channels and how these roles change under ice-covered conditions. The experimental results are then presented, showing how ice cover alters flow velocity profiles, turbulence intensity, and sediment deposition within and around vegetated patches.

The findings reveal that ice cover enhances the flow resistance created by vegetation, leading to more complex flow patterns and localized sediment accumulation. This chapter provides insights into the ecological implications of these flow structure changes, particularly regarding habitat formation and sediment management in vegetated riverine environments.

Chapter Six: General Conclusion

Chapter Six provides a comprehensive summary of the key findings and contributions of the study. This chapter synthesizes the results from the previous chapters, highlighting the significant insights gained into bed deformation and flow field changes caused by local and regional obstructions under ice cover.

The chapter discusses the study's implications for river management and hydraulic engineering in cold regions. It addresses the limitations of the research, acknowledging the challenges and constraints encountered during the experiments and suggesting areas for further investigation.

Finally, Chapter Six outlines potential directions for future research, emphasizing the need for continued exploration of the complex interactions between ice cover, flow dynamics, and sediment transport in cold-region rivers. This chapter concludes the thesis by reinforcing the importance of understanding these interactions to develop effective and sustainable river management practices.

2. CHAPTER TWO: MATERIALS, METHODS AND EXPERIMENTAL DESIGN

In Chapter Two, the materials and methods for the experimental and numerical study are meticulously chosen to simulate natural river conditions as closely as possible. This chapter details the experimental design, focusing on the materials and methodologies used.

The flume, which forms the core of the experimental setup, is described in detail, covering its dimensions, slope, and overall functionality. Emphasis is placed on how the flume's configuration is designed to replicate real-world conditions for examining bed deformation and velocity field changes. The study also employs a variety of equipment to measure and monitor flow characteristics, such as velocity, discharge, and stage, with detailed descriptions provided for each instrument. The purpose, specifications, and data processing methods are discussed, underscoring these tools' importance in ensuring the experimental data's accuracy and reliability. The sand used in the study is analyzed, focusing on its grain size distribution and standard deviation, factors that significantly influence sediment transport dynamics. The simulation of smooth and rough ice covers within the flume is also discussed, essential for replicating the conditions under ice cover and understanding their effects on river restoration structures like spur dikes and vegetation patches.

This chapter also introduces the submerged spur dike models constructed from marine plywood. These models play a vital role in the experimental setup, allowing for the detailed study of flow and sediment interactions with river restoration structures under ice cover. The artificial submerged vegetation patches, representing rigid leafless vegetation, are also crucial for this study. The characteristics of these vegetation patches, such as height, are detailed to highlight their impact on flow patterns and sediment transport within the flume.

Finally, this chapter discusses the application of numerical modeling using Flow-3D, a Computational Fluid Dynamics (CFD) software. Flow-3D simulates and analyzes the complex interactions between flow, vegetation, and submerged structures, providing additional insights into the experimental findings and enhancing the overall understanding of the study's objectives.

2.1 Experimental Flume and Apparatus

The experiments were conducted in a large-scale outdoor flume, measuring 38 meters in length, 2.0 meters in width, and 1.3 meters in depth, as depicted in Figure 2.1. The flume bed was set at a longitudinal slope of 0.2%. Two different water depths, 20 cm and 30 cm were utilized by adjusting the tailgates at the downstream end of the flume. These depths were chosen to reflect real-world scenarios, where spur dikes are constructed in wide channels and submerged vegetation typically thrives in the shallow regions of rivers. Water was introduced into the system using a gravitational pump and two valves that controlled the flow to the upstream holding tank, ensuring a constant water discharge. The target flow rate for this study was maintained by adjusting the valves. The holding tank, with a capacity of 90 m^3, was designed to sustain a stable water level throughout each experimental session. The flume's aspect ratio, defined as the ratio of width to water depth (W/H), indicated that the flume could be categorized as a wide flume, given that the aspect ratio exceeded 5 to 10 for both water depths tested. This classification suggests that the influence of the side walls and secondary currents in the central zone of the flume can be considered negligible (Chow, 2009). Further CFD simulation for non-vegetated open channel flow also verifies the assumption that secondary currents can be ignored (Figure 2.2). Two sandboxes were positioned 10.2 meters apart within the flume. The upstream sandbox measured 5.60 meters in length, 2.00 meters in width, and 0.30 meters in depth, while the downstream sandbox was slightly longer at 5.80 meters in length but maintained the same width and depth. Each sandbox was equipped with a plexiglass viewing window, allowing for clear observation of the scouring and deposition processes occurring around the sandbed.

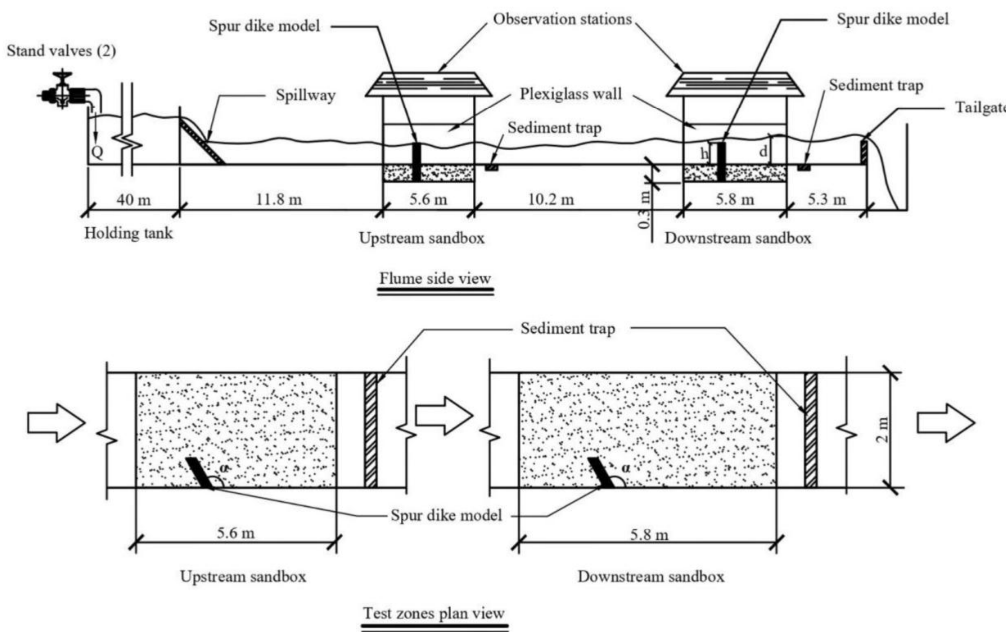

(a) Flume schematic for submerged angled spur dike setup

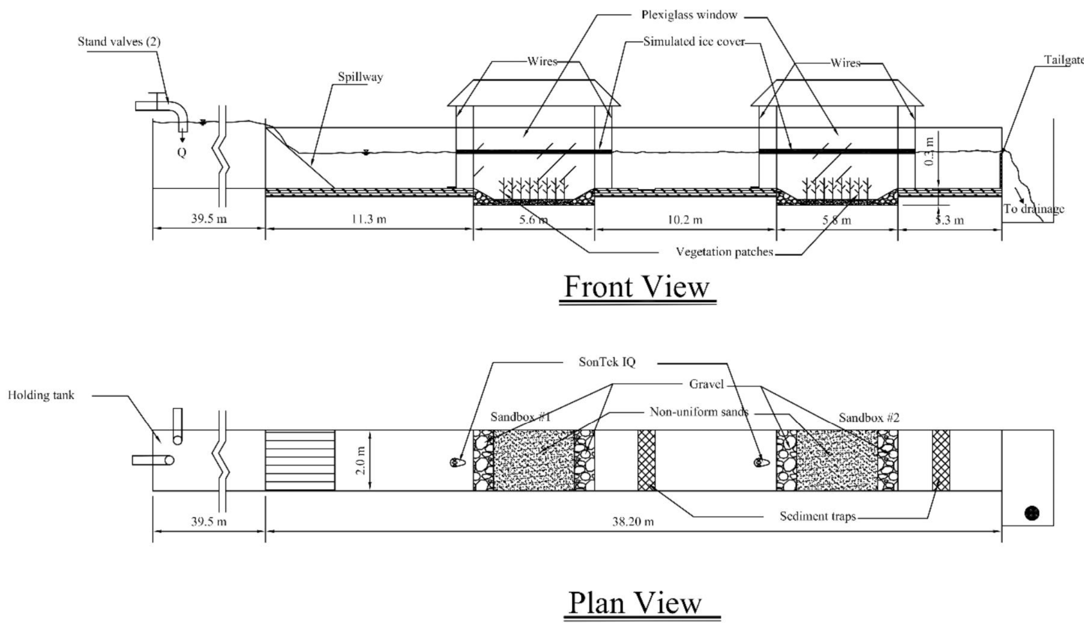

(b) Flume schematic for submerged rigid leafless vegetation patch setup.

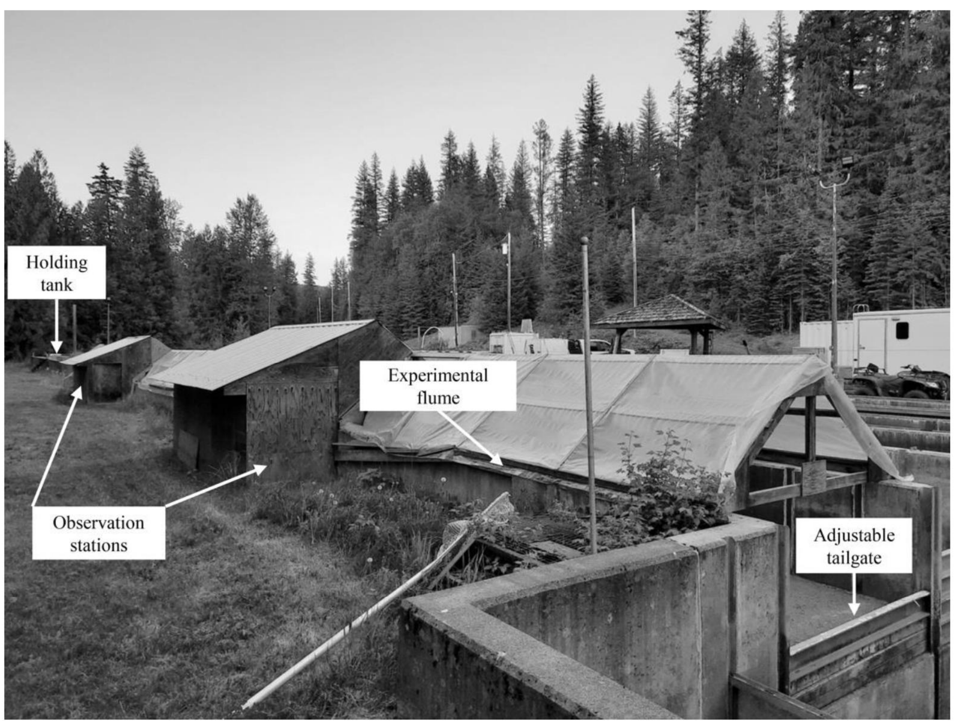

(c) Field photo of the experimental flume used

Figure 2.1 The layout of the experimental flume.

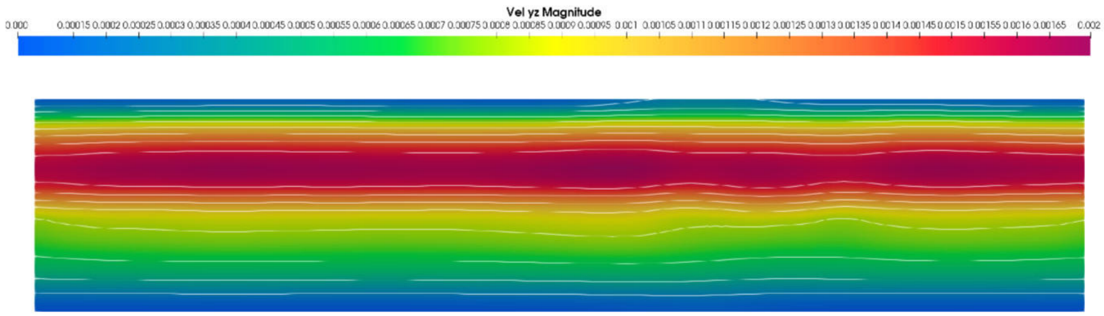

Figure 2.2 Flow-3D simulation results of the cross-sectional velocity contour. Contour lines are distributed evenly in the flume cross-section, indicating that the impacts of secondary currents and side walls are negligible.

In this experimental study, a down-looking Acoustic Doppler Velocimeter (ADV) with a frequency of 10 MHz, developed by Nortek, was employed to measure instantaneous three-dimensional velocity components at a sampling rate of 25 Hz, with a sampling volume of 0.25 cc. The ADV, known for its precision, reliability, and ease of use, was crucial in recording velocity data, particularly in turbulent flow around river restoration structures under ice cover. Each measurement session lasted 2 minutes, yielding 3,000 data points per location, with vertical intervals of 10 mm between consecutive points in each velocity profile. The ADV's capability to measure velocity components in the x, y, and z directions was leveraged to determine critical flow characteristics such as shear velocity, turbulent kinetic energy, and overall flow field dynamics around structures like submerged spur dikes. River hydraulic studies (Ruonan et al., 2016; Zhao et al., 2021) have highlighted the ADV's effectiveness in capturing detailed flow properties, making it an invaluable tool in this research.

The study also considered the impact of Doppler noise and turbulence on velocity measurements, which required careful data post-processing. The filtering method proposed by Goring & Nikora (2002) and Wahl (2000) was applied to eliminate noise and ensure the integrity of the data, particularly when analyzing bed shear stress. Given that raw ADV data may contain noises, proper filtering and examination were essential steps before further analysis. The velocity measurements were processed using WinADV software, ensuring that data with an average correlation of less than or equal to 70% were filtered out to maintain accuracy.

A SonTek-IQ Plus maintained a constant flow rate over a 24-hour period and ensured the scour process's equilibrium state. With advanced post-processing functions, this robust apparatus accurately measured average velocity and water depth. To prevent sediment starvation, as described by Yang et al. (2017), sandboxes were designed deeper than the maximum equilibrium scour depth, and sediment traps were cleaned and replenished after each run. Both experimental data and past research confirmed that a 24-hour run duration effectively avoided sediment starvation (Barahimi & Sui, 2024b; Jafari & Sui, 2024; M. Namaee et al., 2023; Sediqi et al., 2024; P. Wu et al., 2016). Equilibrium flow within the vegetated zones, particularly in streamwise velocity, indicated a fully developed state, essential for analyzing vegetation impacts on flow and sediment transport (Figure 5.7, PF 4). Reaching equilibrium scour depth, which depends on structural and hydraulic factors, is more complex under ice cover, as noted by Oliveto and Hager (2002). Namaee and Sui (2020) recommend a 24-hour duration for scour equilibrium under ice-covered flow, while Mia and Nago (2003) suggest a criterion of less than 1 mm/hour scour fluctuation. Using this guideline, scour changes at the dike tip were monitored with ±0.1 mm accuracy, confirming that 24 hours was sufficient to reach equilibrium without sediment depletion.

Despite the use of a gravitational pump at the Quesnel River Research Center (QRRC), SonTek IQ Plus readings slightly varied over time due to several factors. Flow instabilities can occur as gravitational pumps, which depend on natural elevation differences, may experience minor flow rate variations based on head changes. Groundwater sources, while generally stable, are subject to fluctuations in the water table from factors like nearby irrigation or natural recharge and discharge events, which can slightly alter pressure and flow. Additionally, small shifts in the hydraulic gradient driving the gravitational pump may introduce minor variations. Environmental factors, such as wind, atmospheric pressure changes, and water temperature gradients, can also subtly affect flow or measurement precision, which can be detected by the highly sensitive SonTek IQ Plus. Finally, sensor calibration drift and electrical noise may contribute to slight variations in readings.

2.2 Submerged Spur Dike and Vegetated Pool Setup

Since the erosive process is caused by the shear stress imposed on the bed sediment (Khan et al., 2016), the influence of spur dike materials was not investigated. Waterproof marine plywood was selected to build the vertical wall spur dikes. The average depths in the two sandboxes vary marginally due to the smaller flume slope of 0.20%. Therefore, the height of the spur dikes above the initial sand bed was set as 15 cm and 20 cm in the upstream sandbox and 20 cm and 25 cm in the downstream sandbox to keep the overtopping ratios in the two sandboxes varying within 5.0%. Richardson and Simons (1984) proposed that dikes with angles between 100° and 110° may be applied to channelize or direct flow. However, Jansen et al. (1979) stated that no uniform standards should be set for all spur dikes. Thus, the model spur dikes with a uniform spur dike width of 0.05 m were set up at alignment angles of 90°, 120°, and 135° in the current study.

The design length of submerged spur dikes in practice is often set as a percentage of the channel width, typically ranging from 10% to 25% of the bank-full width. Richardson et al. (1975) recommend lengths of 10% to 15% of channel width for straight reaches and large-radius bends to effectively manage flow and reduce scour near the structure. Studies such as Bahrami-Yarahmadi et al. (2020) have explored spur dike lengths from 9% to 44% of channel width in various hydraulic conditions to achieve objectives like flood control, bank stabilization, or navigation. Generally, a ratio of 0.1 to 0.25 is applied in real-world projects, tailored to site-specific hydraulic and sediment transport requirements. In this study, a 50 cm dike length—25% of the 2 m channel width—was selected, with a 35 cm length (cosine of 50 cm) used for comparison to assess the effectiveness of an alternate length.

Spur dikes are often deployed in groups in river engineering; however, to establish a foundational understanding of flow and scour mechanisms under ice-covered conditions, the research was designed to isolate the hydrodynamic behavior around individual submerged spur dikes. By focusing on single-dike dynamics, this study aims to provide insights that can inform future research on grouped configurations. Kuhnle et al. (2002) found that scour tail lengths remain under 20 times the normal length, regardless of dike alignment angles, supporting the use of a single spur dike in the experimental flume to capture the complete scour profile within the sandbox's dimensions. While grouped spur dikes in practice create complex interactions, such as shielding effects that modify flow and sediment transport between structures, leading to more pronounced scour at individual dikes (Ning et al., 2019).

Figure 2.3 The submerged angled spur dike model was built with marine plywood (120° alignment with flume wall, water flowing from left to right).

The study examined a flow depth of 20 cm from the flume's false floor (30 cm in the pool zone) to simulate shallow river environments. In each sandbox, a pool is constructed. Each pool consists of three sections, namely, entrance, pool center (or deep pool), and exit section, as shown in Figure 2.4. In this study, the pools were built with three different slopes for the pool's entrance and exit sections. Three different slopes for entrance and exit sections of the pools were first trialed in non-vegetated channels under open channel conditions, namely, 5°, 7°, and 10°. The 5° and 7° slopes for the entrance and exit sections revealed significant velocity variations in the transition between the deep pool and slopes of the pools, as indicated by ADV measurements in the unvegetated open channel. The limited pool area at these 5° and 7° slopes prevented fully developed flow and constrained the planting of additional vegetation arrays. Consequently, a 10° slope for both entrance and exit sections was chosen for the numerical model to address these limitations. The non-uniform gravels were used as the bed material of both pool entrance and exit sections, with a median particle size of 10 cm. The gravels used in this study are sourced from the Quesnel River. Non-uniform sand with a median particle size (d_{50}) of 0.90 mm was used along the deep pool section. The pool entrance section features an increase in flow depth, forming a decelerating zone; the deep pool, characterized by a flat channel bed, served as a transition zone; and the pool exit section, with a decreasing flow depth, generated accelerating flow. One case study demonstrates that the slopes of the pool entrance and exit sections for natural pools range from 4° to 7.80° (Nosrati et al., 2022), suggesting that the slopes of entrance and exit sections used in this study reasonably approximate actual conditions found in natural rivers.

(a)

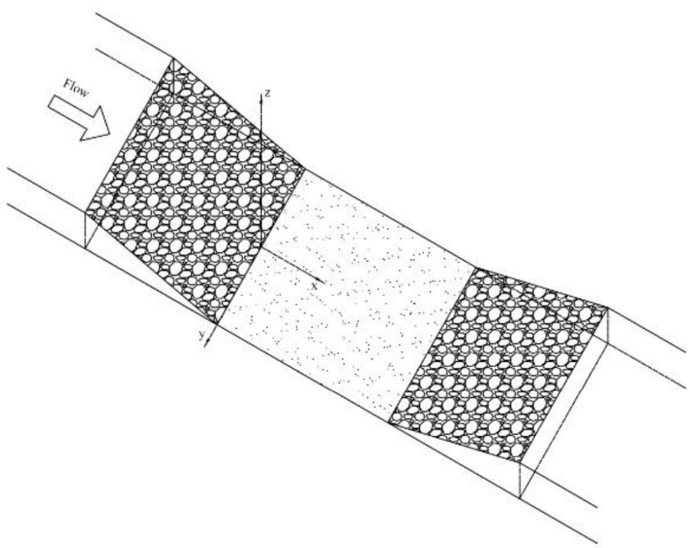

(b)

Figure 2.4 (a) Picture of the non-vegetated pool; (b) Pool section and the cartesian coordinate system for the experimental setup.

In natural environments, the distribution of aquatic plants is typically random, with vegetation forming communities that are neither symmetrical nor uniformly distributed. Engineered stream restoration projects, however, could benefit from adopting standard practices that mimic these natural patterns. Implementing a staggered arrangement of vegetation in such projects can simplify numerical simulations while enhancing biodiversity, improving habitat complexity, and providing better erosion control. Therefore, in addition to single circular vegetation setups, paired or staggered vegetation groups should be considered to achieve these benefits (Fu et al., 2021; Tinoco et al., 2020). In this study, plastic artificial flower stems with diameters of 0.5 cm were used to simulate rigid vegetation, such as common reeds (Phragmites australis). These synthetic vegetation stems were anchored to the sand bed of the deep pool section and arranged in staggered configurations with a spacing distance of 20 cm between adjacent stems in the same row to cover the sand bed of the entire deep pool section.

The vegetation heights of 10 cm and 15 cm were selected to balance research objectives with logistical constraints. These heights simulate typical submerged vegetation found in natural or engineered channels, where vegetation impacts flow resistance, sediment transport, and turbulence. Field observations show that submergence ratios (water depth to vegetation height) commonly range between 1 and 2 for rigid vegetation Lu et al. (2024). This range ensures full submergence while allowing vegetation to influence flow dynamics. Studies on aquatic vegetation like Zostera noltii similarly report vegetation heights of 10 to 30 cm, reflecting realistic conditions where vegetation affects both near-bed and water column flow characteristics (Paul et al., 2012). Practical constraints, including the flume dimensions, also influenced the choice, as these heights ensured full submergence under the flow conditions, crucial for studying interactions between flow and submerged vegetation.

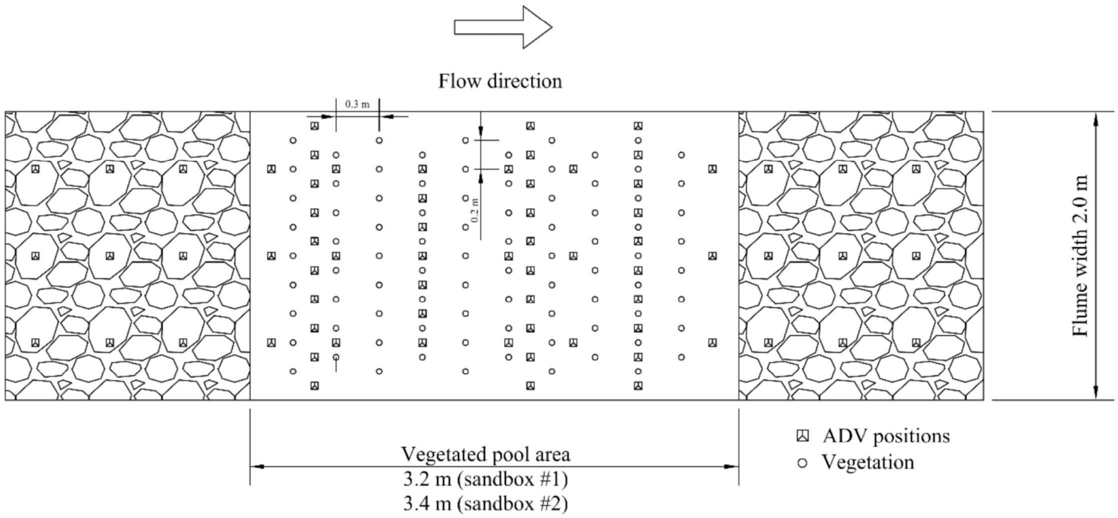

Figure 2.5 Top view of a vegetation zone and ADV measurement positions within the pool area.

The spacing pattern in this study was chosen to replicate realistic vegetation densities observed in natural and engineered aquatic environments, allowing flow interaction with individual stems while maintaining consistent density. In many studies, similar spacings of 20 cm to 30 cm between vegetation stems and 30 cm to 60 cm between rows are used to balance flow resistance and flow-through, simulating vegetation arrangements that promote turbulence and sediment deposition without excessive flow blockage (John et al., 2023; USDA, 2021). This arrangement reflects common practices in engineered vegetation patches, where spacing is tailored to project goals and environmental needs, ensuring sufficient flow interaction while maintaining vegetation stability against erosion. In flume studies, such as those by Bouma et al. (2005) and Paul et al. (2012), similar spacing patterns have been applied to explore flow-vegetation interactions, facilitating turbulence and wake formation while allowing comparisons with prior research. The selected 20 cm by 30 cm pattern in this study thus aligns with these established practices, supporting both experimental control and real-world relevance in assessing flow dynamics and sediment transport.

2.3 Sediments and Gravel

The sandboxes were filled with non-uniform sediment, with median particle sizes of 0.58 mm and 0.90 mm. The sands used in the experiments were sourced from River Road Landscape Supply in Prince George, which obtains its sand directly from the Nechako River, representing sediment found in Northern Canadian rivers. The gravel used for constructing the pool slope was collected from the Quesnel River near the Quesnel River Research Centre (QRRC). Similar sediment sizes have been employed in other experiments by Barahimi and Sui (2024b), Jafari and Sui (2024), Sediqi et al. (2024), Namaee and Sui (2020), and Wu et al. (2016). These sediment sizes were also chosen to prevent ripple formation, given that sediments with $L/d_{50} \geq 50$ are less prone to forming ripples (Rezaie et al., 2023), where L represents the characteristic length of the hydraulic structure.

The standard deviation (σ) of the sediment sizes was calculated using the equation:

$$\sigma = \sqrt{d_{84}/d_{16}} \tag{2.1}$$

This parameter was utilized to assess the uniformity of sediment distribution, where d_{84} and d_{16} denote the particle diameters at which 84% and 16% of the sample are finer. A lower value of σ indicates better sorting of the sediment. Sands with geometric standard deviations greater than 1.6 can be categorized as non-uniform sediments (van der Mark et al., 2008). The standard deviation (σ) for these sands was calculated as 1.97 and 2.39, making both sands non-uniform. The grain size distribution was determined using a mechanical shaker and a series of sieves, with the sediment grain size distributions illustrated in Figure 2.6. The selected d_{50} represents the typical sediments found in the natural rivers in northern British Columbia, as revealed by a survey conducted by Northwest Hydraulic Consultants (2013) (Appendix IV).

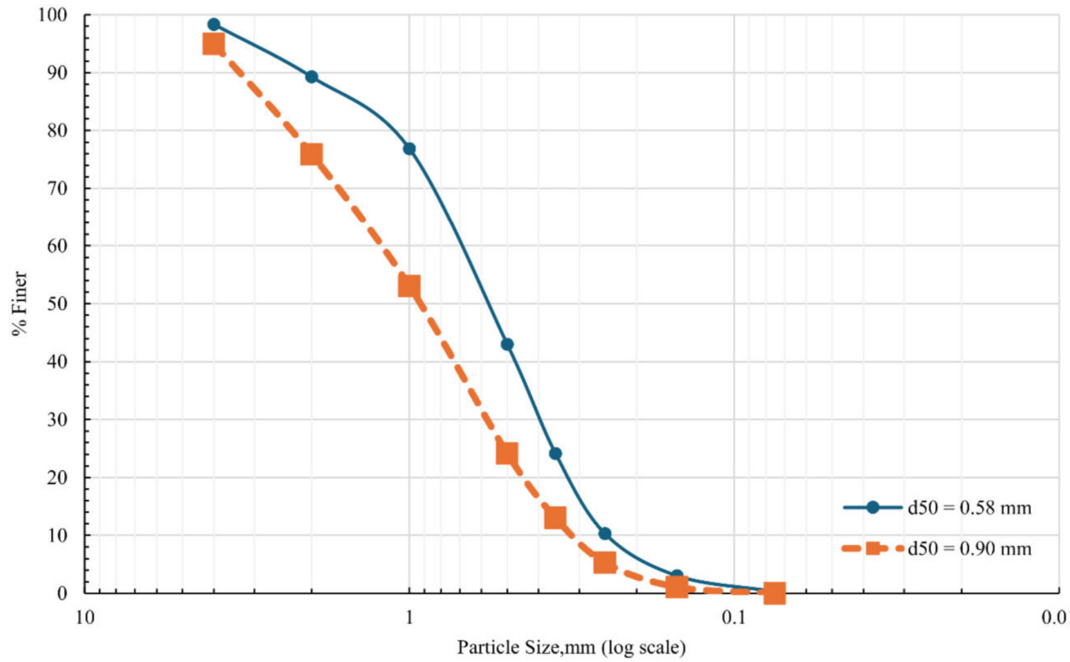

Figure 2.6 Sieve analysis results of the bed sediments used in this study.

2.4 Synthetic Ice Cover

Three major categories of the available materials for model ice cover are rigid, synthetic, and natural ice. When strength is not a concern, rigid, unbreakable ice replacements such as wood, paraffin, polyethylene, polypropylene plastic, and polystyrene foam (Styrofoam) have been utilized effectively (Jafari & Sui, 2021; Wuebben, 1996). This study used Styrofoam panels to model smooth ice cover, and a rough model ice cover was prepared by attaching 2.5 cm Styrofoam cubes to the panel bottom. Manning's coefficient for Styrofoam panels (smooth cover) is estimated as 0.010 (Hains & Zabilansky, 2005). Applying Li's (2012) equation (Eq. 2.2) for calculating the cover Manning's n (n_i) and adopting 0.025 m as the roughness height, n_i is estimated as 0.021 for rough ice cover. Both values are consistent with the calculated results for surveyed ice-covered channels using either average roughness height estimation (method I, 0.0075 - 0.029) or logarithmic law (method II, 0.0088–0.033) (Li, 2012). Equation 3 is employed for calculating n_i

$$n_i = 0.039\,\mathrm{k}_\mathrm{s}^{1/6} \tag{2.2}$$

in which k_s is the average height (m) of the ice cover affected region.

Beltaos and Bonsal (2021) report that ice thickness on the Peace River ranges from 0.4 to 1.4 meters, with river depths between 6 and 20 meters. Similarly, Environment Canada (2013) data for the Fraser River near Prince George shows depths of 3 to 20 meters, with ice thicknesses up to 1.09 meters, according to BC Ministry of Agriculture and Lands (2006). In this study, the flume depth of 20 to 35 cm, combined with 25 mm ice cubes, represents a scaled version of maximum ice thickness relative to river depth, effectively simulating ice roughness. A 35 mm spacing between cubes was chosen to replicate realistic river ice roughness, balancing natural turbulence effects with controlled laboratory conditions while avoiding excessive flow blockage.

Hains and Zabilansky (2005) noted that the local scour processes under fixed and floating ice covers were similar, with increased ice cover roughness leading to greater local scour depths. Since each Styrofoam panel measures 1.95 meters in length, 1.20 meters in width, and 0.025 meters in thickness, it is extremely challenging to keep them fixed. During experiments, these model ice covers floated freely on the water surface, adjusting with slight changes caused by surface waves. A sample piece of synthetic Styrofoam ice cover in the flume is shown in Figure 2.7.

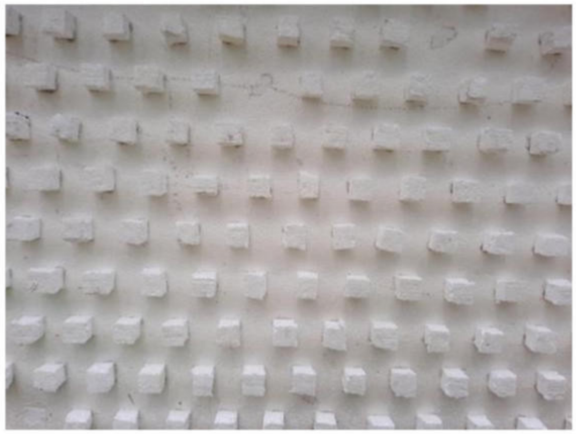

Figure 2.7 Styrofoam cubes are attached to the Styrofoam panel to simulate the rough ice cover.

Water temperature was not included as a variable in these experiments, as the study focused on the structural and dynamic interactions among spur dikes, vegetation, and ice cover under steady flow conditions. This approach isolated the physical effects of these elements without the confounding influence of temperature fluctuations, allowing a clearer interpretation of how spur dikes and vegetation impact flow patterns and sediment transport with ice cover as the primary flow modifier. While temperature can affect flow viscosity and sediment cohesion in natural environments, the controlled laboratory setting aimed to establish baseline principles of flow-structure interaction under consistent conditions. The subcritical flow regime (Froude number < 1) in this study indicated that gravitational forces dominated, with turbulent flow largely unaffected by minor viscosity changes due to temperature. Given that turbulent flows are relatively insensitive to viscosity compared to laminar flows, temperature-induced viscosity changes were expected to minimally impact flow behavior. To ensure consistency, the analysis in Chapter 4 normalizes Reynolds shear stress (RSS) to critical shear stress ($-\overline{u'w'}/u_*^2$), enabling comparisons across flows with different Reynolds numbers and eliminating density-related variations from temperature. This normalization supports the validity of findings across potential temperature differences.

2.5 Numerical Simulation Setup

FLOW-3D® HYDRO, a widely used computational fluid dynamics (CFD) model, was employed to simulate the velocity profiles for the vegetated pool. This model utilizes the volume of fluid (VOF) method to track the water's free surface accurately and employs the Fractional Area/Volume Obstacle Representation (FAVOR) method, developed by Hirt and Nichols (1981), to effectively manage complex geometries (Flow Science Inc., 2023). Recent studies have demonstrated the robustness of FLOW-3D in modeling hydrodynamic behaviors across various engineering applications, confirming its reliability in simulating intricate flow patterns around structural obstacles (e.g., Namaee et al., 2021, 2023).

2.5.1 Governing equations

The governing equations for an incompressible Newtonian fluid, incorporating the Reynolds-averaged Navier-Stokes (RANS) equations and continuity equation, are presented in Equations 5 to 8, including the Fractional Area/Volume Obstacle Representation (FAVOR) variables (Hirt & Nichols, 1981).

$$\frac{\partial}{\partial x_i}(u_i A_i) = 0 \tag{2.3}$$

$$\frac{\partial u}{\partial t} + \frac{1}{V_F}\left(u_j A_j \frac{\partial u_i}{\partial x_j}\right) = -\frac{1}{\rho}\frac{\partial P}{\partial x_i} + g_i + f_i \tag{2.4}$$

and

$$\rho V_F f_i = \tau_{b,i} - \left[\frac{\partial}{\partial x_j}\left(A_j S_{ij}\right)\right] \tag{2.5}$$

where

$$S_{ij} = -(\mu + \mu_T)\left(\frac{\partial u_i}{\partial x_j} + \frac{\partial u_j}{\partial x_i}\right) \tag{2.6}$$

Here, u_i represents the velocity component in the i-th direction, V_F is the volume fraction of fluid in each grid cell, and A_i denotes the fractional area open to flow in the i-th direction. Additionally, P is the pressure, ρ is the fluid's mass density, and t is time. The term g_i corresponds to the gravitational force in the i-th direction, f_i is the diffusion transport term, and S_{ij} is the strain rate tensor. The wall shear stress is indicated by $\tau_{b,i}$, and the total dynamic viscosity accounts for both molecular viscosity (μ) and eddy viscosity (μ_T).

FLOW-3D offers several turbulence models, including the standard k-ε, RNG k-ε, k-ω models, and large eddy simulation (LES). When turbulent flow encounters obstacles like vegetation stems, it generates a complex system known as the turbulent horseshoe vortex (THV) due to the adverse pressure gradient. Large-eddy simulation models, particularly the detached-eddy simulation (DES) approach, are effective in resolving most turbulence scales generated by obstacles while maintaining relatively low computational demands (Kang et al., 2019). Gazi and Afzal (2020) reviewed the formation mechanisms of vortices, highlighting the separation of both laminar and turbulent boundary layers, and noted the successful application of DES in simulating the intricate dynamics of THV. The Re-Normalization Group (RNG) k-ε turbulence model, which modifies the Navier-Stokes equations to account for smaller-scale motions, is favored for vegetated channels due to its cost-effectiveness, accuracy, and efficiency in capturing turbulence structures (Dehrashid et al., 2023). The RNG k-ε model includes enhancements over the standard k-ε model, improving efficiency. Therefore, in this study, the RNG k-ε turbulence model is employed to simulate the flow field in the pool zone with vegetation under ice-covered flow conditions, using this model to close the equations of motion.

The transport equations for k and ε can be expressed in various forms. One straightforward interpretation, which neglects the buoyancy effects, is as follows (Yakhot et al., 1992):

$$\frac{\partial}{\partial t}(\rho k) + \frac{\partial}{\partial x_i}(\rho k u_i) = \frac{\partial}{\partial x_j}\left[\left(\mu + \frac{\mu_t}{\sigma_k}\right)\frac{\partial k}{\partial x_j}\right] + P_k - \rho\varepsilon \tag{2.7}$$

$$\frac{\partial}{\partial t}(\rho \varepsilon) + \frac{\partial}{\partial x_i}(\rho \varepsilon u_i) = \frac{\partial}{\partial x_j}\left[\left(\mu + \frac{\mu_t}{\sigma_\varepsilon}\right)\frac{\partial k}{\partial x_j}\right] + C_{1\varepsilon}\frac{\varepsilon}{k}P_k - C_{2\varepsilon}^{*}\rho\frac{\varepsilon^2}{k} \tag{2.8}$$

where,

$$C_{2\varepsilon}^{*} = C_{2\varepsilon} + \frac{C_\mu \eta^3(1-\eta/\eta_0)}{1+\beta\eta^3} \tag{2.9}$$

$$\eta = Sk/\varepsilon \tag{2.10}$$

$$S = \left(2S_{ij}S_{ij}\right)^{1/2} \tag{2.11}$$

The turbulent viscosity is calculated using the same method as the standard k-ε model. Notably, the RNG procedure explicitly derives the values of all constants except for β. The commonly used values are $C_\mu = 0.0845$, $C_{\varepsilon 1} = 1.42$, $C_{\varepsilon 2} = 1.68$, $\sigma_k = \sigma_\varepsilon = 0.7194$, $\eta_0 = 4.38$, and $\beta = 0.012$ (Yakhot et al., 1992).

FLOW-3D utilizes the VOF method to solve the governing equations on an orthogonal mesh grid, which allows for accurate capture of the interface between different fluid phases. The solver iteratively computes the flow field by updating the velocity and pressure fields until convergence is achieved, involving the solution of continuity, momentum, and turbulence transport equations (Lee & Wahab, 2019). The simulation results are validated against experimental data to ensure accuracy, with model parameters adjusted as necessary to achieve better alignment with observed data.

2.5.2 Model Setup

In the computational domain, no-slip wall conditions were applied to the sidewalls, rigid vegetation (represented by cylinders with diameters of 0.5 cm), ice cover bottom surfaces, and mesh boundaries. The cylinders simulate rigid vegetation such as common reed (Phragmites australis) found in natural rivers (Nosrati et al., 2024). The top boundary was modeled using a “symmetry” condition, while a “no-slip wall” condition was applied to the bottom boundary. The upstream inlet of the pool was set with a “specified velocity” condition, and the downstream outlet of the pool was designated as “outflow.” The inlet velocity (v_0), controlling the flow rate into the channel, was determined using the average flow velocity. The symmetry condition was chosen for the top boundary to save computational time, a method validated by Smith and Foster (2005), who observed no significant differences between the usage of symmetry and a free-surface boundary. A smooth ice cover was simulated at the same flow depth in the numerical model as the physical model for smooth ice-covered flow conditions. Rough ice cover was simulated by adjusting the roughness height of the ice cover to match Manning’s n_i value used in the flume experiments. The flow moved from upstream to downstream across the pool section, passing over the vegetated pool section and causing changes in flow fields until reaching the outflow boundary.

In numerical modeling, addressing uncertainties related to the mesh resolution and computational domain size is crucial. To mitigate these uncertainties, sensitivity analyses have been conducted for domain size and mesh resolution. Initially, two computational domain sizes were compared under constant conditions: the first domain was set to 5.8 meters, corresponding to the length used in the experimental studies, with a uniform mesh grid of 20 mm × 20 mm. It was observed that reducing the domain length to 5.0 meters did not alter flow characteristics near the vegetated zone in the pool, indicating that this reduction had no significant effect on the flow field. This adjustment was primarily aimed at optimizing simulation time without compromising the accuracy of the simulation results.

Mesh refinement is crucial for achieving high-precision computational results, given the complex vegetation arrangements and significant flow variations within these areas. Two different mesh grids have been tested to optimize the mesh resolution. The computational domain was divided into two mesh blocks. Initially, all blocks utilized a uniform mesh size of 20 mm × 20 mm. After optimization, the central mesh block encompassing the vegetated pool area retained a finer grid of 20 mm × 20 mm. In comparison, the pool entry and exit sections were adjusted to a coarser grid of 30 mm × 30 mm to improve the computational efficiency. Comparisons of the model outputs indicate that these mesh size adjustments do not significantly impact the velocity profiles, confirming the model's robustness. This approach ensures efficient use of the computational resources while maintaining simulation accuracy. Figure 2.8 illustrates the simulation model of the vegetated pool area and the boundary conditions employed in the numerical models.

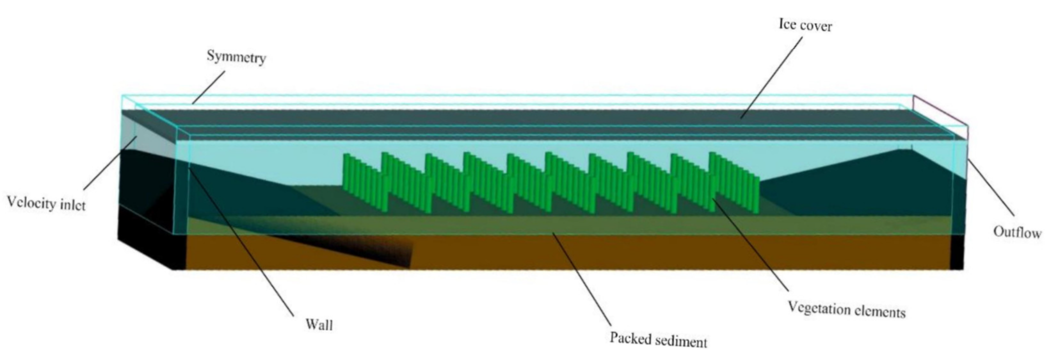

Figure 2.8 The vegetated pool's simulation model and boundary conditions under ice-covered flow conditions.

2.6 Research Innovation

This study represents an extensive experimental investigation into the effects of local obstruction (i.e., submerged angled spur dike) and regional obstruction (i.e., vegetated pool) on flow structure and bed deformation. Conducted in a large-scale outdoor flume that closely mimics natural stream conditions, with dimensions of 2 meters in width, 1.3 meters in depth, and 38 meters in length, the research systematically examines the impacts of different types of hydraulic obstructions. The submerged spur dikes were aligned with deflecting and retracting angles, namely, 90°, 120°, and 135°. The vegetation patches were arranged in staggered arrays with 20 cm between vegetation elements and 30 cm between planting rows. Two different non-uniform sands were utilized to explore local scour and flow field change around submerged angled spur dike under ice cover and flow field variation in the vegetated pool area. The analysis focused on key parameters such as velocity profiles, Reynolds shear stress, turbulent kinetic energy (TKE), bed deformation, and scouring. In this thesis, the term "obstruction" denotes artificial and constructed nature-based solutions, such as spur dikes and vegetation patches. These obstructions are introduced strategically within the channel to influence flow dynamics and sediment behavior, particularly under ice-covered conditions. The study examines how these interventions impact hydrodynamics, turbulence, and bed morphology, highlighting their role in shaping flow patterns within submerged, ice-affected environments.

This research provides insights into the combined effects of hydraulic obstructions and ice cover on flow resistance and channel bed deformation. It elucidates the relationship between ice-cover roughness, bed roughness, and scour hole depth, identifying the most significant variables influencing scour formation under ice-covered conditions. These findings are valuable for predicting and managing channel bed erosion in cold regions and for enhancing the design of hydraulic structures to mitigate the impacts of ice cover. The study also explores the relationship between vegetation and ice cover roughness on velocity profiles, which is crucial for understanding sediment transport, pollutant dispersion, and habitat suitability.

A novel estimation equation for the maximum scour depth around angled submerged spur dikes was developed, showing strong agreement with experimental data. Additionally, computational fluid dynamics (CFD) simulations using Flow-3D software were applied to vegetated pools to investigate flow-related parameters such as TKE, further enhancing the study's contribution to understanding the complex interactions between vegetation, ice cover, and river hydraulics. This research advances the field by comprehensively addressing these factors simultaneously.

3. CHAPTER THREE: LOCAL SCOUR AROUND SUBMERGED ANGLED SPUR DIKES UNDER ICE COVER

3.1 Introduction

Spur dikes are common structures in riverine and coastal engineering. They are mainly used to protect riverbanks from erosion and alter channel water depth for better navigation. Based on the submergence level, spur dikes can be distinguished into submerged and non-submerged types (Wei et al., 2018). Spur dikes will significantly change the flow patterns in the vicinity of where they are built, causing powerful vortices that can enhance erosion. Deep scour holes can affect the stability of the spur dike foundation, posing significant safety concerns (Hong et al., 2019). Therefore, the scour depth around a spur dike is an essential parameter in the design of this type of infrastructure.

Currently, studies on local scour around spur dikes have primarily focused on non-submerged spur dikes. In practice, however, non-submerged spur dikes on the flood plain may be submerged during the flood season if the flow exceeds the design flood (Keshavarzi et al., 2010). For submerged spur dikes, the repelling type is preferable since the sediment can be carried to the side of the river bank, which is conducive to sediment deposition after the water flows over the top of the spur dike (Kuhnle et al., 2002). The attracting alignment for submerged spur dikes will function adversely, causing deposition in the river center and endangering the safety of the dike foundation. It has been reported that the flow patterns near submerged spur dikes are more complex than those for non-submerged spur dikes, and the contributing factors are also more diverse (Fang et al., 2006; Kuhnle et al., 2002). As claimed by Fang et al. (2006), a sloped upstream face of a submerged spur dike plays a significant role in the local scour pattern around the submerged spur dike. The milder the slope of the upstream face of a submerged spur dike, the higher the approaching velocity and Froude number needed for scour initiation and the smaller the maximum scour depth resulting from submerged spur dikes.

It also has been found that the alignment angle between the axis of a dike and the stream-wise direction of water flow plays a significant role on the local scour process around a spur dike. According to the alignment angle between the axis of a dike and the stream-wise direction of water flow, spur dikes can be classified as attracting (acute angles), deflecting (right angle), and repelling (obtuse angles). These three types of spur dikes have very different effects on flow patterns. Nagy (2005) examined impacts of the dike alignment angles (denoted as α in the current study) on the local scour imposed by submerged spur dikes. The potential near-bank erosion was found to be at a minimum for an angle of 135° according to measured maximum scour volume. Giglou et al. (2018) tested a single spur dike with angles of 45°, 75°, 90°, 105°, and 120°, and reported that by increasing the spur dike angle relative to the flow direction, the length and diameter of the produced vortex grow. The velocity decreased the most when the spur dike model was oriented at 120°. However, Yazdi et al. (2010) studied the angles that deviated from the normal orientation (90°) and concluded that the length and width of the recirculation zone (reattachment length) remained virtually constant at varied angles ($\alpha < 20°$).

Han et al. (2022) used the porous medium method (PMM) in a three-dimensional numerical model to simulate the flow fields and scouring processes around grouped attracting and deflecting spur dikes. It was found that compared to grouped deflecting spur dikes, attracting spur dikes reduced the blockage of approaching flow, leading to a moderate increase in the flow velocity magnitude from upstream to downstream within the grouped spur dikes field. Shampa et al. (2020) investigated the characteristics of three-dimensional flow fields around slit-type grouped permeable spur dikes. They found that deflecting spur dikes more effectively generated transverse flow to the opposite bank. To simulate the flow recirculation characteristics of grouped non-submerged spur dike sequences oriented at different angles in a 60° channel bend, the MIKE3 FM model was applied by Chen et al. (2019). The results revealed that increasing the angle of the spur dike changed the flow field and surface morphology surrounding the spur dike. For the attracting arrangement of spur dikes, the range of the recirculation zone expanded, and the center of the vortex moved further away from the dike with the increase of the alignment angle. Contrarily, for the repelling arrangement of spur dikes, the range of the recirculation zone steadily shrinks with the increase of the alignment angle.

Previous research on local scour at in-stream infrastructure, including spur dikes, has mainly focused on non-submerged structures, and open channel flow conditions. However, in natural rivers, ice cover often develops in rivers in cold regions during winter. Thermally grown ice cover has a small roughness, and its water-immersed bottom is smooth. Contrarily, a rough ice cover is formed if shoving and mechanical thickening processes are involved (Valela et al., 2021). The presence of an ice cover on the water surface causes complicated local scour development processes due to the dynamic interactions among the ice cover, water flow, and channel morphology evolution. The sedimentation process consequently exhibits drastic changes compared to that under open-channel flow conditions (Pan & Shen, 2022). Zabilansky and White (2005) identified a river as narrow when the variations in water levels do not alter the position of the ice cover, based on which the experimental flume can be categorized as a narrow channel. When the discharge exceeds the freeze-up datum in a narrow river, the ice cover will induce a pressurized flow state underneath, which causes a shifting in the maximum velocity position. Additionally, the formation of a stationary ice cover increases the wetted perimeter and shifts the maximum velocity to the boundary with a smoother roughness (Sui et al., 2010).

Local scour under ice-covered flow conditions has attracted more attention from researchers over the past decade: Sui et al. (2009) did local scour experiments under open channel flow and smooth and rough ice-covered conditions. They discovered that the local scour process differs between covered and open channels, and that the rougher the ice cover, the deeper the scour hole. Wu et al. (2014a, b, 2015, 2016) investigated the impacts of channel bed sediment composition on scour around bridge abutments and bridge piers under ice-covered flow conditions, and their results showed that the maximum scour depth is affected by the roughness of ice cover, grain size of bed material, abutment shape, densimetric Froude number, and grain size of the armor layer in scour holes. Valela et al. (2021) found that an increase in ice cover submergence results in a greater maximum velocity and an associated increase in the near-bed velocity gradient. Rough ice cover generates more scour than smooth ice cover. Sirianni et al. (2022) studied the effects of developing ice covers on bridge pier scour. Namaee and Sui (2019a, b, 2020) established empirical equations for the maximum local scour depth around two side-by-side bridge piers under both open channel flow and ice-covered conditions. Jafari and Sui (2021) analyzed the velocity fields and turbulence patterns along unsubmerged spur dikes under ice cover with dike orientation angles of 45°, 60°, and 90°. As the dike becomes oriented closer towards the upstream, the velocity component values increased correspondingly, resulting in a deeper scour hole.

Overall, in comparison to open channel flow, very little research has been done on the local scour process under ice-covered conditions. The impacts of alignment angles of submerged spur dikes on equilibrium scour depth under ice-covered flow conditions have never been explored. And thus, in the current study, the variations of the maximum depth of scour holes around submerged spur dikes with changes in the submerged spur dike's design parameters (length, overtopping ratio, and alignment angle) under different cover conditions are analyzed based on laboratory experiments done in a large-scale outdoor flume.

3.2 Materials and Methods

3.2.1 Site description

The experiments were done in a large-scale outdoor flume at the Quesnel River Research Centre (QRRC) in Likely, British Columbia. This flume is 38.20-m long, 2.00-m wide, and 1.30-m deep. A holding tank was built to provide constant discharge feeding to the flume, and two valves were installed to regulate the flow rate at the end of the holding tank. An adjustable tailgate was installed at the downstream end of the flume to control the flow depth. The distance from the tailgate to the downstream edge of the downstream sandbox is 5.3 m. The upstream sandbox is 5.60-m long, 2.00-m wide, and 0.30-m deep, while the downstream sandbox is 5.80-m long, 2.00-m wide, and 0.30-m deep, and these two sandboxes are located 10.20 m apart from each other (Figure 3.1).

In natural rivers, channel beds are filled with non-uniform sediment particles. To better understand the contrasts between mechanisms of clear-water and live-bed scour, non-uniform channel bed materials have been utilized for flume experiments since the 1980s (Guan et al., 2022). As pointed out by Yang (2003), non-uniform sediment particles will form an armor layer, a barrier consisting of a residue of coarser particles when the finer sediment particles are transported more rapidly by the flow. Local scour caused by an in-stream hydraulic structure will grow through the armor layer and into the finer, more erodible sediment. Occasionally, it can also produce a more widespread local scour area when the armor layer starts to erode (Raudkivi & Ettema, 1985). Utilizing non-uniform sediment particles to represent natural riverbeds could result in a better knowledge of local scour mechanisms, improving the authenticity of experimental simulations.

Hydraulic modeling is subject to scale effects. Scale effects are the distorted model outputs caused by the force ratio mismatch between a laboratory model and a field prototype. Deeper scour holes can be caused by a scale effect inherent in laboratory flume experiments, and this limitation necessitates the use of sediment that is the same size as or no smaller than 0.1 of the size of natural channel bed sediment in the field for flume studies (Ettema et al., 1998). Thus, in the current study, non-uniform sediment particles with median particle sizes (d_{50}) of 0.90 mm and 0.59 mm were selected for the clear water scour experiments for simulating the natural erodible sand bed.

The channel bed Manning roughness coefficient (n_b) can be calculated using Equation (3.1) and was determined as 0.018 and 0.020 for d_{50} = 0.58 mm and d_{50} = 0.90 mm, respectively (Julien, 2018).

$$n_b = 0.064 d_{50}^{1/6} \tag{3.1}$$

As reported by Kuhnle et al. (2002) the measured tail length of the scour area is below 20 times of the dike normal length regardless of the alignment angles. In the current study, considering the dimension of the model spur dikes and the sandboxes, the position of the model spur dikes was determined to be at one-third of each sandbox to eliminate interferences to the downstream, as shown in Figure 3.1. Figure 3.2 is a photo of the laboratory flume.

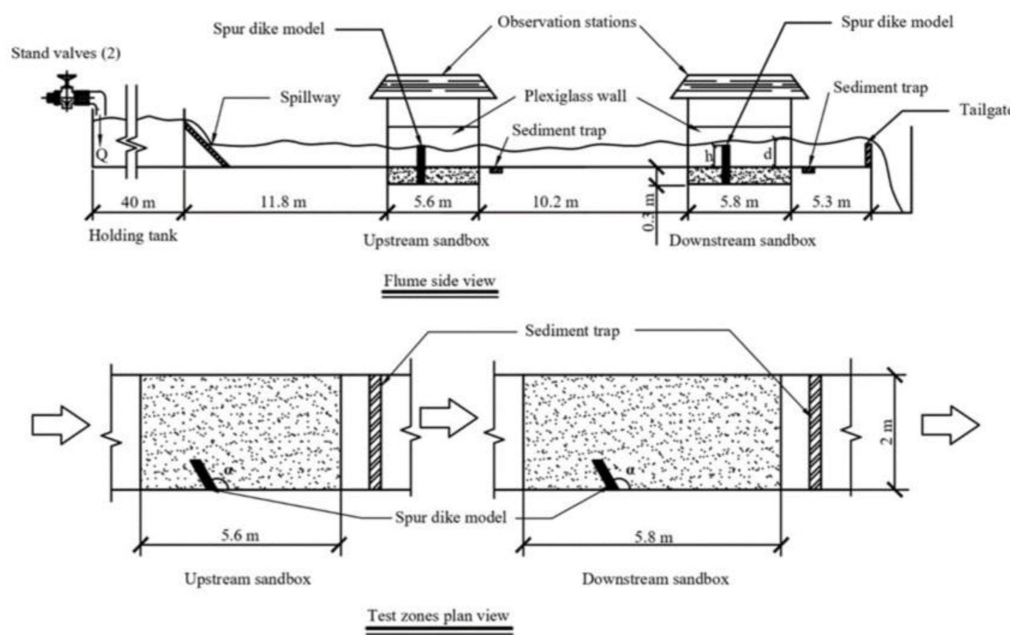

Figure 3.1 Schematic diagram of the experimental flume setup for local scour around submerged angled spur dikes.

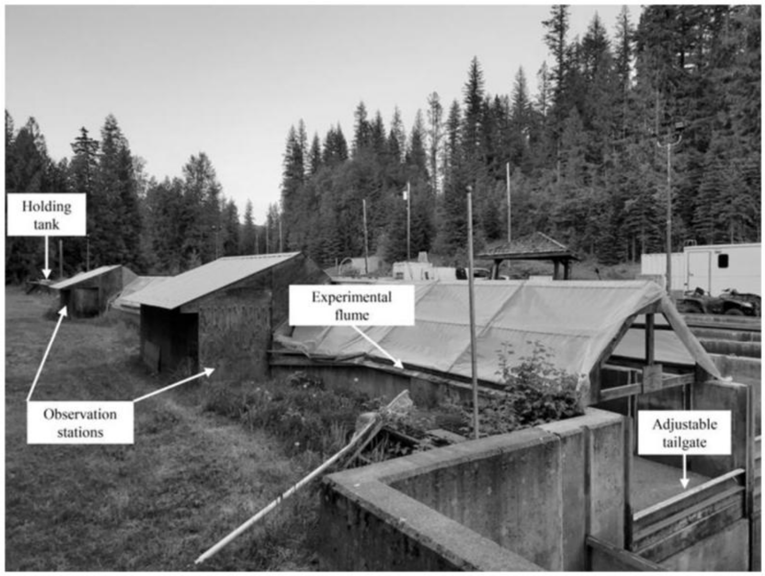

Figure 3.2 Field photo of the Quesnel River Research Center (QRRC) experimental flume.

Since the erosive process is caused by the shear stress imposed on the bed sediment (Khan et al., 2016), the influence of spur dike materials was not investigated. Waterproof marine plywood was selected to build the vertical wall spur dikes. The average depths in the two sandboxes vary marginally due to the smaller flume slope of 0.20%. Therefore, the height of the spur dikes above the initial sand bed were set as 15 cm and 20 cm in the upstream sand box and 20 cm and 25 cm in the downstream sandbox to keep the overtopping ratios in two sandboxes varying within 5.0%. Richardson and Simons (1984) proposed that dikes with angles between 100° and 110° may be applied to channelize or direct flow. However, Jansen et al. (1979) stated that no uniform standards should be set for all spur dikes. Thus, the model spur dikes with a uniform spur dike width of 0.05 m were set up at alignment angles of 90°, 120°, and 135° in the current study.

When the strength is not a concern, rigid unbreakable ice replacements such as wood, paraffin, and Styrofoam have been utilized effectively for ice cover simulation (Jafari & Sui, 2021; Wuebben, 1996). In the current study, the styrofoam panels were used as the smooth ice cover, and the rough ice cover was prepared by attaching 2.5 cm Styrofoam cubes to the bottom of the smooth Styrofoam panels. Manning's coefficient for the synthetic smooth cover (n_i) is estimated as 0.010 (Hains & Zabilansky, 2005). The rough cover Manning's roughness coefficient is estimated as 0.021 by applying Equation (3.2) (Li, 2012).

$$n_i = 0.039\, k_s^{1/6} \tag{3.2}$$

in which k_s is the average roughness height (m). Field observations in natural rivers prove that ice covers appearing in most rivers belongs to smooth, floating ice covers (Turcotte et al., 2011). The Styrofoam panels used as model ice cover in the current study were positioned using wires to simulate the presence of stable floating ice cover in a natural channel. The flow under the ice cover resembles a turbulent pipe flow (Sirianni et al., 2022). Equation (3.3) can be used to estimate the entry length for fully developed flow (l_e) (Çengel & Cimbala, 2014).

$$l_e = 1.359 L Re^{1/4} \tag{3.3}$$

where Re is the flow Reynolds number, and L is the characteristic length. In the current study, the lengths and widths of the model ice cover on the water surface are 9.60 and 2.00 m for the upstream sandbox, and 9.80 and 2.00 m for the downstream sandbox (extending 2.0 m toward upstream from the frontal edge of the sandbox and 2.0 m toward downstream from the rear edge of the sandbox). The model ice cover encompassed sufficient upstream area from the spur dike tip for the underneath flow to become fully developed.

3.2.2 Instrumentation

A SonTek Acoustic Doppler Velocimeter (ADV) was used to measure the approaching flow velocity. The Sontek ADV is a single-point, high-resolution velocity meter comprising one transmitter and three receivers in accordance with the acoustic Doppler effect to detect the change in received frequency (Doppler shift) reflected by the moving solid particles scattered in the water body (Rehmel, 2007). The WinADV software was applied to post-process data by filtering the measured reflected signal and other parameters. The signal-to-noise ratio (SNR) and correlation (COR) were selected as data filtration criteria. The COR indicates the uniformity of the particle movement during the sample interval, whereas the SNR denotes the relative density of the scatters in the flow (Wahl, 2000). At the selected ADV frequency of 25 Hz, SNRs greater than 15 dB are advised, and CORs over 70% should be set as the acceptable data threshold (SonTek/YSI Inc., 2001). In the current study, both aforementioned values were set for filtering data collected using the ADV. The approaching water depth, flow rate, and average flow velocity were monitored using a SonTek-IQ Plus (SonTek, 2012).

3.2.3 Experimental Protocol

Initially, the sandboxes were filled with non-uniform sand, and the surface was leveled to the same elevation as the flume bed. The tailgate was adjusted to the desired height. One valve then was opened slightly to allow water to gradually soak the sandboxes. The sandbox surface was monitored carefully to avoid initial scour. Once the desired flow depth was reached, the two control valves were turned on completely.

The duration required to attain an equilibrium state is crucial in investigating a local scour process. Oliveto and Hager's (2002) experimental research found that the time variation of local scour development is mainly determined by the in-stream structure geometrical variables, the hydraulic parameters, and the granulometric characteristics. The local scour under an ice-covered flow condition is more complicated than that under an open channel flow condition. Namaee and Sui (2020) did an experimental investigation on local scour under ice-covered flow conditions and suggested that equilibrium scour depth should be reached after 24 h. The current study applied the criteria for reaching the equilibrium scour process proposed by Mia and Nago (2003), namely when the scour depth fluctuation was less than 1 mm/h. A thin standard ruler with millimeter increments and a reading error of +/- 0.1 mm was attached at the dike tip to observe the temporal scour changes during the test trial, after which the duration of 24 h was selected for all experimental runs.

Once the scour process reached equilibrium, the ADV was used to measure the instantaneous velocity to verify readings from the SonTek IQ. After all required measurements were finished, the valves were carefully closed to allow the water to recede gradually to avoid disturbances in the scour pattern. After water was drained completely from the flume, the deformation zone including both scour hole and deposition dune was divided into a grid which has a side length of 1-cm. The depths at the vertices of the grids were carefully recorded using a laser distance measurer with an accuracy of 3 mm. When all the measurements were done, the spur dike was aligned to another desired angle to prepare for the next experimental run. If a new overtopping ratio was required, the aforementioned procedures were repeated. Table 3.1 lists the experimental conditions under the smooth ice-covered flow condition, which was repeated for both open-channel and rough ice-covered flow conditions.

Table 3.1 Summary of working parameter setups under the smooth ice cover

Run #	Sandbox position	Median grain size d_{50} (mm)	Spur dike height T (m)	Design length L (m)	Alignment angle α (°)	Flow depth h (m)	Average velocity U (m/s)
1	Upstream	0.90	0.15	0.50	90	0.21	0.37
2	Upstream	0.90	0.15	0.50	120	0.21	0.37

3	Upstream	0.90	0.15	0.50	135	0.21	0.40
4	Upstream	0.90	0.15	0.35	90	0.20	0.38
5	Upstream	0.90	0.15	0.35	120	0.20	0.37
6	Upstream	0.90	0.15	0.35	135	0.20	0.38
7	Upstream	0.90	0.20	0.50	90	0.20	0.39
8	Upstream	0.90	0.20	0.50	120	0.20	0.38
9	Upstream	0.90	0.20	0.50	135	0.20	0.35
10	Upstream	0.90	0.20	0.35	90	0.21	0.37
11	Upstream	0.90	0.20	0.35	120	0.21	0.38
12	Upstream	0.90	0.20	0.35	135	0.21	0.37
13	Downstream	0.58	0.20	0.50	90	0.25	0.28
14	Downstream	0.58	0.20	0.50	120	0.25	0.31
15	Downstream	0.58	0.20	0.50	135	0.26	0.27
16	Downstream	0.58	0.20	0.35	90	0.26	0.25
17	Downstream	0.58	0.20	0.35	120	0.25	0.28
18	Downstream	0.58	0.20	0.35	135	0.26	0.31
19	Downstream	0.58	0.25	0.50	90	0.25	0.32
20	Downstream	0.58	0.25	0.50	120	0.26	0.33
21	Downstream	0.58	0.25	0.50	135	0.25	0.31
22	Downstream	0.58	0.25	0.35	90	0.25	0.32
23	Downstream	0.58	0.25	0.35	120	0.25	0.27
24	Downstream	0.58	0.25	0.35	135	0.25	0.27

3.3 Results and Discussions

The critical velocity (U_c) for beginning of motion of sediment particles was calculated and compared to the measured approach velocity (U). Clear-water scour occurs when $U_c > U$ at the cross section where the spur dike tip is located. The equation proposed by Laursen (1963) was applied to calculate U_c.

$$U_c = K_u h^{1/6} d_{50}^{1/3} \tag{3.4}$$

where h is the average approaching flow depth (m) and K_u is equal to 6.19 in S.I. units. The measured U all fell below the calculated U_c, affirming the clear-water scour assumption.

Figure 3.3 was generated using the Surfer 2D/3D Mapping Software to exemplify the scour pattern around submerged spur dikes under open, smooth ice-covered, and rough ice-covered flow conditions, where d_{50}, T, L, and α are 0.90 mm, 0.20 m, 0.35 m, and 90°, respectively. Terrain elevation change contours for all experiments can be found at Appendix I. The depths of scour holes are represented by negative values, while the positive values depict the heights of deposition dunes. The maximum scour depths were observed at the upstream toe of the submerged spur dike. Meanwhile, downstream of a spur dike, the wake zone yielded the highest deposition values.

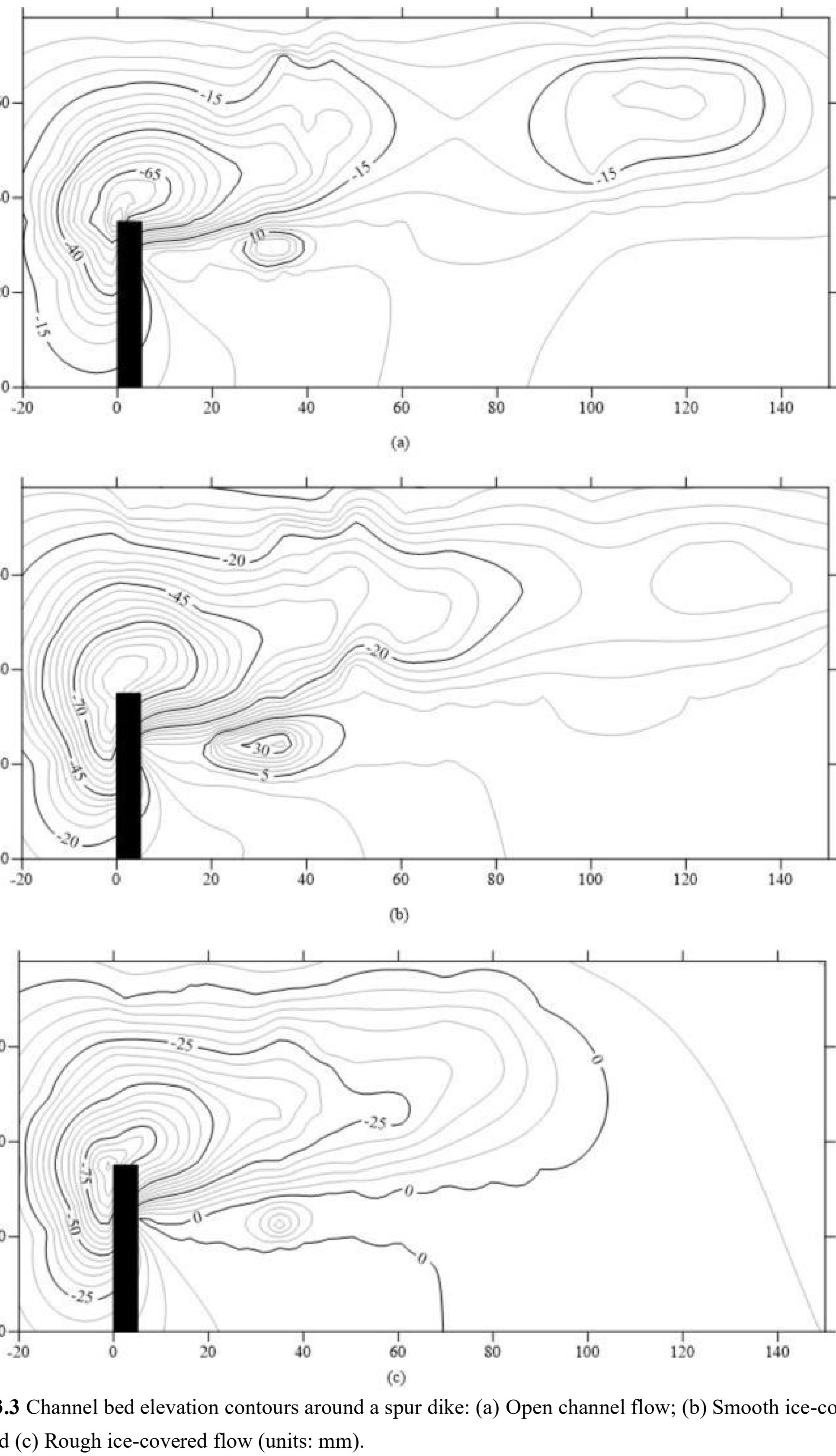

Figure 3.3 Channel bed elevation contours around a spur dike: (a) Open channel flow; (b) Smooth ice-covered flow; and (c) Rough ice-covered flow (units: mm).

3.3.1 Impacts of spur-dike related parameters on local scour around spur dikes

The submergence ratio is one of the most crucial variables for a submerged spur dike design. This study applied the submergence ratio as the ratio of flow depth to the spur dike height ($S = h/T$), also referred to as the overtopping ratio by McCoy et al. (2007). The variation of the non-dimensional maximum scour depth related to normal length $d_s/(L\sin\alpha)$ (where d_s is the measured scour depth) is plotted against different cover conditions for both minor submergence (left) and moderate submergence (right) for different bed material (d_{50}) in Figure 3.4.

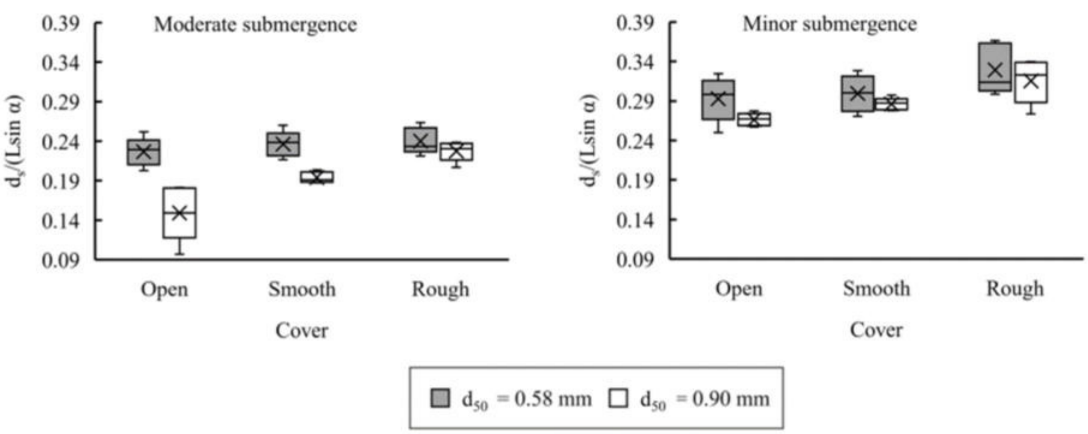

Figure 3.4 Variations of $d_s/(L\sin\alpha)$ values for different cover conditions under different submergence levels.

The spur dike normal length ($L\sin\alpha$) is the vertical distance from the flume sidewall to the outer edge of the spur dike. Figure 3.4 shows that the presence of ice cover led to the increase of $d_s/(L\sin\alpha)$ regardless of d_{50} and submergence levels. Under the smooth cover condition, the scour depths increased to a moderate degree compared to that under an open channel flow condition, namely, about 12 and 36% for minor and moderate submergence, respectively. Under the rough cover condition, a significant increase in the scour depth was found, namely, about 20 and 64% for minor and moderate submergence, respectively. The greater the distance from the dike tip to water surface was, the smaller the $d_s/(L\sin \alpha)$ became. Results showed that the range of the $d_s/(L\sin \alpha)$ values for the moderate and minor submergence scenarios is 0.10–0.15 and 0.25–0.38, respectively. Figure 3.5 shows a noticeable decreasing trend of the $d_s/(L\sin \alpha)$ values when the submergence ratio (S) grows. The decreasing trend is due to the boundary layer flow passing over the spur dike tip, weakening the energy carried through the wake vortices, thereby reducing the sediment load carried by the flow and decreasing the scour depth (Du et al., 2022).

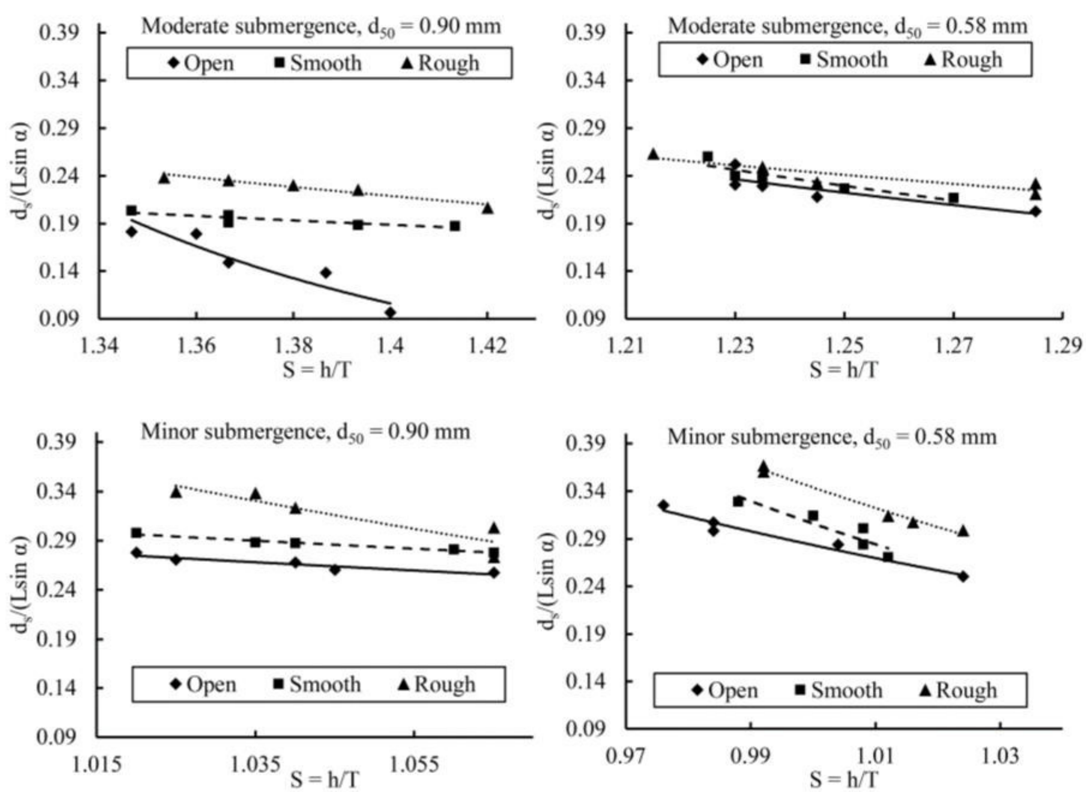

Figure 3.5 Dependence of $d_s/(L\sin \alpha)$ values on submergence ratio (S).

In the current study, the alignment angle (α) is defined as the angle between the spur dike axis and flow direction. For all experimental runs, the alignment angles were set as the non-attracting angles ($\geq$ 90°). Özyaman et al. (2022) examined the relation between the non-dimensional maximum scour depth related to design length (d_s/L) to assess the effects of α. For the current study, the variation of the (d_s/L) values against the alignment angle (α) is illustrated in Figures 3.6 and 3.7.

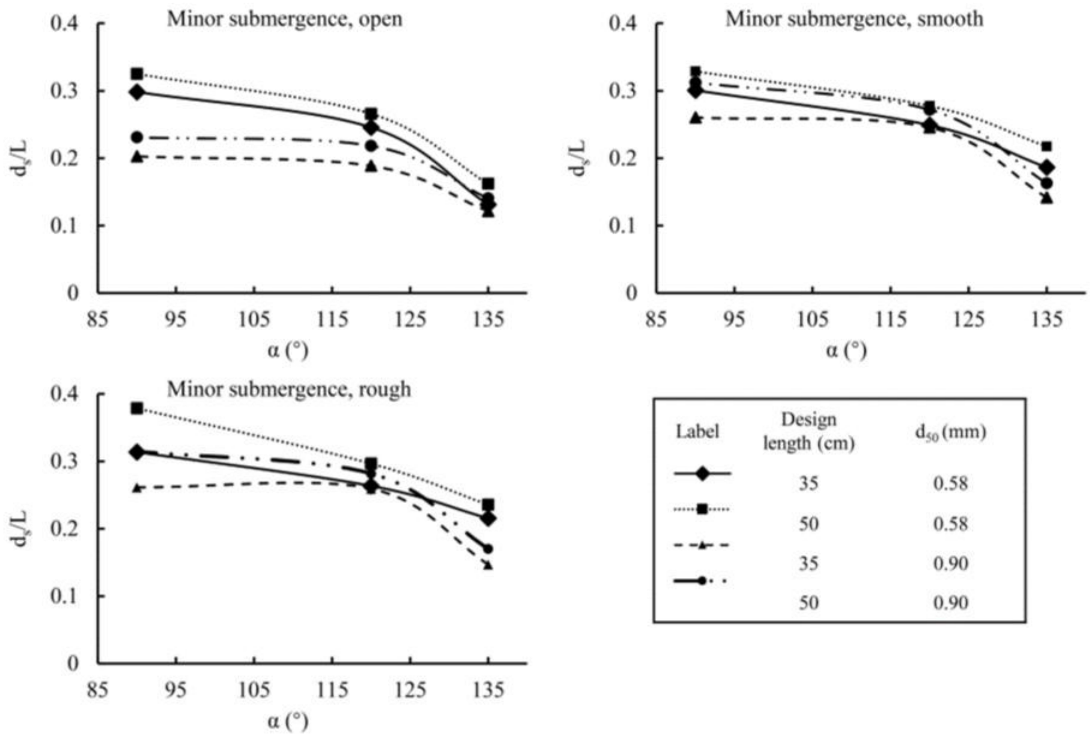

Figure 3.6 Variation of d_s/L against α (minor submergence).

For a constant α, the larger the dike length (L) is, the more the sediment movement would be, reflected by a higher (d_s/L)-value. When the spur dike height (T) and dike length (L) stay identical, it can be observed that the (d_s/L)-value decreases with the increase of α. This decrease can be explained by the sidewall effects posed by the channel confinement, which alters the flow pattern and changes the strength of the vortices. A plexiglass wall installed at the observation station, poses sidewall effects on the local scour mechanisms. The influence of the sidewalls on the flow can be linked to the effect of the corner vortex found in wide duct flows (Kohyama et al., 2022). Yang et al. (2012) did a mathematical analysis and revealed that the presence of sidewalls would lead to secondary flows. Rodríguez and García (2008) claimed that sidewall effects are more prominent when the aspect ratio (channel width (B) to the flow depth, B/h) is less than 5. Blanckaert et al. (2010) investigated secondary flows across gravel beds in a channel with the aspect ratio (B/h) ranging from 6.2 to 11.9, and found that the secondary flows were present across the entire width of the flow for all aspect ratios. However, the strength of the secondary flow reduced as the distance got further from the channel sidewall. Since the aspect ratio (B/h) ranges from 6 to 10 in the current study, secondary flow disturbs the flow field around the submerged spur dike.

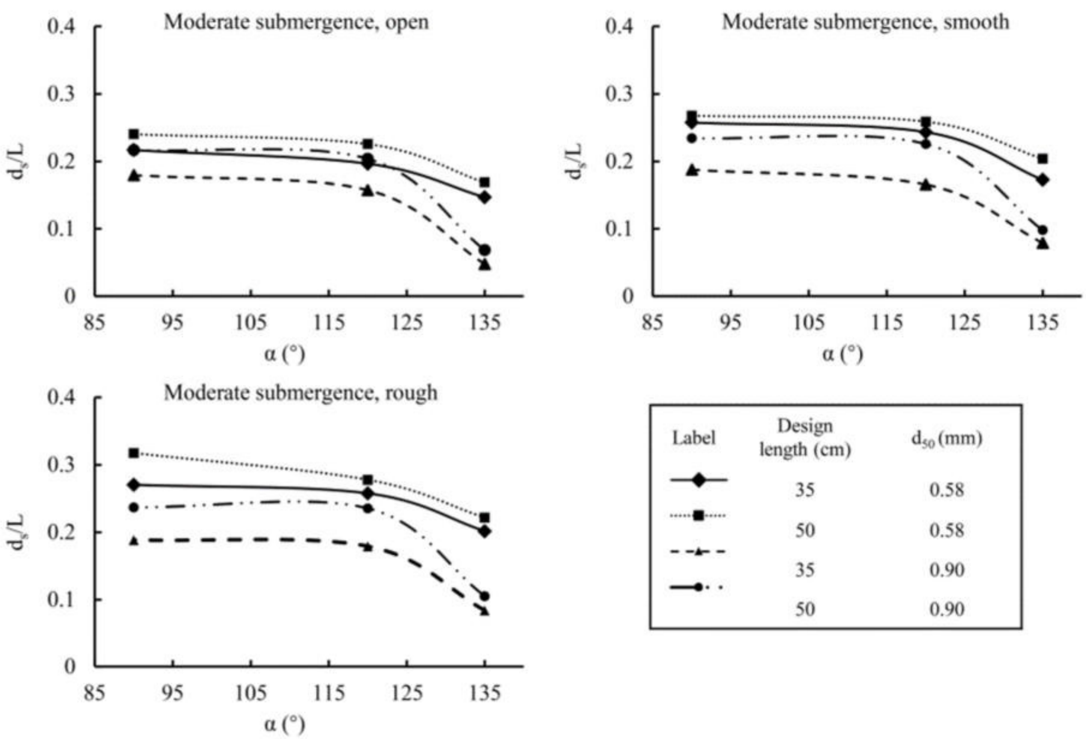

Figure 3.7 Variation of d_s/L against α (moderate submergence).

As the alignment angle (α) changed, the distance of the channel wall to the dike tip where the scour hole would appear also altered. The closer the dike tip to the channel wall, the more prominent the sidewall effects will be. One can also see from Figures 3.6 and 3.7 that a rougher cover exacerbates the change in the (d_s/L)-value more significantly. Compared to the open-channel flow scenario, the increase in the (d_s/L)-value under the rough cover is about 10–37% regardless of the alignment angle (α) and the submergence levels, whereas the increase in the (d_s/L)-value under the smooth cover is about 5–28%. The dike with an alignment angle of 90° will be the least vulnerable to the covered flow. Contrarily, the dike with the alignment angle of 135° experiences the most drastic changes in the (d_s/L)-value when ice cover is introduced.

3.3.2 Impacts of hydraulic parameters on local scour around spur dikes

Scale effects are unavoidable in physical models, but their impacts on experimental outcomes might be minimized by ensuring the flow Froude number ($Fr = U/(gh)^{1/2}$, where g is the acceleration of gravity) similarity between the model and prototype (Heller, 2011). The variation of the $d_s/(L\sin\alpha)$ values against Fr is shown in Figure 3.8.

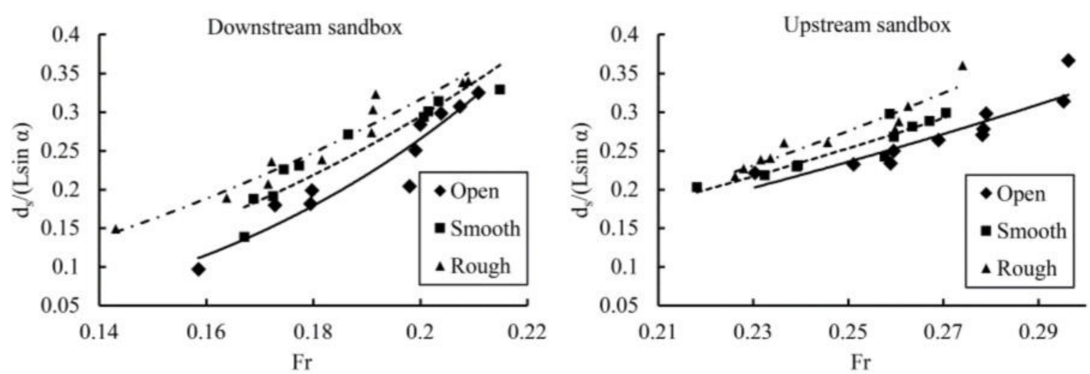

Figure 3.8 Dependence of the dimensionless maximum scour depth $d_s/(L\sin\alpha)$ on Froude number (Fr).

It is apparent from Figure 3.8 that the $d_s/(L\sin\alpha)$-value can be fitted relatively well to cover the specified range of Fr despite the differences in other factors. The measured $d_s/(L\sin\alpha)$ values show a growing trend with the increase of Fr. Based on the interpolated best-fitting curves for data collected in the downstream sandbox, when $Fr = 0.17$ representing flows with a lower Fr, the $d_s/(L\sin\alpha)$ values under open channel, smooth, and rough ice cover are 0.14, 0.19, and 0.22, respectively. When $Fr = 0.21$ representing flows with a higher Fr, the $d_s/(L\sin\alpha)$ values under open channel, smooth, and rough ice cover are 0.32, 0.34, and 0.35, respectively. Comparable trends can also be observed for the upstream sandbox.

Regardless of the cover roughness, the $d_s/(L\sin\alpha)$ values and Fr values universally maintain a high correlation, indicating that the flow around the spur dike is exceedingly turbulent (Chanson, 2004). The calculated Fr in the downstream sandbox ranging from 0.14 to 0.22 are smaller than those in the upstream sandbox that ranged from 0.22 to 0.31, partially due to the decrease in U resulting from the energy dissipation by the flume wall and bed. Additionally, since the SonTek-IQ readings proved that the pumps supplied steady, non-uniform flow in a prismatic flume, the flow is considered as gradually varied flow (GVF) (Gadissa, 2017). The depth increases gradually as the water flows toward downstream and forms backwater when it hits the tailgate at the downstream end of the flume.

Since non-uniform sediment particles are used as bed materials, after the initiation of scour, the coarsening process of non-uniform sediment has an inhibitory effect on the further development of a scour hole. Thus, the densimetric Froude number (Fr_d) (Eq. 3.5) is used as an alternative parameter to characterize the local scour process (Namaee & Sui, 2019a).

$$Fr_d = \frac{U}{\sqrt{(s-1)gd_{50}}} \tag{3.5}$$

where, $s = \rho_s/\rho$, is the ratio of sediment density (ρ_s) to water density (ρ). Figure 3.9 shows the relations between $d_s/(L\sin\alpha)$ and Fr_d for different submergence levels.

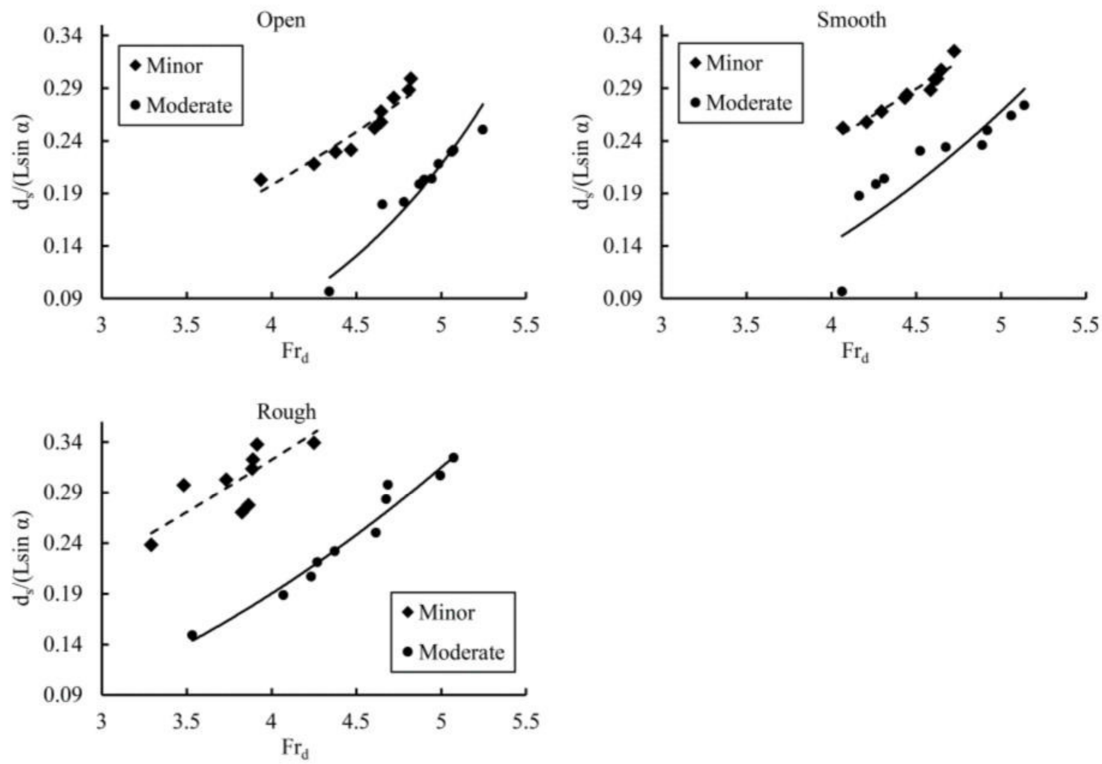

Figure 3.9 Comparison of dependence of $d_s/(L\sin\alpha)$ on Fr_d for different submergence levels under different cover conditions.

As shown in Figure 3.9, the $d_s/(L\sin\alpha)$-value increases with the increase of Fr_d regardless of submergence levels and cover conditions. Comparing fitted curves in Figure 3.9, one can see that for a given Fr_d and cover condition, the more immersive the spur dike is positioned, namely, a larger S, the shallower the scour hole. Variations under different cover conditions can be explained by the expansion of the separation zone around the submerged spur dike accompanied by the increase of channel cover roughness. Greater cover roughness shifts the maximum velocity closer to the channel bed and consequently increasing the bed shear stresses, resulting in deeper scour holes (Sui et al., 2010). Further, regardless of the cover roughness, under the same Fr_d, the differences in the $d_s/(L\sin\alpha)$ values between minor and moderate submergence remain relatively consistent and can be determined at any Fr_d where data are available.

Figure 3.10 shows the variation of $d_s/(L\sin\alpha)$ with Fr_d under different cover conditions. Figure 3.10 confirms the trend found in Figure 3.4 that for the same bed material and approach velocity, the appearance of an ice cover resulted in a higher scour depth. Additionally, regardless of the submergence level, results show that to reach the same dimensionless scour depth, Fr_d is the smallest under the rough cover condition, followed by smooth cover and the open channel flow condition (e.g., when $d_s/(L\sin\alpha) = 0.30$, $Fr_d = 4.89$, 5.19, and 5.34, respectively, for rough ice cover, smooth ice cover, and open channel under moderate submergence). Referring to Equation (5), a smaller approach velocity is required to reach the same dimensionless scour depth for covered flow compared to that under the open channel flow condition.

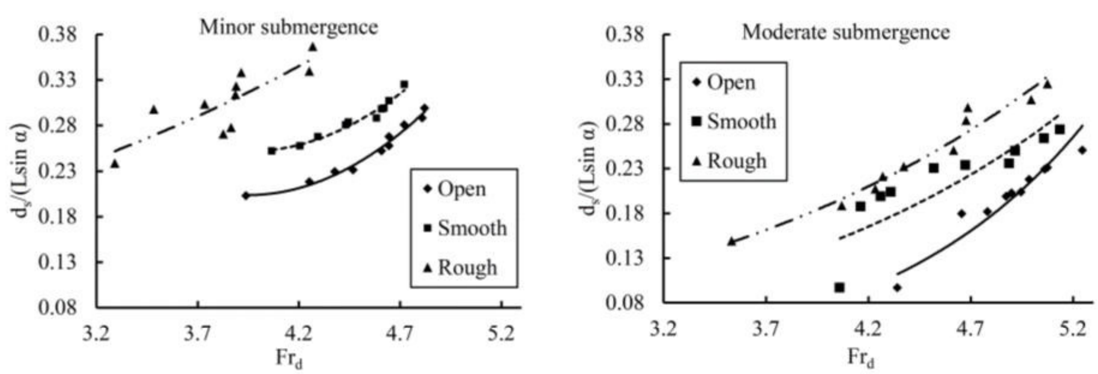

Figure 3.10 Dependence of $d_s/(L\sin\alpha)$ on Fr_d under different cover conditions for different submergence levels.

3.3.3 Modification of existing equation

Researchers have derived several formulas to predict the maximum scour depth around in-stream hydraulic structures. Based on the ratio of wetted embankment length (L_w) to the approach flow depth (h), the Highways In the River Environment (HIRE) equation (Richardson et al., 1989) is recommended when $L_w/h > 25$, whereas the Froehlich (1989) equation is advised when $L_w/h \leq 25$ (USACE, n.d.). Dey and Barbhuiya (2005) proposed an empirical scour depth equation based on 99 experiments using uniform sediment and 27 experiments using non-uniform sediment. They determined that the excess abutment Froude number, the ratio of flow depth to abutment length, and the ratio of abutment length to sediment size influence the equilibrium scour depth. Due to the intricacy of the scour processes, predictions of scour depth using existing scour equations around abutments will yield results with significant differences when applying them to spur dikes (Oğuz & Bor, 2022).

Lim (1997) proposed the following equation for determining the dimensionless maximum scour depth (d_s/h) based on 252 datasets using non-uniform sediment for laboratory experiments under the clear water scour condition,

$$d_s/h = K_s(0.9X_a - 2) \tag{3.6}$$

where K_s is the abutment shape factor, taken as 1.0 for vertical wall structures (such as the model spur dike in the current study), and X_a is calculated as

$$X_a = \{(\theta_{ca})^{-0.375}(Fr_d)^{0.75}(d_{50a}/h)^{0.25}[0.9(L\sin\alpha\,/h)^{0.5} + 1]\} \tag{3.7}$$

in which θ_{ca} is Shield's (1936) entrainment function and d_{50a} is the median grain size for the armor layer, obtained by sieve analysis of the samples collected from the armor layer. Shield's diagram offers a reference for critical shear stress by plotting it against the boundary shear Reynolds number, helping contextualize sediment movement tendencies in this study. Equation (3.6) is valid when X_a is over 2.2 and Lim (1997) proposed that θ_{ca} can be calculated based on the following functions:

$$\theta_{ca} = \begin{cases} 0.055, \quad D_{*a} > 150 \\ 0.013D_{*a}^{0.29}, \quad 20 < D_{*a} \leq 150 \\ 0.04D_{*a}^{-0.61}, \quad 10 < D_{*a} \leq 20 \\ 0.14D_{*a}^{-0.64}, \quad 4 < D_{*a} \leq 10 \\ 0.24D_{*a}^{-1}, \quad D_{*a} \leq 4 \end{cases} \tag{3.8}$$

where D_{*a} is the armor layer particle parameter, calculated as

$$D_{*a} = d_{50a}[(s-1)g/v^2]^{1/3} \tag{3.9}$$

where v is the kinematic viscosity of water at the experiment temperature. However, in the equation proposed by Lim (1997), the channel cover and submergence level are not considered.

The current study proposes a new factor (X') to replace X_a in Lim's (1997) equation by incorporating the channel roughness factor (N) and the overtopping ratio (S). Data for derivation of the new equations are attached in Appendix II. Flume experiments are generally impacted by the flume's sidewall. Since the hydraulic radius (R_h) reflects an effective flow depth that compensates for sidewall effects, Equations (3.6) and (3.7) may be adjusted by substituting R_h for h. The experimental data were randomly split into two samples such that 80% of the measurement data were used to train the model and 20% were used for the model validation. Regression analyses yielded the following equations.

$$X' = 0.21(\theta_{ca})^{-0.37}(Fr_d)^{-0.11}(d_{50a}/R_h)^{-0.17}(L\sin\alpha/R_h)^{0.15}(N)^{0.013}(S)^{-0.27} \tag{3.10}$$

where

$$N = \frac{n_0 U}{R_h^{2/3}} \tag{3.11}$$

Brunner (2016) suggested using Equation (3.12) for determining the composite roughness coefficient for an ice-covered flow, n_0, as follows:

$$n_0 = \left[\frac{(n_b)^{1.5} + (n_c)^{1.5}}{2}\right]^{\frac{2}{3}} \tag{3.12}$$

where n_b and n_c are the Manning roughness coefficients for the channel bed and ice cover, respectively. For open channel flow, n_0 is taken as n_b. The resulting coefficient of determination (R^2) and root mean square error (RMSE) for the modified equation are 0.846 and 0.018, respectively. The comparison of the calculated relative maximum scour depth (d_s/R_h) to those of measurements is shown in Figure 3.11.

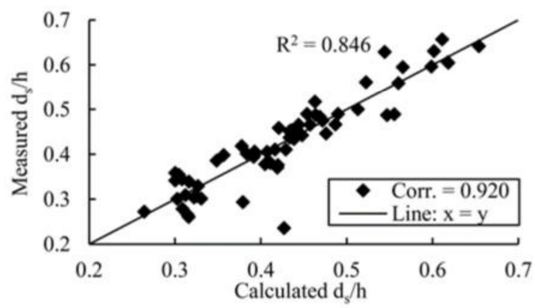

Figure 3.11 Comparison between measured and calculated (using Equation (10)) values of maximum relative scour.

The percent bias (PBIAS) and root mean deviation ratio (RSR) are applied to further assess the accuracy of the modified equation. The calculated PBIAS and RSR are 0.00193 and 0.0637, based on which the modified equation predicts the local scour relatively well (Abeysingha et al., 2015). Type III sum of squares (SS) analysis was done to assess the influence of each independent variable on the relative maximum scour depth (d_s/R_h). The Type III SS was selected because the sequence in which the variables are chosen has no influence on the scores. The higher the model SS, the lower the residual SS, and, hence, the greater the variable's impacts (Neter et al., 1991). By means of the Type III sum of squares analysis, both "F" and "p" values have been calculated. Table 3.2 lists the performance of each predictor in the new equation.

Table 3.2 Type III sum of squares analysis results

Source	DF	Sum of squares	Mean squares	F	Pr > F	Significance codes[1]
θ_{ca}	1.000	0.002	0.002	2.993	0.089	.
Fr_d	1.000	0.004	0.004	11.750	0.001	***
d_{50a}/R_h	1.000	0.000	0.000	0.456	0.502	°
$L\sin\alpha/R_h$	1.000	0.039	0.039	114.478	<0.0001	***
N	1.000	0.001	0.001	0.497	0.484	°
S	1.000	0.064	0.064	187.009	<0.0001	***

[1]Significance codes: 0 < *** < 0.001 < ** < 0.01 < * < 0.05 < . < 0.1 < ° < 1, generally, values less than 0.05 are considered statistically significant; note: DF is the degrees of freedom in the statistical test.

In Table 3.2, "*Pr>F*" is the probability of the test results that are at least as extreme as the observed results assuming the null hypothesis applies, is also called the *p*-value. "*F*" is called the *F*-value and represents how predictive the model is, which helps to determine whether statically significant differences exist in the means of multiple data groups. The dependent variable, the relative maximum scour depth (d_s/R_h) is found to be significantly influenced by following dimensionless variables: Fr_d, $L\sin\,\alpha/R_h$, and S. On the other hand, other dimensionless variables including θ_{ca}, d_{50a}/R_h, and N do not show a high statistical significance. The overtopping ratio S (with $F = 187.009$, $p < 0.0001$) displays the highest model SS (0.064) and is deemed to be the most significant variable in determining the relative maximum scour depth (d_s/R_h), whereas d_{50a}/R_h (with $F = 0.001$, $p = 0.502$) representing the impacts of the non-uniformity of sediment has the least statistical significance. The general form of the modified equation is as follows:

$$d_s/R_h = K_s(0.9X' - 2) \tag{3.13}$$

where

$$X' = f(\theta_{ca}, Fr_d, d_{50a}/R_h, L\sin\,\alpha/R_h, N, S\,) \tag{3.14}$$

Additional investigations should be done for individual spur dike designs to validate this equation and determine the function in Equation (3.14).

3.4 Chapter Summary

Chapter three describes the study that utilized the physical model testing method, focusing on the non-dimensional maximum equilibrium scour depths around angled, submerged spur dikes under open and ice-covered flow conditions. The impacts of parameters related to spur dike design and water surface cover conditions on local scour have been inspected. Based on data analysis, the following conclusions have been obtained.

1) The non-dimensional scour depth related to the dike normal length $d_s/(L\sin\alpha)$ decreases with the increase of the overtopping ratio (S), implying that the wake vortices are weakened more by the boundary layer flow on the top of the spur dike as the submergence increases. For a submerged vertical wall spur dike, non-dimensional scour depth related to the non-dimensional maximum scour depth related to design length (d_s/L) decreases with the increase in the alignment angle (α). However, the sensitivity towards the addition of an ice cover on the water surface increases with α. Moreover, for a fixed α, the longer the design length of a spur dike (L) is, the more aggressive the sediment movement becomes, as shown by a higher d_s/L value.
2) With an increase in the Froude number (Fr), the non-dimensional scour depth related to the spur dike normal length $d_s/(L\sin\alpha)$ increases. Regardless of the cover condition, variables $d_s/(L\sin\alpha)$ and (Fr) are strongly correlated, indicating that the flow near a spur dike is exceptionally turbulent. The calculated Fr in the downstream sandbox has

a smaller range than those in the upstream sandbox, potentially caused by energy dissipation because of the channel sidewalls and bed. For a given densimetric Froude number (Fr_d) and cover condition, the more immersed the spur dike is positioned (namely, a greater S), the smaller the relative maximum scour depth $d_s/(L\sin\alpha)$. The presence of an ice cover on the water surface, regardless of the cover roughness, reduces the difference in the rates of change between the minor submergence and moderate submergence. When other factors don't change, to reach the same relative maximum scour depth $d_s/(L\sin\alpha)$, the densimetric Froude number, Fr_d, under a rough cover is the least, followed by smooth ice-covered and open-channel flow conditions.

3) To modify the equation for estimating scour depth proposed by Lim (1997), the hydraulic radius (R_h) has been proposed to substitute for the approach flow depth (h) to minimize the sidewall effect inherent in flume experiments. Type III Sum of Squares analysis was done to determine the individual factors' significance in the modified equation. The results show that the submergence level is the most influential predictor in determining the maximum local scour depth. Both PBIAS and RSR were selected as the statistical criteria used to further to validate the accuracy of the modified empirical equation. Coupled with the coefficient of determination (R^2) and root mean square error (RMSE) values, the performance of the modified equation for calculating the relative maximum scour depth $d_s/(L\sin\alpha)$ is relatively good.

The current study is limited to the analyses of the equilibrium scour depths (namely, the maximum scour depths around spur dikes). However, the results of field observations showed that the time-development of scour holes also varies under different experimental setups (i.e., open channel flow or ice-covered flow conditions). Further research in this field should be done to examine the temporal development of scour holes and the protection mechanisms of the armor layer inside scour holes around angled, submerged spur dikes.

4. CHAPTER FOUR: TURBULENT FLOW STRUCTURE AROUND SUBMERGED ANGLED SPUR DIKES UNDER ICE COVER

4.1 Introduction

Installing spur dikes in a channel represents a typical engineering practice to enhance channel functions and control floods. Spur dikes are designed to interrupt the flowing water and sediment transport along the shoreline or riverbank, thereby preventing erosion and ensuring the stability of channel banks. Spur dikes extend from riverbanks into the water, forming a barrier that alters flow patterns compared to rivers without them. This alteration aids in trapping sediment, thus preventing further erosion along the coastline or river. Spur dikes can induce turbulence and the formation of eddies in the flow field. The interaction between a dike and flowing water generates vortices and swirling motions, which lead to increased mixing and turbulence. These turbulent conditions can affect sediment transport, erosion, and deposition patterns near the dike and can also result in local scour (Fang et al, 2006; Li et al., 2023). The modified flow fields in the presence of spur dikes are complex and depend on various factors such as dike geometry, flow velocity, sediment characteristics, and overall hydraulic conditions. Various hydraulic modeling and site-specific studies are typically conducted to understand and predict the flow behavior around spur dikes before their construction to minimize adverse effects and optimize their designs. Spur dikes can be classified into submerged and non-submerged categories based on their submergence level. Based on the alignment angle (α) between the axis of a dike and the streamwise direction of the flowing water, spur dikes can also be grouped into attracting (acute angles), deflecting (right angles), or repelling (obtuse angles). The repelling type is preferred for submerged spur dikes, as the sediment can be directed toward the side of the river bank, contributing to the sediment deposition and mitigating the damage to the dikes' foundation as the water passes over the top of the spur dike (Zhang et al., 2018).

Rivers in cold regions seldom experience periods without ice cover development. Ice cover exerts non-negligible influence on the evolution of channel bed morphology (F. Wang et al., 2021). Hydraulic riverine structures, such as spur dikes and bridge piers/abutments, result in complex flow fields under ice-covered flow conditions. Hu et al. (2022) investigated the evolution of channel bed deformation and ice jam around a single pier. The study concluded that turbulence intensities in the scour hole around the pier increased when ice cover was present on the water surface without initiating ice jams. Zabilansky and White (2005) characterized a river as narrow if changes in water level have no impact on the position of the ice cover. When the flow discharge in a narrow river exceeds the freeze-up datum, the ice cover induces a pressurized flow condition beneath, shifting the maximum velocity position towards the channel bed. Moreover, a stationary ice cover increases the wetted perimeter and pushes the maximum velocity toward a smoother boundary (Smith et al., 2023; Sui et al., 2010).

The research focuses on turbulent flow characteristics around non-submerged spur dikes, analyzing velocities in three dimensions at specific locations. Barbhuiya and Dey (2004) employed an Acoustic Doppler Velocimeter (ADV) to assess the three-dimensional turbulent flow field around a vertical semicircular cylinder affixed to the sidewall of a rectangular channel in a laboratory setting. The vector graphs of the flow field in the azimuthal and horizontal planes indicate the presence of a main vortex upstream from the cylinder. Hei et al. (2009) utilized a laser three-dimensional particle dynamics analyzer (3D-PDA) to determine the flow velocity around a spur dike. They categorized the general flow field into three sub-regions according to velocity distribution: the reverse-velocity region, the positive-velocity region, and the central flow region.

Kline et al. (1967) identified the burst phenomenon through visual and quantitative investigations into turbulent boundary layers. Low-speed streaks (areas of slow-moving flow) interact with the flow's outer edges through a slow "lift-up" followed by rapid oscillation, bursting, and ejection. The quadrant analysis proposed by Lu and Willmarth (1973) for analyzing the bursting phenomenon is frequently utilized to examine turbulent flow configurations and identify the coherent structures responsible for the turbulent transport of momentum (Huai et al., 2019).

Realistically, due to the changes in hydraulic conditions in a river, a spur dike should be aligned at variable angles. Considering extreme precipitation events' increasing frequency and intensity, non-submerged spur dikes can fully submerge when the design flood is exceeded. Also, the presence of an ice cover or ice jam in a river significantly increases the water level (Sui et al., 2002, 2005), and thus, non-submerged spur dikes become submerged. To the authors' knowledge, the flow fields around submerged angled spur dikes under ice-covered flow conditions have never been investigated.

This research investigates turbulent flow dynamics near a single submerged spur dike within a laboratory flume, utilizing a SonTek Acoustic Doppler Velocimeter (ADV) to measure instantaneous velocities under both open-channel and ice-covered conditions. The study examines how the geometries of such single submerged spur dike influence turbulent flow characteristics through quadrant analysis of velocity fluctuation components, thereby quantifying the contribution of each quadrant and assessing changes in dominant burst processes near angled submerged spur dikes across different flow conditions and experimental configurations. The objectives include identifying velocity field patterns using ADV data, quantifying Reynolds shear stress, and analyzing dominant turbulent events via quadrant analysis to understand the interaction between flow conditions, dike geometry, and turbulent flow structures. Although real-world applications often involve groups of spur dikes, this study isolates single structures to provide fundamental insights into hydrodynamic behavior under ice-covered conditions.

4.2 Material and Methods

4.2.1 Facilities for Experiments

Experiments were conducted in a large concrete outdoor flume at the Quesnel River Research Center (QRRC) in Likely, British Columbia, measuring 38.20 m in length, 2.00 m in width, and 1.30 m in depth. A staff gauge accurate to 1 mm recorded the approaching flow depth upstream of the leveled sandbox surface, ensuring flow uniformity during each experimental run. At the flume exit, a tailgate ensured the flow reached the desired depths along the flume. The current study utilized two sandboxes. As shown in Figure 4.1a, the upstream sandbox measures 5.60 m in length, 2.00 m in width, and 0.30 m in depth, while the downstream sandbox is 5.80 m long, 2.00 m wide, and 0.30 m deep. The distance from the downstream sandbox's exit to the tailgate measures 5.30 m. The flume bed features a 0.20% slope. Due to the backwater effect, water levels at the two sandboxes slightly vary.

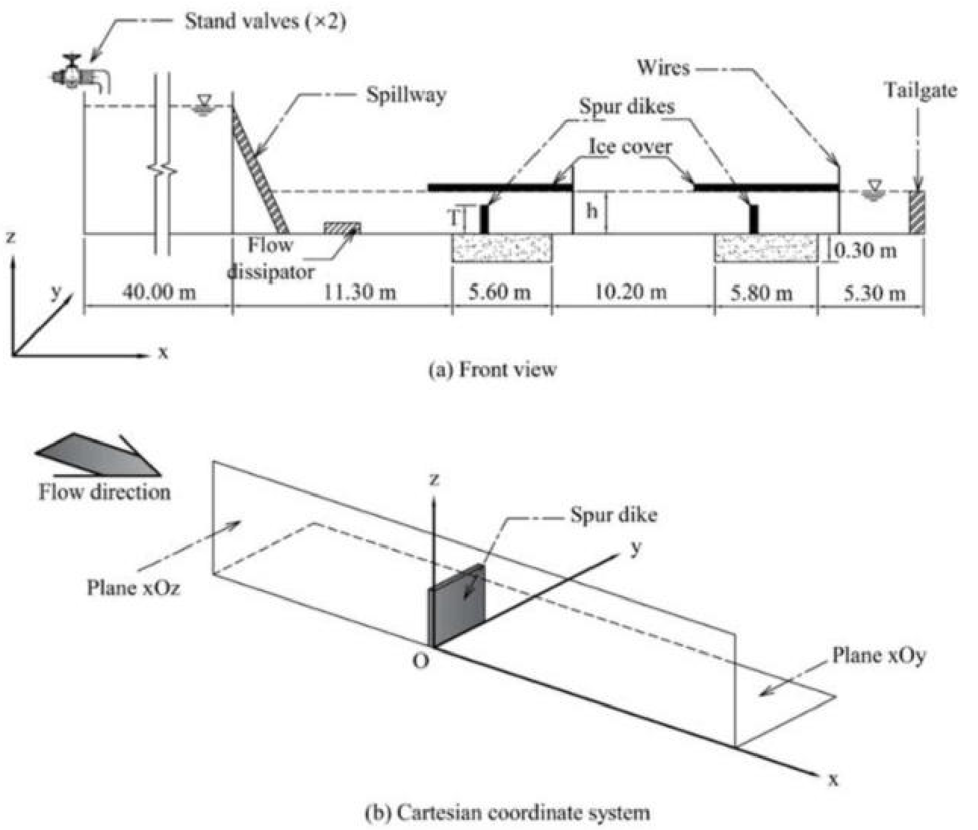

Figure 4.1 Schematic diagram of the experimental flume: (a) Side view; (b) Cartesian coordinate system.

The aspect ratio *B/h*, where *B* is the channel width, and *h* is the approaching flow depth, is a key hydraulic parameter used to classify channels as narrow or wide. This study considers channels wide when $B/h > 5$, consistent with laboratory conditions where sidewalls are assumed smooth. In natural settings, however, lateral roughness elements such as vegetation along riverbanks can increase flow resistance and reduce effective channel width. As a result, a higher aspect ratio threshold may be required to account for these roughness effects (Knight & Macdonald, 1979). A Cartesian coordinate system is established for three-dimensional velocity measurements in the flume. The *x*-axis runs longitudinally along the streamwise flow, the *y*-axis laterally towards the opposite side of the observation station, and the z-axis vertically towards the water surface. The Cartesian coordinate system's origin is positioned at the center of the spur dike surface attached to the sidewall. The $z = 0$ plane corresponds to the flume bottom (or the sandbox's initial surface), with velocity fluctuation components in the x-, y-, and z-directions denoted by u', v', and w', respectively. The placement of the model submerged spur dikes was based on the findings of Kuhnle et al. (2002), who reported that the scour region's tail length around the dike is less than 20 times the spur dike length, regardless of the alignment angles. The model spur dike's width (thickness) is 5 cm, buried at the sandbox bottom, with heights (T) of 20 cm and 25 cm above the initial flat channel bed. The submergence level was quantified using the overtopping ratio S, defined as the ratio of flow depth h to spur dike height T ($S = h/T$), in accordance with Li et al. (2023) and McCoy et al. (2007). For this study, "minor submergence" corresponds to $S = 1$, where the flow depth approximately equals the dike height. "Moderate submergence" occurs when $S = 1.25$, where a larger portion of the dike is submerged. Considering the dimensions of the spur dikes and sandboxes, the model submerged spur dikes were positioned at one-third the length of each sandbox to minimize downstream interferences, as depicted in Figures 4.1a and 4.1b, illustrating the adopted coordinate system.

Velocity data were collected with a SonTek Acoustic Doppler Velocimeter (ADV). The SonTek ADV, featuring a high-resolution current meter, includes a downward-looking probe and three receivers. It monitors flow velocity through the Doppler effect, identifying changes in frequency (Doppler shift) reflected by moving solid particles in the water. Velocity data was analyzed with WinADV to preclude aliasing. WinADV analyzes signal quality through a correlation coefficient (COR) and signal-to-noise ratio (SNR). Following SonTek/YSI's guidance, the study applied criteria of SNRs above 15 dB and CORs exceeding 70% at 25 Hz, rendering 85% of the data suitable. A definitive strategy and standard for determining suitable ADV sampling times for turbulent flow still needs improvement. Previous methods lack universal applicability and are heavily dependent on researchers' judgments. Proposed criteria, rooted in statistical methods, have drawbacks related to experiment scale and flow conditions. Park and Hwang (2021) suggested a sampling time based on the integral time scale (T_i), calculated using Equation 4.1, with a recommended range from $150T_i$ to $200T_i$:

$$T_i \equiv \int_0^{t_0} \frac{\langle u_i(t) u_i(t+\tau) \rangle}{\langle u_i(t) \rangle^2} d\tau \tag{4.1}$$

where τ denotes the lag between two points, t_0 represents the first zero-crossing time in the normalized autocorrelation function, $u_i(t)$ denotes the velocity component, and the subscript i specifies the x, y, and z direction (O'Neill et al., 2004).

The laboratory experiment results in this study show an integral time ranging from 0.21 to 0.74 seconds. Park and Hwang (2021) suggested that the sampling period should range from 31.5 to 148 seconds. In this study, each measurement event's sampling period was 120 seconds, which is considered adequate for accurate turbulence statistics determination (Jafari and Sui, 2021; Namaee and Sui, 2020). Experiments showed that the open-channel flow condition produced the shallowest scour depth (G. Li et al., 2023), which was used as a reference point for the timing of positioning the ADV during instantaneous velocity measurements. Specifically, the ADV was deployed when the scour depth approached the equilibrium depth observed under open-channel conditions. Velocity measurements were restricted to the area near the dike head to further reduce potential interferences of varied terrain elevations under ice-covered flow conditions. Flow velocity measurements started from the lowest point, 3 mm above the bed. Measurements span three cross sections: one 10 cm upstream of the dike, another near the dike's tip, and a third 10 cm downstream. Seven locations were selected for measurements in each spur dike layout. Measurements at each location were conducted vertically from the channel bed to the water surface, covering 8–10 different flow depths. One thousand five hundred (1500) instantaneous velocities in three directions were recorded at each point with 120-second sample periods. Figure 4.2 shows the measuring point locations where instantaneous velocities were recorded. Table 4.1 presents the flume setups and model spur dike features for open-channel studies, consistent across smooth and rough ice-covered conditions.

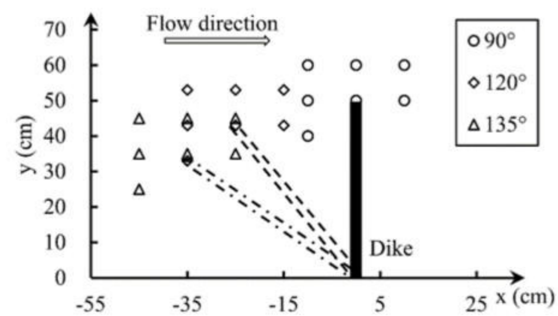

Figure 4.2 Schematic plot of measuring positions (dike length = 50cm).

Table 4.1 Summary of experimental conditions and features of the flume and spur dikes under the open channel condition.

Run #.	Sandbox position	Discharge, Q (L/s)	Spur dike height, T (m)	Alignment angle, α (°)
1	Upstream	148	0.15	90
2	Upstream	148	0.15	120
3	Upstream	160	0.15	135
4	Upstream	156	0.20	90
5	Upstream	152	0.20	120
6	Upstream	140	0.20	135
7	Downstream	112	0.20	90
8	Downstream	124	0.20	120
9	Downstream	108	0.20	135
10	Downstream	128	0.25	90

11	Downstream	132	0.25	120
12	Downstream	124	0.25	135

4.2.2 Ice Cover and Sediment Setups

The available materials for modeling ice cover fall into three categories: rigid, synthetic, and natural. When strength is not a priority, researchers often use rigid, unbreakable substitutes for ice cover, including wood, paraffin, polyethylene, polypropylene plastic, and Styrofoam (Jafari & Sui, 2021). Styrofoam panels modeled smooth ice cover, while rough ice cover was created by affixing Styrofoam cubes (with a 2.5 cm edge length) to the panel bottoms. The Manning's coefficient for smooth Styrofoam panels is estimated at 0.013 (Jafari & Sui, 2021). Using Li's equation to calculate Manning's coefficient (n_i) for rough model ice cover, with a roughness height of 0.025 m, n_i is calculated as 0.021 (Li, 2012). These values align with calculated results for surveyed ice-covered channels, either through average roughness height estimation (0.0075 to 0.029) or the logarithmic law (0.0088 to 0.033) (Li, 2012). Equation 4.2 expresses the calculation for n_i:

$$n_i = 0.039\, k_s^{1/6} \tag{4.2}$$

where k_s denotes the average roughness height at the ice cover's bottom. Field observations indicated that most rivers form smooth, floating ice covers (Turcotte et al., 2011). This study modeled the ice cover using a horizontally fixed, slightly buoyant styrofoam layer anchored at both ends with wires. The attached styrofoam cubes were submerged for rough ice conditions by placing weighted plywood on top. Although floating ice in natural rivers can exhibit lateral movement and minor vertical adjustments due to flow forces and variations in ice thickness, the experimental setup ensured horizontal stability, maintaining controlled conditions for consistent measurement. This design facilitated the analysis of key flow dynamics beneath the ice while minimizing the complexity introduced by vertical fluctuations. Furthermore, the local scour processes observed under fixed and floating ice covers were comparable, with increased ice cover roughness correlating with greater local scour depths (D. Hains & Zabilansky, 2004).

The entrance length for fully developed flow (l_e) can be estimated using the following equation (Çengel & Cimbala, 2014):

$$l_e = 1.359 L_c Re^{1/4} \tag{4.3}$$

where Re represents the flow Reynolds number, and L_c represents the characteristic length. The model floating ice cover, consisting of Styrofoam panels, measures 9.60 m long and 2.00 m wide for the upstream sandbox and 9.80 m long and 2.00 m wide for the downstream sandbox, extending 2.00 m before and after each sandbox (Figure 4.1a). This configuration ensured the model ice cover spanned sufficient space for the flow to fully develop.

Non-uniform bed materials have been utilized in flume studies to understand the clear-water scour processes comprehensively. In laboratory flume investigations, sediment sizes must match or exceed 10% of the natural channel bed sediment sizes in the field (Ettema et al., 1998). This study used non-uniform sediments with a median particle size (d_{50}) of 0.90 mm to imitate the natural riverbed. The channel bed Manning roughness coefficient (n_b) for the sand used as bed material was calculated as 0.020 using Equation 4.4 (Julien, 2018).

$$n_b = 0.064 d_{50}^{1/6} \tag{4.4}$$

4.2.3 Quadrant Analysis

Huai et al. (2019) noted that quadrant analysis frequently assessed turbulent flow structures through conditional statistics of streamwise and vertical velocity variations (u' and w'). This study employed quadrant analysis to investigate how spur dike parameters influence sweep, ejection, outward, and inward movements. A spur dike's submergence level and alignment angle significantly impact turbulence structure under consistent approaching flow conditions (Jafari & Sui, 2021; Vaghefi et al., 2016). In quadrant analysis, the u'-w' plane is divided into four quadrants: Q_1, Q_2, Q_3, and Q_4.

The hole size parameter H_t (threshold level) is introduced through filtration using a hyperbolic area to calculate the frequency of each bursting event, focusing on the predominant contributions to $-\overline{u'w'}$. This approach allows for extracting of significant Reynolds shear stress values in each quadrant while filtering out minor background events (Huai et al., 2019). The conditional function, H_t, differentiates between background disturbances from large magnitude burst events, the latter of which could significantly affect sedimentation processes. H_t is defined as:

$$H_t \equiv \frac{\left|u_j'w_j'\right|}{\sqrt{\overline{u'^2}}\sqrt{\overline{w'^2}}} \tag{4.5}$$

The fluctuation of H_t enables the computation of the fractional contributions to total Reynolds stress from events of varying magnitudes within each quadrant, excluding the hole area, expressed as:

$$\overline{u'w_s'} = \frac{1}{n}\sum_{j=1}^{n} I\left(u_j'w_j'\right) \tag{4.6}$$

where $\overline{u'w_s'}$ represents the proportion of turbulent bursts exceeding the threshold, $u_j'w_j'$ denotes the conditional Reynolds stresses, n signifies the number of events, and the indicator function I is defined to complete the conditional averaging technique:

$$I = \begin{cases} 1, \ if \ |u'w'| \geq H_t(\overline{u'u'})^{0.5}(\overline{w'w'})^{0.5} \\ 0, \ if \ |u'w'| < H_t(\overline{u'u'})^{0.5}(\overline{w'w'})^{0.5} \end{cases} \tag{4.7}$$

The stress proportion, S_i, for the quadrant i is defined as the flux contribution to u' and w' from that quadrant using:

$$S_i = \frac{\langle u'w' \rangle_i}{|\overline{u'w'}|} \tag{4.8}$$

where

$$\langle u'w' \rangle_i = \lim_{t\to\infty} \frac{1}{T_t}\int_0^{T_t} u'(t)w'(t)I\, dt \tag{4.9}$$

where T_t denotes the total time. S_1 and S_3 are positive (> 0), while S_2 and S_4 are negative (< 0). A computer program in RStudio was developed to analyze the bursting phenomena and ascertain each quadrant's contribution to the Reynolds shear stress.

4.3 Results and Discussions

4.3.1 Distributions of Velocity around Angled Spur Dikes

Although the flow fully develops before reaching the cross-section with the spur dike, the dike's obstruction induces a new boundary layer. This study's laboratory setup consists of two isolated, non-interacting spur dikes, with hydrodynamics analyzed individually around each. Despite the presence of two dikes, no interaction effects are considered. Velocity fields around a single spur dike were measured at three cross-sections: 10 cm upstream, at the tip of the dike, and 10 cm downstream. For each dike alignment angle, velocity measurements were taken at seven positions along these cross-sections (CSs, Figure 4.2). Due to ADV device limitations, velocity data can only be acquired 0.10 m away from the probe head. Thus, velocity measurements cannot fully cover the entire depth (z-axis) (Namaee and Sui, 2020). In laboratory flume settings, channel confinement can cause sidewall effects that alter the flow pattern and vortex intensity, leading to velocity dips and shifting maximum velocity below the open channel flow's free surface. The dip phenomena's mechanisms are often qualitatively discussed regarding secondary currents. However, in this study's wide channel, where the flow becomes 2-dimensional in the middle section, the impact of secondary currents is minimal and will not be further discussed (Khanarmuei et al., 2020).

The streamwise velocity (u) is the most critical 3D velocity component for characterizing turbulence structure, demonstrating the highest value and variability compared to the other two velocity components (v, w). Distortion in the streamwise velocity profiles decreases as the dike orientation angle exceeds 90°, leading to more uniformly distributed measured velocities, evidenced by u/u_{avg} values fluctuating less around 1.0. As Figure 4.3 illustrates, increasing the dike orientation angle from 90° to 135° results in lower streamwise velocities under any water surface condition. Of note, $u_{avg.}$ represents the depth-averaged value of u.

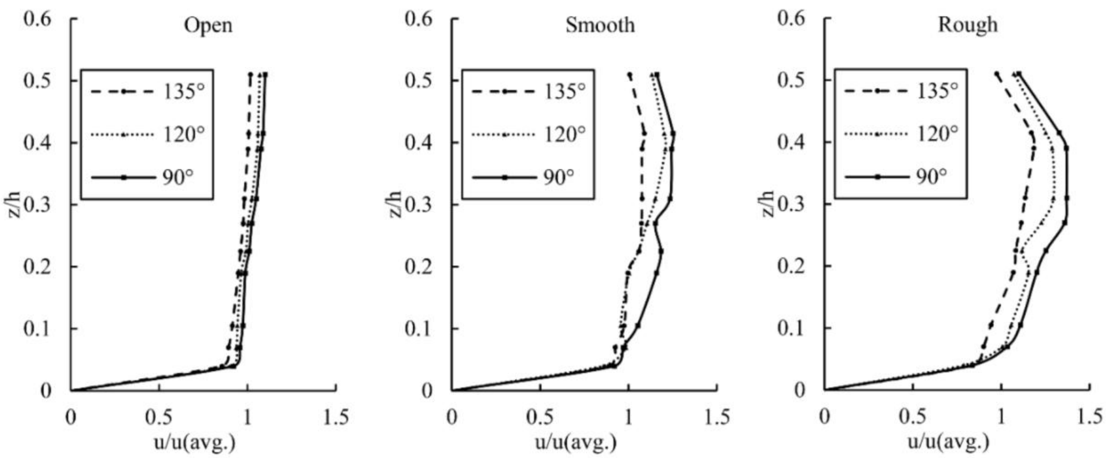

Figure 4.3 The non-dimensional streamwise velocities ($u/u_{avg.}$) in front of the spur dike tip (minor submergence of spur dikes, T = 25 cm).

Figure 4.4 depicts the effects of the alignment angle on velocity vectors in the X-Y plane (z/h = 0.45, the dike height above the initial sand bed T =25 cm). The origin (0,0) is at the center of the spur dike surface attached to the sidewall. The magnitude of the vortex at the front surface of the spur dike tip increases with the spur dike angle in the flow direction, as shown by denser and longer vector arrows. Due to the ADV device's limitations, this study presents only time-averaged velocity fields near the spur dike tip. Therefore, the time-averaged velocity fields do not capture the complete vortex profile in this study. However, in setups with deflecting spur dikes (angles over 90°), the X-Y plane flow field near the dike tip shows low sensitivity to water surface conditions. Unlike the altered vertical velocity profiles in Figure

4.3, ice cover presence minimally affects the X-Y plane velocity vectors. Subsequent analysis further illustrates the velocity distribution in the Y-Z plane at various cross-sections around the spur dike.

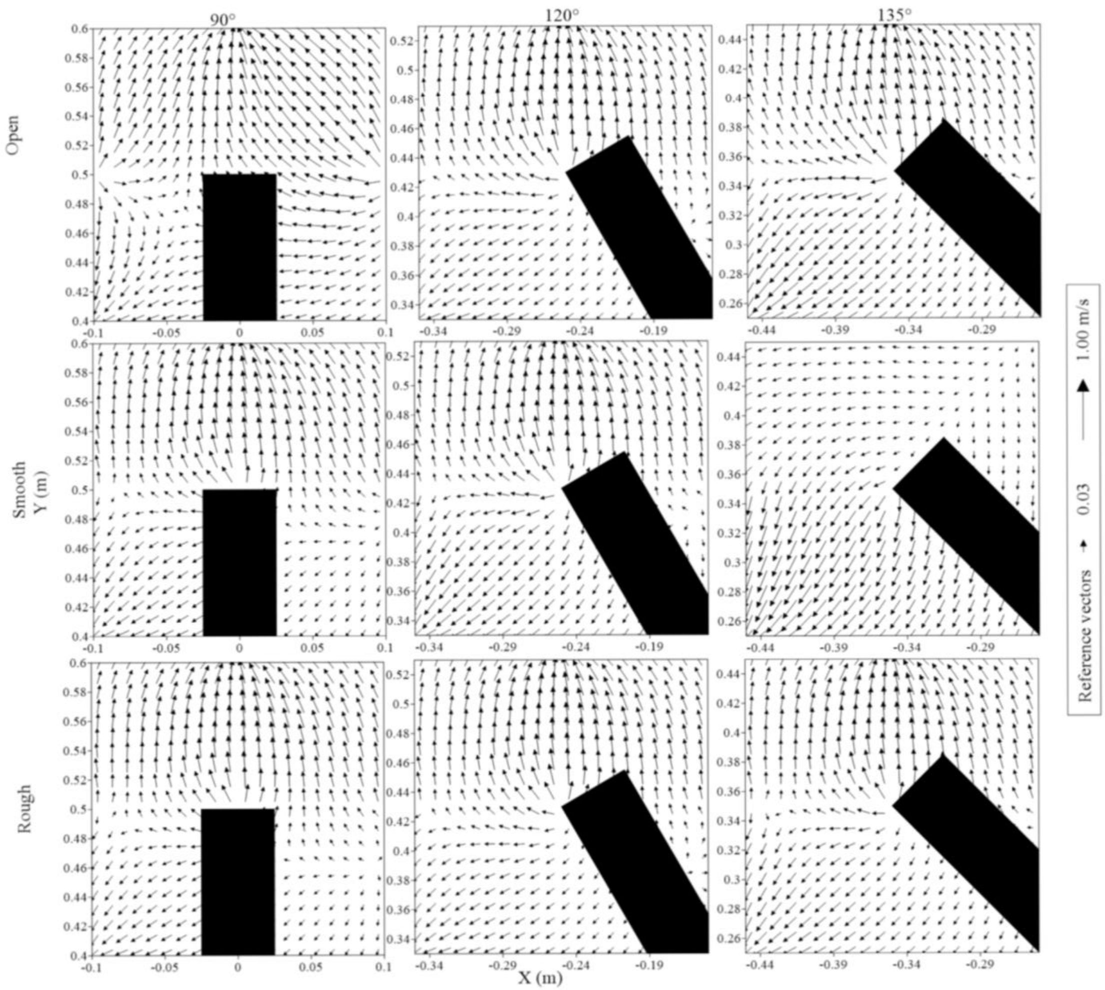

Figure 4.4 Flow velocity vectors generated from measured data in the *X-Y* plane close to the dike tip for different alignment angles (z/h = 0.45). Note: The origin (0,0) is located at the center of the spur dike surface attached to the sidewall, and the flow direction is from left to right.

Figure 4.5 illustrates the distribution of the dimensionless time-averaged streamwise flow velocity (u/U) at the spur dike's rear side, where U represents the average flow velocity, and L' denotes the projected normal length of the spur dike, calculated as $L_d \sin\alpha$. The dimensionless streamwise velocity values at the spur dike's rear side reveal a recirculation zone where reverse flow ($u/U < 0$) occurs due to the spur dike's obstruction. With minor submergence of the spur dike (T = 25 cm), reverse flow velocity magnitudes are higher than moderate submergence. Conversely, in the moderate submergence case, the water flowing over the spur dike reduces the reverse flow's magnitude, depicted by the lighter color.

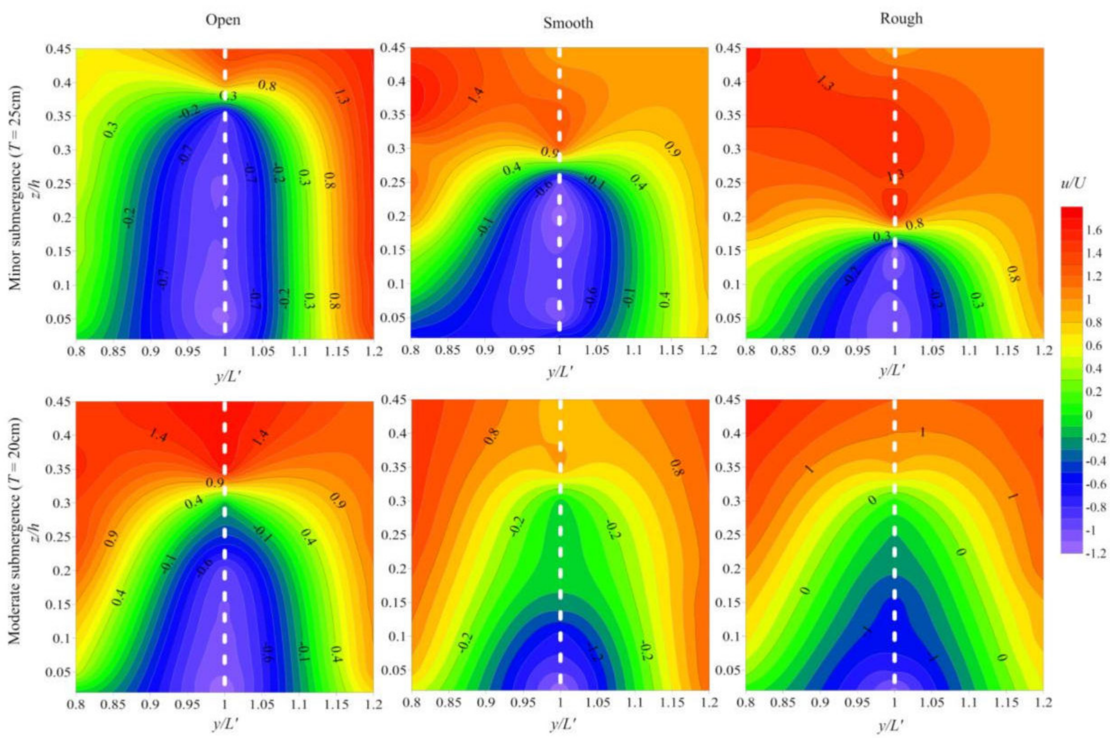

Figure 4.5 Time-averaged streamwise velocity contours at the rear side of the spur dike (x = 0.025 m, α = 90°). The outline of the spur dike is denoted in dash lines, and the flow is oriented towards the viewer and perpendicular to the paper's plane.

Figure 4.6 displays the dimensionless time-averaged lateral velocity (v/U). Similar to the u/U contour patterns, negative v/U values are observed near the channel bed behind the dike (x = 0.025 m). Under open flow conditions, more flow moves laterally above the spur dike when less submerged. However, under ice-covered flow conditions, confirming the impacts of submergence on v/U at the dike's rear side was challenging due to ADV device limitations. Conversely, with ice cover on the water surface, the submergence impact on v/U at the dike's rear side becomes less detectable, regardless of ice cover roughness, as indicated by v/U contours.

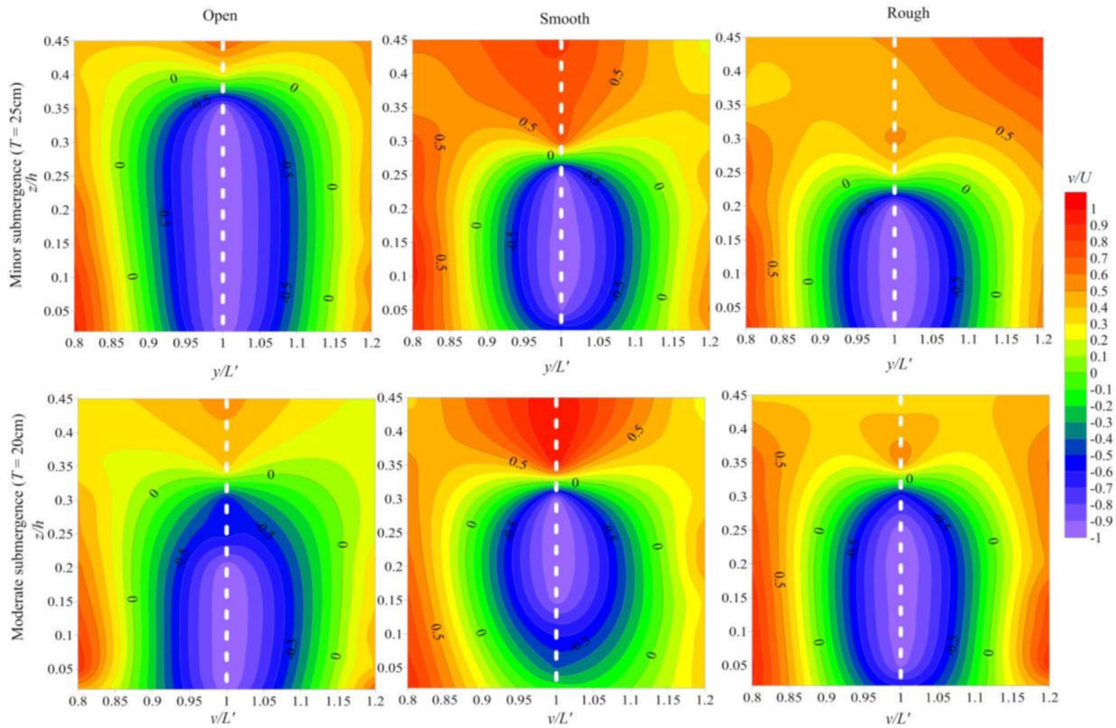

Figure 4.6 Time-averaged lateral velocity contours at the rear side of the spur dike (x = 0.025 m, α = 90°). The outline of the spur dike is denoted in dash lines, and the flow is oriented towards the viewer and perpendicular to the paper's plane.

Figure 4.7 displays the distribution of the dimensionless time-averaged vertical velocity (w/U). The most notable difference from the u/U and v/U distributions is the absence of vertical downward flow near the bed. Under ice-covered conditions, with moderate submergence of a spur dike, downward flow motion is observable near the dike tip, passing through the gap between the dike tip and the ice cover. Negative vertical velocity also occurs under open flow conditions but is less concentrated. The negative vertical velocity is believed to indicate the presence of a horseshoe vortex, characterized by a U-shaped vortex attaching to the dike's rear side, enveloping it, and directing vertical flow toward the bed (Koken & Constantinescu, 2008a). However, detailing the precise profile of the horseshoe vortex is challenging due to limited ADV measurements.

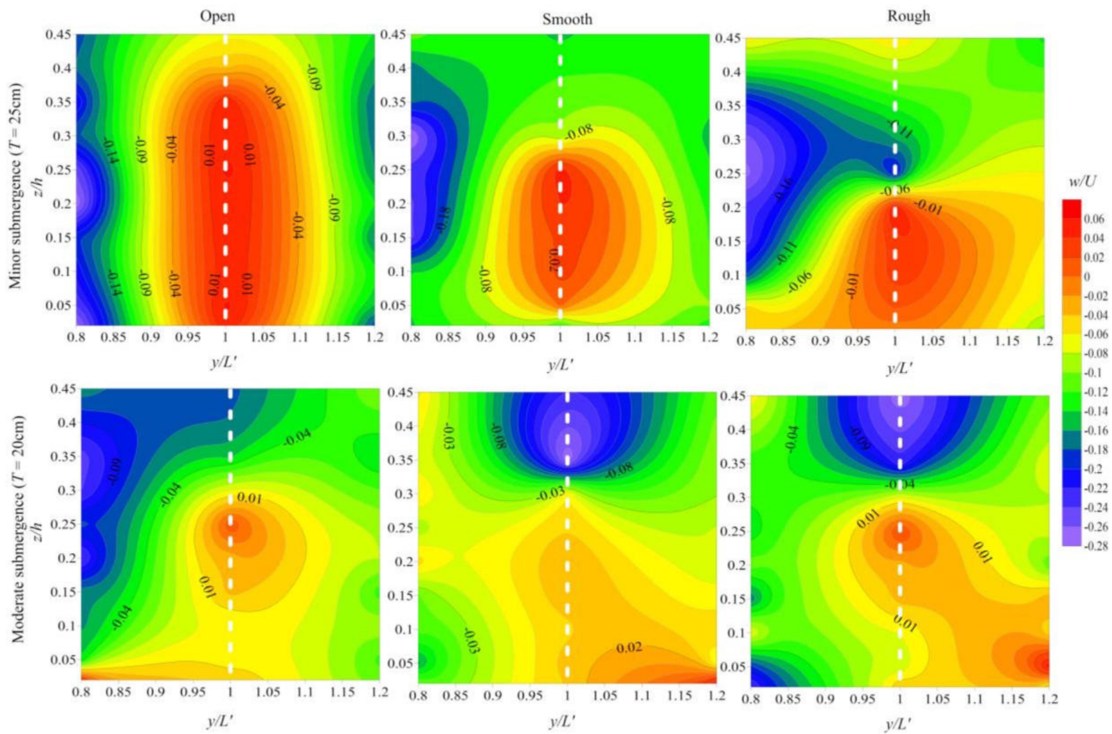

Figure 4.7 Time-averaged vertical velocity contours at the rear side of the spur dike (x = 0.025 m, α = 90°). The outline of the spur dike is denoted in dash lines, and the flow is oriented towards the viewer and perpendicular to the paper's plane.

Figure 4.8 displays vector graphs from velocity data in the X-Z plane for various cover conditions, located 10 cm in front of the dike tip (y = 60 cm, T = 25 cm, α = 90°). Due to the down-looking ADV device's limitations, the flow's velocity field's top 10 cm (z-direction) cannot be monitored or featured in the vector diagrams (M. R. Namaee et al., 2019). Figure 8 shows that the downward flow extends further to the bed under ice-covered conditions. A rough ice cover shifts the downward motion closer to the bed. However, despite the SonTek ADV's capability for high-frequency sampling, preliminary data processing showed excessive data noise at frequencies above 50 Hz. The sampling volume diameter measured approximately 0.6 cm, positioned 10 cm below the probe transmitter. The ADV device's limitation prevented a more accurate capture of the recirculation zone and vortices. Furthermore, despite logistical constraints, using a single ADV for velocity measurements notably limits accurately capturing temporal and spatial intricacies of recirculation zones and vortices in the flume.

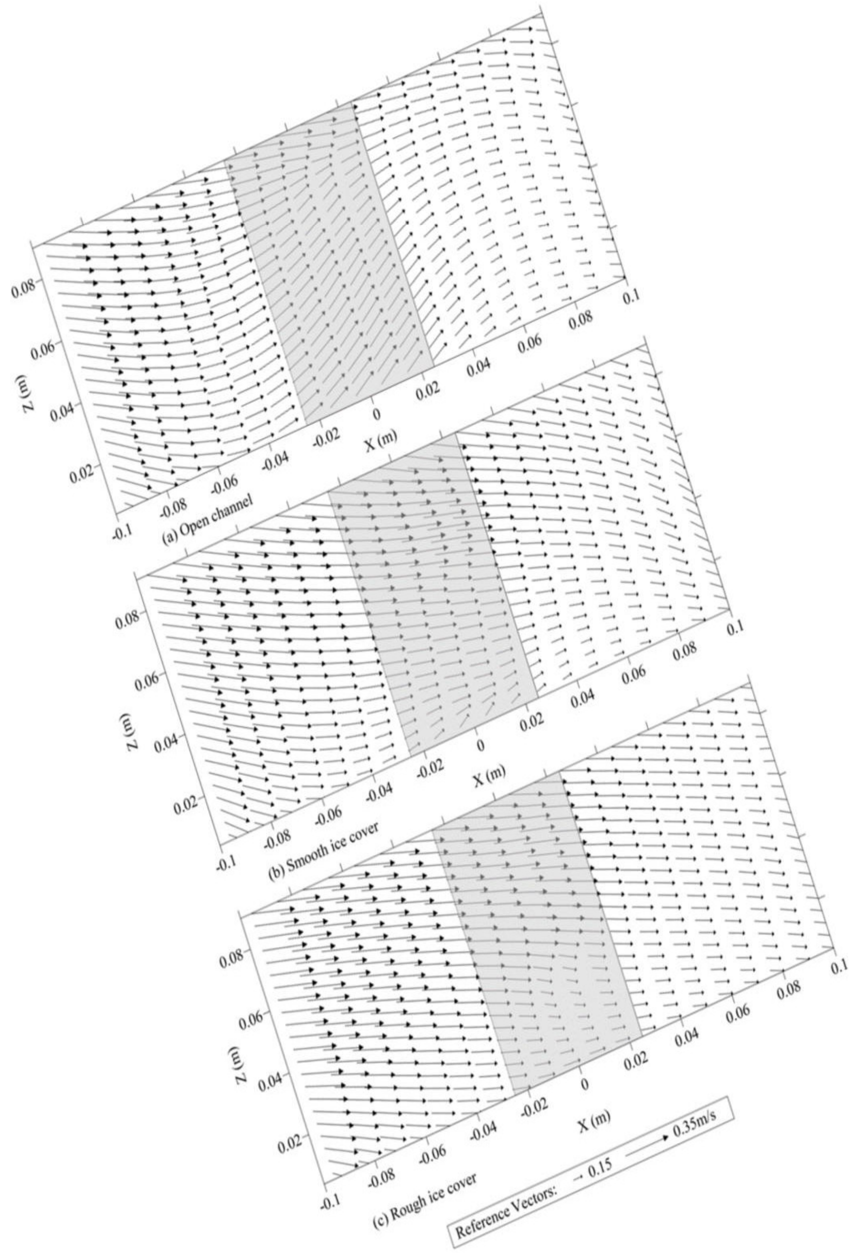

Figure 4.8 Flow vectors in the *X-Z* plane at the dike tip (y = 60 cm, T = 25 cm, α = $90°$). (a) Open channel, (b) Smooth ice cover, (c) Rough ice cover. The spur dike outline is shaded in light grey, and the flow direction is from left to right.

The following analysis focuses on the streamwise velocity component, which has the highest magnitude among the three velocity components. Under ice-covered conditions, the maximum flow velocity occurs between the ice cover and channel bed, influenced by their roughness coefficients, regardless of dike orientation angle and submergence levels. Increasing the ice cover's roughness coefficient relocates the maximum velocity closer to the bed. For example, with a spur dike at a 90° alignment angle and minor submergence, u_{max} occurs at flow depths of z/h = 0.31 under smooth cover and 0.27 under rough cover. Additionally, water surface cover conditions affect the location and magnitude of u_{max} (Figure 4.3). A smooth ice cover can increase maximum streamwise velocity by up to 20%, while a rough ice cover can lead to a 24% increase compared to open channel flow at the same flow depth.

These findings align with experimental studies and analytical simulations (Namaee and Sui, 2020). The study's results indicate that ice cover's influence on velocity distributions increases with increasing dike alignment angles. Moreover, the impact of dike alignment angles becomes more pronounced with increasing ice cover roughness. Negative flow velocity values indicate flow separation, generating a recirculating region. An impermeable spur dike changes the approaching streamwise flow direction, causing the boundary layer to break away from the frontal surface of the dike.

According to the law of the wall (also known as the logarithmic law), turbulent flow's average velocity at a given depth is proportional to the logarithm of the distance from that point to the boundary. The log-law (Equation 4.10) serves as a general expression for velocity distribution across depth in alluvial channels:

$$u_{avg.}(t) = \frac{u_*}{\kappa} \ln\left(\frac{z + Wk_e}{k_e}\right) + C \tag{4.10}$$

where $u_{avg}(t)$ is the time-averaged streamwise velocity, u_* is the shear velocity, κ is the von Karman constant, W is a coefficient of adjustment of the origin below the top roughness elements, C is an empirical constant, and k_e is the equivalent sand grain roughness (or Nikuradse roughness), approximated by d_{50}. W is estimated through trial and error, aiming to maximize the coefficient of determination (R^2) between u and $\ln[(z+Wk_e)/k_e]$. When W equals 0, experiments indicate that κ is approximately 0.41 and C approximately 5.20 for a smooth wall (Afzalimehr & Rennie, 2009). This study analyzed experimental data under open channel flow conditions to determine the best-fit values for W and C using $\kappa = 0.41$. Figure 4.9 displays a sample logarithmic law fitting for measured velocity data under open channel flow conditions. The origin adjustment coefficient W is estimated to be 0. Table 4.2 lists the constants in the sample curve-fitting process.

Table 4.2 Examples of curve-fitting constants in the logarithmic law equation for L = 50 cm spur dike.

Submergence level	Alignment angleα (°)	u_*/κ	C	Root mean square R^2
Minor	90	4.64	4.99	0.89
Minor	120	4.20	4.66	0.95
Minor	135	4.29	4.98	0.88

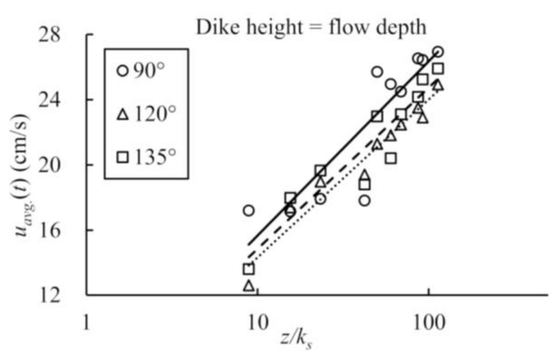

Figure 4.9 Fitting logarithmic law distribution on measured data under the open channel flow condition.

Kuhnle et al. (2008) applied the logarithmic law to simulate mean velocity near the boundary, setting k_e to 0 on the submerged dike surface and 1.0 mm on the sand channel bed.

For minor submergence (T = 25 cm, $h \approx T$), the logarithmic equation was modified using empirical coefficients and adjusted k_e for moderate submergence to simulate the streamwise velocity profile under open channel flow conditions.

Under ice-covered flow conditions, the vertical streamwise velocity profile is divided into the lower layer mainly affected by channel bed and upper layer mainly affected by ice cover. The logarithmic law approach applies separately to each layer under ice-covered conditions (Zhang, et al., 2021), as expressed in the following equation:

$$\begin{cases} u_b = \dfrac{u_{*b}}{\kappa} \ln\left(30 \dfrac{z}{k_{eb}}\right) \\ u_i = \dfrac{u_{*i}}{\kappa} \ln\left(30 \dfrac{h-z}{k_{ei}}\right) \end{cases} \tag{4.11}$$

where subscripts b and i represent the corresponding variables in the lower bed layer and upper ice cover layer, respectively, with z denoting the distance to the channel bed. The bed layer shear velocity (u_{*b}) is determined through regression analysis of the data before the decrease in streamwise velocity (u). Given that the two-layer theory posits that both layers share the same maximum velocity, Equation 4.11 is iteratively solved using the Microsoft Math Solver.

Figure 4.10 shows the estimated velocity profiles under open channel (using Equation 4.9) and ice-covered flow conditions (using Equation 10) for minor submergence cases of spur dikes. Dots with different shapes represent the measured data. Figure 4.10 demonstrates that laboratory measurements' velocity profile trends apply across the flow depth. Additionally, Figure 10 confirms that an ice cover shifts the maximum velocity location to a certain depth beneath it, with the maximum velocity closer to the channel bed under rough ice conditions than under smooth ice conditions (Namaee & Sui, 2019). Note that the flow velocities and depths in Figure 4.10 are not normalized, reflecting the parabolic relationship between instantaneous flow velocity and distance to the channel bed, as shown by the equations.

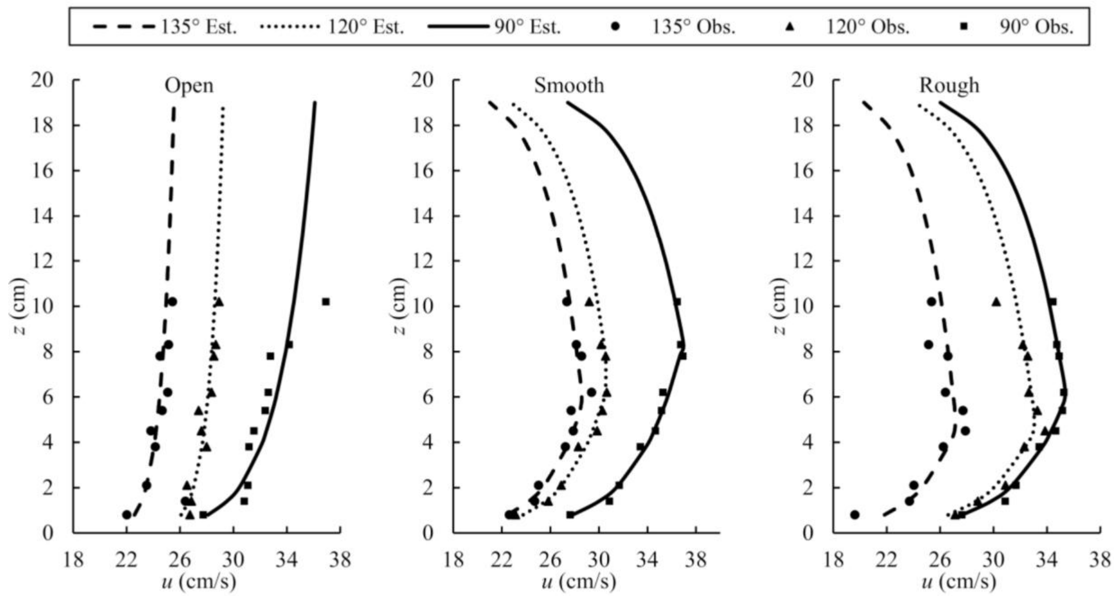

Figure 4.10 Comparison of the measured (Obs.) and equation-estimated (Est.) velocities.

4.3.2 Variation of Reynolds Shear Stress at Different Measurement Positions

Reynolds stress (τ_{ij}) accounts for turbulent variations in fluid momentum. It leads to vertical mixing and longitudinal and vertical momentum exchange (Feddersen & Williams, 2007). Theoretically, Reynolds stress distribution is linear along the flow depth and follows an exponential function for turbulence intensity. Shan et al. (2016) proposed a method for estimating bed shear stress in smooth and vegetated compound channels. For a single channel like the experimental flume, the direct covariance method (COV) (Equation 4.12) provides an unbiased estimation of channel bed stress, considered optimal by Kim et al. (2000):

$$\tau_{ij} = -\rho\overline{u'w'} \tag{4.12}$$

where ρ represents the fluid's mass density, u' and w' are instantaneous longitudinal and vertical velocity variations. Given the water temperature around 8°C (± 2°C), mass density is approximated at 1 g/cm^3. The COV method calculates Reynolds shear stress (RSS) using fluctuating velocity components measured by ADV, efficiently applied amidst sediment movement (Shahmohammadi et al., 2021). The RSS component is normalized by dividing it by the square of the time-averaged shear velocity.

Normalizing RSS to critical shear stress ($-\overline{u'w'}/u_*^2$) aids in comparing flows with varying Reynolds numbers and eliminates density variation effects from water temperature changes. Results for the 90° dike alignment case were selected to analyze RSS variation, as velocity profiles with this alignment show the most significant magnitude and variation. Figures 4.11 and 4.12 display the vertical profiles of the RSS at measuring points 10 cm upstream the dike tip CS (C-10), 10 cm downstream the dike tip CS (C10), and the dike tip CS (C0) in the *X-Z* plane for the 90° alignment dike under minor and moderate submergences, respectively.

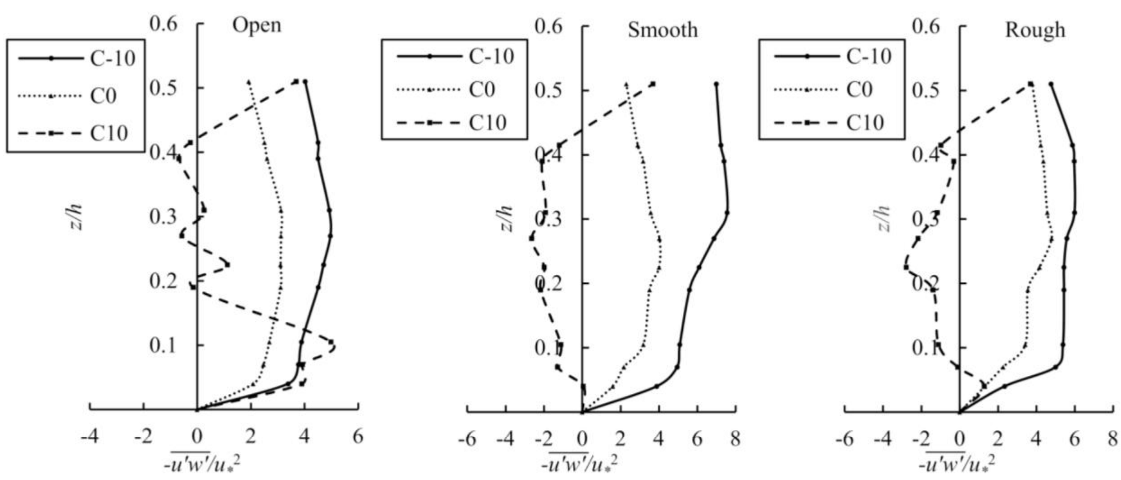

Figure 4.11 Vertical RSS profiles in the *X-Z* plane ($-\overline{u'w'}/u_*^2$) for the minor submergence case of the spur dike.

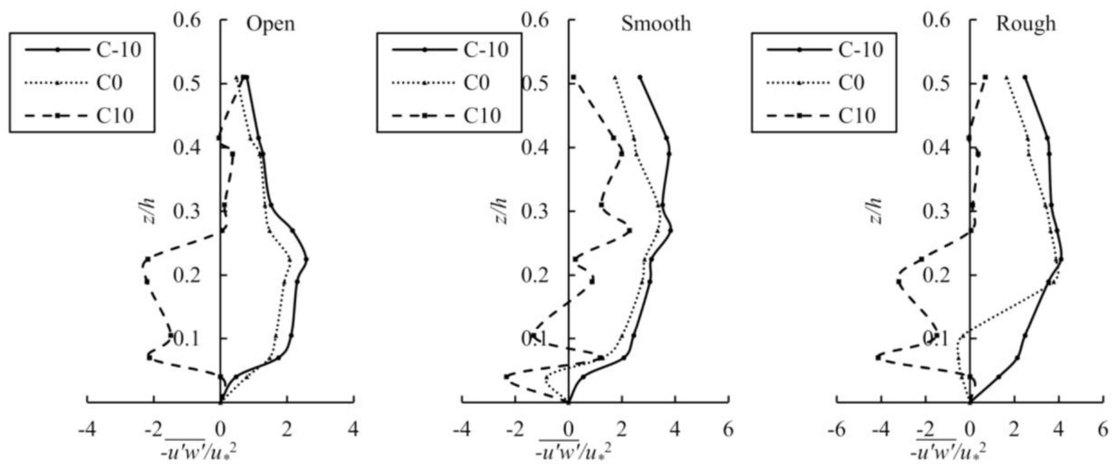

Figure 4.12 Vertical RSS profiles in the *X-Z* plane ($-\overline{u'w'}/u_*^2$) for moderate submergence case of the spur dike.

As observed from Figures 4.11 and 4.12, downstream of the spur dike (C10), the RSS exhibits significant variation compared to those at two other positions due to the recirculation wake zone behind the spur dike, which is generated from flow separation, causing the water to flow in the opposite direction of the main flow in this zone. RSS values decrease steadily in the streamwise flow direction. However, owing to the impacts of a broader separation zone above the dike tip, the monotonic decrease in RSS for moderate submergence spur dikes is more pronounced than for minor submergence cases. A negative RSS value was observed at the dike tip CS (C0), where local scour occurs. These negative RSS values near the channel bed suggest an upward vertical momentum transfer is occurring, attributed to a negative streamwise velocity gradient ($du/dz < 0$) (Jafari & Sui, 2021). RSS is more pronounced under ice-covered flow conditions than in open-channel flows. On average, at the same measuring depth for the minor dike submergence case, the absolute RSS values under smooth and rough ice-covered flow conditions are 5% and 12% higher than in open channel flow conditions. For the moderate dike submergence case, the RSS values under smooth and rough ice cover conditions are 7% and 15% higher than those in open channel conditions.

In both minor and moderate dike submergence cases, RSS increases in the near-bed zone (z/H = 0.2–0.3), followed by an immediate drop. RSS shows a more drastic decrease above the near-bed zone for the moderate submergence case than in the minor submergence scenario. As the submergence ratio increases, more significant variability in RSS values around a moderately submerged dike is directly influenced by the increased breadth of the separation zone above the dike tip. Given the occurrence of local scour around the spur dike tip, the vertical distribution of Reynolds shear stress at C0 has been selected for further analysis.

Shahmohammadi et al. (2022) corroborated findings from reported studies, demonstrating that the vertical distribution of Reynolds stress in shallow transitional flows exhibits three distinct zones: the increasing, damping, and decreasing zones. Figure 4.13 illustrates these three zones by extending the linear regression line in the decreasing zone to a 0 value at the water surface. Upon applying the linear regression extension to the measured data, irregular shapes are revealed for the moderate submergence case of a spur dike. This anomaly is hypothesized to arise from the inadequacy of Acoustic Doppler Velocimetry (ADV) measurements in capturing the separation zone near the spur dike. Consequently, an in-depth RSS analysis is undertaken explicitly for the minor submergence case, wherein the spur dike height closely approaches the flow depth. It is observed that with increasing cover roughness, both the RSS-increasing zone and RSS-decreasing zone expand.

Correspondingly, with increased cover roughness, the RSS-damping zone diminishes by 37.50% and 81.25% for smooth and rough ice-covered flows, respectively, compared to open channel conditions. In the case of the minor dike submergence, the maximum normalized RSS value occurs at depths of z/H = 0.1, 0.2, and 0.2 for the open channel, smooth, and rough ice-covered flow conditions, respectively. Table 4.3 summarizes the normalized depths for three zones—RSS-increasing, RSS-damping, and RSS-decreasing zones—at the dike tip under various water surface cover conditions in the case of minor dike submergence.

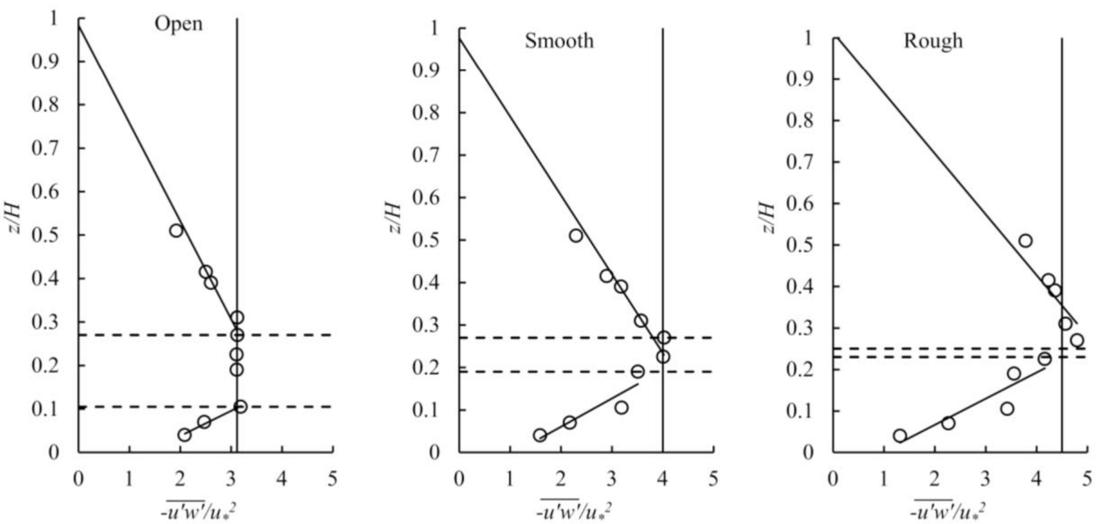

Figure 4.13 Reynolds shear stress distribution in the RSS-increasing, RSS-damping, and RSS-decreasing zones

Table 4.3 Comparison of the RSS-increasing, RSS-damping, and RSS-decreasing zones under open, smooth, and rough ice-covered flow conditions.

Variable	Water surface cover conditions		
	Open	Smooth	Rough
z_1/H	0.11	0.19	0.23
z_2/H	0.27	0.26	0.26
% change of $\lvert z_2/H - z_1/H \rvert$	N/A	-37.50	-81.25

[a] z_1 and z_2 represent the lower and upper boundaries of the damping zone. The percentage change refers to results compared to that under open-channel flow, and negative values indicate decreasing trends. N/A refers to not applicable.

Spatial variations in Reynolds stress components may be influenced by factors beyond mean velocity gradients, including the rotation of the coordinate axes and diffusion. This spatial inhomogeneity in velocity and Reynolds stresses results in wake production, characterized as the excess kinetic energy generated from the work of mean flow against the form drag. Wake phenomena can erode riverbeds and induce local scour, maintaining sediment in suspension and transporting bed materials downstream via eddies protected by the hydraulic structure (Keshavarzi et al., 2018). Analyzing Reynolds shear stress is crucial for comprehending the near-wall region of a boundary layer, where the presence of a solid surface influences fluid dynamics.

4.3.3 Analysis of Dominant Turbulent Events

The spatial variability of flow fields, encompassing both lateral and vertical dimensions, contributes to the turbulent structure in a channel (Yang et al., 2023). Quadrant analysis represents a fundamental yet effective method for processing turbulence data, particularly useful in studying turbulent shear flows to account for the spatial variability of flow fields. The determination of the threshold hole size (H_t) value is somewhat arbitrary, accompanied by significant uncertainties and contradictions regarding the recommendation of an H_t value in the literature (Wan Mohtar et al., 2020).

Analysis of velocity and Reynolds shear stress results indicates that the 90° dike alignment produces the most significant values and variations in the velocity field. At the same time, the ADV sampling volumes are less affected by the dike top flow separation. In this study, different H_t values are investigated, including H_t = 0, 0.1, 0.2, and 0.3, utilizing data from the experimental setup featuring a dike alignment angle (α) of 90°, a dike design length (L_d) of 50 cm, and a dike height approximating flow depth. Figure 4.14 illustrates the percentage of dominant turbulent events at the dike tip across the flow depth, as measured by the ADV under open channel, smooth, and rough ice-covered flow conditions.

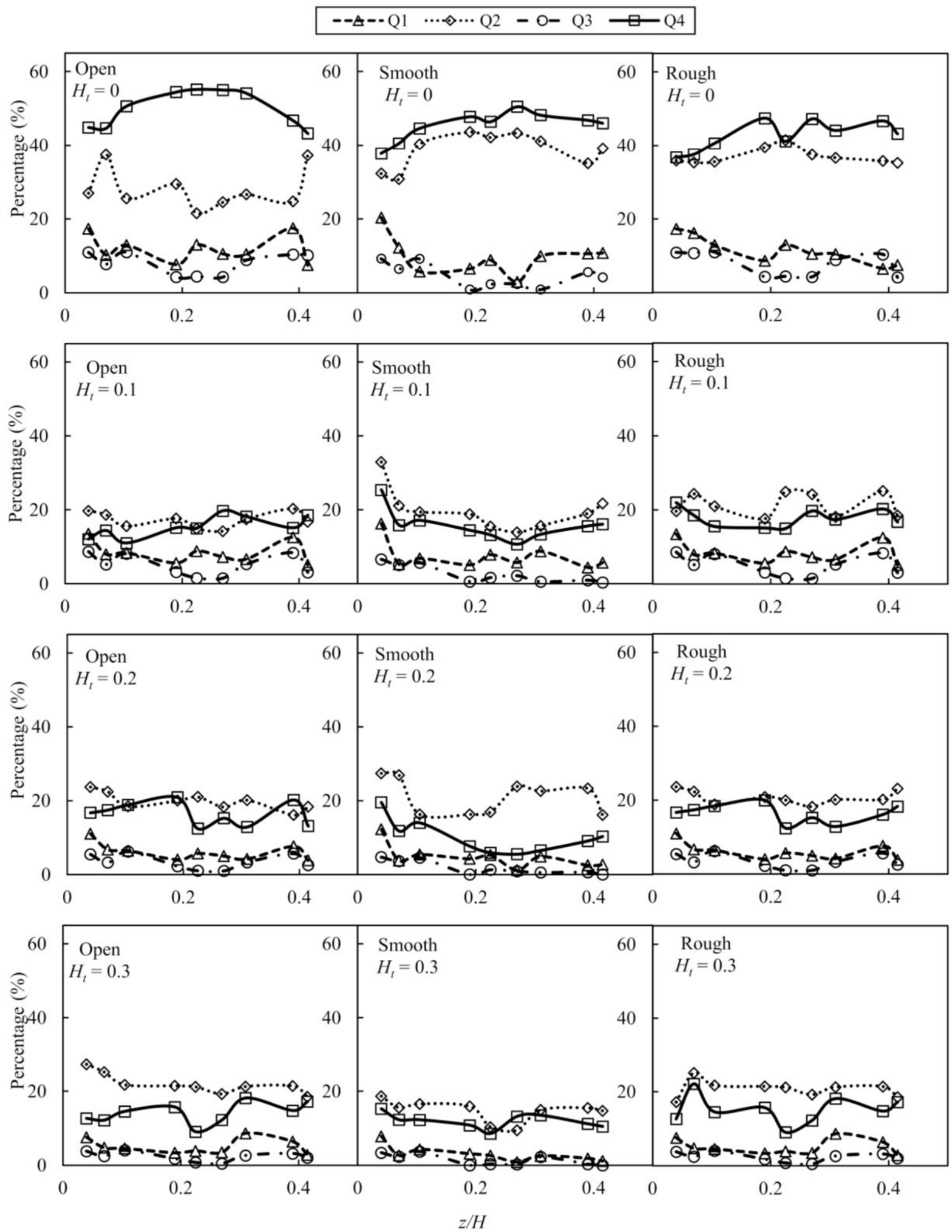

Figure 4.14 Percentage of the dominating turbulent events at the dike tip across the measured flow depth with different hole size values (H_t) (α = 90°, L = 50 cm, T = 25 cm).

The case of H_t = 0 is further examined in this section, as it does not eliminate any Reynolds stress values in the four quadrants. With a hole size of zero (H_t = 0), all recorded events are subject to burst analysis. Results indicate that with H_t = 0, the sweep event (Q4) dominates under all water surface conditions. As the hole size increases, the percentage of ejection events (Q2) grows, becoming the predominant occurrence at H_t = 0.3 for both open channel and covered flows. The predominant sweep and ejection events are vital in facilitating transverse momentum exchange.

Under ice-covered flow conditions, while the sweep event remains dominant, the percentages for ejection events closely follow those of the sweep event. Moreover, the substantial contributions of sweep and ejection events lead to increased momentum flux and more severe shear under ice-covered conditions than open channel flows. As ice cover roughness increases, the distribution percentages of inward (Q1) and outward (Q3) interactions become more similar, and the likelihood of these events disappearing (0%) decreases, indicating increasingly complex turbulence with greater ice cover roughness.

Figure 4.15 illustrates the absolute values of the contributions of each quadrant ($|S_i|$, according to Equation 8) across various dike alignment angles under both open channel and ice-covered flow conditions, specifically for the case where H_t = 0, at multiple distances from the channel bed. Regardless of flow depth, ejection (Q2) and sweep (Q4) events significantly contribute to the Reynolds stress under smooth and rough ice-covered flow conditions alike. In contrast, sweep events (Q4) emerge as the sole dominant contributor under open channel flow conditions. An increase in dike alignment angle beyond 90° leads to a decrease in the dike blockage ratio (the ratio of the dike's frontal area to the flow cross-sectional area), diminishing the absolute contributions values ($|S_i|$) from both ejection and sweep events. Furthermore, as the dike alignment angle increases, the disparity between dominant ($|S_2|$ and $|S_4|$) and marginal contributions ($|S_1|$ and $|S_3|$) gradually narrows.

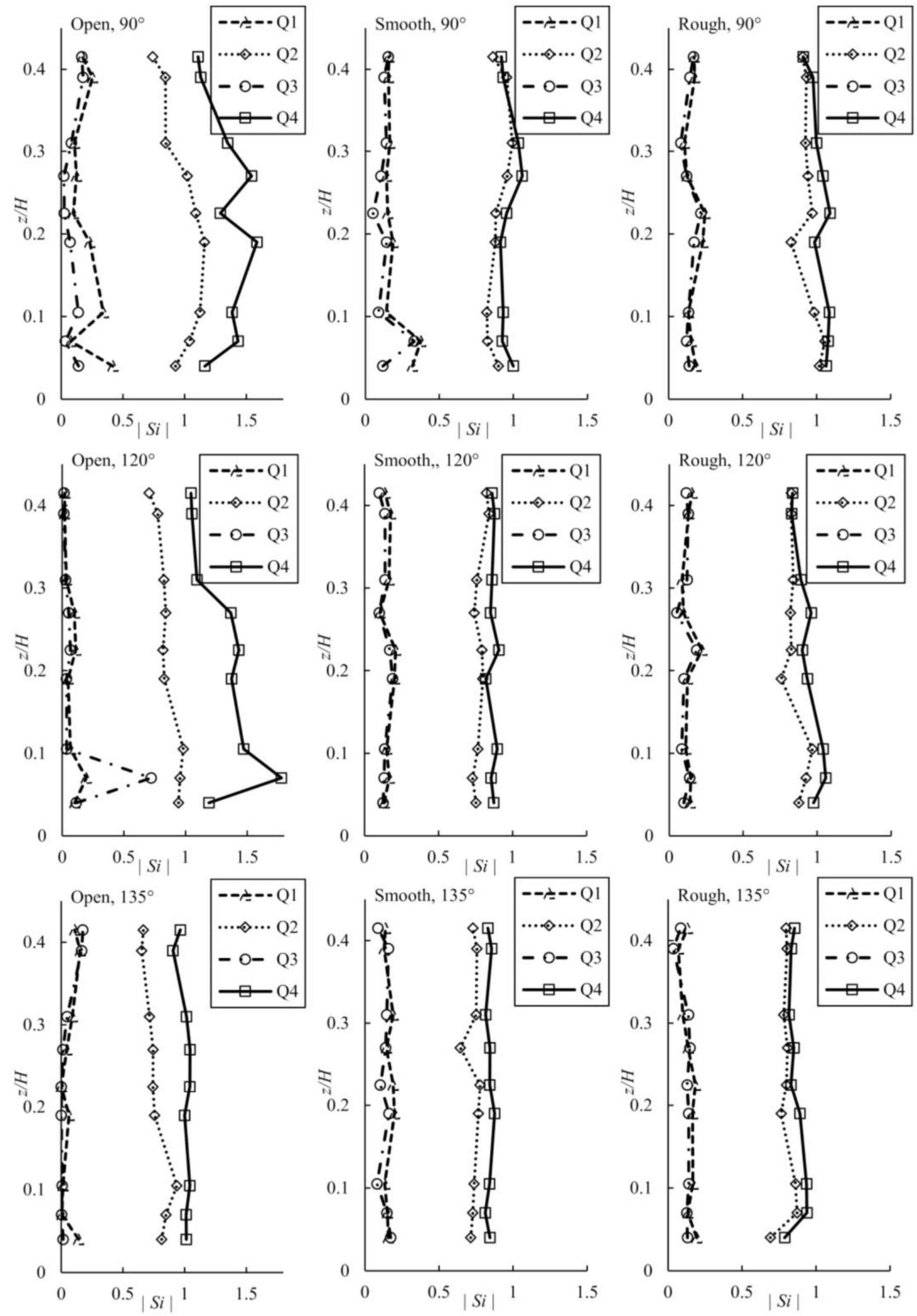

Figure 4.15 Variation of the absolute contributions values $|S_i|$ along the measured results around spur dikes for the case of $H_t = 0$.

Spur dikes with an alignment angle of 90° (deflecting dike) have been widely adopted in both submerged and non-submerged configurations (Zhang et al., 2018). Therefore, burst events around the 90° alignment dike are further analyzed. Drawing on laboratory experiments, the results of burst events at three cross-sectional positions at the lowest measuring depth ($z/H = 0.04$) are depicted in Figure 4.16, illustrating scoured bed turbulence. Irrespective of water surface conditions, burst events concentrate in the second and fourth quadrants upstream of the dike, dispersing evenly across all four downstream quadrants. The predominance of the second and fourth quadrants indicates that sweep and ejection events play a pivotal role in mobilizing sediment particles within the scour hole. In the presence of ice cover, the disparity in contribution percentages between sweep and ejection events diminishes. Furthermore, it is observed that an increase in ice cover roughness correlates with higher contribution percentages for inward and outward interactions, suggesting a decrease in the significance of ejection and sweep events as roughness increases. It is important to note that near the dike tip, noise becomes more pronounced, leading to reduced data that is considered valid by the WinADV software.

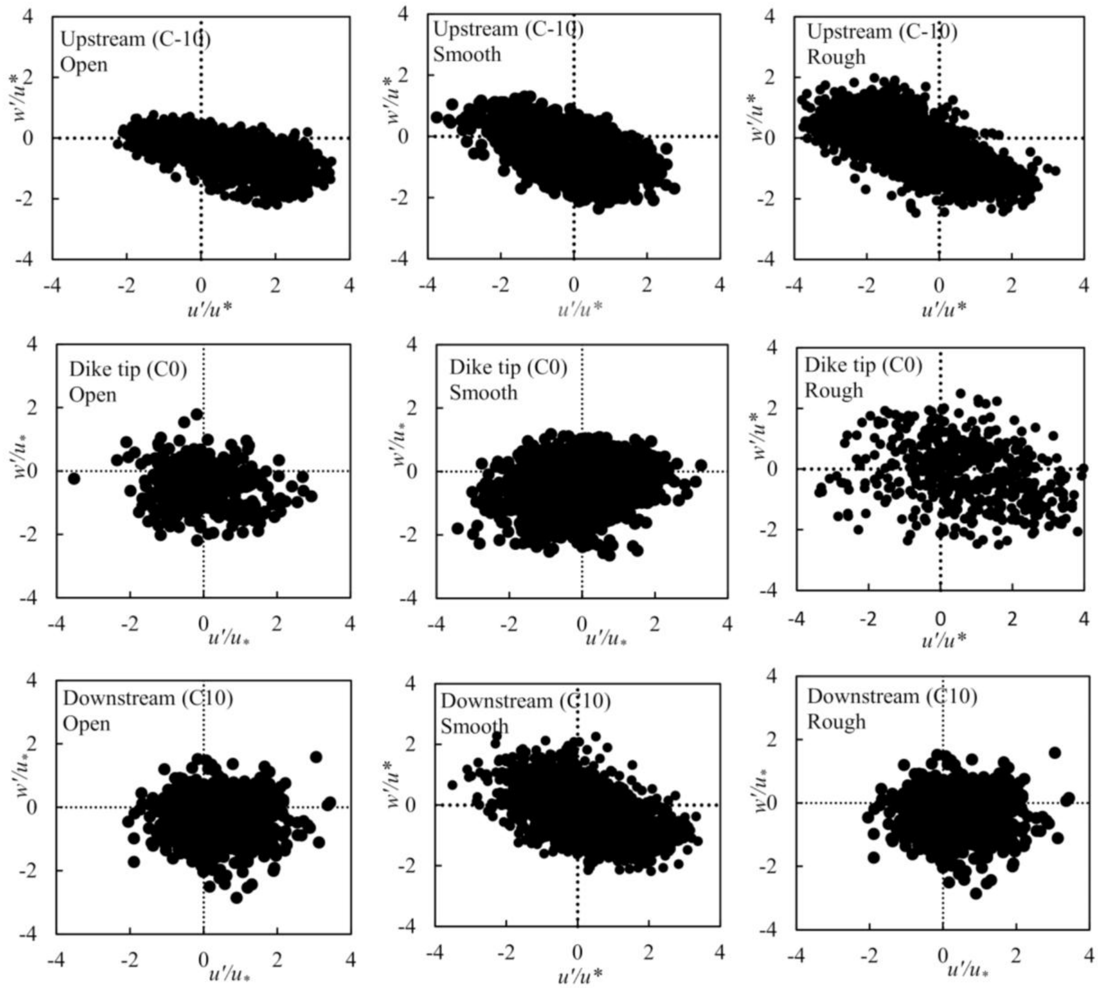

Figure 4.16 Probability distributions of u'/u_* and w'/u_* at z/H = 0.04 when $H_t = 0$ ($\alpha = 90°$, $L = 50$cm, $T = H$).

4.4 Limitations and Recommendations

The constrained spatial coverage beyond designated measuring points around the spur dike limits this study. Data collection, confined to specific locations, may overlook the broader dynamics of flow influenced by the spur dike's alignment angle and submergence. Furthermore, the study relies solely on an Acoustic Doppler Velocimeter (ADV) for point velocity measurements. Although an ADV yields valuable velocity data, its application at discrete points may not capture the full complexity and variability of turbulent flow structures across a wider area. Thus, the measurement technique used in this study may overlook subtle variations and intricacies in flow patterns. Due to logistical constraints, using a single ADV for velocity assessments introduces significant limitations in capturing the temporal and spatial characteristics of recirculation zones and vortices within a fluid system. The inherent complexity of fluid dynamics necessitates a comprehensive assessment that accounts for the dynamic nature of flow phenomena. Reliance on a single ADV device overlooks nuanced variations from the spur dike's obstruction. Consequently, using only one ADV device led to an incomplete flow field characterization, limiting the precision and comprehensiveness of the obtained velocity measurements.

Future research should prioritize expanding spatial coverage of data collection beyond the existing measuring points. Employing a broader array of measurement devices or deploying multiple ADVs simultaneously could contribute to a more comprehensive understanding of the turbulent flow structures around spur dikes of varying alignment angles. Combining data measured by ADV devices with other techniques, such as imaging technologies or numerical simulations, is recommended to provide a more holistic view of flow dynamics. Integrating multiple approaches would enhance the findings' accuracy and reliability, facilitating a more detailed analysis of turbulent flow structures in the presence of submerged spur dikes and ice cover on the water surface.

4.5 Chapter Summary

Chapter four describes the study conducted within a large-scale flume environment, investigates the turbulence dynamics surrounding submerged spur dikes under various ice-cover conditions, and analyzes three-dimensional velocity components, Reynolds shear stress, and turbulent burst events. It delineates the intricate interactions between dike geometry, flow conditions, and ice cover, offering insights into hydrodynamic behavior influenced by submerged spur dikes. Key findings include:

1) Despite the experimental flume used in this study having an aspect ratio greater than 5.0, hydrodynamic instabilities in the flow fields, attributed to the additional boundary layer from the spur dike, have been observed through the examination of the three time-averaged velocity components (u/U, v/U, w/U) at the dike-tip cross-section (CS) in the Y-Z plane. Velocity contours derived from the measured data suggest that as the submergence level of a spur dike increases, the water flow over the dike mitigates the impact of the recirculation region by diminishing the amplitude of reverse flow. Measured data reveal that near the dike front, the distributions of streamwise (u/U) and lateral (v/U) velocities indicate transverse flow regions (negative values) near the channel bed. In contrast, the negative vertical (w/U) flow region is not discernible at the channel bed but is higher in the flow region.

2) Irrespective of dike alignment angles in minor submergence cases and with consistent approaching flow depth, ice cover on the water surface leads to an average increase in maximum streamwise velocity by 12% for smooth and 20% for rough ice-covered conditions. Increasing the dike alignment angle from 90° to 135°, thereby reducing the blockage ratio of the cross-sectional area, decreases flow velocity (u/u_{avg}) irrespective of water surface cover conditions. With the increase in the spur dike alignment angle, the amplitudes of measured velocities (in the X-Y plane) at the front surface of the spur dike

also increase. The measured streamwise velocity profile trends align with the original and adjusted logarithmic laws for flows, applicable under open channel and ice-covered conditions.

3) Downstream of submerged spur dikes, the Reynolds Shear Stress (RSS) varies significantly due to the recirculation wake zone formed by flow separation behind the dike, causing water to flow opposite to the main flow in this zone. Along the streamwise direction, RSS values steadily decrease. However, with a moderately submerged dike, the monotonic decreases in RSS values are more pronounced than in cases of minor submergence due to a more extensive separation zone above the dike tip. RSS distribution across flow depth is categorized into increasing, damping, and decreasing zones. A linear regression line extends to a zero value at the water surface within the RSS-decreasing zone. As ice cover roughness increases, both the RSS-increasing and RSS-decreasing zones expand while the RSS-damping zone contracts.

4) Quadrant analysis results show that irrespective of flow depth, ejection and sweep events significantly contribute to Reynolds shear stress in both smooth and rough ice-covered conditions. In contrast, sweep events alone contribute to open channel flow. With an increase in the dike alignment angle from 90° to 135°, a reduced contribution from ejection and sweep events results from a decreased blockage ratio of the flow cross-section. Furthermore, as the alignment angle exceeds 90°, the disparity between dominant contributors (sweep and ejection events) and marginal contributors (inward and outward interactions) gradually diminishes.

This study advances knowledge of turbulent flow characteristics around submerged spur dikes under ice-covered conditions. It elucidates the nuanced effects of dike geometry and ice cover on flow dynamics, providing valuable insights for river engineering and management. Further investigations should expand the spatial and methodological scope to encompass the complex interrelations between environmental factors and hydraulic structures. Integrating advanced measurement techniques and numerical simulations is recommended for a more holistic understanding of flow dynamics in natural river systems.

5. CHAPTER FIVE: HYDRODYNAMIC CHARACTERISTICS IN POOLS WITH LEAFLESS VEGETATION UNDER ICE COVER

5.1 Introduction

Natural riverbeds often feature uneven structures, forming pools and riffles. During low-flow periods, pools serve as reservoirs, sustaining baseflow in streams, while during floods, they decelerate flow velocity and facilitate the sedimentation of debris transported by the water. Recent research on pool structures in channel environments has significantly enhanced our understanding of their formation, dynamics, and ecological significance. Pools, characterized by deeper water zones within a channel, are critical for sediment transport, energy dissipation, and providing habitat for aquatic organisms (Nosrati et al., 2024). Pools often contain diverse living and dead vegetation, such as underwater grasses, shrubs, and tree trunks. Pools in a pool-riffle sequence are known to have calmer waters compared to other sections, such as riffles or slopes, making them more conducive to nutrient enrichment and the growth of aquatic vegetation (Calderon & An, 2016; Rodríguez et al., 2013). The interaction between flow dynamics and pool morphology has been thoroughly studied, with particular attention to the effects of discharge, channel slope, and sediment size on pool stability and development (Mofrad et al., 2023). Results of experimental and field studies have shown that pools are shaped and sustained by complex hydraulic processes, including turbulence and secondary currents, which contribute to their persistent yet dynamic nature (Shumilova & Sukhodolov, 2023). However, to the authors' knowledge, no research has been conducted on the impact of vegetation on the flow field within pools under ice-covered flow conditions. Understanding these interactions is crucial for effective river management and restoration, especially given the increasing anthropogenic pressures and climate change impacts on fluvial systems.

Traditionally, underwater vegetation is recognized for its ability to slow water flow, reduce soil erosion, stabilize riverbanks, and enhance water quality and aesthetics, making it a cost-effective and efficient measure of ecological river management (Cui et al., 2023). However, during flood events, the presence of vegetation in channels can significantly alter the original flow structure. The interaction between vegetation and water can convert part of the flow's energy into turbulent kinetic energy near the vegetation, reducing the river's flood-carrying capacity (Rahimi et al., 2023). Understanding the disturbance characteristics of submerged vegetation on flow dynamics and evaluating its advantages and challenges is crucial for effective flood control, embankment engineering, and river ecological protection and restoration. The impact of submerged vegetation on embankment stabilization, bank protection, and flood control has increasingly become a focal point of research. Numerous researchers have conducted experiments in vegetated channels to investigate flow parameters, including turbulent kinetic energy (TKE) and shear stress under open channel flow conditions. For instance, Barahimi and Sui (2023) found that a staggered arrangement of deflected and non-bending vegetation on the channel bed resulted in higher streamwise velocity, TKE, and Reynolds shear stress (RSS) than a square configuration. To date, only limited research has been conducted to investigate the flow characteristics in the presence of vegetation in channel beds and ice cover on water surfaces. Based on extensive laboratory experiments conducted in a large-scale flume, Sediqi et al. (2024) and Barahimi & Sui (2024a, 2024b) assessed the effects of varying vegetation densities arranged in square and staggered patterns, incorporating the influence of ice covers with differing roughness (smooth and rough). Key turbulence parameters, such as turbulence intensity, RSS, and TKE, were analyzed. The findings indicate that flow velocity profiles over a vegetated channel bed transition from an S-shaped curve under open flow conditions to a convex shape under ice-covered flow conditions. Their experiments, conducted under open channel and ice-covered flow conditions using three types of non-uniform sands as bed material, revealed that vegetation patches, combined with ice cover, produced distinctive velocity profiles with two peak values.

With advancements in computing power and numerical algorithms, numerical simulation techniques have been successfully applied to experimental flumes, lakes, rivers, bays, and coastal environments. Numerous studies have utilized two-dimensional (2D) and three-dimensional (3D) mathematical models to simulate flows in open channels with submerged vegetation. For example, Zeng et al. (2022) employed a large eddy model to simulate 3D flow characteristics in open channels influenced by vegetation, elucidating the interaction patterns between rigid plants and water flow. Rahim et al. (2020) investigated the effects of a two-layered cylindrical vegetation system on water flow and proposed an analytical model that aligns with field-measured data. Koken and Constantinescu (2021) utilized 3D eddy-resolving numerical simulations to examine the interactions between emerged cylinders and water flow in open channels, revealing significant upwelling and downwelling near the leading and side edges of vegetation patches and within the shear layer. Toda et al. (2020) combined four sub-models to study the dynamics of riparian vegetation and the interactions between river flow and sediment transport, concluding that riparian vegetation plays a crucial role in enhancing the stability and relative elevation of fluvial bars. Zhang et al. (2021) solved the width-averaged Navier-Stokes equations with a first-order closure scheme for the Reynolds stress, successfully obtaining vertical velocity profiles in open-channel flows with submerged flexible canopies. Rahim et al. (2023) applied ANSYS Fluent and the k–ϵ turbulence model to simulate and analyze complex flow dynamics in considering different vegetation arrangements in channel beds. The results of simulations indicated a reduction in turbulent kinetic energy in the gaps between vegetation patches, which was attributed to the drag force exerted by vegetation. Aydogdu (2023) examined the behavior of rigid vegetation using two distinct turbulence models (Realizable k-ε and Reynolds Stress) within the CFD software ANSYS Fluent, exploring the formation of vortices and complex turbulent flows from the channel bottom to the water surface, influenced by the diameter and arrangement of rigid vegetation rods. Lama et al. (2020) evaluated two resistance models, the Baptist and Stone & Shen (S&S) models, in a reclamation channel with common reeds. Their study found that combining the S&S resistance predictor model and the Horton composite cross-section method yielded the lowest relative prediction error. Qiu et al. (2024) used large eddy simulation to investigate the impact of emergent vegetation on flow dynamics in natural rivers, identifying two distinct stages of flow alteration: the development of a stable wake region behind densely vegetated areas and a more gradual velocity recovery in regions with sparse vegetation.

Recent research has further explored the complex hydrodynamics of compound channels influenced by submerged vegetation on channel beds, emphasizing that vegetation density, arrangement, and height significantly affect flow dynamics. However, the specific effects of rigid, leafless submerged vegetation on flow conveyance in pools and how varying vegetation heights influence hydrodynamics still need to be more adequately understood. Most existing studies utilize simple drag force models to quantify vegetation resistance, with detailed simulations of hydrodynamic-vegetation interactions still limited. Therefore, further investigation in this area is crucial.

Submerged vegetation helps maintain suitable temperatures for aquatic organisms, even during winter when ice cover forms (Sebilian Wittyngham et al., 2019). However, studies on the impact of ice cover on flow fields in vegetated channels have revealed significant changes in flow dynamics and turbulence. Vegetation in channels, particularly under ice-covered flow conditions, introduces complex interactions that alter velocity distribution and turbulence characteristics. Research indicates that ice cover shifts the maximum flow velocity closer to the riverbed, increasing turbulence and bed shear stress (Sui et al., 2010), especially around vegetative patches and in-stream structures (Sui, 2023). Additionally, laboratory experiments have demonstrated that the combination of ice cover and vegetation significantly influences hydrodynamic behavior, leading to distinct velocity profiles and elevated turbulent kinetic energy near the vegetation (Barahimi & Sui, 2024b). These results highlight the need for detailed modeling - encompassing analytical, computational, and experimental approaches - of vegetated channels under ice-covered conditions to enhance our understanding of their hydraulic and ecological functions.

In this study, laboratory experiments have been conducted in a large-scale outdoor flume considering different water surface cover conditions, submergence heights of vegetation, pool features, and hydraulic conditions to investigate the effects of leafless vegetation on flow velocity, TKE, and secondary flow variations. Then, the computational fluid dynamics software Flow3D was utilized to perform numerical simulations of flow in channels with rigid submerged vegetation in pools under various cover conditions. The model's accuracy was validated against flume experiment data. Flow field distribution patterns were analyzed for different vegetation submergence heights, focusing on the distribution of side and bottom flow velocities and turbulence kinetic energy along the vertical profile under varying inflow conditions. An analytical model for the streamwise velocity vector has also been developed based on experimental results. The objective is to simulate the turbulent behaviors of flow passing through rigid, leafless vegetation in channels with pool - scenarios that are difficult to capture through experimental flumes - thereby providing scientific support for flood control, riverbank restoration, and ecological protection efforts.

5.2 Laboratory Experiments

A series of experiments were conducted in a large-scale outdoor flume measuring 38 meters in length, 2 meters in width, and 1.3 meters in depth, as shown in Figure 5.1. The flume bed was designed with a gentle longitudinal slope of 0.2%. Within this setup, two sandboxes were positioned 10.2 meters apart. The upstream sandbox measures 5.6 meters in length, 2 meters in width, and 0.3 meters in depth, while the downstream sandbox is slightly longer at 5.8 meters, maintaining the same width and depth. To ensure consistency in experimental conditions, the water level in the upstream holding tank was kept constant, supporting a steady flow rate of up to 120 L/s, controlled via a pump and two valves. The study examined a flow depth of 20 cm from the flume's false floor (30 cm in the pool zone) to simulate shallow river environments. In each sandbox, a pool is constructed. Each pool consists of three sections: entrance, pool center (or deep pool), and exit section, as shown in Figures 5.1 and 5.2. In this study, the pools were built with three different slopes for the pool’s entrance and exit sections.

Three different slopes for entrance and exit sections of the pools were first trialed in non-vegetated channels under open channel conditions, namely, 5°, 7°, and 10°. The 5° and 7° slopes for the entrance and exit sections revealed significant velocity variations in the transition between the deep pool and slopes of the pools, as indicated by ADV measurements in the unvegetated open channel. The limited pool area at these 5° and 7° slopes prevented fully developed flow and constrained the planting of additional vegetation arrays. Consequently, a 10° slope for both entrance and exit sections was chosen for the flume experiments and numerical model to address these limitations. The non-uniform gravel was used as the bed material of both pool entrance and exit sections, with a median particle size of 10 cm. The gravels used in this study are sourced from the Quesnel River. Non-uniform sand with a median particle size (d_{50}) of 0.90 mm was used along the deep pool section. Figure 5.2b shows the Cartesian coordinate system with the origin (0, 0, 0) located at the center of the pool edge. The pool entrance section features an increase in flow depth, forming a decelerating zone; the deep pool, characterized by a flat channel bed, served as a transition zone; and the pool exit section, with a decreasing flow depth, generated accelerating flow. One case study demonstrates that the slopes of the pool entrance and exit sections for natural pools range from 4° to 7.80° (Nosrati et al., 2022), suggesting that the slopes of entrance and exit sections used in this study reasonably approximate actual conditions found in natural rivers. The relationship between the channel width (W) and flow depth (H) is referred to as the aspect ratio (W/H). In this study, with flow depths of 30 cm in the deep pool section and 20 cm in the false bed zones, this channel, including the entire pool section, is considered a wide channel since the aspect ratios in this study significantly exceed the typical range of 5 to 10. As a result, the influence of the channel's sidewalls and secondary currents on flow dynamics in the central zone of the channel can be negligible. This assumption simplifies the analysis by allowing the focus to remain on primary flow characteristics without interference from side effects (Jing et al., 2019).

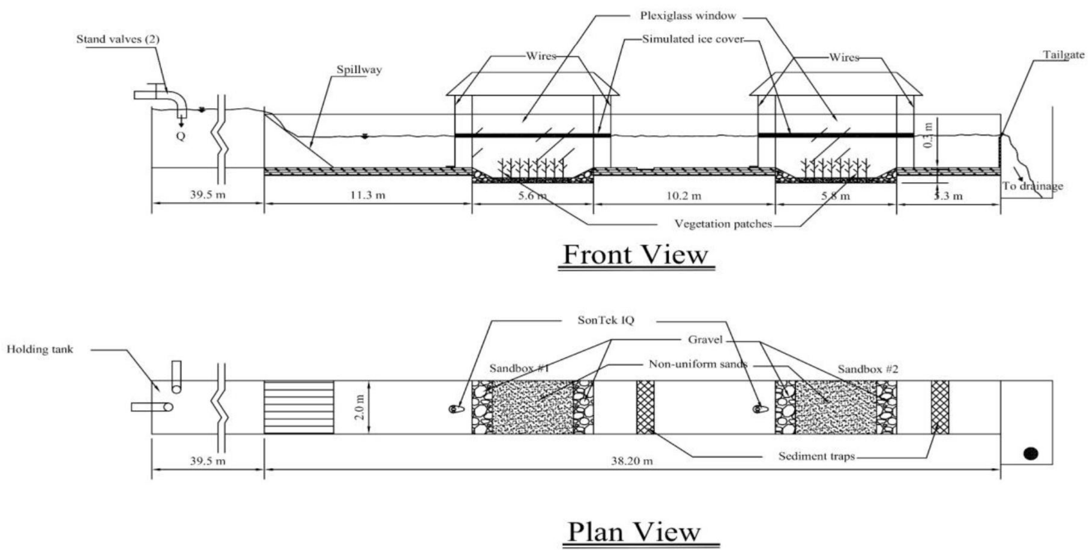

Figure 5.1 (a) Front view and (b) plan view of the experimental flume.

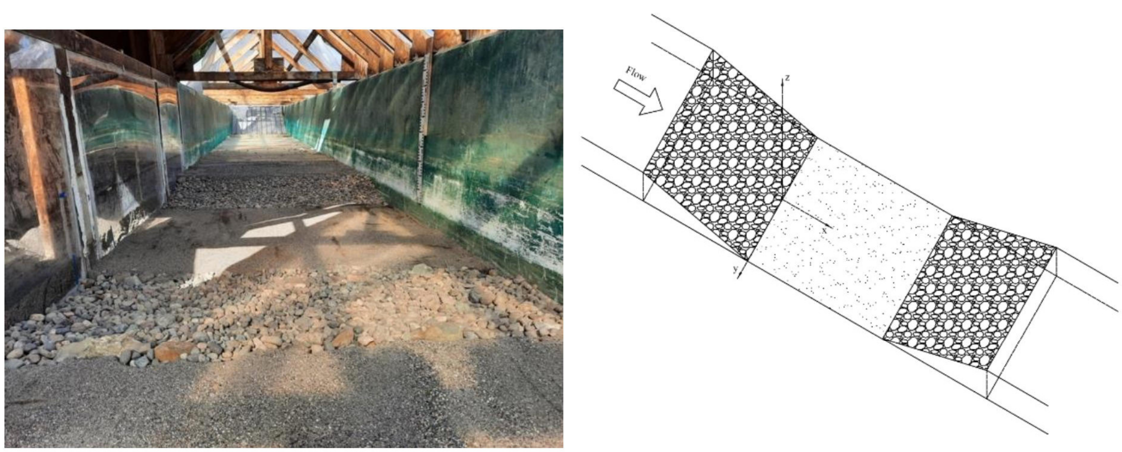

(a) (b)

Figure 5.2 (a). Picture of the non-vegetated pool; **(b**) Pool section and the cartesian coordinate system for the experimental setup.

In natural environments, the distribution of aquatic plants is typically random, with vegetation forming communities that are neither symmetrical nor uniformly distributed. Engineered stream restoration projects, however, could benefit from adopting standard practices that mimic these natural patterns. Implementing a staggered arrangement of vegetation in such projects can simplify numerical simulations while enhancing biodiversity, improving habitat complexity, and providing better erosion control. Therefore, in addition to single circular vegetation setups, paired or staggered vegetation groups should be considered to achieve these benefits (Fu et al., 2021; Tinoco et al., 2020). In this study, plastic artificial flower stems with diameters of 0.5 cm were used to simulate rigid vegetation, such as common reeds (Phragmites australis). These synthetic vegetation stems were anchored to the sand bed of the deep pool section and arranged in staggered configurations with a spacing distance of 20 cm between adjacent stems in the same row to cover the sand bed of the entire deep pool section.

This study measured the 3D velocity components using an Acoustic Doppler Velocimeter (ADV). The ADV had a sampling volume of 0.25 mL and operated at a sampling rate of 25 Hz, with each measurement at a specific point lasting two minutes, capturing 3,000 instantaneous velocity data points. Measurements were taken at vertical intervals of 10 mm. The strength of the received acoustic signal relative to the ambient electronic noise was assessed using the signal-to-noise ratio (SNR) recorded in the ADV's data log. Adequate SNR values - exceeding 5 dB for mean flow velocity and over 15 dB for turbulence measurements - were essential for reliable data (Namaee & Sui, 2019a, 2019b). The data filtering approach that Goring and Nikora (2002) recommended was employed, and WinADV software was used to process the data. This setup included generating a statistical correlation as a real-time output to verify the accuracy of the velocity measurements and discarding any data where the average correlation fell below 70%. After removing spikes using WinADV software, the velocity fluctuations in the x, y, and z directions were calculated and are represented as u', v', and w', respectively

(Namaee & Sui, 2019a, 2019b).

$$u' = u_i - \bar{u}, \qquad v' = v_i - \bar{v}, \qquad w' = w_i - \bar{w} \tag{5.1}$$

in which, $\bar{u}$, $\bar{v}$, and $\bar{w}$ are the mean velocities in the x, y, and z directions. Instantaneous velocities corresponding to these directions are denoted as u_i, v_i, and w_i. To achieve precise data collection of flow characteristics, this study also employed a SonTek-IQ Plus, which measures mean velocity and water depth, leveraging its advanced post-processing capabilities.

Figure 5.3 shows the details of the placement of vegetation and measurement positions. The location of the ADV, positioned between adjacent vegetation stems, was carefully selected to avoid noise interference from the stems and adequately represent the entire wake zone. Circles indicate the locations of individual vegetation elements, while squares represent the points where ADV measurements were taken. Measurements were conducted at various cross-sections along the entire pool, including entrance and exit sections. The flow becomes fully developed as the velocity profiles remain consistent after traveling a certain distance from the upstream edge of each sandbox. Upon reaching the vegetation patch in the deep pool section, the flow transitions to a mixing layer condition, leading to the formation of a shear layer and the development of Kelvin-Helmholtz (KH) vortices (Wang et al., 2023). When equilibrium is achieved, characterized by the stabilization of streamwise velocity within the vegetation zone, the flow inside the submerged vegetation patch becomes fully developed again (Barahimi & Sui, 2024a).

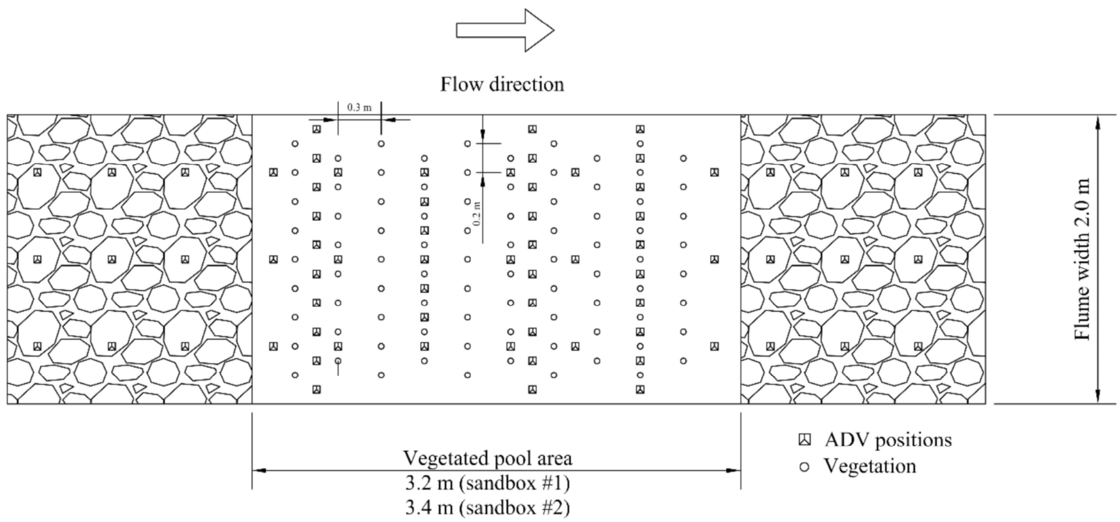

Figure 5.3 Top view of a vegetation zone and ADV measurement positions within the pool area.

Styrofoam panels were used to simulate ice cover on the water surface. These panels floated on the water surface, with two types of model ice covers employed: smooth and rough ice cover. The model smooth ice cover was created using untreated Styrofoam panels, while the model rough cover was formed by attaching small Styrofoam cubes to the underside of the smooth panels. Each Styrofoam cube measured 25 mm on each side, with a spacing distance of 35 mm between adjacent cubes (Figure 5.4). The roughness of the channel bed and ice covers significantly influences the flow structure (Beltaos, 2008; Li et al., 2023; Sui et al., 2010). The Manning roughness coefficient for the channel bed (n_b) was calculated using Equation (5.2) (Julien, 2018) and determined as 0.020 for the sand bed of d_{50} = 0.90 mm in the deep pool section.

$$n_b = 0.064 d_{50}^{1/6} \tag{5.2}$$

Manning's coefficient for the model smooth ice cover (n_i) is estimated to be 0.010, as reported by Hains and Zabilansky (2005). For the model rough ice cover, Manning's roughness coefficient is determined to be 0.021 using Equation (5.3), as proposed by Li (2012).

$$n_i = 0.039 k_s^{1/6} \tag{5.3}$$

where k_s is the average roughness height (m) and is calculated from

$$k_s = 30 y_i \exp[-(1 - v_i/v_m)] \tag{5.4}$$

in which y_i is the ice-affected thickness irregular layer, taken as the Styrofoam cube edge length (0.025 m), v_i is the depth-averaged velocity of the ice-affected layer, and v_m is the maximum velocity.

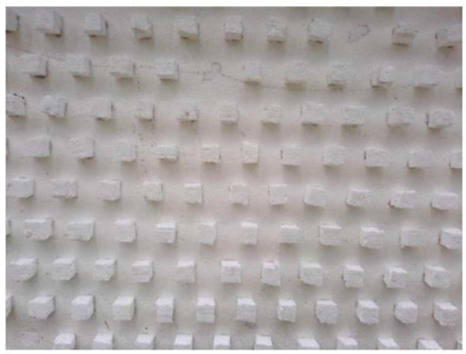

Figure 5.4 Styrofoam cubes are attached to the Styrofoam panel to simulate the rough ice cover.

5.3 Numerical Model

FLOW-3D® HYDRO, a widely used computational fluid dynamics (CFD) model, was employed to simulate the velocity profiles. This model utilizes the volume of fluid (VOF) method to track the water's free surface accurately and employs the Fractional Area/Volume Obstacle Representation (FAVOR) method, developed by Hirt and Nichols (1981), to effectively manage complex geometries (Flow Science Inc., 2023). Recent studies have demonstrated the robustness of FLOW-3D in modeling hydrodynamic behaviors across various engineering applications, confirming its reliability in simulating intricate flow patterns around structural obstacles (e.g., Namaee et al., 2021, 2023).

5.3.1 Governing Equations

The governing equations for an incompressible Newtonian fluid, incorporating the Reynolds-averaged Navier-Stokes (RANS) equations and continuity equation, are presented in Equations 5.5 to 5.8, including the Fractional Area/Volume Obstacle Representation (FAVOR) variables (Hirt & Nichols, 1981).

$$\frac{\partial}{\partial x_i}(u_i A_i) = 0 \tag{5.5}$$

$$\frac{\partial u}{\partial t} + \frac{1}{V_F}\left(u_j A_j \frac{\partial u_i}{\partial x_j}\right) = -\frac{1}{\rho}\frac{\partial P}{\partial x_i} + g_i + f_i \tag{5.6}$$

and

$$\rho V_F f_i = \tau_{b,i} - \left[\frac{\partial}{\partial x_j}\left(A_j S_{ij}\right)\right] \tag{5.7}$$

where

$$S_{ij} = -(\mu + \mu_T)\left(\frac{\partial u_i}{\partial x_j} + \frac{\partial u_j}{\partial x_i}\right) \tag{5.8}$$

Here, u_i represents the velocity component in the i-th direction, V_F is the volume fraction of fluid in each grid cell, and A_i denotes the fractional area open to flow in the i-th direction. P is the pressure, ρ is the fluid's mass density, and t is time. The term g_i corresponds to the gravitational force in the i-th direction, f_i is the diffusion transport term, and S_{ij} is the strain rate tensor. The wall shear stress is indicated by $\tau_{b,i}$, and the total dynamic viscosity accounts for both molecular viscosity (μ) and eddy viscosity (μ_T).

FLOW-3D offers several turbulence models, including the standard k-ε, RNG k-ε, k-ω models, and large eddy simulation (LES). When turbulent flow encounters obstacles like vegetation stems, it generates a complex system known as the turbulent horseshoe vortex (THV) due to the adverse pressure gradient. Large-eddy simulation models, particularly the detached-eddy simulation (DES) approach, effectively resolve most turbulence scales generated by obstacles while maintaining relatively low computational demands (Kang et al., 2019). Gazi and Afzal (2020) reviewed the formation mechanisms of vortices, highlighting the separation of both laminar and turbulent boundary layers, and noted the successful application of DES in simulating the intricate dynamics of THV. The Re-Normalization Group (RNG) *k-ε* turbulence model, which modifies the Navier-Stokes equations to account for smaller-scale motions, is favored for vegetated channels due to its cost-effectiveness, accuracy, and efficiency in capturing turbulence structures (Dehrashid et al., 2023). The RNG *k-ε* model includes enhancements over the standard *k-ε* model, improving its efficiency. Therefore, in this study, the RNG *k-ε* turbulence model is employed to simulate the flow field in the pool zone with vegetation under ice-covered flow conditions, using this model to close the equations of motion.

The transport equations for *k* and *ε* can be expressed in various forms. One straightforward interpretation, which neglects the buoyancy effects, is as follows (Yakhot et al., 1992):

$$\frac{\partial}{\partial t}(\rho k) + \frac{\partial}{\partial x_i}(\rho k u_i) = \frac{\partial}{\partial x_j}\left[\left(\mu + \frac{\mu_t}{\sigma_k}\right)\frac{\partial k}{\partial x_j}\right] + P_k - \rho\varepsilon \tag{5.9}$$

$$\frac{\partial}{\partial t}(\rho \varepsilon) + \frac{\partial}{\partial x_i}(\rho \varepsilon u_i) = \frac{\partial}{\partial x_j}\left[\left(\mu + \frac{\mu_t}{\sigma_\varepsilon}\right)\frac{\partial k}{\partial x_j}\right] + C_{1\varepsilon}\frac{\varepsilon}{k}P_k - C_{2\varepsilon}^{*}\rho\frac{\varepsilon^2}{k} \tag{5.10}$$

where

$$C_{2\varepsilon}^{*} = C_{2\varepsilon} + \frac{C_\mu \eta^3(1-\eta/\eta_0)}{1+\beta\eta^3} \tag{5.11}$$

$$\eta = Sk/\varepsilon \tag{5.12}$$

$$S = \left(2S_{ij}S_{ij}\right)^{1/2} \tag{5.13}$$

The turbulent viscosity is calculated using the same method as the standard *k-ε* model.

Notably, the RNG procedure explicitly derives the values of all constants except for β. The commonly used values are $C_\mu = 0.0845$, $C_{\varepsilon 1} = 1.42$, $C_{\varepsilon 2} = 1.68$, $\sigma_k = \sigma_\varepsilon = 0.7194$, $\eta_0 = 4.38$, and $\beta = 0.012$ (Yakhot et al., 1992).

FLOW-3D utilizes the VOF method to solve the governing equations on an orthogonal mesh grid, which allows for accurate capture of the interface between different fluid phases. The solver iteratively computes the flow field by updating the velocity and pressure fields until convergence is achieved, involving the solution of continuity, momentum, and turbulence transport equations (Lee & Wahab, 2019). The simulation results are validated against experimental data to ensure accuracy, with model parameters adjusted as necessary to achieve better alignment with observed data.

5.3.2 Model Setup in Flow 3D

Twenty-seven numerical models with and without the presence of vegetation in the section of pool bed with non-uniform bed material of $d_{50} = 0.90$ mm have been developed to generate distinct datasets and compare them to the results of flume experiments. In the computational domain, no-slip wall conditions were applied to the sidewalls, rigid vegetation (represented by cylinders with diameters of 0.5 cm), ice cover bottom surfaces, and mesh boundaries. The cylinders simulate rigid vegetation such as common reed (Phragmites australis) found in natural rivers (Nosrati et al., 2024). The top boundary was modeled using a "symmetry" condition, while a "no-slip wall" condition was applied to the bottom boundary. The upstream inlet of the pool was set with a "specified velocity" condition, and the downstream outlet of the pool was designated as "outflow." The inlet velocity (v_0), controlling the flow rate into the channel, was determined using the average flow velocity. The symmetry condition was chosen for the top boundary to save computational time, a method validated by Smith and Foster (2005), who observed no significant differences between the usage of symmetry and a free-surface boundary. A smooth ice cover was simulated at the same flow depth in the numerical model as the physical model for smooth ice-covered flow conditions. Rough ice cover was simulated by adjusting the roughness height of the ice cover to match Manning's n_i value used in the flume experiments. The flow moved from upstream to downstream across the pool section, passing over the vegetated pool section and causing changes in flow fields until reaching the outflow boundary.

In numerical modeling, addressing uncertainties related to the mesh resolution and computational domain size is crucial. Sensitivity analyses have been conducted for domain size and mesh resolution to mitigate these uncertainties. Initially, two computational domain sizes were compared under constant conditions: the first domain was set to 5.8 meters, corresponding to the length used in the experimental studies, with a uniform mesh grid of 20 mm × 20 mm. It was observed that reducing the domain length to 5.0 meters did not alter flow characteristics near the vegetated zone in the pool, indicating that this reduction had no significant effect on the flow field. This adjustment was primarily aimed at optimizing simulation time without compromising the accuracy of the simulation results.

Mesh refinement is crucial for achieving high-precision computational results, given the complex vegetation arrangements and significant flow variations within these areas. Two different mesh grids have been tested to optimize the mesh resolution. The computational domain was divided into two mesh blocks. Initially, all blocks utilized a uniform mesh size of

20 mm × 20 mm. After optimization, the central mesh block encompassing the vegetated pool area retained a finer grid of 20 mm × 20 mm. In comparison, the pool entry and exit sections were adjusted to a coarser grid of 30 mm × 30 mm to improve the computational efficiency. Comparisons of the model outputs indicate that these mesh size adjustments do not significantly impact the velocity profiles, confirming the model's robustness. This approach ensures efficient use of the computational resources while maintaining simulation accuracy. Figure 5.5 illustrates the simulation model of the vegetated pool area and the boundary conditions employed in the numerical models. Simulation time was optimized based on the program tips to enhance computing efficiency, as seen in Appendix III.

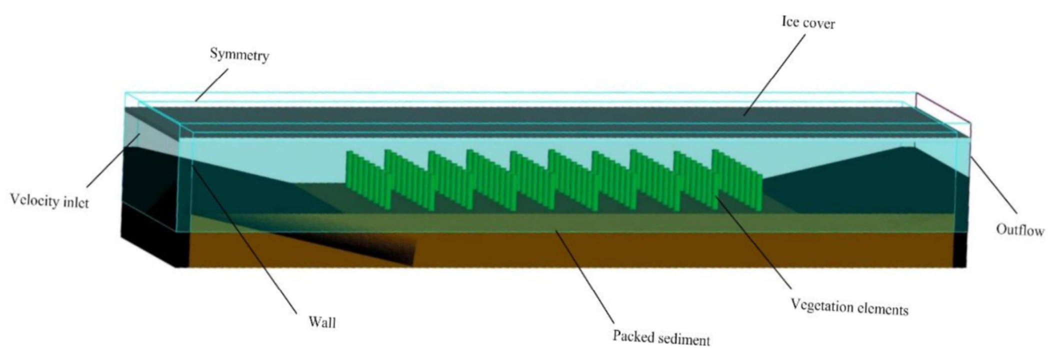

Figure 5.5 The vegetated pool's simulation model and boundary conditions under ice-covered flow conditions.

5.4 Results and Discussions

This section examines the experimental results under varying flow and cover conditions, focusing on the flow field in the vegetated pool. The validity of the simulation model is assessed by comparing the simulation results to the results of measured velocity in pools without vegetation and with vegetation in the pool bed under open channel flow scenarios. Additionally, the velocity vectors and streamlines in the vegetated pools are analyzed to gain insights into the flow dynamics. Table 1 summarizes the conditions for 27 experimental runs and the data used for the numerical simulations. In this table, Q denotes the approaching discharge, d_L refers to the line spacing (distance between two rows), d_R indicates the distance between two adjacent vegetation elements in the same row, and h represents the vegetation height.

Table 5.1 Parameters in the Pool Section and Model Setups

Run #	Water surface cover conditions	Q (L/s)	Planting patterns		
			d_L (m)	d_R (m)	h (m)
1	Open	50		Non-vegetated	
2	Smooth	50		Non-vegetated	
3	Rough	50		Non-vegetated	
4	Open	50	0.3	0.2	0.15
5	Open	50	0.3	0.2	0.10
6	Smooth	50	0.3	0.2	0.15
7	Smooth	50	0.3	0.2	0.10
8	Rough	50	0.3	0.2	0.15
9	Rough	50	0.3	0.2	0.10
10	Open	100		Non-vegetated	
11	Smooth	100		Non-vegetated	
12	Rough	100		Non-vegetated	
13	Open	100	0.3	0.2	0.15
14	Open	100	0.3	0.2	0.10
15	Smooth	100	0.3	0.2	0.15
16	Smooth	100	0.3	0.2	0.10
17	Rough	100	0.3	0.2	0.15
18	Rough	100	0.3	0.2	0.10
19	Open	120		Non-vegetated	
20	Smooth	120		Non-vegetated	
21	Rough	120		Non-vegetated	
22	Open	120	0.3	0.2	0.15
23	Open	120	0.3	0.2	0.10
24	Smooth	120	0.3	0.2	0.15
25	Smooth	120	0.3	0.2	0.10
26	Rough	120	0.3	0.2	0.15
27	Rough	120	0.3	0.2	0.10

5.4.1 Validation of Numerical Model

The flow fields in the pool section with three different slopes (5°, 7°, and 10°) were simulated using Flow-3D for a non-vegetated channel under open flow conditions. Based on the ADV measurements, the experimental data validated the numerical model, confirming that pools with entrance and exit slopes of 5° and 7° are not ideal for achieving fully developed flow within the deep pool section, given the length of the deep pool required for the vegetation arrangement used in the experiment (Figure 5.6). Therefore, the slope of 10° for both entrance and exit sections of the pool was selected for further analysis.

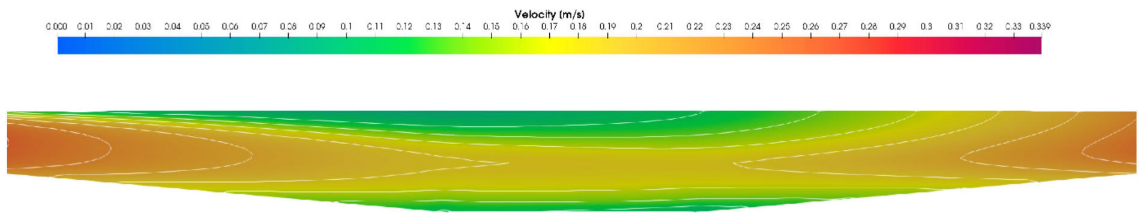

(a)

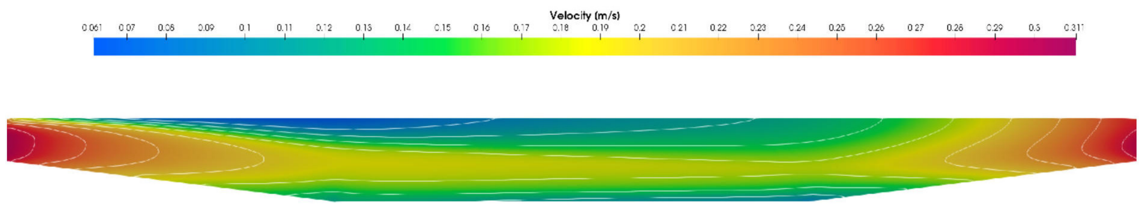

(b)

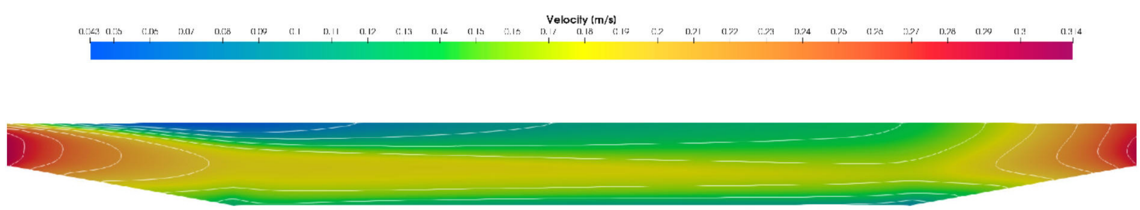

(c)

Figure 5.6 Simulated streamwise velocity profiles using Flow-3D for non-vegetated flume under open channel conditions for pools with entrance and exit slopes of (a) 5°, (b) 7°, and (c) 10°. Simulation results for the pool with an entrance and exit slope of 10° show optimal conditions for fully developed flow, consistent with ADV measurements.

The simulation was conducted for Scenario 1 (open channel, non-vegetated pool) to verify the accuracy of the model parameter settings in Flow-3D software. In this scenario, the numerical results were non-dimensionalized, with the horizontal and vertical coordinates represented by z/H (relative height), where z is the distance from the measurement point to the pool bed, and H is the water depth. Thus, the relative height is zero (0) at the pool bed and one (1) at the water surface. The relative velocity is denoted as u/U_0, where u is the streamwise instantaneous flow velocity, and U_0 is the depth-averaged velocity. Figure 5.7 compares the numerical results to those of experiments, showing six time-averaged streamwise velocity profiles (PF1 – PF6, y = 0) normalized by depth-averaged velocity (u/U_0) at various points along the channel centerline across the entire pool, including both entrance and exit sections. Due to the positioning of the ADV measuring volume, which requires 0.10 m away from the probe head, the measured velocity profiles cannot extend entirely to the water surface. The numerical simulation results generally fall within 10% of the experimental results, with the vertical distribution of streamwise velocity under open channel flow conditions at six measurement positions typically exhibiting a logarithmic profile. Due to the frictional resistance at the channel bottom, the velocity near the bed is relatively low and increases with the distance from the bed. However, at PF2 and PF5, slight underpredictions and overpredictions of the near-bed velocities were observed (with measured results scattering around the simulation curve), likely due to the uncertainty of experiments associated with the ADV measurement technique. This point-measurement method is less accurate in regions of high turbulence, such as near the transition zone between the entrance/exit slopes and the pool bed (PF2 and PF5).

Figure 5.7(c) compares the calculated and measured streamwise velocities along the water depth for Case 4. With vegetation in the pool bed, the vertical distribution of streamwise velocity in the deep pool section (PF3 and PF4) deviates from the typical logarithmic pattern. Within the vegetated zone, the velocity change is minimal. However, a significant velocity gradient is observed in the transition layer between the vegetation canopy and the flow above vegetation, primarily due to the resistance caused by the vegetation patch. Above the vegetation patch, the velocity resumes a logarithmic distribution pattern. The velocity profile PF4 showed that the calculated and measured velocities agree very well, with only slight differences. This discrepancy is mainly attributed to the numerical model's inability to account for plant deformation under flow conditions and the complex flow patterns in the boundary region, where secondary flows may influence the lateral deformation of the vegetation. Along the entrance and exit sections of the pool, where the flow has not yet interacted with the vegetation, a relatively consistent logarithmic distribution of u/U along the depth is still observed. Interestingly, the simulated velocity at the bed of the entrance section is no longer zero, which may be attributed to numerical diffusion. Numerical schemes in CFD simulations, particularly those involving complex geometries like vegetated beds, can exhibit numerical diffusion, which may artificially elevate velocity magnitudes near boundaries (such as the bed) where they would theoretically be zero (Karadimou et al., 2018). Despite these calculated non-zero bed velocities using the RNG k-ε model, the results remain scientifically valid due to well-accepted model assumptions, such as the Boussinesq hypothesis, which does not fully capture the range of turbulence structures, especially in complex flows (Briganti et al., 2004). These simplifications, typical in turbulence modeling, are acknowledged within the scientific community and do not significantly detract from the overall applicability of the findings in capturing major flow characteristics. As shown in Figure 7, streamwise velocity profiles in the non-vegetated slope sections follow the logarithmic law regardless of the presence of vegetation in the deep pool section. Therefore, the focus of this research is on the flow field within the deep pool section with the presence of vegetation in the pool bed.

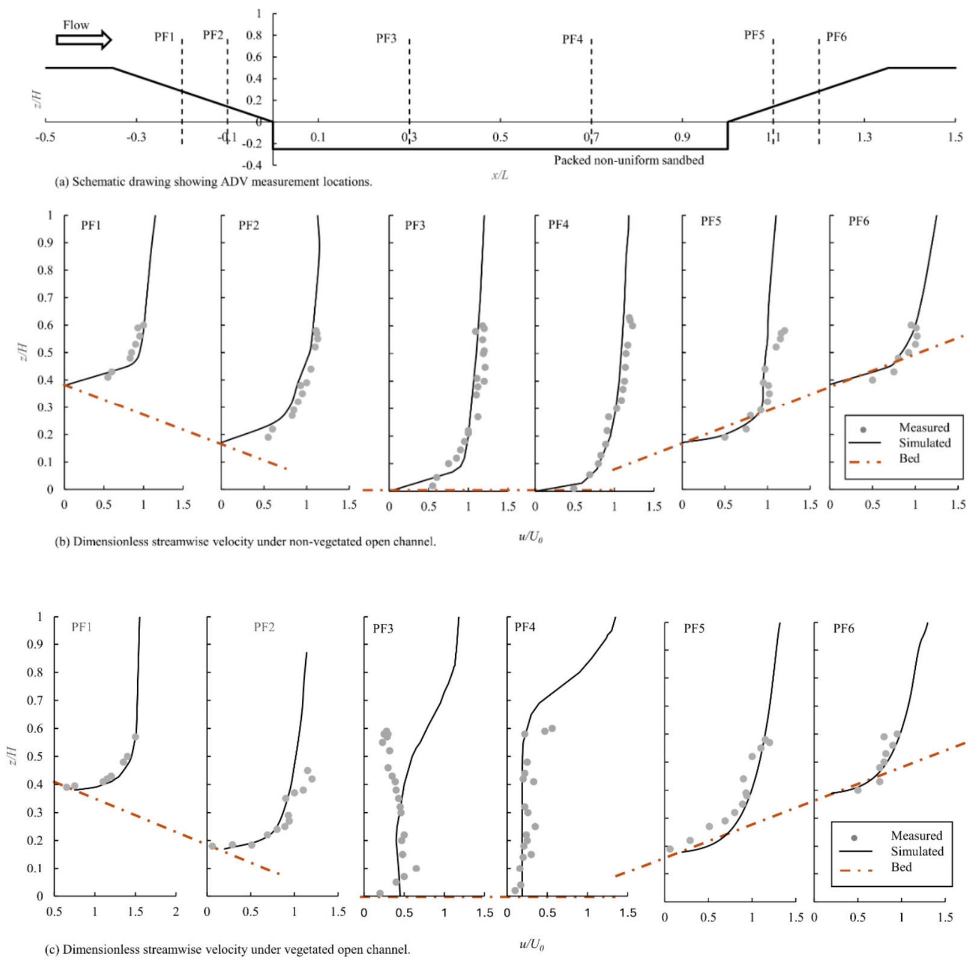

Figure 5.7 Validation of numerical results against those of experiments. Red lines indicate the slope. However, the figures indicate the velocity variation with depth, and thus velocity measurements were all conducted above the channel bed and slope. (a) ADV measurement locations along the centerline; (b) Averaged streamwise velocity profiles in the pool without vegetation under open flow conditions; (c) Averaged streamwise velocity profiles in the pool with vegetation under open flow conditions.

Note that the non-zero velocity at the channel bed in this figure results from the inherent characteristics of numerical simulations. In computational fluid dynamics (CFD), convergence is achieved when residuals, or errors between iterations, decrease to negligible levels, while stability ensures bounded, physically meaningful results. Stability was maintained through careful selection of solver parameters, such as time step size and relaxation factors, and convergence was monitored via residual reduction, particularly near the no-slip boundary at the bed. Mesh resolution impacted velocity profile accuracy; finer meshes improved alignment with expected results. However, due to numerical representation, CFD methods calculate velocity at the first node adjacent to the wall, not directly on it, resulting in a slight non-zero velocity at the bed. This standard practice does not indicate poor convergence or instability but reflects a recognized limitation of numerical post-processing. Nonetheless, the results are congruent with figures displayed in Eraky et al. (2022). Equilibrium, as indicated in Figure 5.7 (PF 4), signifies that flow inside the submerged vegetation has stabilized, particularly in the streamwise velocity component. This stabilization shows that the flow has fully adapted to the vegetation's presence, leading to a steady velocity profile and fully developed flow.

5.4.2 Velocity Profiles

In fluvial hydraulics, the cross-sectional velocity is typically assessed to capture the distribution of momentum and the influence of secondary flows. The cross-sectional velocity refers to the resultant velocity vector obtained by summing the velocity components in the y-direction (lateral direction) and z-direction (vertical direction) within a given cross-section of a flow field. This velocity is significant as it provides a detailed representation of the flow characteristics across the cross-section. Understanding the cross-sectional velocity is crucial for accurately predicting flow patterns, assessing turbulence kinetic energy, and evaluating the stability and uniformity of the flow field.

Figure 5.8 presents simulated cross-sectional velocity contour plots under various conditions, including with and without the presence of vegetation (vegetation height = 15 cm) under different water surface cover conditions. In the absence of vegetation on the pool bed, both the y-velocity (lateral direction) and z-velocity (vertical direction) are negligible, indicating the absence of secondary currents and allowing the sidewall effect to be ignored. However, when vegetation is present in the pool bed, the flow velocity contour in the zone near the bed significantly bends due to the obstructive effect of the vegetation. This creates distinct high-velocity zones within the vegetated area and shifts the maximum flow velocity behind the vegetation stems. The proximity of high-velocity flow to the channel bed can result in elevated bed shear stress, potentially increasing sediment transport, bed erosion, and scour in the zone directly behind the vegetation. While vegetation typically increases flow resistance, the presence of fast flow zones near the pool bed alters overall energy dissipation patterns, which can affect the hydraulic efficiency of the channel and alter flow conveyance. This impact will be further discussed in detail in the Turbulent Kinetic Energy section. Under ice-covered flow conditions, although the cover bottom surface shows negligible secondary current activity (with velocity contours approaching zero), the low-velocity region near the cover bottom surface expands its size, which can lead to decreased transport of frazil ice or debris when ice cover begins to melt. This effect becomes more pronounced as the surface roughness of the ice cover increases.

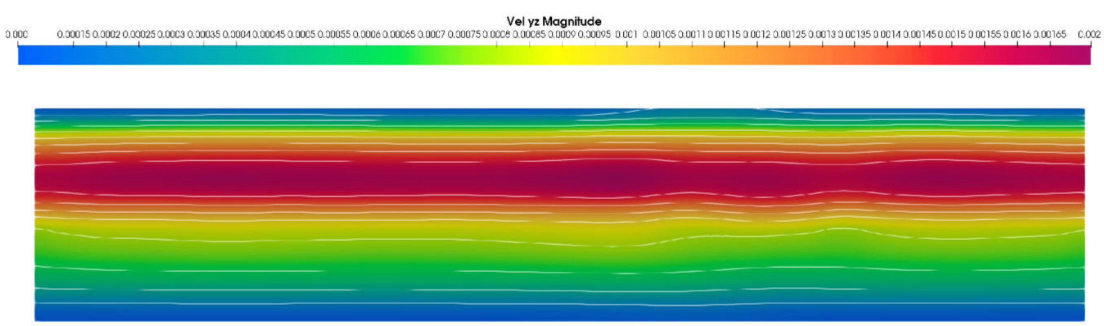

(a)

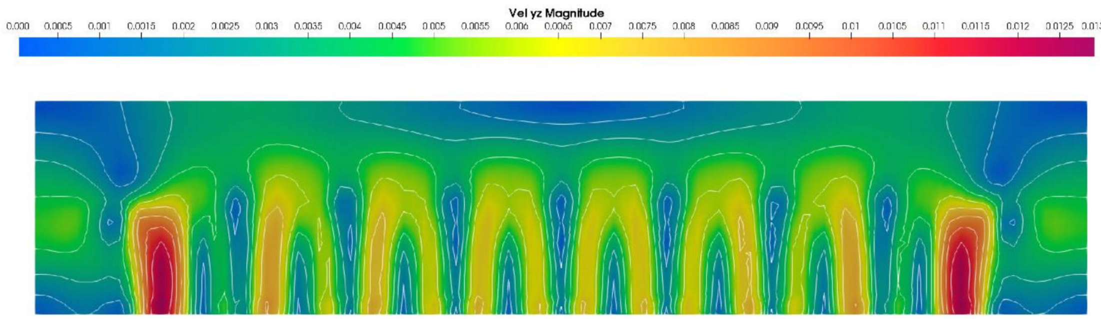

(b)

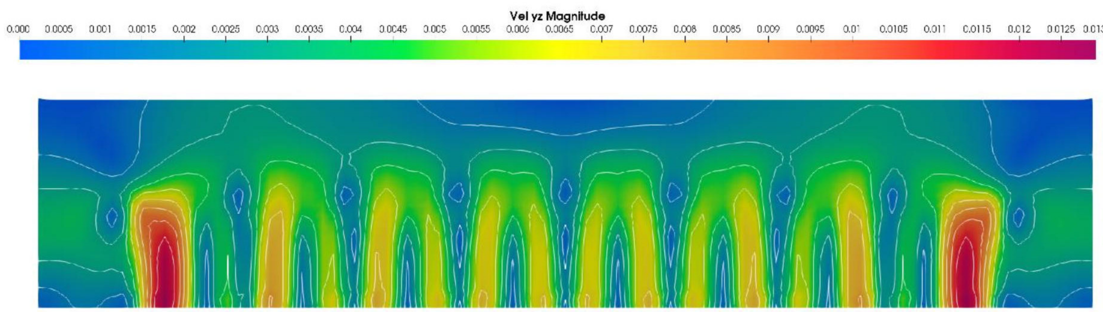

(c)

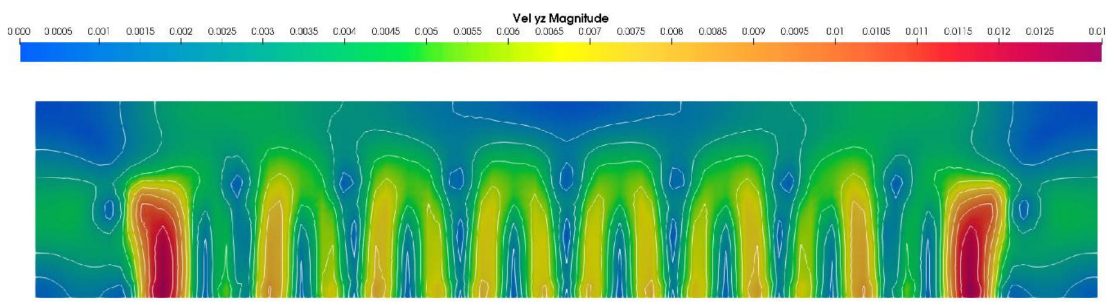

(d)

Figure 5.8 Simulated cross-sectional velocity contours in the pool (a) without the presence of vegetation in the pool (open channel flow); (b) with vegetation in the pool (vegetation height =15 cm, open channel flow); (c) with vegetation in the pool (vegetation height =15 cm, smooth ice-covered flow); (d) with vegetation in the pool (vegetation height =15 cm, rough ice-covered flow) (unit: m/s).

Figure 5.9 shows the computed cross-sectional flow vector field for different water surface cover conditions in the presence of vegetation in the pool bed (vegetation height = 15). Results of the analysis reveal that the resistance caused by vegetation generates non-negligible lateral velocity near the vegetated zone, acting as a strong disturbance source that diffuses outward.

This secondary flow moves toward the channel wall, forming a circulating secondary flow pattern. Under ice-covered flow conditions, the secondary currents are more detectable, and a more prominent circular motion has been observed under a rough ice-covered flow condition.

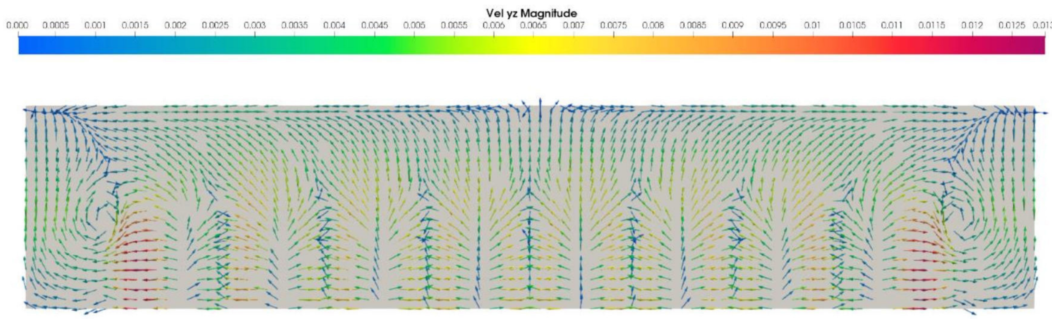

(a) Cross-sectional velocity vector plot for open channel flow in the presence of vegetation (vegetation height = 15cm).

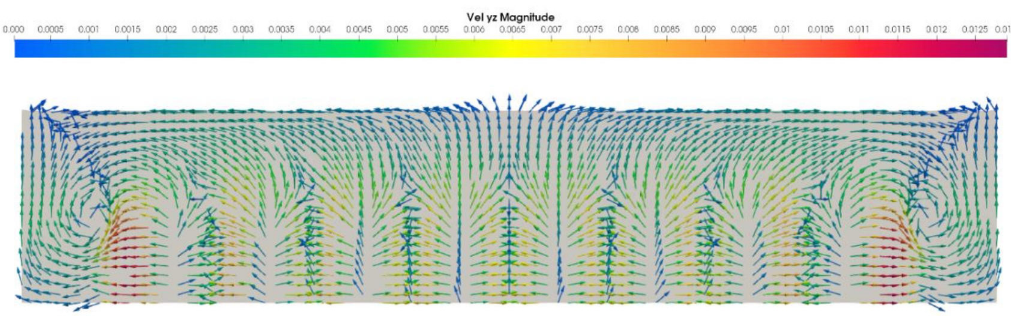

(b) Cross-sectional velocity vector plot for smooth ice-covered flow in the presence of vegetation (vegetation height = 15cm).

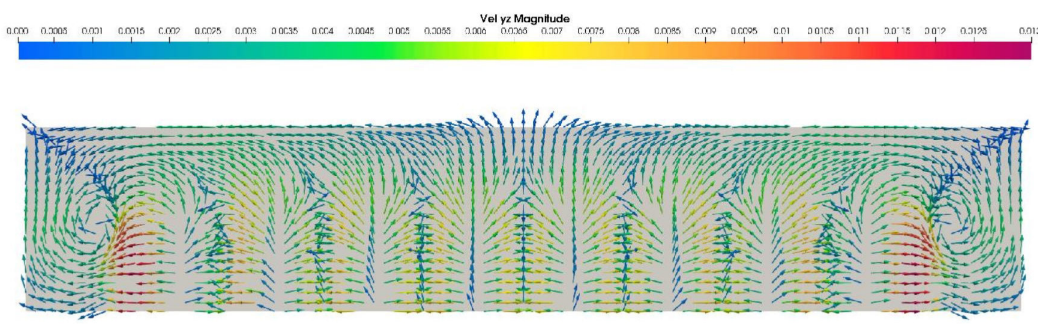

(c) Cross-sectional velocity vector plot for rough ice-covered flow in the presence of vegetation (vegetation height = 15cm).

Figure 5.9 Secondary flow velocity vector diagram in the presence of vegetation in the pool bed under different water surface cover conditions (vegetation height = 15cm; unit: m/s).

Figures 5.10(a) and (b) present the calculated streamwise velocity field under different water surface cover conditions at $z/H = 0.25$ from the pool bed in the presence of vegetation in the pool bed with a vegetation height of 15 cm. The results indicate that the flow field in front of each vegetation element remains relatively steady. One can observe from these figures that a low-velocity zone appears behind each vegetation element, but the flow velocity between individual vegetation elements in the sheath layer increases. Regardless of the water surface cover conditions, the wake vortex zone behind each vegetation element expands downstream. The presence of an ice cover on the water surface does not significantly alter the velocity field in the sheath layer of the vegetated zone.

Figure 5.10(c) illustrates the spatial distribution of streamwise velocity contours at the distance of $z/H = 0.25$ from the pool bed in the presence of vegetation with a vegetation height of 10 cm under open channel conditions. Similar to the velocity profile observed for deeper vegetation (15 cm), when the flow reaches the first row of vegetation, the obstruction from vegetation causes backflow, reducing velocity in front of the vegetation but sharply increasing it on both sides of each vegetation element in the sheath layer. In the rear side of vegetation elements, wake and vortex are formed, with flow velocity increasing between vegetation elements in the sheath layer until it stabilizes after overcoming the obstructive effects. This flow pattern repeats as the flow encounters subsequent rows of vegetation elements. Within the vegetated section of the pool, the velocity exhibits a sawtooth pattern, peaks at the edges of the vegetation, and the velocity in the sheath layer increases as the vegetation height grows. This occurs due to the decrease in the effective cross-sectional area for passing flow, which compresses the flow and increases velocity immediately entering the vegetation patch. The maximum velocities occur in the sheath layer between the adjacent vegetation elements in the first row of vegetation elements, as subsequent vegetation elements cause kinetic energy dissipation, reducing flow velocities. The velocity behind the vegetation patch is lower than that passing through the vegetation patch due to the decrease in the cross-sectional area for passing flow caused by the obstruction of vegetation. As vegetation height increases, the wake area expands (Figures 5.10a and 5.10c). Such detailed flow structures around cylindrical vegetation elements are challenging to capture experimentally, highlighting the importance of numerical simulations. Previous studies suggest that the wake zones behind vegetation elements promote the deposition of fine particles, stimulating the growth and expansion of aquatic organisms (Kondziolka & Nepf, 2014). This creates a positive feedback loop between the aquatic ecosystem and sediment deposition (Yamasaki et al., 2021).

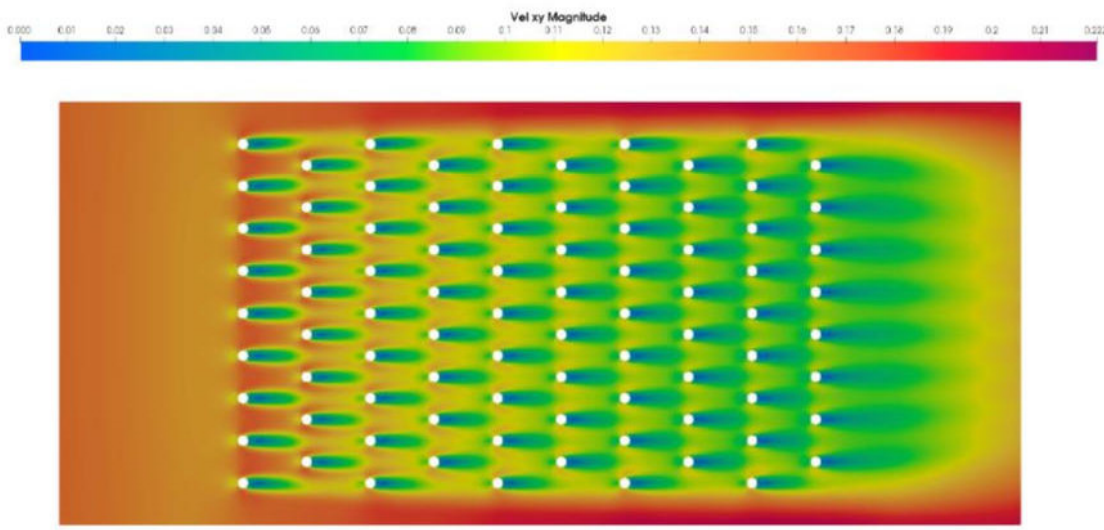

(a)

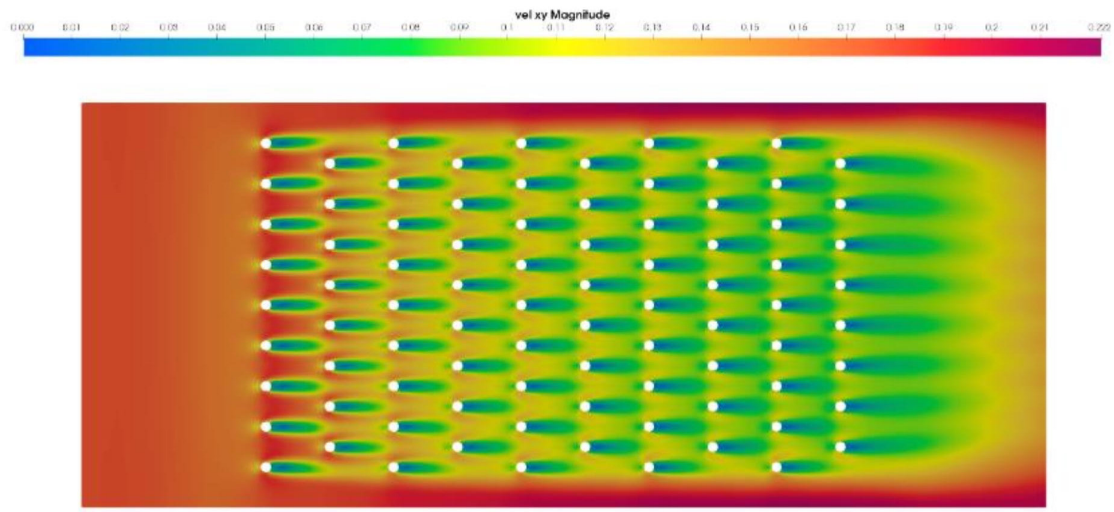

(b)

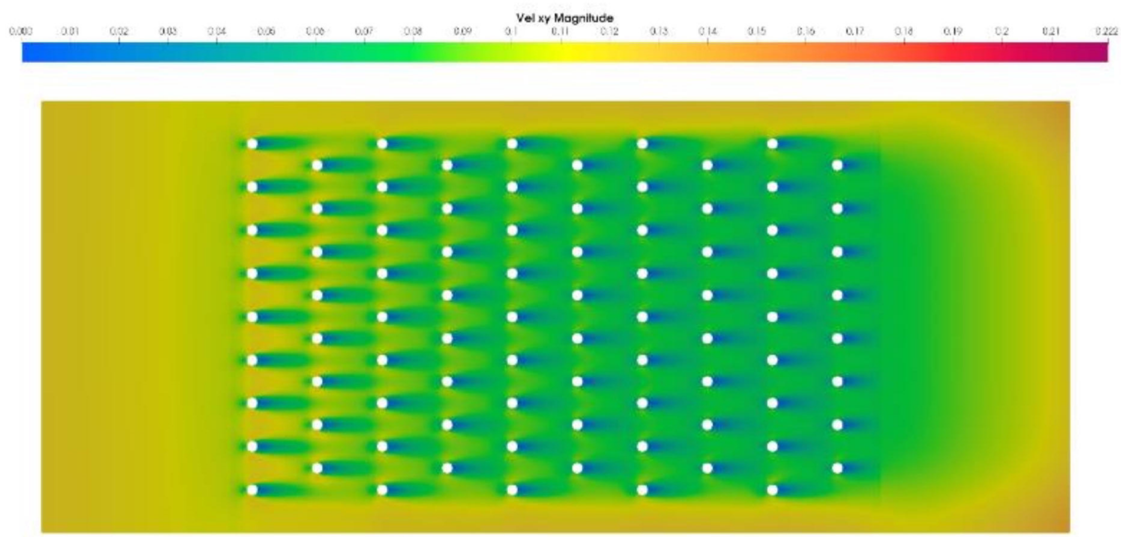

(c)

Figure 5.10 Streamwise velocity contour diagram near the vegetation zone in the pool (unit: m/s): (a) open flow, vegetation height = 15 cm, (b) smooth ice-covered flow, vegetation height = 15 cm, (c) open channel flow, vegetation height = 10 cm

Results of the numerical simulations indicate that the slope zones of both entrance and exit sections of the pool where the cross-section changes significantly influence the flow and turbulence patterns within the pool. The time-averaged velocity contours reveal higher velocities over the slopes of both entrance and exit sections and lower velocities near the pool bed (Figure 5.11). Additionally, turbulence intensities increase near the slope bed in the convectively decelerating flow (CDF) zone where the average velocity is low. The flow pattern in the model closely resembles that observed in flume experiments. In the absence of vegetation under open flow conditions, high-velocity zones are observed in the entrance and exit sections of the pool. The time-averaged velocity is evenly distributed throughout the deep pool section, with slow flow zones at the channel bed and water surface (Figure 5.11a). In the presence of vegetation in the deep pool section, flow velocity decreases starting at the upstream edge of the vegetated patch, with the highest time-averaged velocity occurring in the water column above the vegetation (Figure 5.11b). Additionally, taller vegetation introduces an elongated slow surface flow zone in the water column between the entrance slope and the deep pool sections (Figure 5.11c). Initially, high turbulence zones are concentrated beneath the water surface and near the bed, with zones of significant velocity variation observed both near the water surface and the bed over the entrance slope section, namely the dip phenomenon. As the flow progresses downstream, the velocity variation becomes more distributed across the entire flow depth, and the surface slow flow zone disappears after passing the deep pool (about the fifth row in the planting array). Under ice-covered flow conditions, in the presence of vegetation, the velocity profile in the X-Z plane becomes more symmetrical, resembling a pipe flow in the deep pool section. Under ice-cover flow conditions, with the increase in ice-cover roughness, the low flow zone elongates in the deep pool section, and forming a conduit-shaped velocity profile is delayed. It has been observed that a quasi-uniform velocity profile develops under smooth ice-covered flow conditions after passing the third row of vegetation elements in the deep pool. In contrast, under rough ice-covered flow conditions, the velocity profile becomes quasi-uniform after passing the fifth row of vegetation elements.

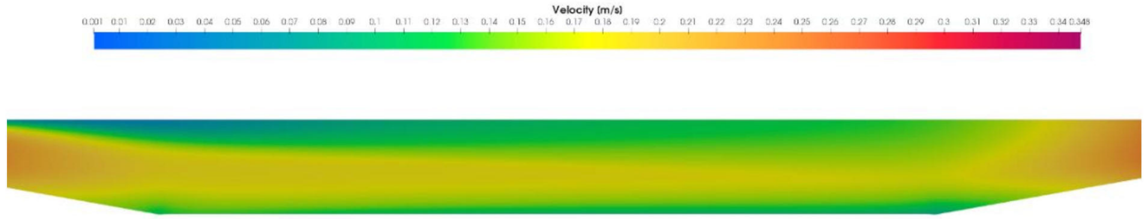

(a)

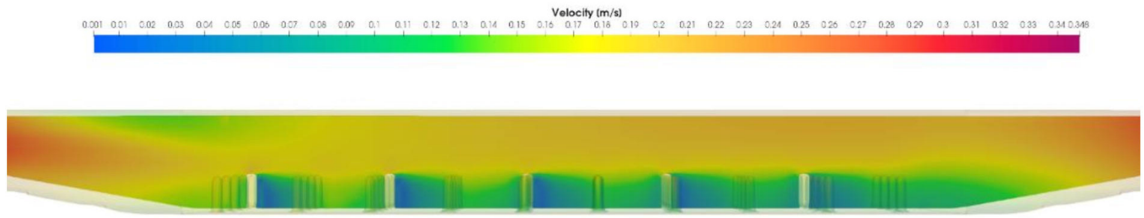

(b)

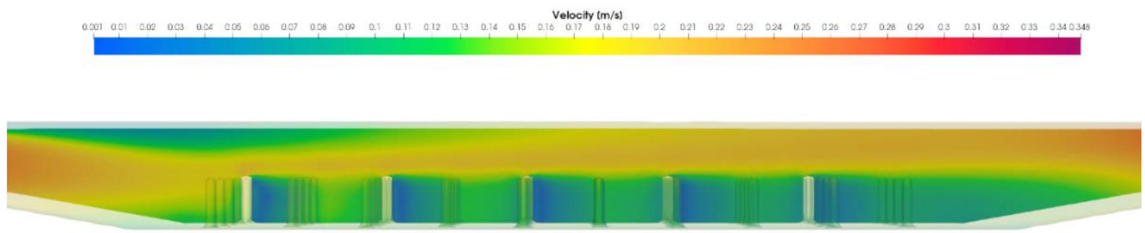

(c)

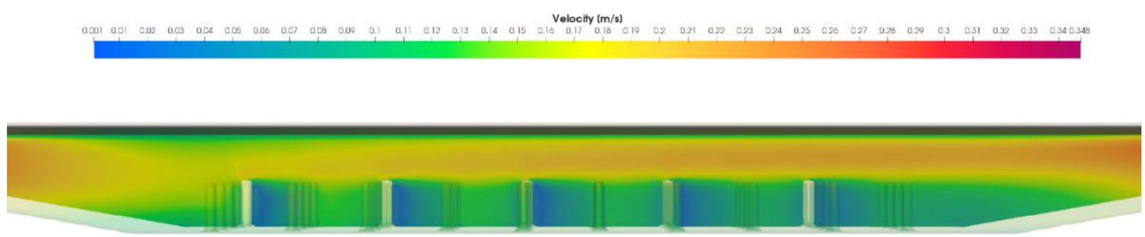

(d)

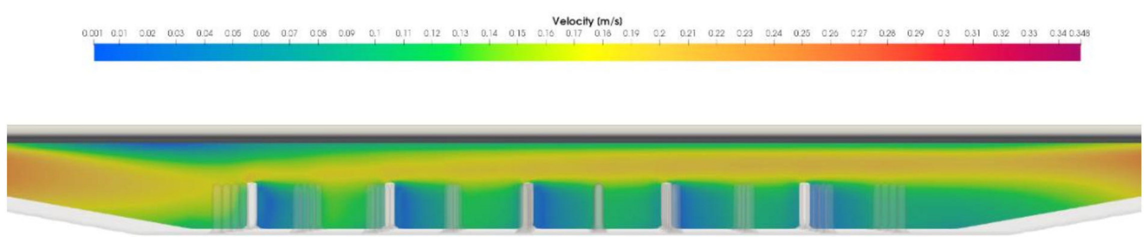

(e)

Figure 5.11 Time-averaged velocity fields along the central axis (*X*-*Z* plane) of the pool channel: (a) Non-vegetated open channel flow; (b) vegetated open channel flow (vegetation height =10 cm); (c) vegetated open channel flow (vegetation height =15 cm); (d) vegetated smooth ice-covered flow (vegetation height =15 cm); (d) vegetated rough ice-covered flow (vegetation height =15 cm)

To investigate the impact of vegetation height on flow patterns in the vegetated pool, various scenarios were considered by varying the vegetation heights on the deep pool bed, specifically with vegetation heights of 10.0 cm and 15.0 cm under open channel conditions. Given that the water depth before approaching the upstream cross-section of the entrance section of the pool is set at 20.0 cm (approximately 30.0 cm deep in the deep pool section), these vegetation settings in this study represent the condition of fully submerged vegetation. Figure 5.12 illustrates the positions for analyzing the streamwise velocity profiles. A 2D slice is taken in the *X-Z* plane, where the solid line denotes vegetation elements within the slice, and the dashed line represents vegetation elements in the adjacent planting arrays.

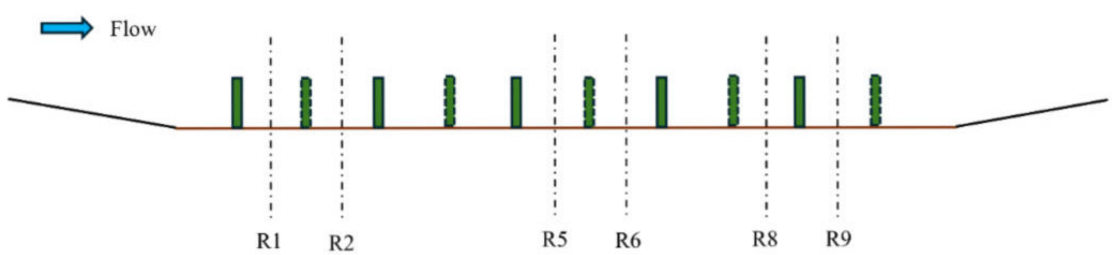

Figure 5.12 Profiling positions for the streamwise velocity in the numerical model (staggered vegetation arrangement).

Figure 5.13 compares the streamwise velocities (u) at various measurement points with different vegetation heights. It is observed from Figure 5.13 that the vegetation height significantly affects the streamwise velocity along the centerline (y = 0), particularly in the vegetation-flow transition zone. In the deep pool section near the pool entry section (R2) and exit section (R8), vegetation height variations notably influence streamwise velocity distribution. Despite differences in vegetation height, the vertical distribution trend of streamwise velocity remains generally consistent in the middle of the deep pool section. Within the vegetation zone, before the relative streamwise velocity (u/U_0) suddenly increases, the relative velocity (u/U_0) shows a consistent pattern as z/H increases.

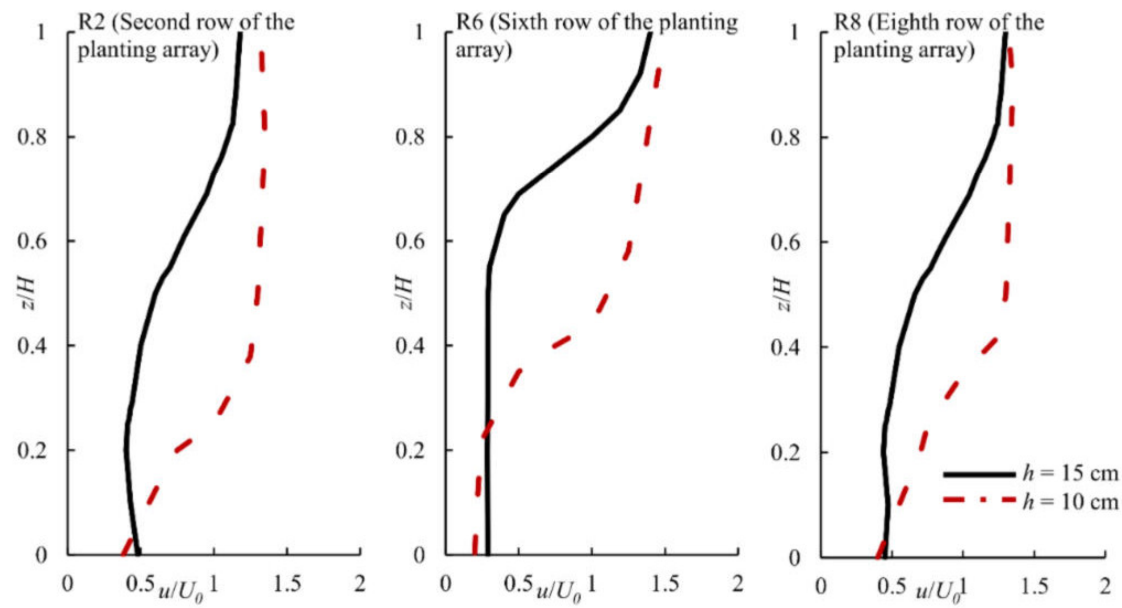

Figure 5.13 Comparison of streamwise velocity at various positions with different submerged vegetation heights (staggered vegetation arrangement).

When ice cover is introduced in the model, the position of the maximum streamwise velocity under the ice is influenced by the relative roughness of the channel bed and the ice cover. The maximum velocity typically shifts toward the surface that offers the least resistance to the flow (Sui et al., 2009, 2010). Figure 5.14 presents streamwise velocity profiles under the open channel, smooth, and rough ice-covered flow conditions downstream of the vegetation patch. These profiles differ from those observed without vegetation on the channel bed, as shown in the verification case. Figure 5.14 captures the velocity profiles immediately downstream of the wake zone of individual vegetation elements, where severe fluctuations can be observed, mirroring trends seen in experimental data from plain channels (Barahimi & Sui, 2024b). The velocity profiles in Figure 5.14 reflect the combined effects of ice cover, turbulent flow, and the interaction between vegetation and the sand bed of the pool. In the presence of vegetation, velocity profiles measured closely behind the vegetation element where vegetation is present in the measuring 2D slice (R1, R5, R9) under ice-covered flow conditions exhibit two peak values: one at the sheath section of the vegetation (or stem section) and another above the vegetation tops. The sheath section reduces the cross-sectional area for passing flow, accommodating greater flow velocity. The second velocity peak occurs between the ice cover and the vegetation. Results show that the ice cover shifts the maximum velocity to the region between z/H = 0.50 and 0.70. Under open flow conditions, the streamwise velocity (u) profile above the vegetation zone follows a logarithmic function, with the maximum velocity near the water surface. In contrast, under ice-covered flow conditions, the streamwise velocity profile resembles that of a pipe flow, with the peak velocity between the vegetation canopy and ice cover depending on the relative roughness of the ice cover to that of the vegetation canopy. Velocity fluctuations are prominent behind the vegetation elements, with more significant variations observed near the transition between the slope and deep vegetated pool sections (R1 and R9).

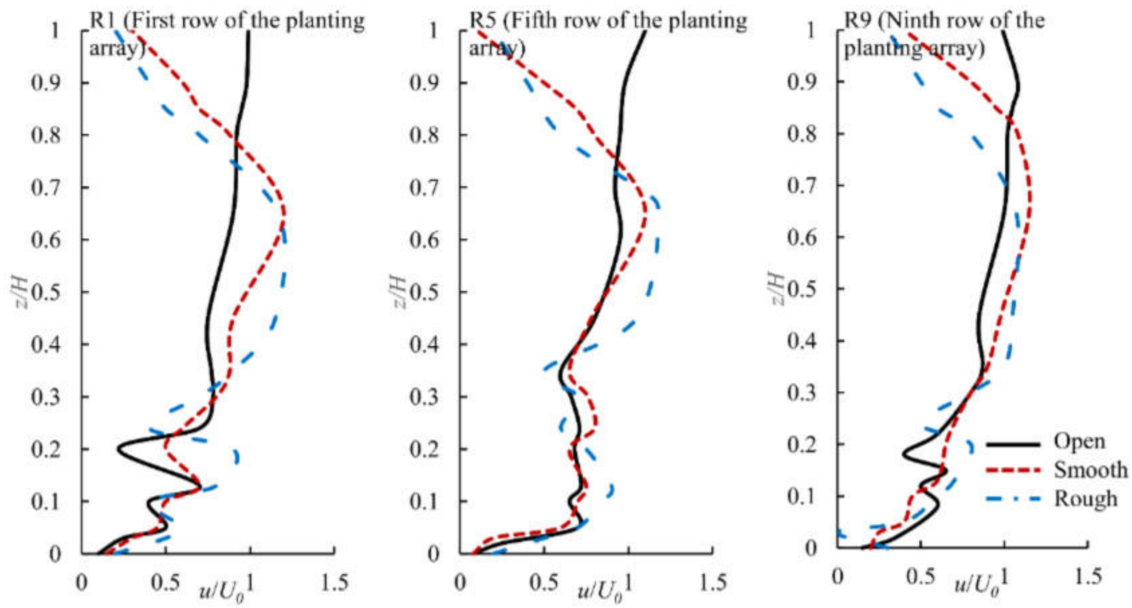

Figure 5.14 Streamwise velocity under different surface cover conditions behind vegetation elements (vegetation height = 10 cm, staggered vegetation arrangement).

5.4.3 Turbulent Kinetic Energy

Vortex formation in the wake behind vegetation elements extracts energy from the mean flow, converting it into turbulent kinetic energy (TKE). The turbulence levels are mainly driven by vegetation-induced drag and are largely unaffected by bed shear stress. Local turbulent kinetic energy is defined as follows:

$$TKE = \frac{1}{2}\left(\overline{u'^2} + \overline{v'^2} + \overline{w'^2}\right) \tag{5.14}$$

where

$$\overline{u'^2} = \frac{1}{T}\int_0^T (u(t) - \bar{u})^2 \, dt \geq 0 \tag{5.15}$$

and $\overline{v'^2}$ and $\overline{w'^2}$ are calculated in a similar approach.

Figure 5.15 illustrates the calculated turbulent kinetic energy (TKE) values using the y-axis (*X-Z* plane) as the cutting plane for the 2D slice under the open channel flow condition with the vegetation height of 15 cm (Scenario 4). While theoretically, TKE should approach zero at the very bottom due to the no-slip condition, a peak in TKE, with values ranging from 0.0017 to 0.0020 m²/s², is observed just above the pool bottom immediately after the flow passing through the vegetation zone (within the boundary layer). This peak reflects the interaction between the fluid flow and the vegetation, which is accurately captured by the simulation. Within the vegetation zone, particularly near the bottom, high-velocity gradients exist due to the interaction between the moving fluid and the stationary vegetation elements. These gradients can generate significant shear stress, producing turbulence and elevated TKE. Additionally, the RNG *k-ε* model predicts higher TKE near the boundary due to the turbulence closure scheme, which calculates TKE based on local velocity gradients. These gradients are steepest near the pool bed, thus predicting higher TKE in this region. As the distance from the bed (*z/H*) increases, the turbulent kinetic energy gradually decreases and levels off near the water surface, consistent with the findings of Huang et al. (2019).

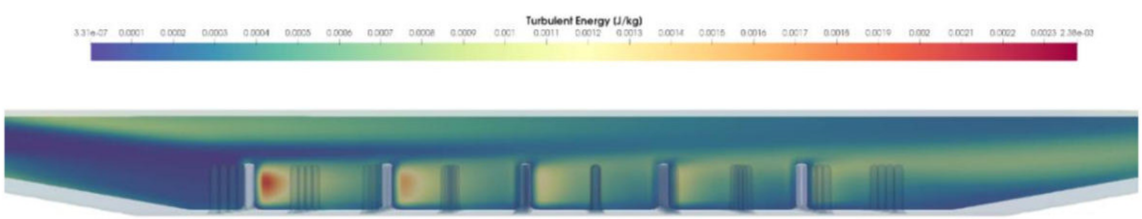

Figure 5.15 The numerical model simulated the TKE contour in the *X-Z* plane (staggered vegetation arrangement).

Figure 5.16 presents the vertical distribution curves of the calculated TKE in the presence of vegetation with different heights under open channel flow conditions. As shown in Figure 16, when the flow is obstructed by vegetation, the TKE curves in the presence of submerged vegetation exhibit a mirrored "C" shape in the stem zone, with a transition point near the top of the vegetation canopy. As the relative distance from the bed (z/H) increases, the interference of the vegetation stem with the flow gradually decreases. Results showed that the vegetation height significantly influences the TKE at the water surface, with the TKE for vegetation 10 cm high being, on average, twice that observed for the submerged vegetation 15 cm high.

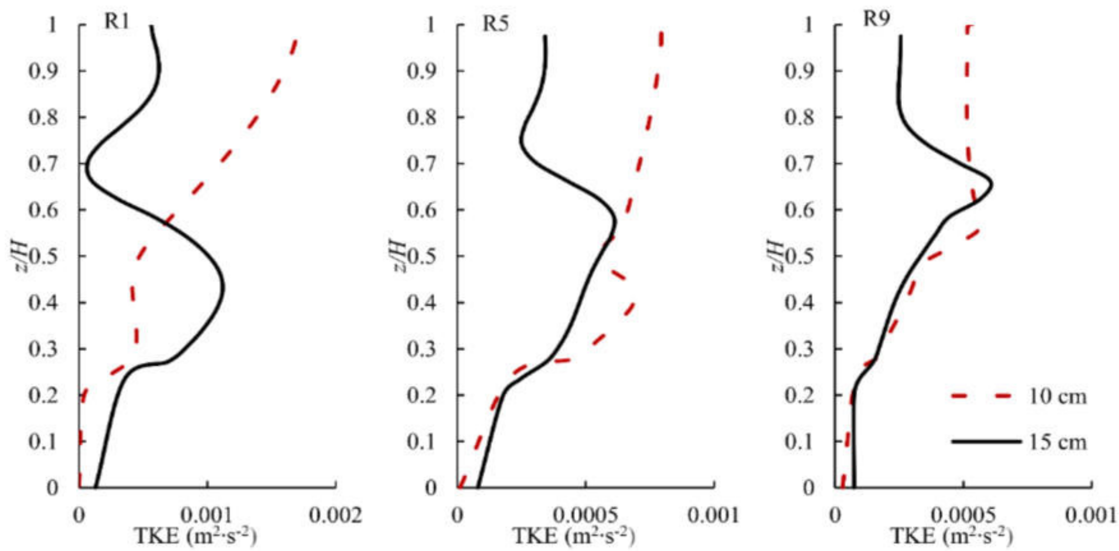

Figure 5.16 Comparison of turbulent kinetic energy across various positions in the vegetated pool zone (y = 0, staggered vegetation arrangement).

Figure 5.17 shows the depth-averaged turbulent kinetic energy (TKE) distribution along the longitudinal section (or streamwise direction) at a distance from the bed of z/H = 0.25. In the model constructed in Flow-3D, x represents the longitudinal coordinate, with x = 0 positioned at the center of the deep pool, while the y and z axes are consistent with Figure 2. As shown in Figure 17, flow disturbances caused by vegetation create significant non-uniformity in the TKE distribution. In all simulation scenarios, the TKE gradually increases as the flow encounters vegetation in the deep pool. It peaks at x = -1.34 m as it passes the first row of vegetation elements. This sharp increase is attributed to the vegetation's substantial drag, elevating the TKE value. Then, the TKE value decreases sharply but rises again between vegetation clusters, with additional peaks observed at x = -0.72 m, x = -0.12 m, x = 0.48 m, and x = 1.08 m as the flow passes the second, third, fourth, and fifth rows of vegetation elements. After passing the last row of vegetation elements, the TKE value drops to the average value found in the middle between two adjacent vegetation columns (y = 0.15 m) and stabilizes due to the absence of vegetation, with the TKE value primarily influenced solely by bed drag force, which remains constant. The TKE distribution exhibits a sawtooth pattern as the flow moves through zones with low and high flow velocities, aligning with findings by Wang et al. (2019). The overall variation of the TKE values between vegetation clusters shows a decreasing trend. From upstream to the downstream of the vegetated pool, in the longitudinal zone between the columns of vegetation elements (y = 0.15 m), the TKE values in the non-vegetated zone change gradually along a certain distance from x = -1.5 m to -0.86 m, and then stabilizes when x > -0.86 m until the end of the deep pool. This is because vegetation elements do not directly influence the TKE in the zone between the columns of vegetation elements but are affected by wake vortices generated by the vegetation elements toward this zone. As the influence of vegetation diminishes, the TKE values stabilize beyond x = 1.5 m. The presence of an ice cover leads to the reduction of the TKE values at the entrance section of the pool, which increases near the exit section of the pool. Results showed that, within the vegetation patch, for instance, at a distance from the bed of z/H = 0.25, under smooth ice-covered flow condition (n = 0.010 was used in this model), the TKE value reduces on average by 15% more than that of rough ice-covered flow condition (n = 0.021).

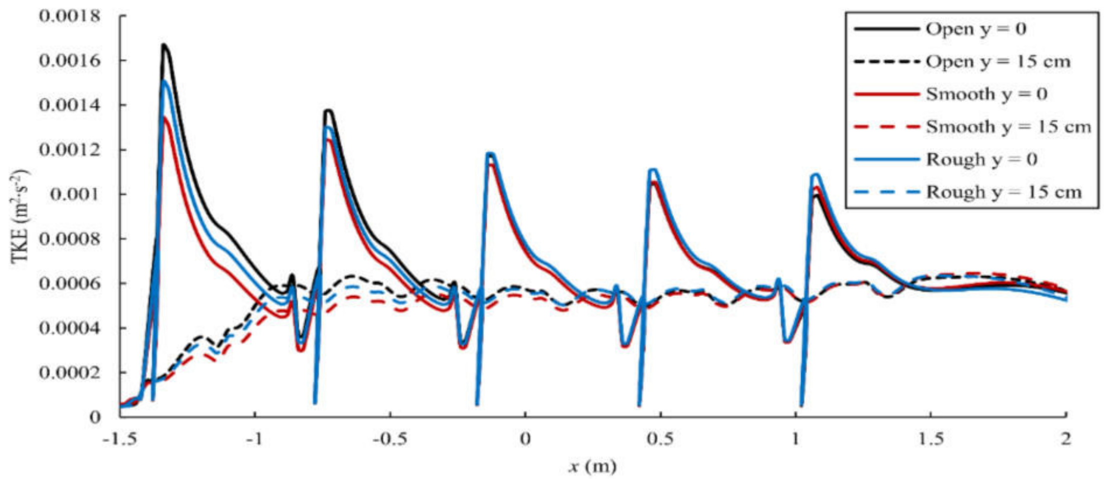

Figure 5.17 Streamwise turbulent kinetic energy distribution along the vegetated deep pool.

Figure 5.18 presents the TKE profiles behind vegetation elements arranged in staggered configuration (vegetation height = 15 cm) under different water surface cover conditions. In the open channel scenarios, the TKE profiles typically exhibit peaks at the sheath section, followed by a general decrease as the water flows downstream. Under both smooth and rough ice-covered flow conditions, the TKE profiles show an increasing trend toward the ice cover. In the region near the vegetation canopy ($z/H \approx 0.60$), the TKE values reach their maximum due to significant velocity gradients arising from the interaction between the moving fluid and the vegetation canopy, except in the regions near the pool entrance in the open channel scenario. In the pool region with the distance from the pool bed to $z/H = 0.60$ (or inside of the vegetation patch), vegetation blockage reduces the cross-sectional area for flow, thereby reducing the TKE fluctuations. Around the distance from the channel bed of $z/H = 0.80$, which marks the boundary zone influenced by the ice cover, the TKE values increase again. Near the bottom surface of the ice cover, the TKE value gradually increases due to the no-slip condition.

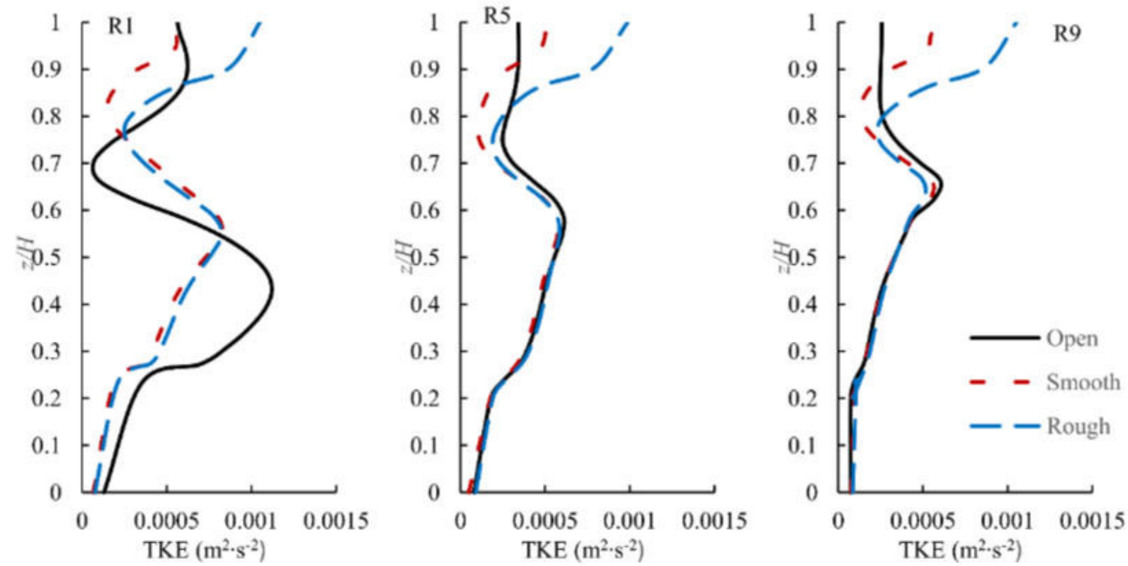

Figure 5.18 Comparison of turbulent kinetic energy (TKE) behind vegetation elements arranged in a staggered configuration under different water surface cover conditions.

To investigate the impact of the inflow rates on turbulent kinetic energy (TKE) in the vegetated pool, this study examined three inflow conditions with flow rates of 50, 100, and 120 L/s. According to the continuity theory, with a constant water depth, a higher inflow rate results in a higher approaching velocity. Figure 5.19 compares the simulated turbulent kinetic energy at different cross sections under different inflow conditions in the presence of vegetation in the deep pool (vegetation height = 15 cm) in open channel. In the sheath section of vegetation (near the pool bed), the impact of the inflow rates on the TKE values is less than in the zone of vegetation canopy. One can see from Figure 5.19 that, with the increase in the inflow rate, the TKE value in the vegetation canopy increases first and decreases later. When the flow encounters the first row of vegetation elements, the TKE value consistently increases with the inflow. However, the vertical TKE profile on the rear side of the first-row vegetation indicates more intense turbulence than in other locations. Figure 5.19 shows a noticeable decrease in the TKE value as the flow moves further downstream (or as the longitudinal distance *x* increases).

Under open channel flow conditions, after the TKE value reaches a maximum, the TKE value decreases and stabilizes at a distance from the pool bed of approximately 0.6 < *z/H* < 0.8.

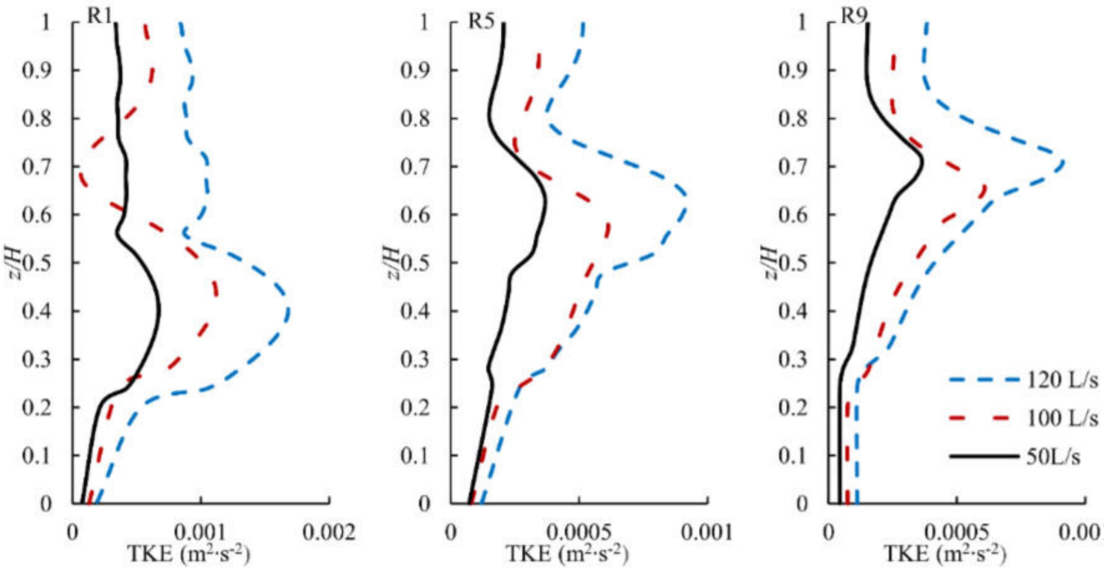

Figure 5.19 Comparison of the simulated turbulent kinetic energy (TKE) under different inflow conditions under open channel flow.

Interestingly, ice-covered flow demonstrates higher TKE at the surface below the ice cover. In Reynolds-Averaged Navier-Stokes (RANS) simulations, turbulent fluctuations are not directly resolved but approximated through turbulence closure models, so TKE is not derived from the instantaneous flow field but predicted via a modeled equation, referred to as "modeled TKE." The TKE profiles in this study align with existing literature for open-channel flows, where peak TKE is observed within vegetation stems and near-zero values occur at the free surface (Farhadi et al., 2018; Jing et al., 2023; P. Kumar et al., 2024). Although flume studies of ice-covered flows are limited, literature and field data indicate that TKE near the ice interface is not necessarily near-zero, as suggested by studies on radiatively driven convection (Mironov et al., 2002). Additionally, Kumar et al. (2024) observed elevated TKE near a solid wall under non-slip conditions, which is consistent with the results here. The styrofoam panel used in this study floated, allowing minimal wave action that has little impact on scour (Hains & Zabilansky, 2005). However, the ice cover in FLOW-3D was modeled as a fixed plate, simulating Poiseuille-type flow conditions that support higher TKE near boundaries (Gretler & Meile, 1997). Despite this, very low TKE values were recorded near the bed, attributable to the non-slip condition applied to the sandbox bottom at -0.3 m rather than porous sands.

5.4.4 Analytical Model

Research has been conducted on flow fields in the presence of vegetation in open channels based on various approaches, such as the logarithmic law (also known as the law of the wall) and the boundary layer method. As observed in the velocity profiles, turbulence forms within the vegetation zone, but in the zone above the vegetation patch under the ice cover, the streamwise velocity profiles resemble those of a pipe flow once the flow is fully developed (Figure 5.11).

Since the streamwise velocity shows the most drastic variations, the following discussion targets the streamwise velocity vector ($\mathbf{u}$) above the vegetation zone under ice-covered flow conditions, assuming the flow becomes mildly disturbed. The derivation of the analytical model for the flow field in the presence of a vegetation patch in the deep pool bed under an ice cover begins with applying the fundamental Navier-Stokes equations for incompressible flow, which describe the conservation of momentum. These equations can be expressed as:

$$\rho\left(\frac{\partial \mathbf{u}}{\partial t} + \mathbf{u}\cdot\nabla\mathbf{u}\right) = -\nabla p + \mu\nabla^2\mathbf{u} + \mathbf{f}_{vegetation} + \mathbf{f}_{ice} \tag{5.16}$$

where p is the pressure, ρ is the fluid density, μ is the dynamic viscosity, $\mathbf{f}_{vegetation}$ represents the drag force caused by vegetation, and $\mathbf{f}_{ice}$ represents the boundary effects due to the ice cover. To simplify the problem, assuming the flow reaches a steady state, where $\partial\mathbf{u}/\partial t = 0$, and the water is incompressible, implying $\nabla \cdot \mathbf{u} = 0$. The vegetation drag is a significant factor in this model, as it acts as a resistive force proportional to the square of the flow velocity. This drag force can be modeled using the following equation:

$$\mathbf{f}_{vegetation} = -\frac{1}{2} C_D \rho A_V \mathbf{u} |\mathbf{u}| \tag{5.17}$$

where C_D is the drag coefficient, and A_v represents the frontal area of the vegetation per unit volume. Additionally, the effect of the ice cover is incorporated through a boundary condition that assumes a no-slip condition at the ice-water interface, i.e., the flow velocity at the ice boundary (at depth $z = h$) is zero.

Potential flow conditions are assumed to solve for the flow field, where the flow is irrotational, allowing the introduction of a stream function ψ such that $\mathbf{u} = \nabla\psi$. This assumption leads to the Laplace equation for the stream function, $\nabla^2\psi = 0$, which serves as the basis for incorporating the effects of both vegetation and ice cover into the model. The influence of the ice cover is modeled as an exponential decay in velocity with depth, while the spatial variation of the flow field is represented using a cosine function. The resulting expression for the velocity field is derived using *RStudio* based on data collected from the vegetated pool in the upstream sandbox:

$$\mathbf{u}(x, y, z) = U_0 \exp\left(-\alpha \frac{z}{H}\right) \cos\left(\frac{2\pi x}{L}\right) \cos\left(\frac{2\pi y}{B}\right) \tag{5.18}$$

where U_0 is a characteristic velocity, α is a decay coefficient that captures the suppressive effect of the ice cover on the flow, L is the characteristic streamwise length scale of the deep pool section, and B is the width of the pool zone. The origin (0, 0, 0) of the coordinate system is set at the midpoint of the last cross-section of the entrance section of the pool (Figure 5.2). Finally, the vegetation drag force is incorporated as a loss term in the momentum equation, leading to the final form of the model:

$$\mathbf{u}(x,y,z) = U_0 \exp\left(-\alpha \frac{z}{H}\right) \cos\left(\frac{2\pi x}{L}\right) \cos\left(\frac{2\pi y}{B}\right) - \frac{1}{2} C_D \rho A_V \mathbf{u}|\mathbf{u}| \quad (5.19)$$

Since the derived equation targets the flow above the vegetation zone, the distance from the pool bed (z) is always greater than h. Equation (5.19) is further modified by introducing some non-dimensional variables: u/U_0 and A_v/A, let $\alpha = k \cdot n_i/n_b$, and $C_D = m \cdot h/H$, where A is the cross-sectional area where the vegetation is situated, n_i and n_b are the Manning roughness coefficient of the ice cover and the channel bed respectively, h is the vegetation height, k and m are empirical constants influenced by pool geometry and vegetation patch layouts such as entry and exit slopes and vegetation density. Then, Equation (5.19) is modified as follows:

$$\frac{u}{U_0} = \exp\left(-k \frac{n_i}{n_b} \frac{z}{H}\right) \cos\left(\frac{2\pi x}{L}\right) \cos\left(\frac{2\pi y}{B}\right) - \frac{m \rho A_V U_0}{2A} \frac{h}{H} \frac{u}{U_0} \left|\frac{u}{U_0}\right| \quad (5.20)$$

defining a non-dimensional parameter β:

$$\beta = \frac{m \rho A_V U_0}{2A} \quad (5.21)$$

then Equation (5.20) can be written as

$$\frac{u}{U_0} = \exp\left(-k \frac{n_i}{n_b} \frac{z}{H}\right) \cos\left(\frac{2\pi x}{L}\right) \cos\left(\frac{2\pi y}{B}\right) - \beta \frac{h}{H} \frac{u}{U_0} \left|\frac{u}{U_0}\right| \quad (5.22)$$

The non-dimensional term, u/U_0, is present on both sides of Equation (5.22), suggesting that u/U_0 is influenced by a function that includes u/U_0 as an input. Therefore, solving for u/U_0 requires iterative methods. This equation does not apply to open channels, as the profile I the upper region no longer resembles pipe flows.

Using all ADV measured results from experiments in the pool in the upstream sandbox, k and m are determined as 0.56 and -0.017. The ADV-measured streamwise velocities in the pool in the downstream sandbox are used to verify the derived equation. As shown in Figure 20, the experimental results are compared to those calculated using Equation (5.22). The results showed that the experimental results align well with the analytical solution with $R^2 = 0.876$, indicating that Equation (5.22) can effectively simulate the streamwise velocity distribution above the submerged vegetation in the pool center section under ice-covered flow conditions.

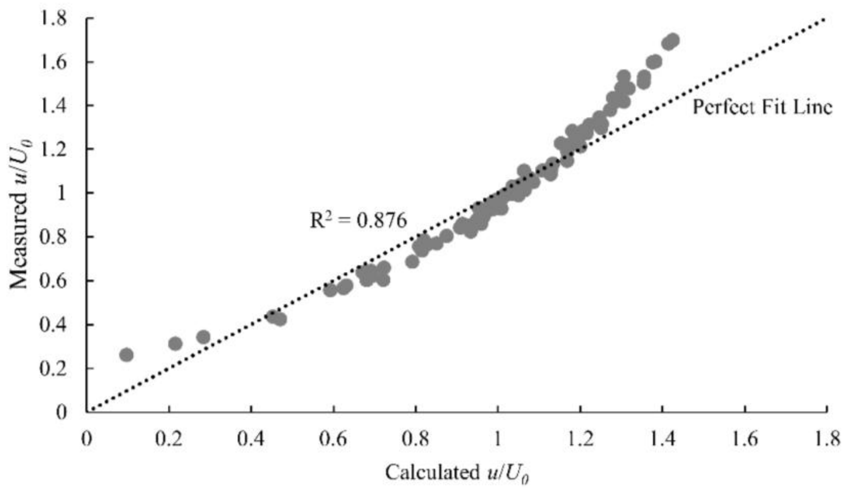

Figure 5.20 Comparison of measured velocity values (u/U_0) to calculation using Equation (5.22).

5.5 Chapter Summary

In this chapter, laboratory experiments have been conducted in a large-scale outdoor flume considering different water surface conditions, different submergence heights of vegetation, pool features, and hydraulic conditions to investigate the effects of leafless vegetation on flow velocity, turbulent kinetic energy, and secondary flow variations. A numerical simulation model of the 3D flow field in pools with submerged vegetation in the pool bed has been conducted using Flow3D software. The focus was on the impact of the pool bed vegetation on the pool section's hydrodynamic characteristics under ice-covered flow conditions. The comparison of measured velocity values (u/U_0) to those of calculation using the derived equation exhibits good agreement, indicating that the Flow-3D model can accurately replicate the flow characteristics of the flow in the vegetated pool under ice-covered flow conditions. The following conclusions can be drawn from this study:

1) Vegetation on the pool bed significantly alters flow distribution, particularly redirecting the main flow towards the water surface. As submerged vegetation height increases (or the submergence ratio decreases), flow velocity within the vegetated zone decreases while velocity above the vegetation increases, particularly under ice-covered conditions. Under ice-covered flow conditions, velocity profiles exhibit two distinct patterns: a pronounced variation within the vegetation zone, dominated by the drag caused by the pool bed and vegetation, and a mild fluctuation above the vegetation top under ice cover, where the maximum velocity is observed in this zone. The velocity profile in the non-vegetated slope sections of the pool adheres to the conventional logarithmic law, regardless of the presence of vegetation in the deep pool section. However, vegetation on the pool bed alters flow distribution, redirecting the main flow towards the water surface.
2) The entrance section of the pool, where the cross-section expands, plays a critical role in shaping the flow and turbulence patterns within the vegetated pool. Results show that, in the presence of vegetation in the deep pool section, high velocities are concentrated in the deep pool section near the entrance slope. In contrast, lower velocities and increased turbulence intensities are observed near the pool bed, particularly upstream of the pool near the entrance section.
3) The presence of vegetation in the pool bed leads to increased streamwise TKE value within the pool. Under the same water depth, as inflow rates increase, although the velocity across

the pool section rises, the TKE shows slight variation within the vegetation zone but significantly increases at the top of the vegetation. The presence of vegetation in the pool section increases streamwise TKE value. An ice cover on the water surface reduces the TKE value near the vegetation patch in the pool section. However, it increases near the end of the deep pool section, and more pronounced fluctuations of the TKE value are observed under rough ice-cover flow conditions.

4) An analytical model has been developed to account for the impact of vegetation and ice cover on the streamwise velocity in the vegetated pool section. This model incorporates potential flow assumptions and a stream function to simulate velocity distribution considering the presence of both vegetation in the pool bed and ice cover on the water surface. The proposed equation, solved iteratively to address non-dimensional variables, models vegetation drag as a loss term in the momentum equation. Validation against the measured streamwise velocities in the vegetated pool in the downstream sandbox showed strong alignment with experimental results ($R^2 = 0.876$), demonstrating the model's effectiveness in simulating streamwise velocity distribution in the flow above the submerged vegetation under ice cover, with potential applications for predicting flow behavior in similar environments.

The use of rigid cylinders to simulate vegetation in flume experiments, though typical for controlled and replicable results, can lead to deviations from natural conditions. Unlike the uniform layout pattern of vegetation elements used in this study, natural vegetation varies in stem diameter, flexibility, and spatial distribution, critically influencing flow dynamics, turbulence, and sediment transport. The staggered configuration of vegetation elements used in this study can create preferential flow paths, which are unrepresentative of the random distribution found in nature, potentially skewing drag force and turbulence estimates. While laboratory experiments and computer simulations offer valuable insights, their applicability to real-world scenarios requires cautious interpretation. More sophisticated models that incorporate the natural variability of vegetation are essential for accurate predictions of flow behavior in vegetated pools.

6. CHAPTER SIX: GENERAL CONCLUSIONS

This research, through comprehensive experimental studies conducted in a large-scale flume and Flow-3D numerical simulation, provides an in-depth understanding of the complex interactions between submerged spur dikes, submerged vegetation, and flow dynamics under various conditions, including ice-covered and open-channel scenarios. The studies revealed that both spur dikes' orientation and submergence levels and the morphology and arrangement of submerged vegetation influence flow patterns, including velocity distributions, Turbulence Kinetic Energy (TKE), bed deformation, and scouring processes. Notably, the presence of ice cover further amplified the complexity of these interactions by altering flow structures and intensifying local scouring around the spur dikes. The results indicate that the flow dynamics notably differ between the open channel and ice-covered conditions. Reynolds shear stress and turbulent events are more pronounced under ice cover, leading to more severe scouring around the spur dikes. These findings provide critical insights into the design and implementation of hydraulic structures in cold regions, contributing to enhanced river management and engineering practices.

6.1 Synthesis

Chapter 3 investigates the local scour dynamics around submerged angled spur dikes under ice cover. The research focuses on the effects of dike orientation and submergence levels on flow patterns, including velocity distributions and Reynolds shear stress, under various ice-covered conditions. The study reveals that ice cover alters the flow structure around spur dikes, leading to more pronounced scouring and sediment transport than open channel conditions.

The findings provide insights into the complex interactions between hydraulic structures and ice cover, emphasizing the need for careful consideration in the design of spur dikes in cold regions.

Chapter 4 builds upon the previous chapter by examining the turbulent flow around submerged angled spur dikes under ice cover. This chapter delves into the detailed analysis of flow velocity fields and turbulence characteristics, including identifying transverse flow regions and recirculation zones induced by spur dikes. The quadrant analysis of turbulent events reveals that ice cover amplifies the intensity of ejection and sweep events near the dike tip, leading to increased turbulence and sediment mobilization. These results contribute to a deeper understanding of how submerged spur dikes influence flow dynamics in ice-covered rivers, with implications for flood management and sediment control.

Chapter 5 focuses on the hydrodynamic characteristics within pools containing leafless vegetation under ice cover, representing a regional disturbance for the flow field rather than a local disturbance such as spur dikes. The study explores how vegetation and ice cover interaction affect flow velocity profiles and turbulence generation within pool structures. The presence of vegetation mitigates flow velocity and enhances sediment deposition, while the ice cover further modifies the flow patterns, leading to unique hydrodynamic conditions. This research highlights the possible role of vegetation in riverbank restoration projects and controlling sediment transport, particularly in cold climates where ice cover is a significant factor.

These chapters comprehensively analyze the interactions between submerged hydraulic structures, vegetation, and ice cover, offering valuable insights for river engineering and management in cold regions. Collected data supporting these findings are provided in the appendices, offering a detailed account of the experimental conditions and results across the different flow scenarios.

6.2 Conclusions of Chapter Three

1) This study demonstrates that submerged angled spur dikes' orientation and submergence level influence local scour patterns under ice-covered conditions. The findings reveal that as the angle of the spur dike increases beyond 90°, the extent of scour around the dike decreases, highlighting the critical role of dike alignment in controlling sediment transport and erosion. The ice cover intensifies the scouring process, particularly at higher submergence levels, by altering the flow velocity and turbulence around the dike, underscoring the importance of considering ice cover in designing and placing hydraulic structures in cold regions.
2) The analysis showed that the Froude number (Fr) is critical in determining the severity of local scour. Higher Froude numbers, indicative of more turbulent flow conditions, correspond to increased scour depths around the dikes. The study also found that the submergence ratio (S), which reflects the extent to which the dike is submerged, inversely affects the scour depth. As the submergence ratio increases, the scour depth decreases, suggesting that higher submergence provides some protection against scouring.
3) A modified empirical equation was proposed in this study to predict the maximum scour depth around submerged angled spur dikes. This equation incorporates the hydraulic radius (R_h) and other relevant factors, such as the roughness of the channel cover and the

overtopping ratio. The equation was validated against experimental data, accurately predicting scour depths under various conditions. This new model offers a valuable tool for engineers to estimate scour depths more reliably in environments with ice cover.

4) This research provides crucial insights into the interaction between submerged spur dikes and ice-covered flow conditions. The study's findings are particularly relevant for designing and constructing hydraulic structures in cold regions, where ice cover can significantly alter flow dynamics and exacerbate scouring. By incorporating the factors identified in this research, engineers can better predict and mitigate the risks associated with local scour, leading to more resilient infrastructure in these challenging environments.

6.3 Conclusions of Chapter Four

1) This study comprehensively analyzes the turbulent flow structure around submerged angled spur dikes under various ice cover conditions, focusing on the effects of dike orientation and submergence levels. The findings reveal that dike alignment angles greater than 90°reduce streamwise velocity components near the dike, with a notable increase in velocity magnitude observed at the dike tip, especially under ice-covered conditions. The presence of ice cover, particularly rough ice, amplifies turbulence intensity and alters the velocity field, pushing the maximum velocity closer to the channel bed.

2) The research demonstrates that the formation of transverse flow regions and recirculation zones downstream of the dike is heavily influenced by the dike's orientation and the nature of the ice cover. Quadrant analysis indicates that both ejection and sweep events dominate turbulent interactions near the dike tip under ice-covered conditions, contrasting with open

channel conditions where sweep events are more prevalent. These findings highlight the significant impact of ice cover on flow dynamics around submerged spur dikes, emphasizing the need for careful consideration of ice cover characteristics in hydraulic structure design.

3) The study presents a detailed examination of Reynolds shear stress (RSS) distribution, showing that RSS values are higher under ice-covered conditions, particularly with rough ice cover, compared to open-channel conditions. The RSS variation is more pronounced downstream of the dike due to the recirculation wake zone formed by flow separation. The results underscore the importance of considering both dike orientation and ice cover roughness in predicting and managing turbulent flow around submerged spur dikes.

4) Overall, this research advances the understanding of flow dynamics in cold regions, providing valuable insights for designing and managing hydraulic structures in ice-affected rivers. Future work should explore the broader implications of these findings in natural river systems and consider further integrating advanced measurement techniques and numerical simulations to refine the understanding of turbulent flow around submerged structures.

6.4 Conclusions of Chapter Five

1) This study has shown that submerged rigid leafless vegetation alters pool flow structure, particularly under ice-covered conditions. The presence of vegetation in the pool bed transforms the vertical distribution of flow velocity from a logarithmic shape to a quasi-S shape within the vegetated zone. The results indicate that vegetation height and

arrangement play a crucial role in redirecting flow towards the water surface, with increased vegetation height leading to greater velocity near the water surface and reduced flow within the vegetated zone. This reconfiguration of flow dynamics highlights the importance of vegetation in modulating flow characteristics, especially in cold regions where ice cover is present.

2) The research also demonstrated that vegetation and ice cover interactions affect the pool's turbulent kinetic energy (TKE) distribution. Under ice-covered flow conditions, TKE values exhibit distinct peaks near the vegetation tops and the ice-water interface, forming a mirrored "C" shape profile. The study found that the roughness of the ice cover further amplifies turbulence near the pool bed and the water surface, contributing to more pronounced variations in TKE compared to open channel conditions. These findings are critical for understanding the complex flow-vegetation interactions in ice-covered rivers and designing more effective flood control and river restoration strategies.

3) The study successfully used experimental data to validate the numerical simulation model FLOW-3D, demonstrating the model's effectiveness in replicating flow characteristics in vegetated pools under ice-covered conditions. The simulation results closely aligned with the experimental measurements, particularly in capturing variations in streamwise velocity and TKE across different vegetation heights and water surface conditions. This validation highlights the potential of numerical models to predict flow behavior in complex environments, offering a valuable tool for river management and ecological protection efforts.

4) An analytical model was developed to simulate the streamwise velocity distribution above

the vegetation zone under ice-covered conditions. This model incorporates the effects of both vegetation drag and ice cover on the flow field, offering a practical approach for predicting velocity profiles in vegetated pools. The model strongly agreed with the experimental results, indicating its potential applicability in real-world scenarios where vegetation and the influence of ice cover on flow dynamics.

5) The research highlights the limitations of using rigid cylinders to simulate vegetation in flume experiments, noting that natural vegetation's variability in stem diameter, flexibility, and spatial distribution can lead to different flow dynamics. The staggered configuration of vegetation elements used in this study may only represent special cases in nature, suggesting the need for more sophisticated models that account for the natural variability of vegetation in future studies.

6.5 Significance of This Study

This section synthesizes the contributions of the conclusions discussed in the previous chapters and their broader applications. The findings from these studies offer valuable insights into river management, particularly in cold regions where ice cover and hydraulic structures play a critical role.

The research demonstrates the impacts of submerged angled spur dikes on flow dynamics, scour formation, and turbulence under ice-covered conditions. The inverse relationship between the spur dikes' alignment angle and the scour's depth suggests that strategically orienting these structures can effectively mitigate erosion and protect riverbanks. This insight is valuable and relevant for river managers and engineers designing hydraulic structures to withstand the challenges of ice cover and high-flow conditions. By optimizing the orientation and submergence levels of spur dikes, the erosive potential of high-velocity flows can be reduced, thereby minimizing damage to adjacent infrastructure and enhancing riverbank stability.

The studies also highlight the role of vegetation in modulating flow characteristics within pools, particularly under ice-covered scenarios. The transformation of flow velocity profiles from a logarithmic to a quasi-S shape within vegetated zones underscores the importance of vegetation in creating favorable habitats for aquatic organisms. By incorporating vegetation into river restoration projects, river managers can enhance sediment retention, reduce flow velocities, and promote the formation of sheltered zones that serve as refuges for fish and other aquatic species. The ability of vegetation to modify turbulent kinetic energy profiles further emphasizes its potential to improve water quality and stabilize riverbeds by limiting sediment resuspension.

Moreover, the findings regarding the effects of rough ice cover on scour formation around both vegetation and spur dikes provide critical guidance for managing river systems in cold climates. The increased scour depths associated with rough ice cover conditions highlight the need for careful consideration of ice cover roughness when designing and implementing river management strategies. Protective measures, such as reinforcing vulnerable sections of the riverbed and selecting vegetation and dike configurations that minimize turbulence, can mitigate the adverse effects of ice cover on river morphology.

The development of numerical models further strengthens the applicability of these findings. These models offer a reliable tool for predicting flow behavior and optimizing the design of aquatic habitat restoration projects, such as vegetation replantation and introduction of wood debris, for building diverse habitat environments. Simulating complex interactions between vegetation, ice cover, and channel bed under varying conditions enhances the precision of river management interventions, contributing to more resilient and sustainable river ecosystems.

In conclusion, the research comprehensively explains the interplay between hydraulic structures, vegetation, and ice cover in shaping river dynamics. The practical applications of these findings offer river managers and engineers the tools and knowledge necessary to design more effective and ecologically sound river management strategies, particularly in cold regions where ice cover significantly influences river behavior.

6.6 Limitation of the Current Study

The experimental studies and numerical simulations conducted in this research were subject to several limitations despite efforts to minimize their impact. When interpreting the results and applying the findings to real-world scenarios, these limitations should be considered.

One notable limitation arises from the ice cover conditions simulated in the experiments. The study utilized Styrofoam panels to mimic smooth and rough ice cover, which, while useful for controlled experimentation, may only partially replicate the complexities of natural ice covers in rivers. The roughness of natural ice can vary significantly, and this variability may influence flow and scour patterns in ways not fully captured by the experimental setup.

Additionally, the experimental setup itself posed certain constraints. The flume’s slope and the fixed distance between the sandboxes introduced consistent variations in water depth that may have influenced the flow and turbulence measurements. Additionally, using an Acoustic Doppler Velocimeter (ADV) for velocity measurements had its limitations, particularly in regions close to the water surface and near the channel bed, where signal interference and noise can affect data accuracy.

Another limitation involves using rigid cylinders to model vegetation in the numerical simulations. Although these provided consistency and repeatability, they fall short in representing the natural variability of vegetation, such as differing stem flexibility, diameters, and spatial distributions, potentially leading to deviations from actual flow dynamics and sediment transport.

Moreover, the numerical simulations relied on the FLOW-3D software, which, although effective in replicating flow characteristics, involves certain assumptions and simplifications inherent to computational fluid dynamics models. For example, the RNG k-ε turbulence model used in the simulations may not fully resolve all scales of turbulence, particularly in complex flow conditions involving vegetation and ice cover. The model's inability to account for plant deformation under flow conditions further limits its accuracy in representing the dynamic interactions between flow and flexible vegetation.

Finally, the study's scope was constrained by the controlled laboratory conditions and experimental scale. While these conditions facilitate simplified analysis and reproducibility, they do not entirely capture the intricacies of natural river systems, where diverse sediment sizes, fluctuating water levels, and heterogeneous vegetation significantly influence flow dynamics.

These limitations highlight the need for further research incorporating more diverse and flexible vegetation models, advanced turbulence models, and field studies to validate and expand upon the findings. Such efforts would enhance the applicability of the results to natural river systems and improve the accuracy of predictions in river management and restoration projects.

6.7 Future Directions

6.7.1. Specialized Research in River Ice Hydraulics

Building on the conclusions of this thesis, several avenues for future research are proposed:

1) Advanced Study of Spur Dike Configurations: Future research could explore the effects of varied spur dike configurations, such as multiple dike systems and their interactions under different ice cover conditions. Investigating the impact of dike spacing, alignment variations, and the use of flexible materials could provide a deeper understanding of how to optimize dike design for effective erosion control and flow management. Additionally, studies could focus on the long-term effects of spur dikes in natural rivers, considering factors like sediment deposition, channel migration, and ice dynamics over multiple seasons.

2) Further Integration with Numerical Simulations: Building upon the findings of this thesis, future work could focus on integrating the experimental data with advanced numerical simulations. Enhancing the accuracy of computational models like OpenFOAM and FLUENT by incorporating more complex turbulence models or simulating the interaction between spur dikes and varying ice roughness conditions could improve flow behavior and scour pattern predictions. Such models could also be used to simulate scenarios not

easily replicated in laboratory settings, such as the effects of extreme weather events on spur dike performance.

3) Field Validation and Long-Term Monitoring: While this thesis utilized controlled laboratory experiments, field studies in natural rivers with existing spur dikes under ice cover would provide valuable validation of the experimental results. Long-term monitoring of these sites could offer insights into the real-world performance of spur dikes, including their impact on local ecology, sediment transport, and river morphology over time.
4) Interaction Between Spur Dikes and Vegetation: Further investigation could explore the synergistic effects of spur dikes and submerged vegetation. Understanding how the interactions between these two elements influence flow patterns, sediment deposition, and erosion under ice-covered conditions could inform more holistic river management strategies. For example, research could examine the potential of using vegetation to enhance the stability and effectiveness of spur dikes in river systems.
5) Vegetation Dynamics and Flexibility: While this thesis focused on rigid, leafless vegetation, future research could examine the dynamics of flexible vegetation, including how it responds to varying flow conditions and ice cover. Studies could investigate phenomena such as monami (the oscillatory motion of plants in water) and how vegetation growth and seasonal changes influence flow dynamics and sediment transport. This could lead to a better understanding of utilizing natural vegetation in river management and restoration projects.
6) Climate Change Impacts: As climate change alters river environments, future research

should investigate how changes in temperature, ice cover duration, and flow regimes affect the interaction between spur dikes, vegetation, and river dynamics. Understanding these impacts will be crucial for adapting river management practices to changing environmental conditions.

6.7.2 Interdisciplinary River Science

The intersection of river hydraulics with stream ecology and fluvial geomorphology continues to attract significant academic interest, particularly in understanding how channel obstructions like spur dikes and vegetated pools influence flow dynamics, sediment transport, and habitat formation. While these disciplines have traditionally operated in specialized silos, addressing similar issues from different perspectives, the need for interdisciplinary collaboration is increasingly recognized as essential for achieving more comprehensive solutions.

Spur dikes and vegetated pools play critical roles in shaping river morphology and improving aquatic habitats. Spur dikes, for instance, create stable pools and tributary regions that offer refuge for aquatic organisms and enhance habitat diversity. Meanwhile, vegetated pools modulate flow velocity and sediment deposition, contributing to the stability of riverbanks and the health of aquatic ecosystems. Despite these benefits, research in these areas remains discipline-specific, limiting the potential for cross-disciplinary innovation.

Future research must embrace interdisciplinary frameworks integrating hydraulic, ecological, and geomorphological perspectives to advance understanding of these complex interactions. Such collaboration will improve the design and implementation of river management strategies and foster sustainable relationships between human activities and natural systems. By bridging the gaps between disciplines, researchers can develop more effective solutions for river restoration and conservation, benefiting both the scientific community and the environment.

BIBLIOGRAPHY

Abdolahpour, M., Ghisalberti, M., Mcmahon, K., & Lavery, P. (2020). *Material Residence Time in Marine Canopies Under Wave-Driven Flows*.

Abeysingha, N., Singh, M., Sehgal, V., Khanna, M., Pathak, D. S., Jayakody, P., & Srinivasan, R. (2015). Assessment of water yield and evapotranspiration over 1985 to 2010 in the Gomti River basin in India using the SWAT model. *Current Science*, *108*, 25–2015.

Abid, A. (2020). *Analytical and numerical models for velocity profile in vegetated open-channel flows*. https://doi.org/10.13140/RG.2.2.35075.07207

Ackermann, N. L., Shen, H. T., & Olsson, p. (2002). Local Scour Around Circular Piers Under Ice Covers. *Proceedings of the 16th IAHR International Symposium on Ice*. 16th IAHR International Symposium on Ice, Dunedin. https://www.iahr.org/library/infor?pid=19865

Afzalimehr, H., & Rennie, C. D. (2009). Determination of bed shear stress in gravel-bed rivers using boundary-layer parameters. *Hydrological Sciences Journal*, *54*(1), 147–159. https://doi.org/10.1623/hysj.54.1.147

Ahmad, M. (1953). *Experiments On Design And Behavior Of Spur Dikes*. https://www.semanticscholar.org/paper/Experiments-On-Design-And-Behavior-Of-Spur-Dikes-Ahmad/e9abf616e32a1a4b551ac1a6661bc9c77e948196#citing-papers

Alasadi, L., Alabedi, T., & Abdulabbas Hassan, F. (2023). Experimental investigation for the local scour around V-shaped spur-dikes. *Scientific Review Engineering and Environmental Studies (SREES)*, *32*, 69–86. https://doi.org/10.22630/srees.4506

Alireza, K., Mehdi, V., & James, B. (2010). Experimental Study of the Effects of Submerged Dikes on the Energy and Momentum Coefficients in Compound Channel. *Engineering*, *2010*. https://doi.org/10.4236/eng.2010.211108

Allan, J. D. (2004). Landscapes and Riverscapes: The Influence of Land Use on Stream Ecosystems. *Annu. Rev. Ecol. Evol. Syst*, *35*, 257–284. https://doi.org/10.1146/annurev.ecolsys.35.120202.110122

Allan, J. D., Castillo, M. M., & Capps, K. A. (2021). Fluvial Geomorphology. In J. D. Allan, M. M. Castillo, & K. A. Capps (Eds.), *Stream Ecology: Structure and Function of Running Waters* (pp. 45–73). Springer International Publishing. https://doi.org/10.1007/978-3-030-61286-3_3

Apsilidis, N., Diplas, P., Dancey, C., Vlachos, P., & Raben, S. (2010). Local Scour at Bridge Piers: The Role of Reynolds Number on Horseshoe Vortex Dynamics. In *Geotechnical Special Publication* (p. 94). https://doi.org/10.1061/41147(392)7

Aydogdu, M. (2023). Analysis of the effect of rigid vegetation patches on the hydraulics of an open channel flow with Realizable k-ε and Reynolds stress turbulence models. *Flow Measurement and Instrumentation*, *94*, 102477. https://doi.org/10.1016/j.flowmeasinst.2023.102477

Bahrami-Yarahmadi, M., Pagliara, S., Yabarehpour, E., & Najafi, N. (2020). Study of Scour and Flow Patterns around Triangular-Shaped Spur Dikes. *KSCE Journal of Civil Engineering*, *24*(11), 3279–3288. https://doi.org/10.1007/s12205-020-2261-x

Barahimi, M., & Sui, J. (2023). Effects of Submerged Vegetation Arrangement Patterns and Density on Flow Structure. *Water*, *15*(1), Article 1. https://doi.org/10.3390/w15010176

Barahimi, M., & Sui, J. (2024a). Deformation of vegetated channel bed under ice-covered flow conditions. *Journal of Hydrology*, *636*, 131280. https://doi.org/10.1016/j.jhydrol.2024.131280

Barahimi, M., & Sui, J. (2024b). Flow structure and shear stress in the presence of both ice cover on water surface and leafless vegetation in channel bed. *Journal of Hydrodynamics*, *36*(2), 340–354. https://doi.org/10.1007/s42241-024-0021-y

Barbhuiya, A. K., & Dey, S. (2004). Measurement of turbulent flow field at a vertical semicircular cylinder attached to the sidewall of a rectangular channel. *Flow Measurement and Instrumentation*, *15*(2), 87–96. https://doi.org/10.1016/j.flowmeasinst.2003.11.002

BC Ministry of Agriculture and Lands. (2006). *Winter Considerations—Ice formation, freezing index and frost penetration* (Fact Sheet 590.307-1; Livestock Watering, p. 4). BC Ministry of Agriculture and Lands.

Beechie, T. J., Liermann, M., Beamer, E. M., & Henderson, R. (2005). A Classification of Habitat Types in a Large River and Their Use by Juvenile Salmonids. *Transactions of the American Fisheries Society*, *134*(3), 717–729. https://doi.org/10.1577/T04-062.1

Beltaos, S. (2008). Progress in the study and management of river ice jams. *Cold Regions Science and Technology*, *51*(1), 2–19. https://doi.org/10.1016/j.coldregions.2007.09.001

Beltaos, S., & Bonsal, B. (2021). Climate change impacts on Peace River ice thickness and implications to ice-jam flooding of Peace-Athabasca Delta, Canada. *Cold Regions Science and Technology*, *186*, 103279. https://doi.org/10.1016/j.coldregions.2021.103279

Bisson, P. A., Sullivan, K., & Nielsen, J. L. (1988). Channel Hydraulics, Habitat Use, and Body Form of Juvenile Coho Salmon, Steelhead, and Cutthroat Trout in Streams. *Transactions of the American Fisheries Society*, *117*(3), 262–273. https://doi.org/10.1577/1548-8659(1988)117<0262:CHHUAB>2.3.CO;2

Blanckaert, K., Duarte, A., & Schleiss, A. J. (2010). Influence of shallowness, bank inclination and bank roughness on the variability of flow patterns and boundary shear stress due to secondary currents in straight open-channels. *Advances in Water Resources*, *33*(9), 1062–1074.

https://doi.org/10.1016/j.advwatres.2010.06.012

Boulange, J., Hanasaki, N., Yamazaki, D., & Pokhrel, Y. (2021). Role of dams in reducing global flood exposure under climate change. *Nature Communications*, *12*(1), 417. https://doi.org/10.1038/s41467-020-20704-0

Bouma, T. J., De Vries, M. B., Low, E., Peralta, G., Tánczos, I. C., van de Koppel, J., & Herman, P. M. J. (2005). Trade-Offs Related to Ecosystem Engineering: A Case Study on Stiffness of Emerging Macrophytes. *Ecology*, *86*(8), 2187–2199. https://doi.org/10.1890/04-1588

Briganti, R., Musumeci, R. E., Bellotti, G., Brocchini, M., & Foti, E. (2004). Boussinesq modeling of breaking waves: Description of turbulence. *Journal of Geophysical Research: Oceans*, *109*(C7). https://doi.org/10.1029/2003JC002065

Brookes, A. (1987). River channel adjustments downstream from channelization works in England and Wales. *Earth Surface Processes and Landforms*, *12*(4), 337–351. https://doi.org/10.1002/esp.3290120402

Brunner, G. (2016). *HEC-RAS River Analysis System User's Manual Version 5.0.4* (Computer Program Documentation 0704–0188). Institute for Water Resource.

Buffington, J. M., Montgomery, D. R., & Greenberg, H. M. (2004). Basin-scale availability of salmonid spawning gravel as influenced by channel type and hydraulic roughness in mountain catchments. *Canadian Journal of Fisheries and Aquatic Sciences*, *61*(11), 2085–2096. https://doi.org/10.1139/f04-141

Calderon, M. S., & An, K.-G. (2016). An influence of mesohabitat structures (pool, riffle, and run) and land-use pattern on the index of biological integrity in the Geum River watershed. *Journal of Ecology and Environment*, *40*(1), 13. https://doi.org/10.1186/s41610-016-0018-8

Carling, P. A. (1991). An appraisal of the velocity-reversal hypothesis for stable pool-riffle sequences in the river severn, England. *Earth Surface Processes and Landforms*, *16*(1), 19–31. https://doi.org/10.1002/esp.3290160104

Carollo, F., Ferro, V., & Termini, D. (2002). Flow Velocity Measurements in Vegetated Channels. *Journal of Hydraulic Engineering-Asce - J HYDRAUL ENG-ASCE*, *128*. https://doi.org/10.1061/(ASCE)0733-9429(2002)128:7(664)

Caroppi, G., Västilä, K., Gualtieri, P., Järvelä, J., Giugni, M., & Rowiński, P. M. (2021). Comparison of Flexible and Rigid Vegetation Induced Shear Layers in Partly Vegetated Channels. *Water Resources Research*, *57*(3), e2020WR028243. https://doi.org/10.1029/2020WR028243

Carr, M. L., & Tuthill, A. M. (2012). Modeling of Scour-Inducing Ice Effects at Melvin Price Lock and Dam. *Journal of Hydraulic Engineering*, *138*(1), 85–92. https://doi.org/10.1061/(ASCE)HY.1943-

7900.0000483

Çengel, Y. A., & Cimbala, J. M. (2014). Chapter Eight: Internal Flow. In *Fluid Mechanics: Fundamentals and Applications* (3rd ed., pp. 347–437). McGraw-Hill Education. https://www.mheducation.ca/fluid-mechanics-fundamentals-and-applications-9781259696534-can-group

Chabert, J., & Engelrndinger, P. (1956). *Etude des affouillements autourdes piles de ponts [Study of scour around bridge piers]*. LaboratoriesNational d'Hydraulique.

Chanson, H. (2004). Physical Modelling of Hydraulics. In *Hydraulics of Open Channel Flow: An Introduction Basic Principles, Sediment Motion, Hydraulic Modelling, Design of Hydraulic Structures* (2nd ed., pp. 253–274). https://www.sciencedirect.com/book/9780750659789/hydraulics-of-open-channel-flow

Chen, W., & Olden, J. D. (2017). Designing flows to resolve human and environmental water needs in a dam-regulated river. *Nature Communications*, *8*(1), 2158. https://doi.org/10.1038/s41467-017-02226-4

Chen, Y.-C., Kao, S.-P., Lin, J.-Y., & Yang, H.-C. (2009). Retardance coefficient of vegetated channels estimated by the Froude number. *Ecological Engineering*, *35*(7), 1027–1035. https://doi.org/10.1016/j.ecoleng.2009.03.002

Chen, Z., Zheng, X., & Shen, L. (2019, January 1). *Numerical Study on Influence of Oriented Groin Angle on Hydraulic Characteristics of Curved Water Flow*. https://doi.org/10.2991/masta-19.2019.40

Chipongo, K., Khiadani, M., & Sookhak Lari, K. (2020). Comparison and verification of turbulence Reynolds-averaged Navier–Stokes closures to model spatially varied flows. *Scientific Reports*, *10*(1), 19059. https://doi.org/10.1038/s41598-020-76128-9

Conde-Frias, M., Ghisalberti, M., Lowe, R. J., Abdolahpour, M., & Etminan, V. (2023). The Near-Bed Flow Structure and Bed Shear Stresses Within Emergent Vegetation. *Water Resources Research*, *59*(4), e2022WR032499. https://doi.org/10.1029/2022WR032499

Cui, H., Felder, S., & Kramer, M. (2023). Predicting flow resistance in open-channel flows with submerged vegetation. *Environmental Fluid Mechanics*, *23*(4), 757–778. https://doi.org/10.1007/s10652-023-09929-x

Cui, J., & Neary, V. (2008). LES study of turbulent flows with submerged vegetation. *Journal of Hydraulic Research - J HYDRAUL RES*, *46*, 307–316. https://doi.org/10.3826/jhr.2008.3129

Cunha, D., & Veiga, L. (1970). Discussion of "Local Scour Around Bridge Piers." *Journal of the Hydraulics Division*, *96*(8), 1742–1747. https://doi.org/10.1061/JYCEAJ.0002655 de Almeida, G. A. M., & Rodríguez, J. F. (2011). Understanding pool-riffle dynamics through continuous morphological simulations. *Water Resources Research*, *47*(1). https://doi.org/10.1029/2010WR009170

de Lima, P. H. S., Janzen, J. G., & Nepf, H. M. (2015). Flow patterns around two neighboring patches of emergent vegetation and possible implications for deposition and vegetation growth. *Environmental Fluid Mechanics*, *15*(4), 881–898. https://doi.org/10.1007/s10652-015-9395-2

Dehrashid, F. A., Heidari, M., Rahimi, H., Khoshkonesh, A., Yuan, S., Tang, X., Lu, C., & Wang, X. (2023). CFD modeling the flow dynamics in an open channel with double-layered vegetation. *Modeling Earth Systems and Environment*, *9*(1), 543–555. https://doi.org/10.1007/s40808-022-01513-4

Dey, S., & Barbhuiya, A. K. (2005). Time Variation of Scour at Abutments. *Journal of Hydraulic Engineering*, *131*(1), 11–23. https://doi.org/10.1061/(ASCE)0733-9429(2005)131:1(11)

Dietrich, W. E., & Whiting, P. (1989). Boundary Shear Stress and Sediment Transport in River Meanders of Sand and Gravel. In *River Meandering* (pp. 1–50). American Geophysical Union (AGU). https://doi.org/10.1029/WM012p0001

Du, S., Wu, G., Zhu, D. Z., Wang, R., Lu, Y., & Liang, B. (2022). Experimental study of local scour around submerged square piles in combined waves and current. *Ocean Engineering*, *266*, 113176. https://doi.org/10.1016/j.oceaneng.2022.113176

Duró, G., Crosato, A., Kleinhans, M. G., Roelvink, D., & Uijttewaal, W. S. J. (2020). Bank Erosion Processes in Regulated Navigable Rivers. *Journal of Geophysical Research: Earth Surface*, *125*(7), e2019JF005441. https://doi.org/10.1029/2019JF005441

Ebersole, J. L., Liss, W. J., & Frissell, C. A. (2003). Cold Water Patches in Warm Streams: Physicochemical Characteristics and the Influence of Shading. *JAWRA Journal of the American Water Resources Association*, *39*(2), 355–368. https://doi.org/10.1111/j.1752-1688.2003.tb04390.x

El-Hakim, O., & Salama, M. M. (1992). Velocity Distribution Inside and Above Branched Flexible Roughness. *Journal of Irrigation and Drainage Engineering*, *118*(6), 914–927. https://doi.org/10.1061/(ASCE)0733-9437(1992)118:6(914)

Environment Canada. (2013, February 27). *Avadepth*. https://www2.pac.dfo-mpo.gc.ca/index-eng.html

Eraky, O. M., Eltoukhy, M. A. R., Abdelmoaty, M. S., & Farouk, E. (2022). Effect of rigid, bank vegetation on velocity distribution and water surface profile in open channel. *Water Practice and Technology*, *17*(7), 1445–1457. https://doi.org/10.2166/wpt.2022.068

Errico, A., Lama, G. F. C., Francalanci, S., Chirico, G. B., Solari, L., & Preti, F. (2019). Flow dynamics and turbulence patterns in a drainage channel colonized by common reed (*Phragmites australis*) under different scenarios of vegetation management. *Ecological Engineering*, *133*, 39–52.

https://doi.org/10.1016/j.ecoleng.2019.04.016

Ettema, R., Melville, B. W., & Barkdoll, B. (1998). Scale Effect in Pier-Scour Experiments. *Journal of Hydraulic Engineering*, *124*(6), 639–642. https://doi.org/10.1061/(ASCE)0733-9429(1998)124:6(639)

Farhadi, A., Mayrhofer, A., Tritthart, M., Glas, M., & Habersack, H. (2018). Accuracy and comparison of standard k-ϵ with two variants of k-ω turbulence models in fluvial applications. *Engineering Applications of Computational Fluid Mechanics*, *12*(1), 216–235. https://doi.org/10.1080/19942060.2017.1393006

Farshad, R., Kashefipour, S. M., Ghomeshi, M., & Oliveto, G. (2022). Temporal Scour Variations at Permeable and Angled Spur Dikes under Steady and Unsteady Flows. *Water*, *14*(20), Article 20. https://doi.org/10.3390/w14203310

Feddersen, F., & Williams, A. J. (2007). Direct Estimation of the Reynolds Stress Vertical Structure in the Nearshore. *Journal of Atmospheric and Oceanic Technology*, *24*(1), 102–116. https://doi.org/10.1175/JTECH1953.1

Federal Highway Administration. (2001). *Evaluating Scour at Bridges* (FHWA-NHI-01-001; Hydraulic Engineering Circular No. 18). Federal Highway Administration.

Finotello, A., Ielpi, A., Lapôtre, M. G. A., Lazarus, E. D., Ghinassi, M., Carniello, L., Favaro, S., Tognin, D., & D'Alpaos, A. (2024). Vegetation enhances curvature-driven dynamics in meandering rivers. *Nature Communications*, *15*(1), 1968. https://doi.org/10.1038/s41467-024-46292-x

Flow Science, Inc. (2023). *FLOW-3D® Version 2023R1 Users Manual*. Flow Science, Inc. https://www.flow3d.com/

Froehlich, D. C. (1989). *Local scour at bridge abutments*. 13–18. https://pubs.er.usgs.gov/publication/70015379

Froehlich, D. C. (1991). Analysis of onsite measurements of scour at piers. *Proceedings of the ASCE National Hydraulic Engineering Conference*. https://www.usgs.gov/publications/analysis-onsite-measurements-scour-piers

Fu, H., Wang, D., Li, W., Ren, B., & Yang, K. (2021). Velocity and turbulence characteristics in an open channel with multi-row staggered vegetation patches. *Journal of Hydrodynamics*, *33*(5), 1035–1044. https://doi.org/10.1007/s42241-021-0091-z

Fuller, J. (2018). *Defining Ordinary and Natural Conditions for State Navigability Determinations*.

Gadissa, E. (2017). Estimation of Open Channel Roughness by using Gradual Varied Flow Profiles. *Civil Engineering Research Journal*, *1*(1). https://doi.org/10.19080/CERJ.2017.01.555552

Gazi, A. H., & Afzal, M. S. (2020). A review on hydrodynamics of horseshoe vortex at a vertical cylinder mounted on a flat bed and its implication to scour at a cylinder. *Acta Geophysica*, *68*(3), 861–875. https://doi.org/10.1007/s11600-020-00439-8

Giglou, A. N., Mccorquodale, J. A., & Solari, L. (2018). Numerical study on the effect of the spur dikes on sedimentation pattern. *Ain Shams Engineering Journal*, *9*(4), 2057–2066. https://doi.org/10.1016/j.asej.2017.02.007

Goring, D. G., & Nikora, V. I. (2002). Despiking Acoustic Doppler Velocimeter Data. *Journal of Hydraulic Engineering*, *128*(1), 117–126. https://doi.org/10.1061/(ASCE)0733-9429(2002)128:1(117)

Gray, W., & Miller, C. (2023). On the equations of open channel flow. *Journal of Hydraulic Research*, *61*(1), 1–17. https://doi.org/10.1080/00221686.2022.2106597

Gretler, W., & Meile, W. (1997). Calculation of plane turbulent Couette-Poiseuille flows with a modified *k*-ε model. *Fluid Dynamics Research*, *21*(4), 263–283. https://doi.org/10.1016/S0169-5983(97)00012-9

Guan, D., Xie, Y., Yao, Z., Chiew, Y.-M., Zhang, J., & Zheng, J. (2022). Local scour at offshore windfarm monopile foundations: A review. *Water Science and Engineering*, *15*(1), 29–39. https://doi.org/10.1016/j.wse.2021.12.006

Gul, H., Ijaz, N., Vanicek, I., Rehman, Z. ur, Ijaz, Z., Hassan, G. Z., & Rahim, S. A. (2024). State-of-the-art review on stability and serviceability of dikes as a flood infrastructure and their comprehensive assessment in Indus Plain considering global climate change. *Natural Hazards*. https://doi.org/10.1007/s11069-024-06836-2

Gurnell, A. M., Bertoldi, W., & Corenblit, D. (2012). Changing river channels: The roles of hydrological processes, plants and pioneer fluvial landforms in humid temperate, mixed load, gravel bed rivers. *Earth-Science Reviews*, *111*(1), 129–141. https://doi.org/10.1016/j.earscirev.2011.11.005

Hains, D. B., & Zabilansky, L. J. (2012). *Scour under Ice: Potential Contributing Factor in the Schoharie Creek Bridge Collapse*. 1–9. https://doi.org/10.1061/40836(210)17

Hains, D., & Zabilansky, L. (2004). *Laboratory Test of Scour Under Ice: Data and Preliminary Results* (ERDC/CRREL TR-04-9; p. 182). U.S Army Engineer Research and Development Center, Cold Regions Research and Engineering Laboratory.

Hains, M. D. B., & Zabilansky, L. (2005). *The Effects of River Ice on Scour and Sediment Transport*. 13th Workshop on the Hydraulics of Ice Covered Rivers, Hanover, NH.

Halket, I. H., & Snelgrove, K. R. (2012). *Implications of Pool and Riffle Sequences for Water Quality Modeling*. 1–12. https://doi.org/10.1061/40763(178)61

Han, D., Xiong, J., Xie, X., & Lin, Y. (2021). Effects of emergent and submerged rigid vegetation configurations on gravity current dynamics. *Environmental Fluid Mechanics*, *21*(5), 1165–1187. https://doi.org/10.1007/s10652-021-09814-5

HAN, X., Lin, P., & Parker, G. (2019). *3D NUMERICAL STUDY ON LOCAL SCOUR AROUND SPUR DIKES WITH DIFFERENT LAYOUT ANGLES* (p. 1594). https://doi.org/10.3850/38WC092019-0394

Han, X., Lin, P., & Parker, G. (2022). Influence of layout angles on river flow and local scour in grouped spur dikes field. *Journal of Hydrology*, *614*, 128502. https://doi.org/10.1016/j.jhydrol.2022.128502

Hao, S., Xia, Y., Xu, H., & Wen, Y.-C. (2013). *Review of local scour around submerged spur-dike*.

Harrison, L. R., Legleiter, C. J., Wydzga, M. A., & Dunne, T. (2011). Channel dynamics and habitat development in a meandering, gravel bed river. *Water Resources Research*, *47*(4). https://doi.org/10.1029/2009WR008926

Hei, P., Chen, Z., & Ding, X. (2009). Sediment Carrying Capacity of Open Channel Flow Around Spur Dike. In C. Zhang & H. Tang (Eds.), *Advances in Water Resources and Hydraulic Engineering* (pp. 928–932). Springer. https://doi.org/10.1007/978-3-540-89465-0_163

Heller, V. (2011). Scale effects in physical hydraulic engineering models. *Journal of Hydraulic Research*, *49*(3), 293–306. https://doi.org/10.1080/00221686.2011.578914

Hirt, C. W., & Nichols, B. D. (1981). Volume of fluid (VOF) method for the dynamics of free boundaries. *Journal of Computational Physics*, *39*(1), 201–225. https://doi.org/10.1016/0021-9991(81)90145-5

Hong, V., Zhang, G., Wang, X., & Li, A. (2019). Experimental Investigation on the Shape and Depth of Local Scour Hole Downstream of the Release Structure. *World Journal of Engineering and Technology*, *8*(1), Article 1. https://doi.org/10.4236/wjet.2020.81010

Horvat, Z., Isic, M., & Spasojevic, M. (2015). Two dimensional river flow and sediment transport model. *Environmental Fluid Mechanics*, *15*(3), 595–625. https://doi.org/10.1007/s10652-014-9375-y

Hsieh, P.-C., & Shiu, Y.-S. (2006). Analytical solutions for water flow passing over a vegetal area. *Advances in Water Resources*, *29*(9), 1257–1266. https://doi.org/10.1016/j.advwatres.2005.10.004

Hu, H., Wang, J., Cheng, T., Hou, Z., & Sui, J. (2022). Channel Bed Deformation and Ice Jam Evolution around Bridge Piers. *Water*, *14*(11), Article 11. https://doi.org/10.3390/w14111766

Huai, W., Zhang, J., Katul, G. G., Cheng, Y., Tang, X., & Wang, W. (2019). The structure of turbulent flow through submerged flexible vegetation. *Journal of Hydrodynamics*, *31*(2), 274–292. https://doi.org/10.1007/s42241-019-0023-3

Huang, H., Zhang, H., Zhong, D., & Zhang, Y. J. (2019). Turbulent mechanisms in open channel sediment-laden flows. *International Journal of Sediment Research*, *34*(6), 550–563. https://doi.org/10.1016/j.ijsrc.2019.06.002

Huang, T., Lu, Y., & Liu, H. (2019). Effects of Spur Dikes on Water Flow Diversity and Fish Aggregation. *Water*, *11*(9), Article 9. https://doi.org/10.3390/w11091822

Jafari, R., & Sui, J. (2021). Velocity Field and Turbulence Structure around Spur Dikes with Different Angles of Orientation under Ice Covered Flow Conditions. *Water*, *13*(13), Article 13. https://doi.org/10.3390/w13131844

Jafari, R., & Sui, J. (2024). Channel deformation around non-submerged spur dikes with different alignment angles under ice cover. *Journal of Hydrology and Hydromechanics*, *72*. https://doi.org/10.2478/johh-2024-0014

Jansen, P. P. (1979). *Principles of River Engineering: The Non-tidal Alluvial River*. Pitman.

Jing, S., Yang, W., & Chen, Y. (2019). Smooth Open Channel with Increasing Aspect Ratio: Influence on Secondary Flow. *Water*, *11*(9), Article 9. https://doi.org/10.3390/w11091872

Jing, S. (景思雨), Duan, Y. (段炎冲), & Li, D. (李丹勋). (2023). A quantitative study on the turbulent kinetic energy redistribution in the near free-water-surface region of open channel flows. *AIP Advances*, *13*(3), 035129. https://doi.org/10.1063/5.0138423

John, C. K., Pu, J. H., Guo, Y., Hanmaiahgari, P. R., & Pandey, M. (2023). Flow turbulence presented by different vegetation spacing sizes within a submerged vegetation patch. *Journal of Hydrodynamics*, *35*(6), 1131–1145. https://doi.org/10.1007/s42241-024-0083-x

Jordanova, A. A., & James, C. S. (2003). Experimental Study of Bed Load Transport through Emergent Vegetation. *Journal of Hydraulic Engineering*, *129*(6), 474. https://doi.org/10.1061/(ASCE)0733-9429(2003)129:6(474)

Julien, P. Y. (2018). Steady Flow in Rivers. In *River Mechanics* (2nd ed., pp. 116–152). Cambridge University Press. https://doi.org/10.1017/9781316107072

Kang, D. G., Na, H., & Lee, C. Y. (2019). Detached eddy simulation of turbulent and thermal mixing in a T-junction. *Annals of Nuclear Energy*, *124*, 245–256. https://doi.org/10.1016/j.anucene.2018.10.006

Karadimou, D. P., Markatos, N.-C., Karadimou, D. P., & Markatos, N.-C. (2018). Study of the Numerical Diffusion in Computational Calculations. In *Numerical Simulations in Engineering and Science*. IntechOpen. https://doi.org/10.5772/intechopen.75660

Keshavarzi, A., Shrestha, C. K., Zahedani, M. R., Ball, J., & Khabbaz, H. (2018). Experimental study of flow structure around two in-line bridge piers. *Proceedings of the Institution of Civil Engineers -*

Water Management, *171*(6), 311–327. https://doi.org/10.1680/jwama.16.00104

Khan, M., Muzzammil, M., & Alam, J. (2016). *Bridge Pier Scour: A review of mechanism, causes and geotechnical aspects*.

Khanarmuei, M., Akutina, Y., Dupuis, V., Eiff, O., Trevisson, M., Suara, K., & Brown, R. (2020, August 27). *Secondary Currents in Smooth Wall Open-Channel Flow*.

Kim, S.-C., Friedrichs, C. T., Maa, J. P.-Y., & Wright, L. D. (2000). Estimating Bottom Stress in Tidal Boundary Layer from Acoustic Doppler Velocimeter Data. *Journal of Hydraulic Engineering*, *126*(6), 399–406. https://doi.org/10.1061/(ASCE)0733-9429(2000)126:6(399)

Kline, S. J., Reynolds, W. C., Schraub, F. A., & Runstadler, P. W. (1967). The structure of turbulent boundary layers. *Journal of Fluid Mechanics*, *30*(4), 741–773. https://doi.org/10.1017/S0022112067001740

Knight, D. W., & Macdonald, J. A. (1979). Open Channel Flow with Varying Bed Roughness. *Journal of the Hydraulics Division*, *105*(9), 1167–1183. https://doi.org/10.1061/JYCEAJ.0005274

Koftis, T., & Prinos, P. (2018). Reynolds stress modelling of flow in compound channels with vegetated floodplains. *Journal of Applied Water Engineering and Research*, *6*(1), 17–27. https://doi.org/10.1080/23249676.2016.1209437

Kohyama, K. (神山 一貴), Sano, M. (佐野 雅己), & Tsukahara, T. (塚原 隆裕). (2022). Sidewall effect on turbulent band in subcritical transition of high-aspect-ratio duct flow. *Physics of Fluids*, *34*(8), 084112. https://doi.org/10.1063/5.0096626

Koken, M., & Constantinescu, G. (2008a). An investigation of the flow and scour mechanisms around isolated spur dikes in a shallow open channel: 1. Conditions corresponding to the initiation of the erosion and deposition process. *Water Resources Research*, *44*(8). https://doi.org/10.1029/2007WR006489

Koken, M., & Constantinescu, G. (2008b). An investigation of the flow and scour mechanisms around isolated spur dikes in a shallow open channel: 2. Conditions corresponding to the final stages of the erosion and deposition process. *Water Resources Research - WATER RESOUR RES*, *44*. https://doi.org/10.1029/2007WR006491

Koken, M., & Constantinescu, G. (2021). Flow structure inside and around a rectangular array of rigid emerged cylinders located at the sidewall of an open channel. *Journal of Fluid Mechanics*, *910*, A2. https://doi.org/10.1017/jfm.2020.900

Koken, M., & Gogus, M. (2015). Effect of spur dike length on the horseshoe vortex system and the bed shear stress distribution. *Journal of Hydraulic Research*, *53*(2), 196–206. https://doi.org/10.1080/00221686.2014.967819

Kondolf, G. M. (1997). PROFILE: Hungry Water: Effects of Dams and Gravel Mining on River Channels. *Environmental Management*, *21*(4), 533–551. https://doi.org/10.1007/s002679900048

Kondziolka, J. M., & Nepf, H. M. (2014). Vegetation wakes and wake interaction shaping aquatic landscape evolution. *Limnology and Oceanography: Fluids and Environments*, *4*(1), 106–119. https://doi.org/10.1215/21573689-2846314

Kothyari, U. C., & Ranga Raju, K. G. (2001). Scour around spur dikes and bridge abutments. *Journal of Hydraulic Research*, *39*(4), 367–374. https://doi.org/10.1080/00221680109499841

Kouwen, N., Unny, T. E., & Hill, H. M. (1969). Flow Retardance in Vegetated Channels. *Journal of the Irrigation and Drainage Division*, *95*(2), 329–342. https://doi.org/10.1061/JRCEA4.0000652

Kuhnle, R. A., Alonso, C. V., & Shields, F. D. (2002). Local Scour Associated with Angled Spur Dikes. *Journal of Hydraulic Engineering*, *128*(12), 1087–1093. https://doi.org/10.1061/(ASCE)0733-9429(2002)128:12(1087)

Kuhnle, R. A., Jia, Y., & Alonso, C. V. (2008). Measured and Simulated Flow near a Submerged Spur Dike. *Journal of Hydraulic Engineering*, *134*(7), 916–924. https://doi.org/10.1061/(ASCE)0733-9429(2008)134:7(916)

Kumar, A., & Ojha, C. S. P. (2021). Review on the Field Applications of River Training Structures for River Bank Protection. In M. S. Chauhan & C. S. P. Ojha (Eds.), *The Ganga River Basin: A Hydrometeorological Approach* (pp. 115–133). Springer International Publishing. https://doi.org/10.1007/978-3-030-60869-9_8

Kumar, P., Kumar, A., & Sharma, A. (2024). Numerical modeling of turbulent flow interactions with vegetation in channels with fixed beds. *Modeling Earth Systems and Environment*, *10*(3), 4337–4360. https://doi.org/10.1007/s40808-024-02025-z

Lama, G. F. C., Errico, A., Francalanci, S., Solari, L., Preti, F., & Chirico, G. B. (2020). Evaluation of Flow Resistance Models Based on Field Experiments in a Partly Vegetated Reclamation Channel. *Geosciences (Switzerland)*, *10*, 47. https://doi.org/10.3390/geosciences10020047

Laursen, E. M. (1963). An Analysis of Relief Bridge Scour. *Journal of the Hydraulics Division*, *89*(3), 93–118. https://doi.org/10.1061/JYCEAJ.0000896

Le Minor, M., Zimmer, M., Helfer, V., Gillis, L. G., & Huhn, K. (2021). Chapter 4—Flow and sediment dynamics around structures in mangrove ecosystems—A modeling perspective. In F. Sidik & D. A. Friess (Eds.), *Dynamic Sedimentary Environments of Mangrove Coasts* (pp. 83–120). Elsevier. https://doi.org/10.1016/B978-0-12-816437-2.00012-4

Lee, H. C., & Wahab, A. K. A. (2019). Performance of different turbulence models in predicting flow kinematics around an open offshore intake. *SN Applied Sciences*, *1*(10), 1266.

https://doi.org/10.1007/s42452-019-1320-8

Lee, S. O., & Sturm, T. W. (2009). Effect of Sediment Size Scaling on Physical Modeling of Bridge Pier Scour. *Journal of Hydraulic Engineering*, *135*(10), 793–802. https://doi.org/10.1061/(ASCE)HY.1943-7900.0000091

Lei, Y., Hassan, M. A., Viparelli, E., Chartrand, S. M., An, C., Fu, X., & Hu, C. (2023). The Effect of Sediment Supply on Pool-Riffle Morphology. *Water Resources Research*, *59*(11), e2023WR035983. https://doi.org/10.1029/2023WR035983

Leopold, L. B., & Wolman, M. G. (1957). *River channel patterns: Braided, meandering, and straight* (USGS Numbered Series 282; Professional Paper). U.S. Geological Survey; USGS Publications Warehouse. 10.3133/pp282B

Li, C. W., & Yu, L. H. (2010). Hybrid LES/RANS modelling of free surface flow through vegetation. *Computers & Fluids*, *39*(9), 1722–1732. https://doi.org/10.1016/j.compfluid.2010.06.009

Li, G., Lang, L., & Ning, J. (2013). *3D Numerical Simulation of Flow and Local Scour around a Spur Dike*.

Li, G., Sui, J., Sediqi, S., & Dziedzic, M. (2023). Local scour around submerged angled spur dikes under ice cover. *International Journal of Sediment Research*. https://doi.org/10.1016/j.ijsrc.2023.08.003

Li, J., He, C., Huang, Q., & Li, L. (2024). Spatiotemporal dynamics of flood regulation service under the joint impacts of climate change and Urbanization: A case study in Baiyangdian Lake Basin, China. *Ecological Indicators*, *158*, 111318. https://doi.org/10.1016/j.ecolind.2023.111318

Li, S. S. (2012). Estimates of the Manning's coefficient for ice-covered rivers. *Proceedings of the Institution of Civil Engineers - Water Management*, *165*(9), 495–505. https://doi.org/10.1680/wama.11.00017

Li, Y.-H., Xie, L., & Su, T. (2018). Resistance of Open-Channel Flow under the Effect of Bending Deformation of Submerged Flexible Vegetation. *Journal of Hydraulic Engineering*, *144*(3), 04017072. https://doi.org/10.1061/(ASCE)HY.1943-7900.0001419

Li, Y.-T., Zhan, J.-M., & Wai, W.-H. O. (2024). A study of the effect of local scour on the flow field near the spur dike. *Theoretical and Applied Mechanics Letters*, *14*(2), 100510. https://doi.org/10.1016/j.taml.2024.100510

Liao, C.-T., Yeh, K.-C., & Huang, M.-W. (2014). Development and application of 2-D mobile-bed model with bedrock river evolution mechanism. *Journal of Hydro-Environment Research*, *8*(3), 210–222. https://doi.org/10.1016/j.jher.2013.03.001

Liao, C.-T., Yeh, K.-C., Lan, Y.-C., Jhong, R.-K., & Jia, Y. (2021). Improving the 2D Numerical Simulations on Local Scour Hole around Spur Dikes. *Water*, *13*(11), Article 11. https://doi.org/10.3390/w13111462

Lim, S.-Y. (1997). Equilibrium Clear-Water Scour around an Abutment. *Journal of Hydraulic Engineering*, *123*(3), 237–243. https://doi.org/10.1061/(ASCE)0733-9429(1997)123:3(237)

Lisle, T. (1986). Stabilization of a gravel channel by large streamside obstructions and bedrock bends, Jacoby Creek, northwestern California. *GSA Bulletin*, *97*(8), 999–1011.

Lisle, T. E., & Hilton, S. (1992). The Volume of Fine Sediment in Pools: An Index of Sediment Supply in Gravel-Bed Streams. *JAWRA Journal of the American Water Resources Association*, *28*(2), 371–383. https://doi.org/10.1111/j.1752-1688.1992.tb04003.x

Liu, D., Lv, S., & Li, C. (2024). Impact of Spur Dike Placement on Flow Dynamics in Curved River Channels: A CFD Study on Pick Angle and River-Width-Narrowing Rate. *Water*, *16*(16), Article 16. https://doi.org/10.3390/w16162236

Lodhi, A., Jain, R. K., & Sharma, P. (2015). Influence of cohesion on scour around submerged dike founded in clay–sand–gravel mixtures. *ISH Journal of Hydraulic Engineering*, *22*, 1–18. https://doi.org/10.1080/09715010.2015.1075916

Lou, S., Chen, M., Ma, G., Liu, S., & Wang, H. (2022). Sediment suspension affected by submerged rigid vegetation under waves, currents and combined wave–current flows. *Coastal Engineering*, *173*, 104082. https://doi.org/10.1016/j.coastaleng.2022.104082

Lu, S. S., & Willmarth, W. W. (1973). Measurements of the structure of the Reynolds stress in a turbulent boundary layer. *Journal of Fluid Mechanics*, *60*(3), 481–511. https://doi.org/10.1017/S0022112073000315

Lu, Y., Cheng, N., Wei, M., & Ancey, C. (2024, April 14). *Vegetation Submergence Effects on Bedload Transport Rate*. EGU General Assembly 2024, Vienna, Austria. https://doi.org/10.5194/egusphere-egu24-9559, 2024

Maji, S., Pal, D., Hanmaiahgari, P., & Gupta, U. (2017). Hydrodynamics and turbulence in emergent and sparsely vegetated open channel flow. *Environmental Fluid Mechanics*, *17*. https://doi.org/10.1007/s10652-017-9531-2

Masjedi, A., & Foroushani, E. (2012). Investigation of hydrodynamics on local scour by shape of single spur dike in river bend. *IOP Conference Series: Earth and Environmental Science*, *15*, 2025. https://doi.org/10.1088/1755-1315/15/5/052025

McCoy, A., Constantinescu, G., & Weber, L. (2007). A numerical investigation of coherent structures and mass exchange processes in channel flow with two lateral submerged groynes. *Water Resources Research*, *43*(5). https://doi.org/10.1029/2006WR005267

Melville, B. W. (1997). Pier and Abutment Scour: Integrated Approach. *Journal of Hydraulic Engineering*, *123*(2), 125–136. https://doi.org/10.1061/(ASCE)0733-9429(1997)123:2(125)

Melville, B. W., & Coleman, S. E. (2000). *Bridge Scour*. Water Resources Publications. https://www.wrpllc.com/books/bsr.html

Meng, X., Zhou, Y., Sun, Z., Ding, K., & Chong, L. (2021). Hydraulic Characteristics of Emerged Rigid and Submerged Flexible Vegetations in the Riparian Zone. *Water*, *13*, 1057. https://doi.org/10.3390/w13081057

Mia, M. F., & Nago, H. (2003). Design Method of Time-Dependent Local Scour at Circular Bridge Pier. *Journal of Hydraulic Engineering*, *129*(6), 420–427. https://doi.org/10.1061/(ASCE)0733-9429(2003)129:6(420)

Mironov, D., Terzhevik, A., Kirillin, G., Jonas, T., Malm, J., & Farmer, D. (2002). Radiatively driven convection in ice-covered lakes: Observations, scaling, and a mixed layer model. *Journal of Geophysical Research: Oceans*, *107*(C4), 7–1. https://doi.org/10.1029/2001JC000892

Mofrad, M., Parvizi, P., Afzalimehr, H., & Sui, J. (2023). Turbulence Kinetic Energy and High-Order Moments of Velocity Fluctuations of Flows in the Presence of Submerged Vegetation in Pools. *Water*, *15*, 2170. https://doi.org/10.3390/w15122170

Montgomery, D., Buffington, J., Smith, R., Schmidt, K., & Pess, G. (1995). Pool Spacing in Forest Channels. *Water Resources Research*, *31*(4), 1097–1105.

Mosselman, E. (2018). Modelling in Applied Hydraulics: More Accurate in Decision-Making Than in Science? In P. Gourbesville, J. Cunge, & G. Caignaert (Eds.), *Advances in Hydroinformatics* (pp. 741–749). Springer. https://doi.org/10.1007/978-981-10-7218-5_53

Mulahasan, S., Saleh, M. S., & Muhsun, S. S. (2023). Simulation of flow around a permeable dike using physical and 3D-CFD models. *International Journal of River Basin Management*, *21*(1), 53–65. https://doi.org/10.1080/15715124.2021.1901726

Munteanu, A. (2004). *Scouring around a cylindrical bridge pier under partially ice-covered flow condition* [University of Ottawa (Canada)]. http://hdl.handle.net/10393/26722

Nadaoka, K., & Yagi, H. (1998). Shallow-Water Turbulence Modeling and Horizontal Large-Eddy Computation of River Flow. *Journal of Hydraulic Engineering*, *124*(5), 493–500. https://doi.org/10.1061/(ASCE)0733-9429(1998)124:5(493)

Nagy, H. (2005). *Hydraulic evaluation of emerged and submerged spur-dikes: Temporal bed evolution and equilibrium state characteristics*. *44*.

Nakajima, T., Asaeda, T., Fujino, T., & Nanda, A. (2006). Leaf Litter Decomposition in Aquatic and Terrestrial Realms of a Second-Order Forested Stream System. *Journal of Freshwater Ecology*, *21*(2), 259–263. https://doi.org/10.1080/02705060.2006.9664994

Namaee, M. R., & Sui, J. (2019). Effects of Ice Cover on the Incipient Motion of Bed Material and Shear Stress around Side-by-Side Bridge Piers. *Cold Regions Science and Technology*, *165*(0). https://trid.trb.org/view/1632064

Namaee, M. R., & Sui, J. (2020). Velocity profiles and turbulence intensities around side-by-side bridge piers under ice-covered flow condition. *Journal of Hydrology and Hydromechanics*, *68*(1), 70–82. https://doi.org/10.2478/johh-2019-0029

Namaee, M. R., Sui, J., Wu, P., Namaee, M. R., Sui, J., & Wu, P. (2019). Experimental Study of Local Scour around Side-by-Side Bridge Piers under Ice-Covered Flow Conditions. In *Current Practice in Fluvial Geomorphology—Dynamics and Diversity*. IntechOpen. https://doi.org/10.5772/intechopen.86369

Namaee, M. R., Sui, J., Wu, Y., & Linklater, N. (2021). Three-dimensional numerical simulation of local scour around circular side-by-side bridge piers with ice cover. *Canadian Journal of Civil Engineering*, *48*(10), 1335–1353. https://doi.org/10.1139/cjce-2019-0360

Namaee, M., & Sui, J. (2020). Velocity profiles and turbulence intensities around side-by-side bridge piers under ice-covered flow condition. *Journal of Hydrology and Hydromechanics*, *68*, 70–82. https://doi.org/10.2478/johh-2019-0029

Namaee, M., Wu, P., & Dziedzic, M. (2023). Numerical Modeling of Local Scour in the Vicinity of Bridge Abutments When Covered with Ice. *Water*, *15*, 3330. https://doi.org/10.3390/w15193330

Nasrollahi, A., Ghodsian, M., & Salehi Neyshabouri, S. A. A. (2008). Local Scour at Permeable Spur Dikes. *Journal of Applied Sciences*, *8*. https://doi.org/10.3923/jas.2008.3398.3406

National Academies of Sciences, E. (2021). *Revised Clear-Water and Live-Bed Contraction Scour Analysis*. https://doi.org/10.17226/26198

Nepf, H. M. (1999). Drag, turbulence, and diffusion in flow through emergent vegetation. *Water Resources Research*, *35*(2), 479–489. https://doi.org/10.1029/1998WR900069

Nepf, H. M. (2012). Flow and Transport in Regions with Aquatic Vegetation. *Annual Review of Fluid Mechanics*, *44*(Volume 44, 2012), 123–142. https://doi.org/10.1146/annurev-fluid-120710-101048

Nepf, H., & Vivoni, E. (2000). Flow structure in depth-limited, vegetated flow. *Journal of Geophysical Research*, *105*, 28547–28558. https://doi.org/10.1029/2000JC900145

Neter, J., Wasserman, W., & Kutner, M. H. (1991). *Applied linear statistical models: Regression, analysis of variance, and experimental designs* (3rd ed.). Irwin.

Nezu, I., & Onitsuka, K. (2001). Turbulent structures in partly vegetated open-channel flows with LDA and PI V measurements. *Journal of Hydraulic Research*.

https://www.tandfonline.com/doi/abs/10.1080/00221686.2001.9628292

Nikora, V. (2010). Hydrodynamics of aquatic ecosystems: An interface between ecology, biomechanics and environmental fluid mechanics. *River Research and Applications*, *26*(4), 367–384. https://doi.org/10.1002/rra.1291

Ning, J., Li, G., & Li, S. (2019). Numerical Simulation of the Influence of Spur Dikes Spacing on Local Scour and Flow. *Applied Sciences*, *9*(11), Article 11. https://doi.org/10.3390/app9112306

Northwest Hydraulic Consultants. (2013). *Nechako River 2013 Sediment Transport Investigations*. Prepared for Ministry of Forests, Lands and Renewable Resources.

Nosrati, K., Afzalimehr, H., & Sui, J. (2022). Interaction of Irregular Distribution of Submerged Rigid Vegetation and Flow within a Straight Pool. *Water*, *14*(13), Article 13. https://doi.org/10.3390/w14132036

Nosrati, K., Afzalimehr, H., Sui, J., & Raeisifar, H. R. (2024). Characteristics of turbulent flow in 3-D pools in the presence of submerged rigid vegetation in channel bed. *Journal of Hydrodynamics*, *36*. https://doi.org/10.1007/s42241-024-0009-7

Oğuz, K., & Bor, A. (2022). Prediction of Local Scour around Bridge Piers Using Hierarchical Clustering and Adaptive Genetic Programming. *Applied Artificial Intelligence*, *36*(1), 2001734. https://doi.org/10.1080/08839514.2021.2001734

Okamoto, T., Nezu, I., & Ikeda, H. (2012). Vertical mass and momentum transport in open-channel flows with submerged vegetations. *Journal of Hydro-Environment Research*, *6*(4), 287–297. https://doi.org/10.1016/j.jher.2012.03.002

Oliveto, G., & Hager, W. H. (2002). Temporal Evolution of Clear-Water Pier and Abutment Scour. *Journal of Hydraulic Engineering*, *128*(9), 811–820. https://doi.org/10.1061/(ASCE)0733-9429(2002)128:9(811)

O'Neill, P. L., Nicolaides, D., Honnery, D., & Soria, J. (2004). Autocorrelation Functions and the Determination of Integral Length with Reference to Experimental and Numerical Data. *Proceeding of the 15th Australasian Fluid Mechanics Conference*, *1*.

Özyaman, C., Yerdelen, C., Eris, E., & Daneshfaraz, R. (2022). Experimental investigation of scouring around a single spur under clear water conditions. *Water Supply*, *22*(3), 3484–3497. https://doi.org/10.2166/ws.2021.389

Pan, D., & Li, Y. (2022). Tidal Bore Scour around a Spur Dike. *Journal of Marine Science and Engineering*, *10*(8), Article 8. https://doi.org/10.3390/jmse10081086

Pan, J., Guo, X., Shen, H., Wang, T., Fu, H., Yongxin, G., Li, J., & Chen, Y. (2023). Transverse flow distributions in ice-covered channels. *River*, *2*. https://doi.org/10.1002/rvr2.41

Pan, J., & Shen, H. T. (2022). Modeling ice cover effect on river channel bank stability. *Environmental Fluid Mechanics*, *22*(5), 1121–1133. https://doi.org/10.1007/s10652-022-09881-2

Pandey, M., Ahmad, Z., & Sharma, P. K. (2018). Scour around impermeable spur dikes: A review. *ISH Journal of Hydraulic Engineering*, *24*(1), 25–44. https://doi.org/10.1080/09715010.2017.1342571

Park, H., & Hwang, J. H. (2021). A Standard Criterion for Measuring Turbulence Quantities Using the Four-Receiver Acoustic Doppler Velocimetry. *Frontiers in Marine Science*, *8*. https://www.frontiersin.org/articles/10.3389/fmars.2021.681265

Patel, H., Arora, S., Lade, A., Kumar, B., & Azamathulla, H. (2022). Flow behavior concerning bank stability in the presence of spur dike- A review. *Water Science & Technology Water Supply*, *23*. https://doi.org/10.2166/ws.2022.418

Patel, H. K., Arora, S., Lade, A. D., Kumar, B., & Azamathulla, H. Md. (2022). Flow behaviour concerning bank stability in the presence of spur dike – A review. *Water Supply*, *23*(1), 237–258. https://doi.org/10.2166/ws.2022.418

Patel, H. kumar, & Kumar, B. (2024). Experimental study on the optimal spur dike shape under downward seepage. *Water Science*, *38*(1), 172–191. https://doi.org/10.1080/23570008.2024.2321423

Paul, M., Bouma, T., & Amos, C. (2012). Wave attenuation by submerged vegetation: Combining the effect of organism traits and tidal current. *Marine Ecology Progress Series*, *444*, 31–41. https://doi.org/10.3354/meps09489

Peña, E., & Anta, J. (2021). Editorial—Physical Modelling in Hydraulics Engineering. *Water*, *13*(17), Article 17. https://doi.org/10.3390/w13172317

Pfister, M., & Chanson, H. (2014). Two-phase air-water flows: Scale effects in physical modeling. *Journal of Hydrodynamics*, *26*(2), 291–298. https://doi.org/10.1016/S1001-6058(14)60032-9

Pizarro, A., Manfreda, S., & Tubaldi, E. (2020). The Science behind Scour at Bridge Foundations: A Review. *Water*, *12*(2), Article 2. https://doi.org/10.3390/w12020374

Prowse, T., & Culp, J. (2011). Ice breakup: A neglected factor in river ecology. *Canadian Journal of Civil Engineering*, *30*, 128–144. https://doi.org/10.1139/l02-040

Qi, H., Wang, J., Zou, W., Luo, W., Tian, W., & Li, J. (2024). Characteristics and mechanism of local scour reduction around spur dike using the collar in clear water. *Scientific Reports*, *14*(1), 12299. https://doi.org/10.1038/s41598-024-63131-7

Qiu, H., Li, P., Wang, W., Shi, P., Zhang, J., & Chen, H. (2024). Impacts of emergent rigid vegetation patches on flow characteristics of open channels. *Journal of Hydroinformatics*, jh2024009. https://doi.org/10.2166/hydro.2024.009

Rahimi, H., Fael, C. M. S., Taborda, C. S. B., Yuan, S., Tang, X., Singh, P. K., Fardoost, E., & Santos, C. A. V. (2023). Numerical Modelling of Turbulence Kinetic Energy in Open Channel Flows with Mixed-Layer Vegetation. *Water*, *15*(14), Article 14. https://doi.org/10.3390/w15142544

Rahimi, H. R., Tang, X., Singh, P., Li, M., & Alaghmand, S. (2020). Open channel flow within and above a layered vegetation: Experiments and first-order closure modeling. *Advances in Water Resources*, *137*, 103527. https://doi.org/10.1016/j.advwatres.2020.103527

Raudkivi, A. J., & Ettema, R. (1985). Scour at Cylindrical Bridge Piers in Armored Beds. *Journal of Hydraulic Engineering*, *111*(4), 713–731. https://doi.org/10.1061/(ASCE)0733-9429(1985)111:4(713)

Rehmel, M. (2007). Application of Acoustic Doppler Velocimeters for Streamflow Measurements. *Journal of Hydraulic Engineering*, *133*(12), 1433–1438. https://doi.org/10.1061/(ASCE)0733-9429(2007)133:12(1433)

Rezaie, A., Afzalimehr, H., Sohrabi, S., Nazari-Sharabian, M., Karakouzian, M., & Ahmadi, R. (2023). Reducing Scour around Semi-Elliptical Bridge Abutments: Application of Roughness Elements. *Fluids*, *8*(12), Article 12. https://doi.org/10.3390/fluids8120306

Richardson, E. V., & Simons, D. B. (1984). Use of Spurs and Guidebanks for Highway Crossings. *Transportation Research Record Number 950*, *2*, 184–193.

Richardson, E. V., Simons, D. B., & Julien, P. Y. (1990). *Highways in the River Environment* (Final Report August 1985 - November 1989 FHWA HI-90-016). Federal Highway Administration, U.S. Department of Transportation. https://www.fhwa.dot.gov/engineering/hydraulics/library_arc.cfm?pub_number=62&id=56

Richardson, E. V., Stevens, M. A., & Simons, D. B. (1975). The design of spurs for river training. *XVIth, IAHR Congress*, 382–388.

Rodríguez, J. F., García, C. M., & García, M. H. (2013). Three-dimensional flow in centered pool-riffle sequences. *Water Resources Research*, *49*(1), 202–215. https://doi.org/10.1029/2011WR011789

Rodríguez, J. F., & García, M. H. (2008). Laboratory measurements of 3-D flow patterns and turbulence in straight open channel with rough bed. *Journal of Hydraulic Research*, *46*(4), 454–465. https://doi.org/10.3826/jhr.2008.2994

Ruonan, B., Liekai, C., Xingkui, W., & Danxun, L. (2016). Comparison of ADV and PIV Measurements in Open Channel Flows. *Procedia Engineering*, *154*, 995–1001. https://doi.org/10.1016/j.proeng.2016.07.588

Sahu, S. N., Hossain, S., Sen, S., & Ghoshal, K. (2024). Sediment transport in ice-covered channel under non-equilibrium condition. *Environmental Earth Sciences*, *83*(10), 315. https://doi.org/10.1007/s12665-024-11642-x

Sanjou, M. (2016). Turbulence Diffusion Mechanism in Submerged Vegetation Flows. In *River Basin Management*. IntechOpen. https://doi.org/10.5772/63207

Sarkar, S. (2020). Large Eddy Simulation of Flows of Engineering Interest: A Review. In A. Runchal (Ed.), *50 Years of CFD in Engineering Sciences: A Commemorative Volume in Memory of D. Brian Spalding* (pp. 363–400). Springer. https://doi.org/10.1007/978-981-15-2670-1_11

Schwartz, J. S., Neff, K. J., Dworak, F. E., & Woockman, R. R. (2015). Restoring riffle-pool structure in an incised, straightened urban stream channel using an ecohydraulic modeling approach. *Ecological Engineering*, *78*, 112–126. https://doi.org/10.1016/j.ecoleng.2014.06.002

Schweiger, G., Nilsson, H., Schoeggl, J., Birk, W., & Posch, A. (2020). Modeling and simulation of large-scale systems: A systematic comparison of modeling paradigms. *Applied Mathematics and Computation*, *365*, 124713. https://doi.org/10.1016/j.amc.2019.124713

Sebilian Wittyngham, S., Moderan, J., & Boyer, K. E. (2019). Temperature and salinity effects on submerged aquatic vegetation traits and susceptibility to grazing. *Aquatic Botany*, *158*, 103119. https://doi.org/10.1016/j.aquabot.2019.05.004

Sediqi, S., Sui, J., Li, G., & Dziedzic, M. (2024). Characteristics of turbulent flow around bridge abutments in the presence of vegetation in channel bed under ice-covered flow conditions. *Cold Regions Science and Technology*, *221*, 104172. https://doi.org/10.1016/j.coldregions.2024.104172

Seo, D. C., & Wang, J. (2021). Canada's natural river and navigation regulation. *Volume 7: Polar and Arctic Sciences and Technology*, V007T07A011. https://doi.org/10.1115/OMAE2021-61419

Shahmohammadi, R., Afzalimehr, H., & Sui, J. (2021). Assessment of Critical Shear Stress and Threshold Velocity in Shallow Flow with Sand Particles. *Water*, *13*(7), Article 7. https://doi.org/10.3390/w13070994

Shahmohammadi, R., Afzalimehr, H., & Sui, J. (2022). Estimation of Bed Shear Stress in Shallow Transitional Flows under Condition of Incipient Motion of Sand Particles Using Turbulence Characteristics. *Water*, *14*(16), Article 16. https://doi.org/10.3390/w14162515

Shampa, Hasegawa, Y., Nakagawa, H., Takebayashi, H., & Kawaike, K. (2020). Three-Dimensional Flow Characteristics in Slit-Type Permeable Spur Dike Fields: Efficacy in Riverbank Protection. *Water*, *12*(4), Article 4. https://doi.org/10.3390/w12040964

Shan, Y., Liu, C., Luo, M., & Yang, K. (2016). A simple method for estimating bed shear stress in smooth and vegetated compound channels. *Journal of Hydrodynamics*, *28*(3), 497–505.

https://doi.org/10.1016/S1001-6058(16)60654-6

Shields, A. (1936). Application of similarity principles and turbulence research to bed-load movement. *CalTech Library*. https://repository.tudelft.nl/islandora/object/uuid%3Aa66ea380-ffa3-449b-b59f-38a35b2c6658

Shumilova, O. O., & Sukhodolov, A. N. (2023). Flow dynamics in rivers with riffle-pool morphology: A dataset from case studies and field experiments. *Scientific Data*, *10*(1), 494. https://doi.org/10.1038/s41597-023-02370-1

Sirianni, D. A. B., Valela, C., Rennie, C. D., Nistor, I., & Almansour, H. (2022). Effects of developing ice covers on bridge pier scour. *Journal of Hydraulic Research*, *60*(4), 645–655. https://doi.org/10.1080/00221686.2022.2041497

Smith, B. T., & Ettema, R. (1997). Flow Resistance in Ice-Covered Alluvial Channels. *Journal of Hydraulic Engineering*, *123*(7), 592–599. https://doi.org/10.1061/(ASCE)0733-9429(1997)123:7(592)

Smith, H. D., & Foster, D. L. (2005). Modeling of Flow Around a Cylinder Over a Scoured Bed. *Journal of Waterway, Port, Coastal, and Ocean Engineering*, *131*(1), 14–24. https://doi.org/10.1061/(ASCE)0733-950X(2005)131:1(14)

Smith, K., Cockburn, J. M. H., & Villard, P. V. (2023). Rivers under Ice: Evaluating Simulated Morphodynamics through a Riffle-Pool Sequence. *Water*, *15*(8), Article 8. https://doi.org/10.3390/w15081604

SonTek/YSI, Inc. (2001). *Acoustic Doppler Velocimeter Principles of Operation* (SonTek/YSI ADVField/Hydra Acoustic Doppler Velocimeter (Field) Technical Documentation, p. 6) [Technical Notes]. SonTek/YSI, Inc.

Souliotis, D., & Prinos, P. (2011). Effect of a vegetation patch on turbulent channel flow. *Journal of Hydraulic Research*, *49*(2), 157–167. https://doi.org/10.1080/00221686.2011.557258

Stephan, U., & Gutknecht, D. (2002). Hydraulic resistance of submerged flexible vegetation. *Journal of Hydrology*, *269*, 27–43. https://doi.org/10.1016/S0022-1694(02)00192-0

Stoesser, T., Salvador, G. P., Rodi, W., & Diplas, P. (2009). Large Eddy Simulation of Turbulent Flow Through Submerged Vegetation. *Transport in Porous Media*, *78*(3), 347–365. https://doi.org/10.1007/s11242-009-9371-8

Su, X. H., Li, C. W., & Chen, B. H. (2003). Three-dimensional large eddy simulation of free surface turbulent flow in open channel within submerged vegetation domain. *Journal of Hydrodynamics*, *15*(3), 35–43.

Sui, J. (2023). Fluvial Hydraulics Affected by River Ice and Hydraulic Structures. *Water*, *15*(7), Article 7.

https://doi.org/10.3390/w15071262

Sui, J., Faruque, M. A. A., & Balachandar, R. (2009). Local Scour Caused by Submerged Square Jets under Model Ice Cover. *Journal of Hydraulic Engineering*, *135*. https://doi.org/10.1061/(ASCE)0733-9429(2009)135:4(316)

Sui, J., Karney, B. W., & Fang, D. (2005). Variation in water level under ice-jammed condition – field investigation and experimental study. *Hydrology Research*, *36*(1), 65–84. https://doi.org/10.2166/nh.2005.0006

Sui, J., Karney, B. W., Sun, Z., & Wang, D. (2002). Field Investigation of Frazil Jam Evolution: A Case Study. *Journal of Hydraulic Engineering*, *128*(8), 781–787. https://doi.org/10.1061/(ASCE)0733-9429(2002)128:8(781)

Sui, J., Wang, J., He, Y., & Krol, F. (2010). Velocity profiles and incipient motion of frazil particles under ice cover. *International Journal of Sediment Research*, *25*(1), 39–51. https://doi.org/10.1016/S1001-6279(10)60026-1

Sun, X., & Sakai, M. (2015). Three-dimensional simulation of gas–solid–liquid flows using the DEM–VOF method. *Chemical Engineering Science*, *134*, 531–548. https://doi.org/10.1016/j.ces.2015.05.059

Tang, C., Yi, Y., & Zhang, S. (2023). Flow and turbulence in unevenly obstructed channels with rigid and flexible vegetation. *Journal of Environmental Management*, *326*, 116736. https://doi.org/10.1016/j.jenvman.2022.116736

Thompson, D. M. (2006). The role of vortex shedding in the scour of pools. *Advances in Water Resources*, *29*(2), 121–129. https://doi.org/10.1016/j.advwatres.2005.03.015

Tinoco, R. O., San Juan, J. E., & Mullarney, J. C. (2020). Simplification bias: Lessons from laboratory and field experiments on flow through aquatic vegetation. *Earth Surface Processes and Landforms*, *45*(1), 121–143. https://doi.org/10.1002/esp.4743

Toda, Y., Zhou, Y., & Sakai, N. (2020). Modeling of riparian vegetation dynamics and its application to sand-bed river. *Journal of Hydro-Environment Research*, *30*, 3–13. https://doi.org/10.1016/j.jher.2019.09.003

Trimble, S. W. (1997). Contribution of Stream Channel Erosion to Sediment Yield from an Urbanizing Watershed. *Science*, *278*(5342), 1442–1444. https://doi.org/10.1126/science.278.5342.1442

Turcotte, B., Morse, B., Bergeron, N. E., & Roy, A. G. (2011). Sediment transport in ice-affected rivers. *Journal of Hydrology*, *409*(1), 561–577. https://doi.org/10.1016/j.jhydrol.2011.08.009

Ulu, A. E., Aydin, M. C., & Önen, F. (2023). Energy Dissipation Potentials of Grouped Spur Dikes in an Open Channel. *Water Resources Management*, *37*(11), 4491–4506. https://doi.org/10.1007/s11269-

023-03571-4

USACE. (n.d.). *HEC-RAS Hydraulic Reference Manual*. USACE Hydrologic Engineering Center. Retrieved March 13, 2023, from https://www.hec.usace.army.mil/confluence/rasdocs/ras1dtechref/latest

USDA. (2021). *Conservation Practice Standard Vegetative Barrier (Code 601)* (601-CPS-1).

Vaghefi, M., Alavinezhad, M., & Akbari, M. (2016). The effect of submergence ratio on flow pattern around short T-head spur dike in a mild bend with rigid bed using numerical model. *Journal of the Chinese Institute of Engineers*, *39*(6), 666–674. https://doi.org/10.1080/02533839.2016.1187084

Valela, C., Sirianni, D. A. B., Nistor, I., Rennie, C. D., & Almansour, H. (2021). Bridge Pier Scour under Ice Cover. *Water*, *13*(4), Article 4. https://doi.org/10.3390/w13040536

Van Appledorn, M., Baker, M. E., & Miller, A. J. (2019). River-valley morphology, basin size, and flow-event magnitude interact to produce wide variation in flooding dynamics. *Ecosphere*, *10*(1), e02546. https://doi.org/10.1002/ecs2.2546

van Denderen, R. P., Kater, E., Jans, L. H., & Schielen, R. M. J. (2022). Disentangling changes in the river bed profile: The morphological impact of river interventions in a managed river. *Geomorphology*, *408*, 108244. https://doi.org/10.1016/j.geomorph.2022.108244

van der Mark, C. F., Blom, A., & Hulscher, S. J. M. H. (2008). Quantification of variability in bedform geometry. *Journal of Geophysical Research: Earth Surface*, *113*(F3). https://doi.org/10.1029/2007JF000940

Wahl, T. L. (2000). *Analyzing ADV Data Using WinADV*. 1–10. https://doi.org/10.1061/40517(2000)300

Wan Mohtar, W. H. M., Lee, J. W., Mohammad Azha, N. I., & Cheng, N.-S. (2020). Incipient sediment motion based on turbulent fluctuations. *International Journal of Sediment Research*, *35*(2), 125–133. https://doi.org/10.1016/j.ijsrc.2019.10.008

Wang, B., & Xu, Y. J. (2018). Decadal-Scale Riverbed Deformation and Sand Budget of the Last 500 km of the Mississippi River: Insights Into Natural and River Engineering Effects on a Large Alluvial River. *Journal of Geophysical Research: Earth Surface*, *123*(5), 874–890. https://doi.org/10.1029/2017JF004542

Wang, F., Huai, W., Guo, Y., & Liu, M. (2021). Turbulence Structure and Momentum Exchange in Compound Channel Flows With Shore Ice Covered on the Floodplains. *Water Resources Research*, *57*(4), e2020WR028621. https://doi.org/10.1029/2020WR028621

Wang, F., Huai, W., Liu, M., & Fu, X. (2020). Modeling depth-averaged streamwise velocity in straight trapezoidal compound channels with ice cover. *Journal of Hydrology*, *585*, 124336. https://doi.org/10.1016/j.jhydrol.2019.124336

Wang, J., He, G., Huang, L., Dey, S., & Fang, H. (2023). Effects of Submerged Flexible Vegetation on Scalar Transport in an Open-Channel Flow. *Water Resources Research*, *59*(9), e2022WR034235. https://doi.org/10.1029/2022WR034235

Wang, J., Sui, J., & Karney, B. W. (2008). Incipient Motion of Non-Cohesive Sediment under Ice Cover—An Experimental Study. *Journal of Hydrodynamics*, *20*(1), 117–124. https://doi.org/10.1016/S1001-6058(08)60036-0

Wang, Z., Zhang, H., Xu, W., Wang, H., & Huang, H. (2019). Effects of Emergent Vegetation Patterns on Flow Velocity, Turbulence, and Erosion Around River Banks. *Iranian Journal of Science and Technology, Transactions of Civil Engineering*, *43*(3), 509–519. https://doi.org/10.1007/s40996-018-0200-6

Watt, W. (2013). The national Flood Damage Reduction Program: 1976–1995. *Canadian Water Resources Journal / Revue Canadienne Des Ressources Hydriques*, *20*, 237–247. https://doi.org/10.4296/cwrj2004237

Wei, X., Lu, Y., Wang, Z., Liu, X., & Mo, S. (2018). A Machine Learning Approach to Evaluating the Damage Level of Tooth-Shape Spur Dikes. *Water*, *10*(11), Article 11. https://doi.org/10.3390/w10111680

Widén, Å., Malm Renöfält, B., Degerman, E., Wisaeus, D., & Jansson, R. (2022). Environmental Flow Scenarios for a Regulated River System: Projecting Catchment-Wide Ecosystem Benefits and Consequences for Hydroelectric Production. *Water Resources Research*, *58*(1), e2021WR030297. https://doi.org/10.1029/2021WR030297

Wilcox, A. C., & Wohl, E. E. (2006). Flow resistance dynamics in step-pool stream channels: 1. Large woody debris and controls on total resistance. *Water Resources Research*, *42*(5). https://doi.org/10.1029/2005WR004277

Wu, P., Balachandar, R., & Sui, J. (2016). Local Scour around Bridge Piers under Ice-Covered Conditions. *Journal of Hydraulic Engineering*, *142*(1), 04015038. https://doi.org/10.1061/(ASCE)HY.1943-7900.0001063

Wu, P., Hirshfield, F., & Sui, J. (2013). *ADV measurements of flow field around bridge abutment under ice cover*.

Wu, P., Hirshfield, F., & Sui, J. (2015). Armour Layer Analysis of Local Scour around Bridge Abutments Under Ice Cover. *River Research and Applications*, *31*(6), 736–746. https://doi.org/10.1002/rra.2771

Wu, P., Hirshfield, F., Sui, J., Wang, J., & Chen, P. (2014). Impacts of ice cover on local scour around semi-circular bridge abutment. *Journal of Hydrodynamics, Ser. B*, *26*(1), 10–18. https://doi.org/10.1016/S1001-6058(14)60002-0

Wu, W., Shields Jr., F. D., Bennett, S. J., & Wang, S. S. Y. (2005). A depth-averaged two-dimensional model for flow, sediment transport, and bed topography in curved channels with riparian vegetation. *Water Resources Research*, *41*(3). https://doi.org/10.1029/2004WR003730

Wuebben, J. (1996). Physical Modelling. In *A Primer on Hydraulics of Ice Covered Rivers*. Canadian Committee on River Ice Processes and the Environment.

Xu, H., Li, Y., Zhao, Z., Wang, X., & Zhang, F. (2023). Experimental Study on the Local Scour of Submerged Spur Dike Heads under the Protection of Soft Mattress in Plain Sand-Bed Rivers. *Water*, *15*(3), Article 3. https://doi.org/10.3390/w15030413

Xu, Y. J., Wang, B., Xu, W., Tang, M., Tsai, F. T.-C., & Smith, L. C. (2021). Four-decades of bed elevation changes in the heavily regulated upper Atchafalaya River, Louisiana, USA. *Geomorphology*, *386*, 107748. https://doi.org/10.1016/j.geomorph.2021.107748

Xu, Y., Li, D., & Nepf, H. (2022). Sediment Pickup Rate in Bare and Vegetated Channels. *Geophysical Research Letters*, *49*(21), e2022GL101279. https://doi.org/10.1029/2022GL101279

Xu, Y., & Nepf, H. (2020). Measured and Predicted Turbulent Kinetic Energy in Flow Through Emergent Vegetation With Real Plant Morphology. *Water Resources Research*, *56*(12), e2020WR027892. https://doi.org/10.1029/2020WR027892

Xue, Z., Zhou, L., & Liu, D. (2023). Accurate Numerical Modeling for 1D Open-Channel Flow with Varying Topography. *Water*, *15*(16), Article 16. https://doi.org/10.3390/w15162893

Yakhot, V., Orszag, S. A., Thangam, S., Gatski, T. B., & Speziale, C. G. (1992). Development of turbulence models for shear flows by a double expansion technique. *Physics of Fluids A: Fluid Dynamics*, *4*(7), 1510–1520. https://doi.org/10.1063/1.858424

Yamasaki, T. N., Jiang, B., Janzen, J. G., & Nepf, H. M. (2021). Feedback between vegetation, flow, and deposition: A study of artificial vegetation patch development. *Journal of Hydrology*, *598*, 126232. https://doi.org/10.1016/j.jhydrol.2021.126232

Yan, C., Nepf, H. M., Huang, W.-X., & Cui, G.-X. (2017). Large eddy simulation of flow and scalar transport in a vegetated channel. *Environmental Fluid Mechanics*, *17*(3), 497–519. https://doi.org/10.1007/s10652-016-9503-y

Yang, C. T. (2003). *Sediment Transport: Theory and Practice*. Krieger Pub.

Yang, H. F., Yang, S. L., Xu, K. H., Wu, H., Shi, B. W., Zhu, Q., Zhang, W. X., & Yang, Z. (2017). Erosion potential of the Yangtze Delta under sediment starvation and climate change. *Scientific Reports*, *7*(1), 10535. https://doi.org/10.1038/s41598-017-10958-y

Yang, L., Fang, H., Yang, Z., & Huai, W. (2023). Longitudinal dispersive coefficient in channels with aquatic vegetation: A review. *Journal of Hydrodynamics*, *35*(3), 379–395. https://doi.org/10.1007/s42241-023-0038-7

Yang, S.-Q., Tan, S. K., & Wang, X.-K. (2012). Mechanism of secondary currents in open channel flows. *Journal of Geophysical Research: Earth Surface*, *117*(F4). https://doi.org/10.1029/2012JF002510

Yazdi, J., Sarkardeh, H., Azamathulla, H. Md., & Ghani, A. Ab. (2010). 3D simulation of flow around a single spur dike with free-surface flow. *International Journal of River Basin Management*, *8*(1), 55–62. https://doi.org/10.1080/15715121003715107

Yochum, S. (2018). *Flow Resistance Coefficient Selection in Natural Channels: A Spreadsheet Tool*.

Zabilansky, L., & White, K. (2005). *Ice Cover Effects on Scour in Narrow Rivers (Ice Engineering, April 2005)*. 7.

Zeng, C., Bai, Y., Zhou, J., Qiu, F., Ding, S., Hu, Y., & Wang, L. (2022). Large Eddy Simulation of Compound Open Channel Flows with Floodplain Vegetation. *Water*, *14*(23), Article 23. https://doi.org/10.3390/w14233951

Zhang, J., Wang, W., Li, Z., Li, Q., Zhong, Y., Xia, Z., & Qiu, H. (2021). Analytical Models of Velocity, Reynolds Stress and Turbulence Intensity in Ice-Covered Channels. *Water*, *13*(8), Article 8. https://doi.org/10.3390/w13081107

Zhang, J., Wang, W.-J., Shi, H., Wang, W., Li, Z., Tang, X., & Xia, Z. (2021). An analytical two-layer model for velocity distribution in open-channel flows with submerged flexible canopies considering multiply fluids mechanics. *Journal of Hydrology*, *603*, 127102. https://doi.org/10.1016/j.jhydrol.2021.127102

Zhang, L., Wang, P., Yang, W., Zuo, W., Gu, X., & Yang, X. (2018). Geometric Characteristics of Spur Dike Scour under Clear-Water Scour Conditions. *Water*, *10*(6), Article 6. https://doi.org/10.3390/w10060680

Zhang, M., Hao, Z., Zhang, Y., & Wu, W. (2013). Numerical simulation of solitary and random wave propagation through vegetation based on VOF method. *Acta Oceanologica Sinica*, *32*(7), 38–46. https://doi.org/10.1007/s13131-013-0330-4

Zhang, S., & Liu, X. (2023). Theoretical, experimental, and numerical studies of flow field characteristics and incipient scouring erosion for slope with rigid vegetations. *Journal of Hydrology*, *622*, 129638. https://doi.org/10.1016/j.jhydrol.2023.129638

Zhang, W., Uh Zapata, M., Bai, X., Pham-Van-Bang, D., & Nguyen, K. D. (2020). Three-dimensional simulation of horseshoe vortex and local scour around a vertical cylinder using an unstructured finite-volume technique. *International Journal of Sediment Research*, *35*(3), 295–306. https://doi.org/10.1016/j.ijsrc.2019.09.001

Zhang, X.-F., Yang, W.-T., & Xia, J.-Q. (2016). Bed shear stress in non-uniform flow. *Environmental Fluid Mechanics*, *16*(4), 777–792. https://doi.org/10.1007/s10652-016-9448-1

Zhang, Y., Wang, P., Cheng, J., Wang, W.-J., Zeng, L., & Wang, B. (2020). Drag Coefficient of Emergent Flexible Vegetation in Steady Nonuniform Flow. *Water Resources Research*, *56*(8), e2020WR027613. https://doi.org/10.1029/2020WR027613

Zhao, T., & Nepf, H. M. (2021). Turbulence Dictates Bedload Transport in Vegetated Channels Without Dependence on Stem Diameter and Arrangement. *Geophysical Research Letters*, *48*(21), e2021GL095316. https://doi.org/10.1029/2021GL095316

Zhao, X., Zhang, H., Wei, K., Wang, P., Ren, Q., & Zhang, D. (2021). Flow Field Fitting Method and Acoustic Doppler Velocity Measurement: A New Approach for Detecting Leakage Pathways in Concrete-Face Rockfill Dams. *Earth and Space Science*, *8*(11), e2021EA001875. https://doi.org/10.1029/2021EA001875

Zheng, S., Luo, H., Zhang, J., Cheng, H., Li, Z., Ma, Y., Wu, S., & Liu, E. (2022). Sediment budget and riverbed deformation in the uppermost part of the lower Yangtze River, China. *International Journal of Sediment Research*, *37*(4), 484–492. https://doi.org/10.1016/j.ijsrc.2022.02.004

Zhuang, T., Ren, J., Dai, J., Zhang, H., Wang, J., Ma, Z., Xu, S., Chen, K., Guo, H., & Zhai, Y. (2023). The influence of hyporheic exchange with spur dikes: Laboratory experiments. *Journal of Hydrology*, *622*, 129754. https://doi.org/10.1016/j.jhydrol.2023.129754

APPENDIX I. TERRAIN ELEVATION SHANGE CONTOURS

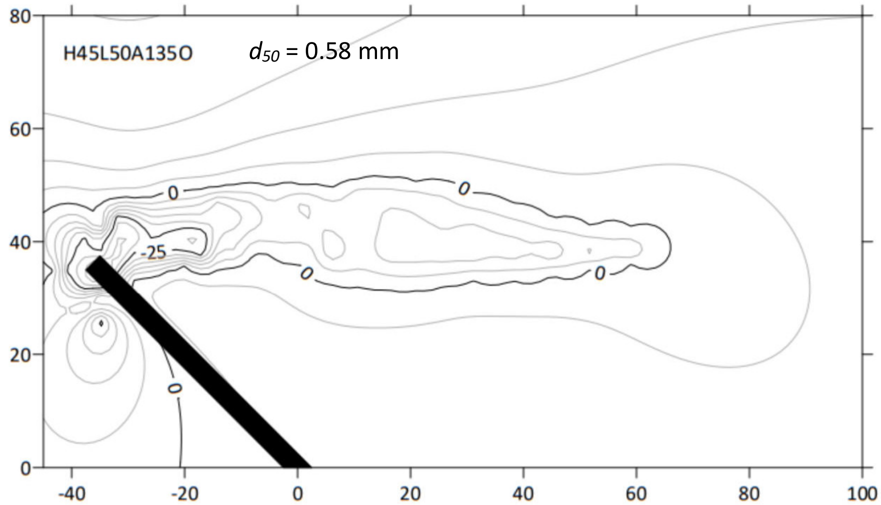

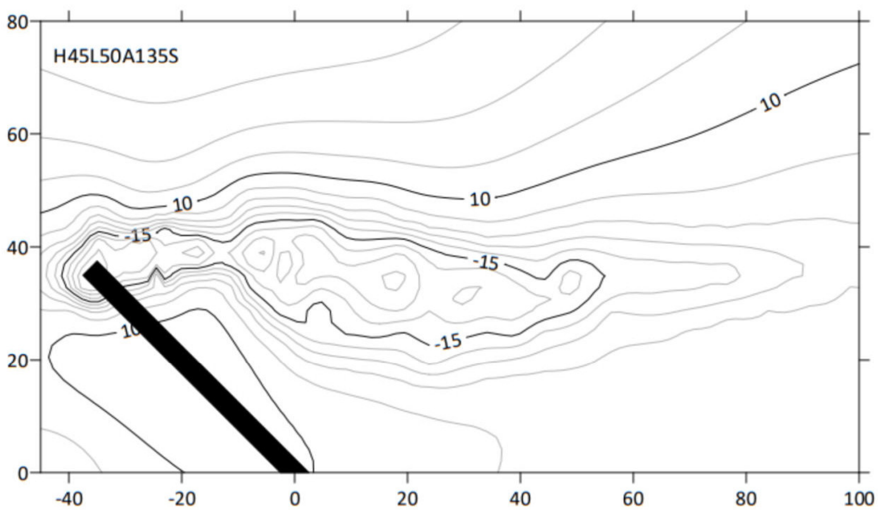

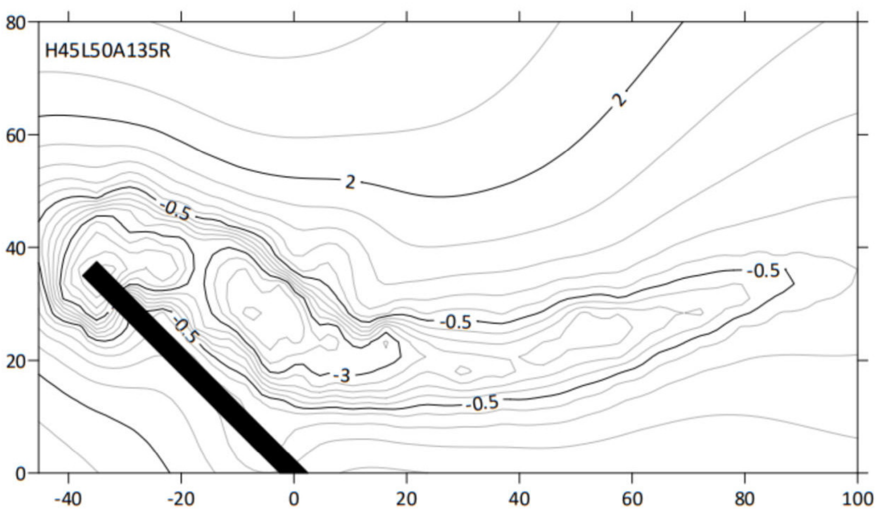

Note: In these contour maps, units for x and y axis are cm, whereas the contour unit is mm. In the experiment serial numbers, *H, L*, and *A* denotes the dike height (including buried in the sands, cm), design length (cm), and alignment angles (°). O, S, R indicate the cover conditions (open channel smooth cover, and rough cover respectively.

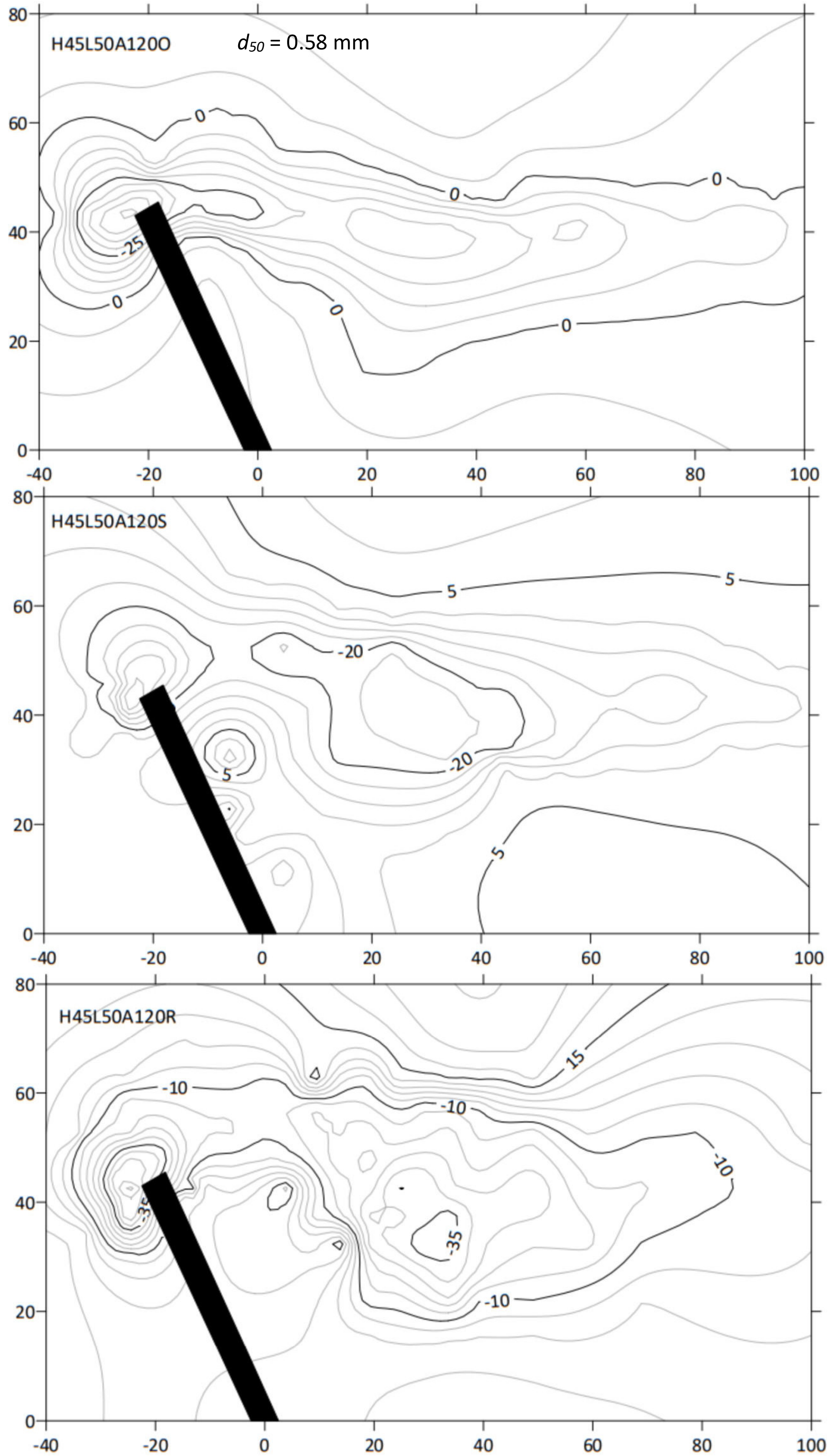

Note: In these contour maps, units for x and y axis are cm, whereas the contour unit is mm. In the experiment serial numbers, *H, L*, and *A* denotes the dike height (including buried in the sands, cm), design length (cm), and alignment angles (°). O, S, R indicate the cover conditions (open channel smooth cover, and rough cover respectively.

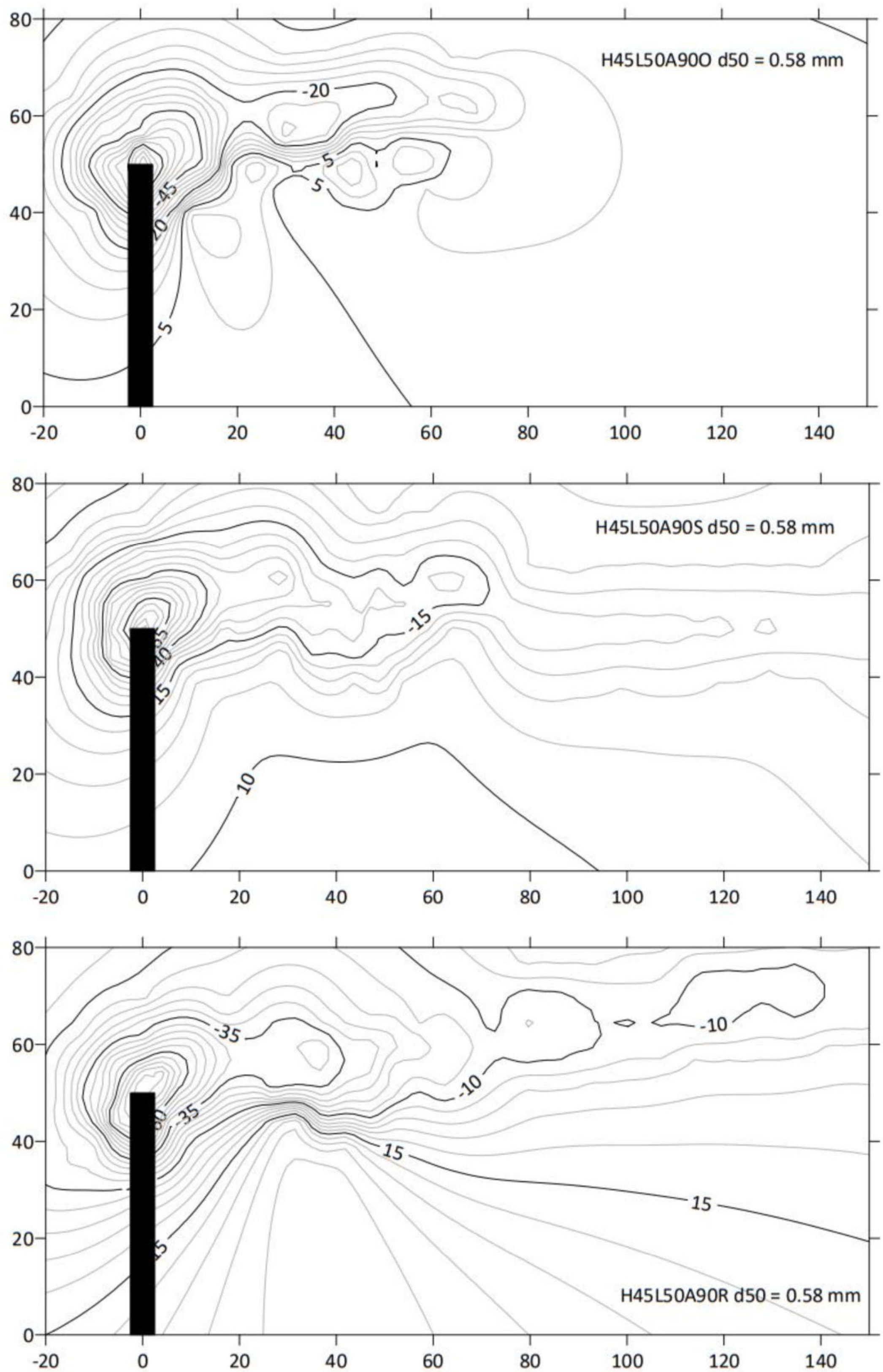

Note: In these contour maps, units for x and y axis are cm, whereas the contour unit is mm. In the experiment serial numbers, *H, L*, and *A* denotes the dike height (including buried in the sands, cm), design length (cm), and alignment angles (°). O, S, R indicate the cover conditions (open channel smooth cover, and rough cover respectively.

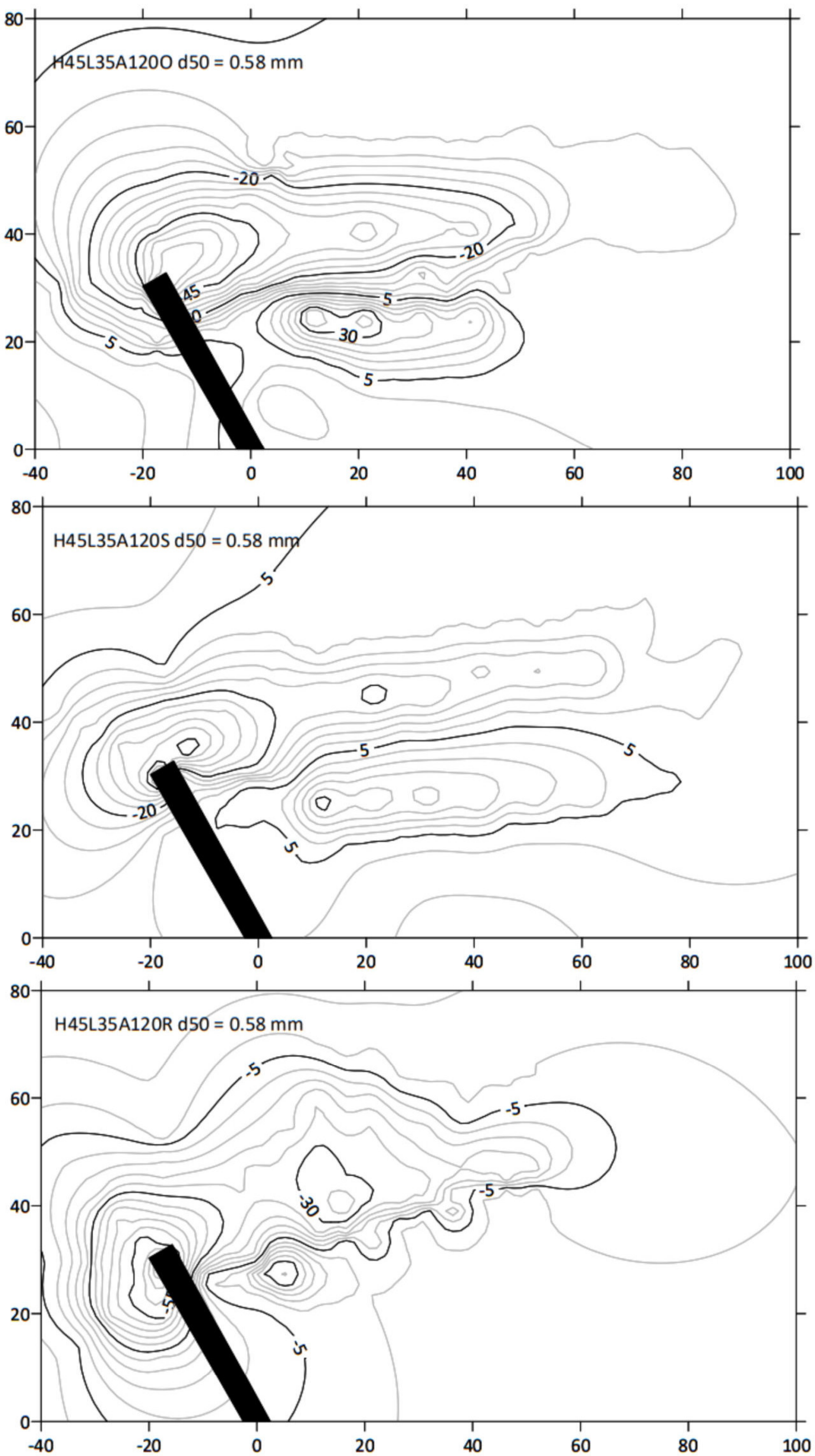

Note: In these contour maps, units for x and y axis are cm, whereas the contour unit is mm. In the experiment serial numbers, *H, L*, and *A* denotes the dike height (including buried in the sands, cm), design length (cm), and alignment angles (°). O, S, R indicate the cover conditions (open channel smooth cover, and rough cover respectively.

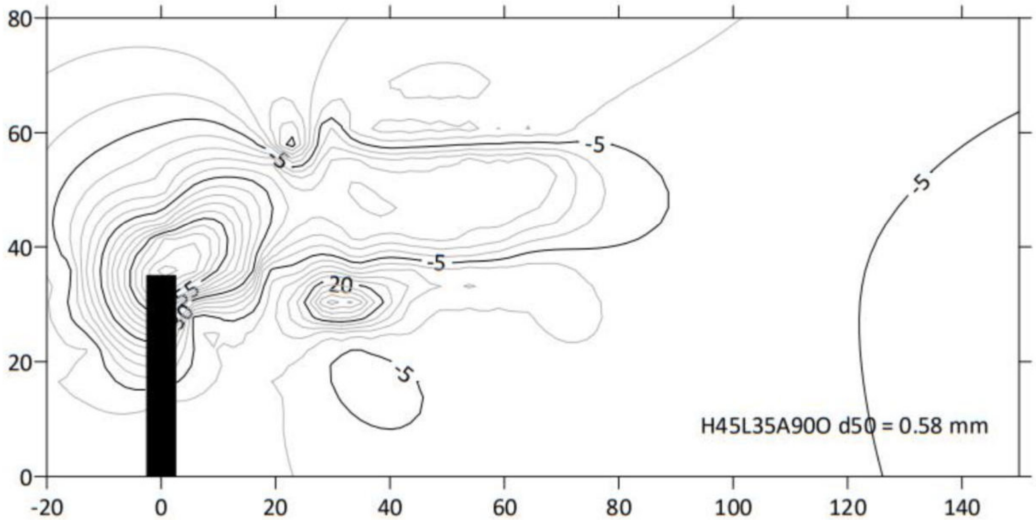

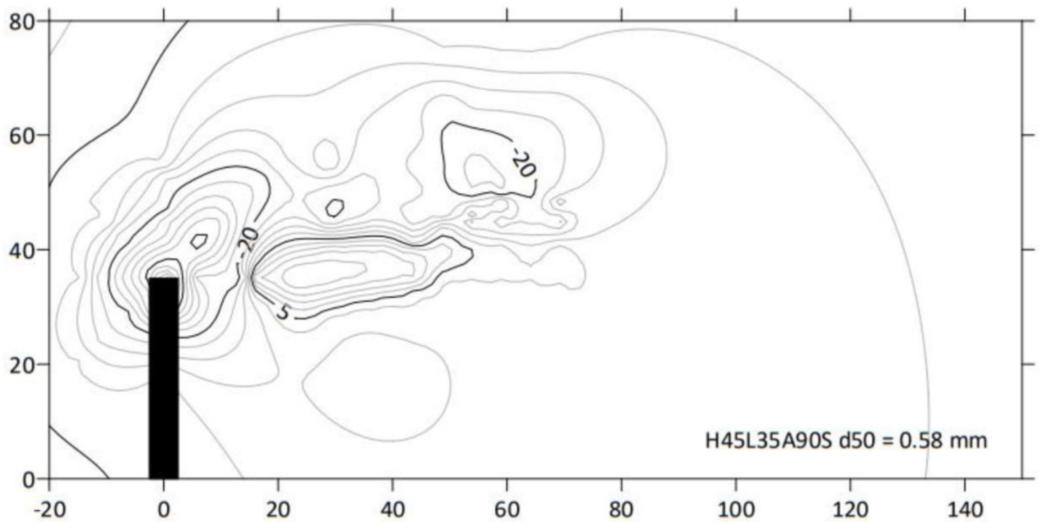

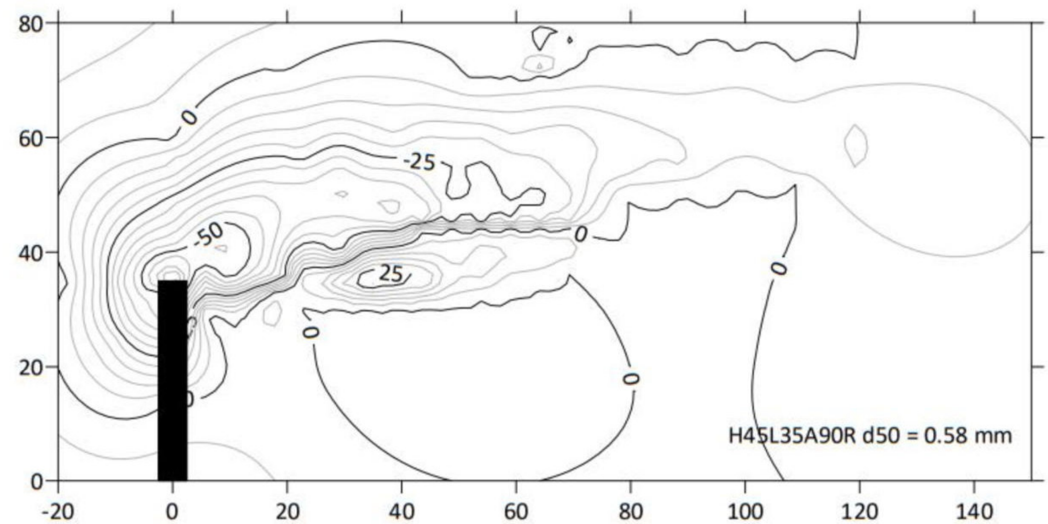

Note: In these contour maps, units for x and y axis are cm, whereas the contour unit is mm. In the experiment serial numbers, *H, L*, and *A* denotes the dike height (including buried in the sands, cm), design length (cm), and alignment angles (°). O, S, R indicate the cover conditions (open channel smooth cover, and rough cover respectively.

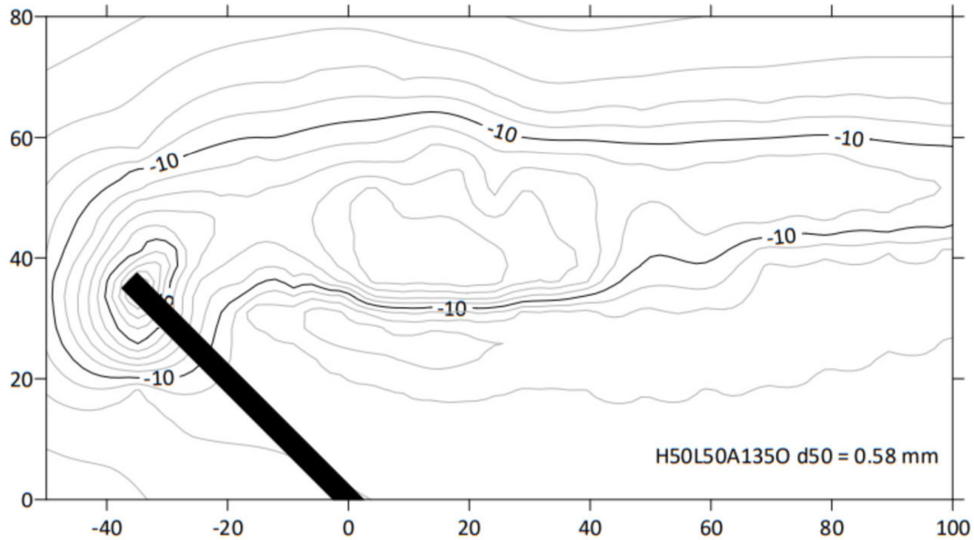

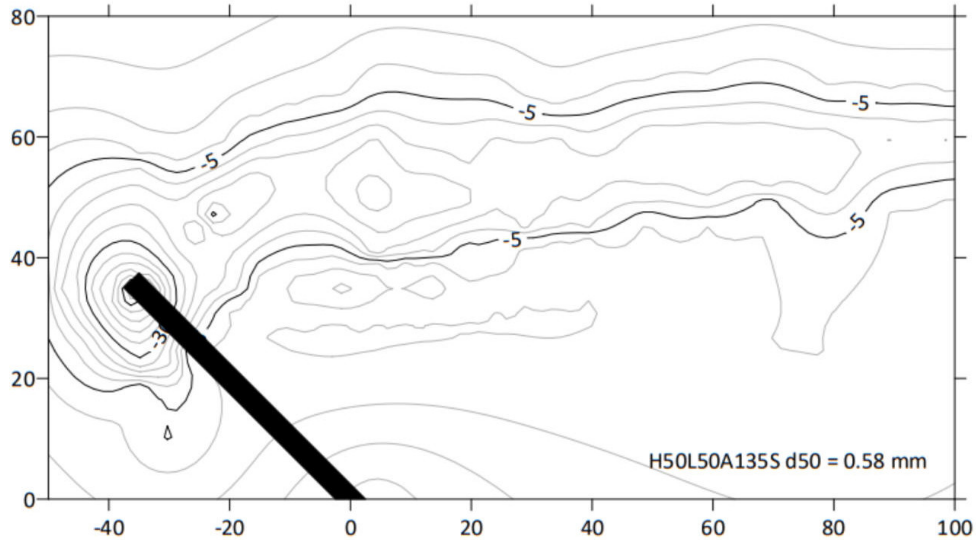

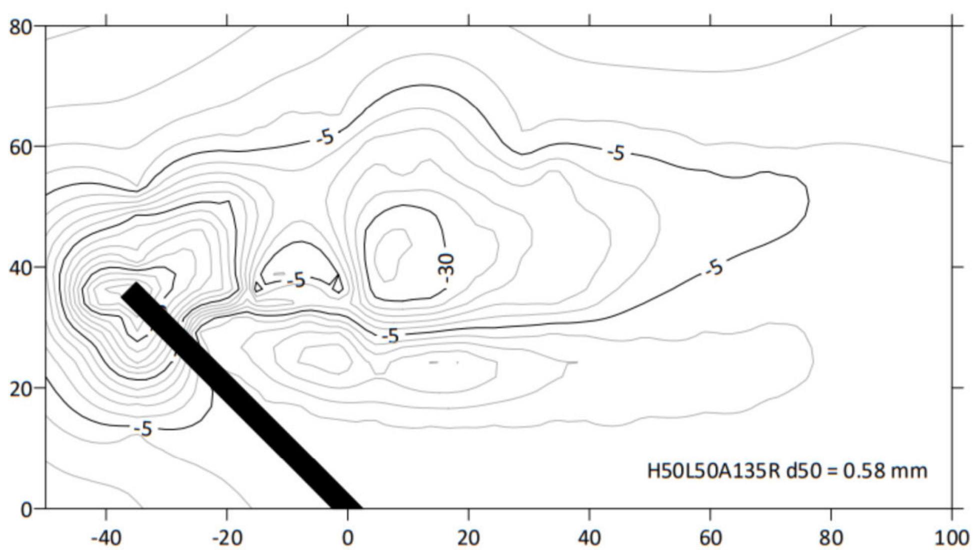

Note: In these contour maps, units for x and y axis are cm, whereas the contour unit is mm. In the experiment serial numbers, *H, L*, and *A* denotes the dike height (including buried in the sands, cm), design length (cm), and alignment angles (°). O, S, R indicate the cover conditions (open channel smooth cover, and rough cover respectively.

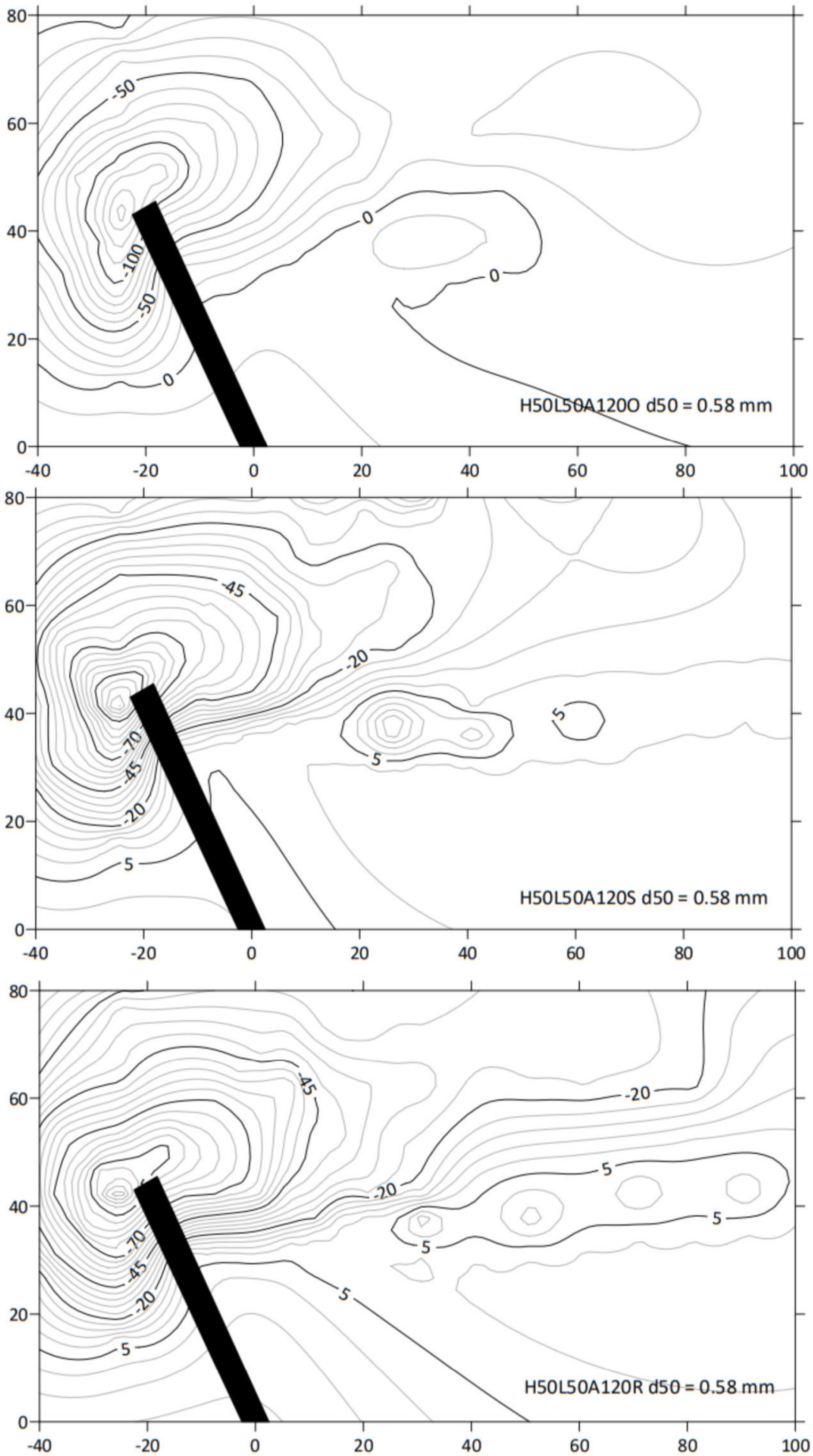

Note: In these contour maps, units for x and y axis are cm, whereas the contour unit is mm. In the experiment serial numbers, *H, L*, and *A* denotes the dike height (including buried in the sands, cm), design length (cm), and alignment angles (°). O, S, R indicate the cover conditions (open channel smooth cover, and rough cover respectively.

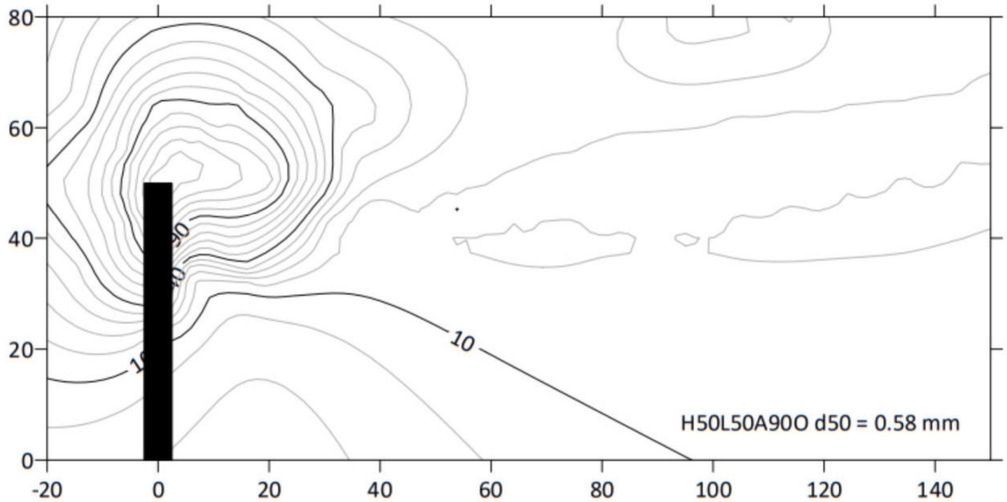

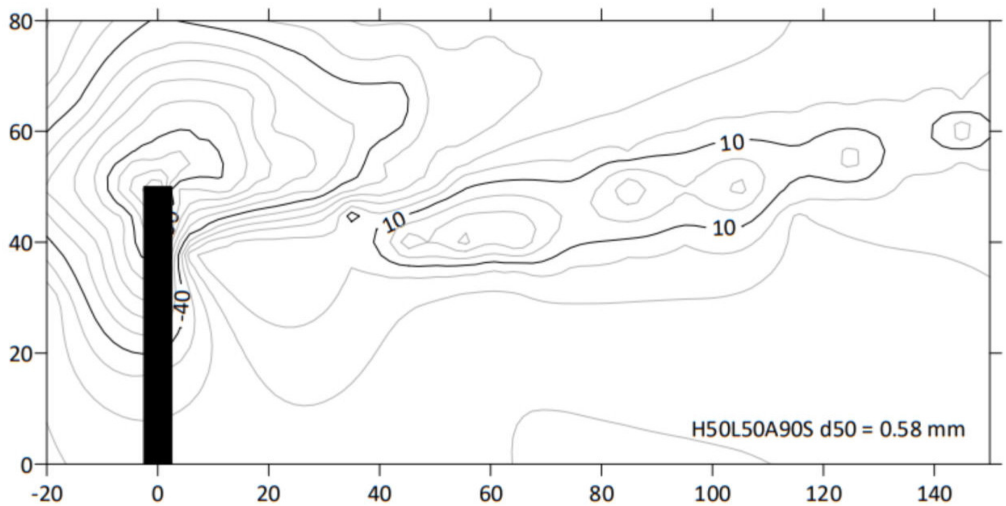

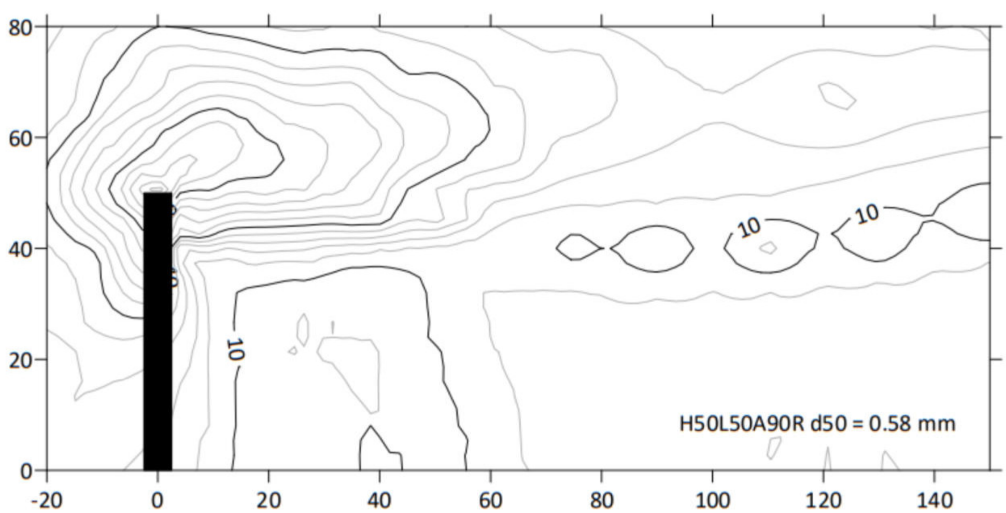

Note: In these contour maps, units for x and y axis are cm, whereas the contour unit is mm. In the experiment serial numbers, *H, L*, and *A* denotes the dike height (including buried in the sands, cm), design length (cm), and alignment angles (°). O, S, R indicate the cover conditions (open channel smooth cover, and rough cover respectively.

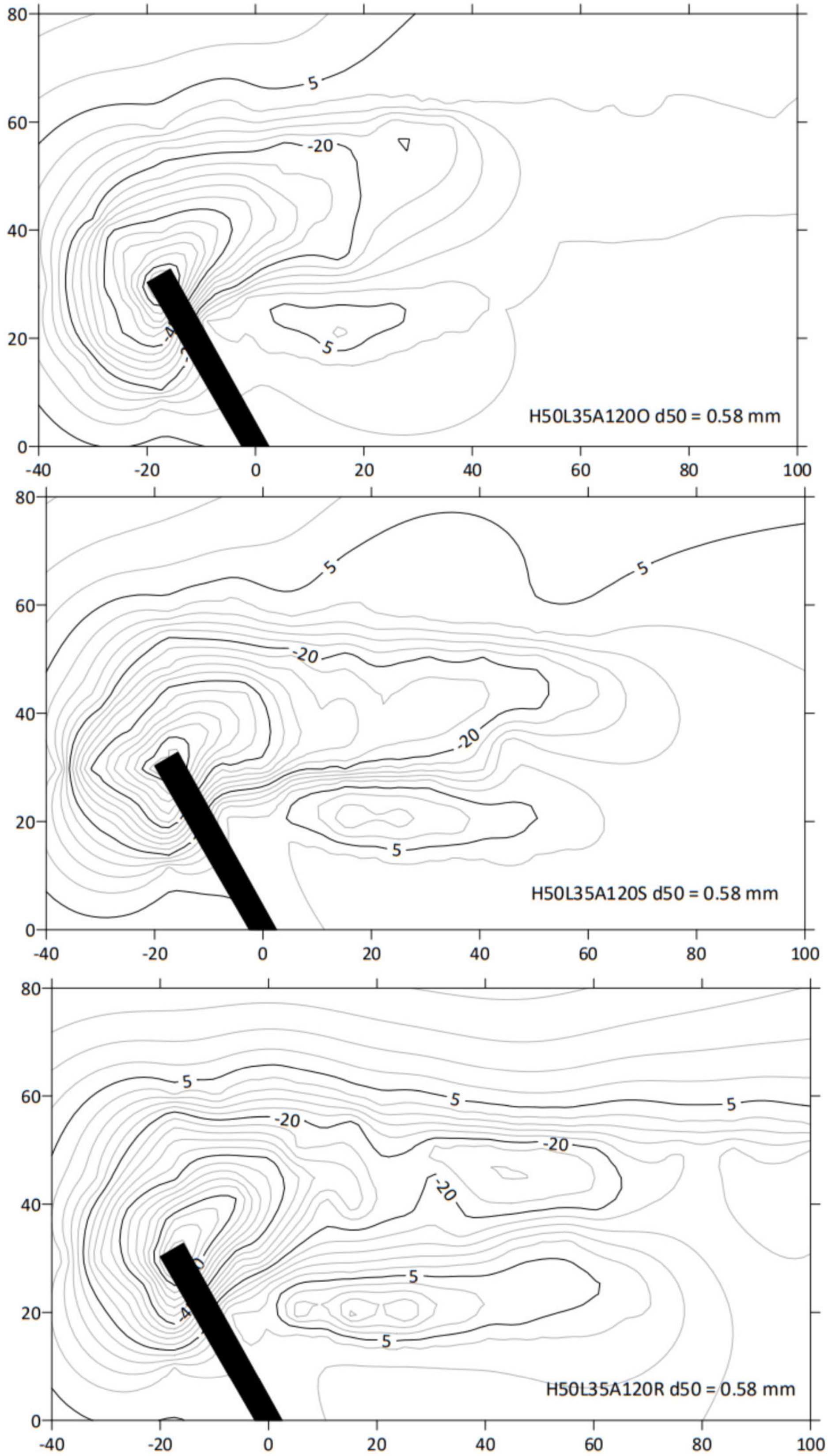

Note: In these contour maps, units for x and y axis are cm, whereas the contour unit is mm. In the experiment serial numbers, *H, L*, and *A* denotes the dike height (including buried in the sands, cm), design length (cm), and alignment angles (°). O, S, R indicate the cover conditions (open channel smooth cover, and rough cover respectively.

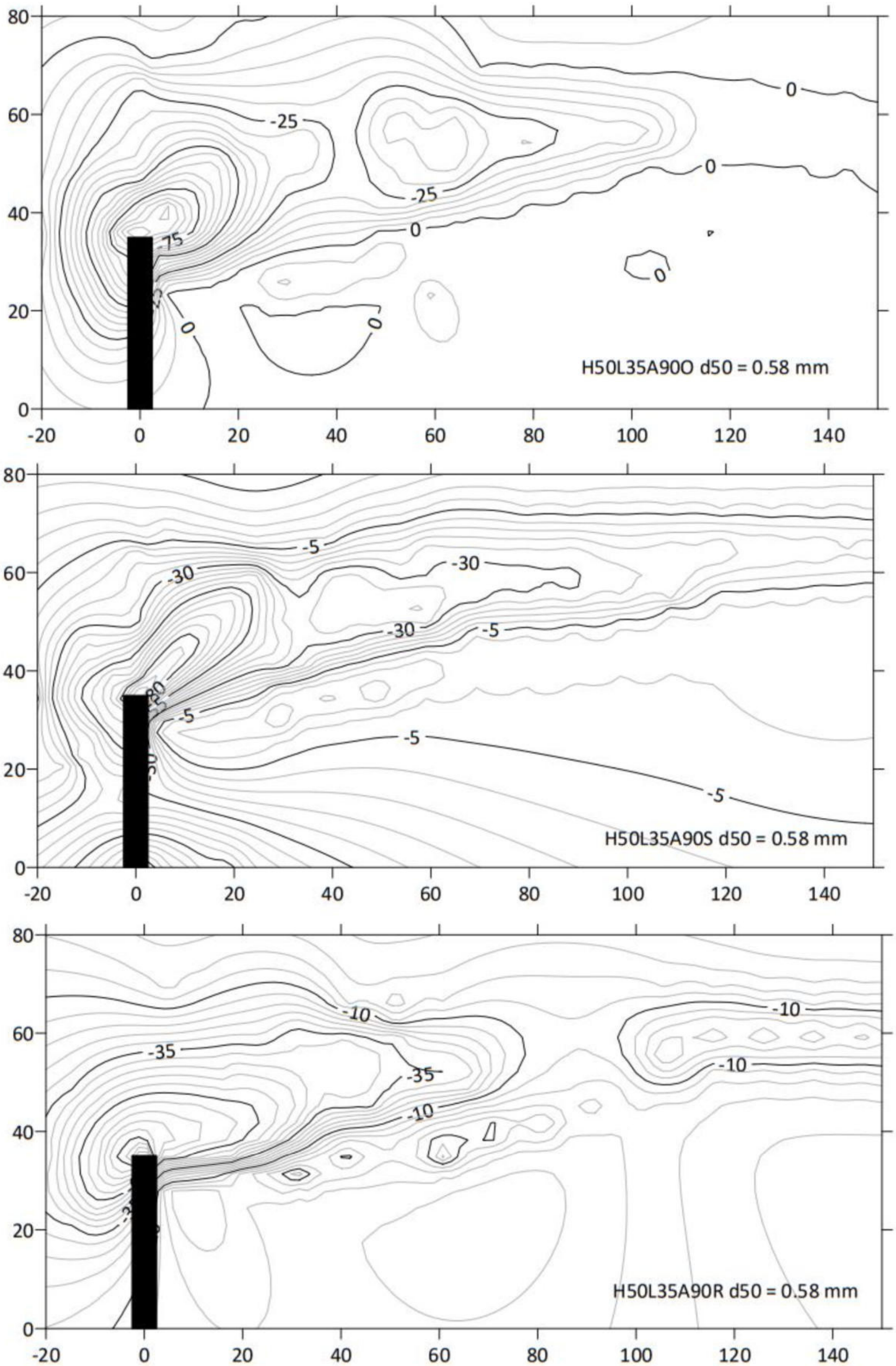

Note: In these contour maps, units for x and y axis are cm, whereas the contour unit is mm. In the experiment serial numbers, *H, L*, and *A* denotes the dike height (including buried in the sands, cm), design length (cm), and alignment angles (°). O, S, R indicate the cover conditions (open channel smooth cover, and rough cover respectively.

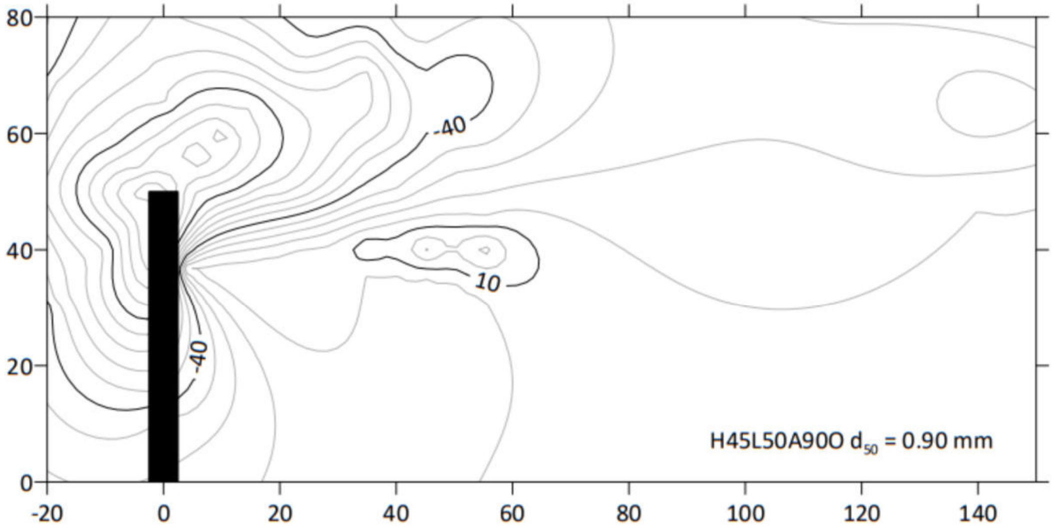

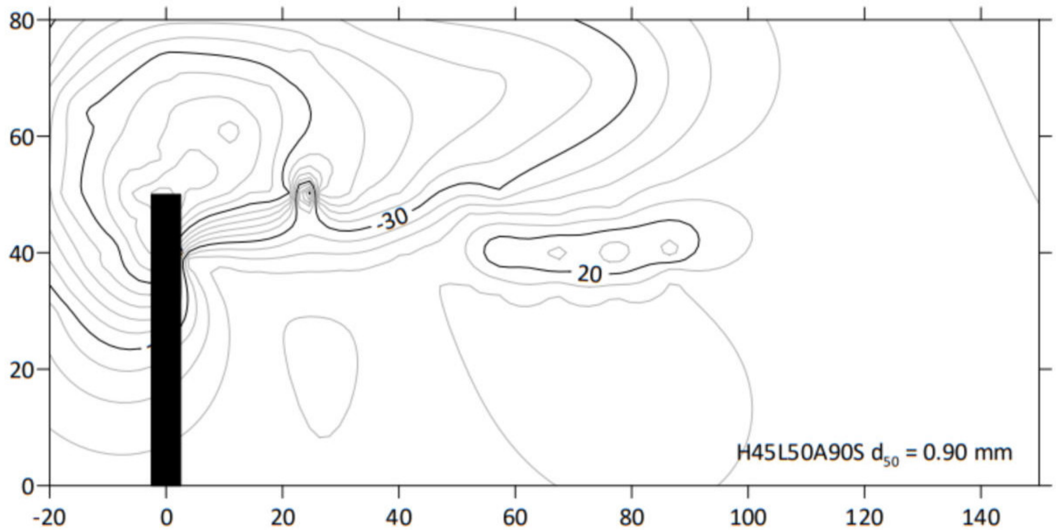

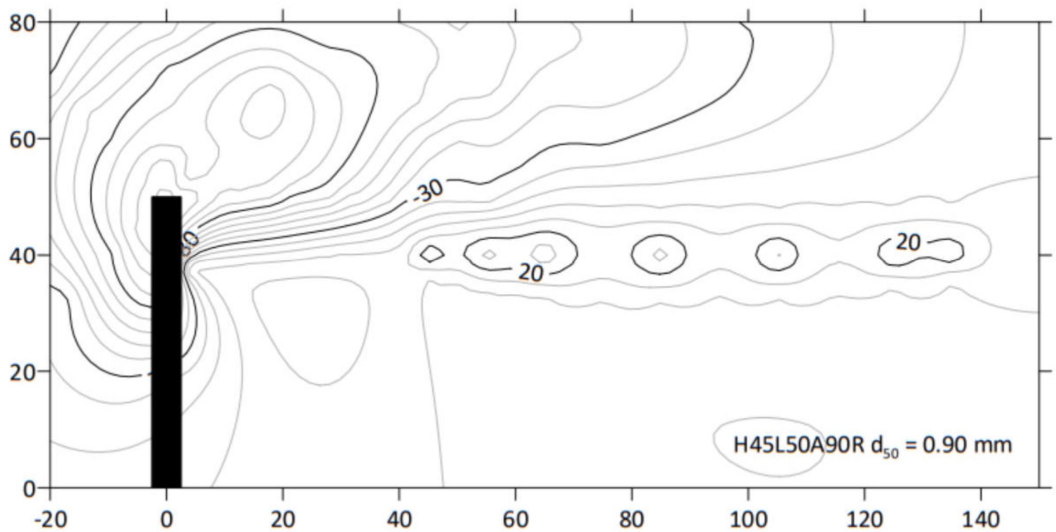

Note: In these contour maps, units for x and y axis are cm, whereas the contour unit is mm. In the experiment serial numbers, *H, L*, and *A* denotes the dike height (including buried in the sands, cm), design length (cm), and alignment angles (°). O, S, R indicate the cover conditions (open channel smooth cover, and rough cover respectively.

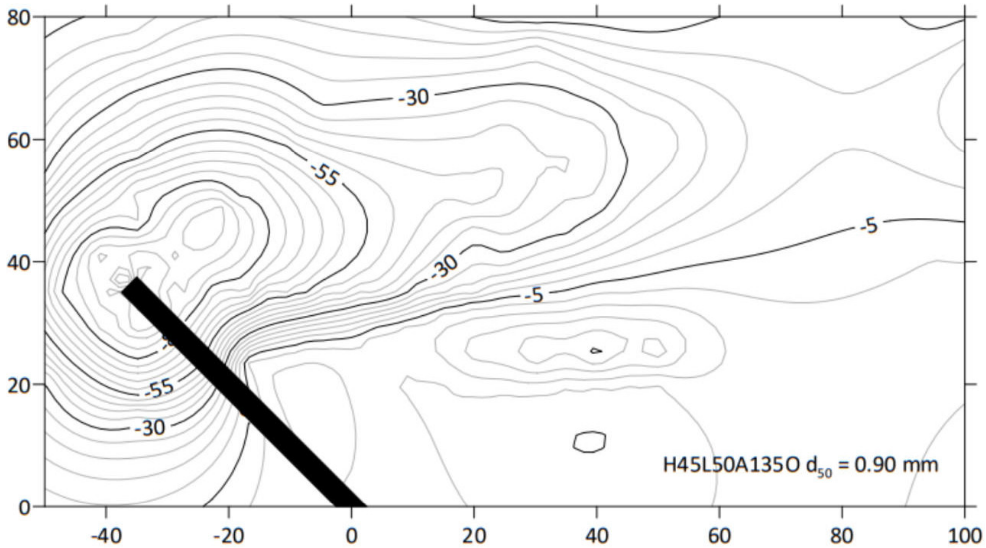

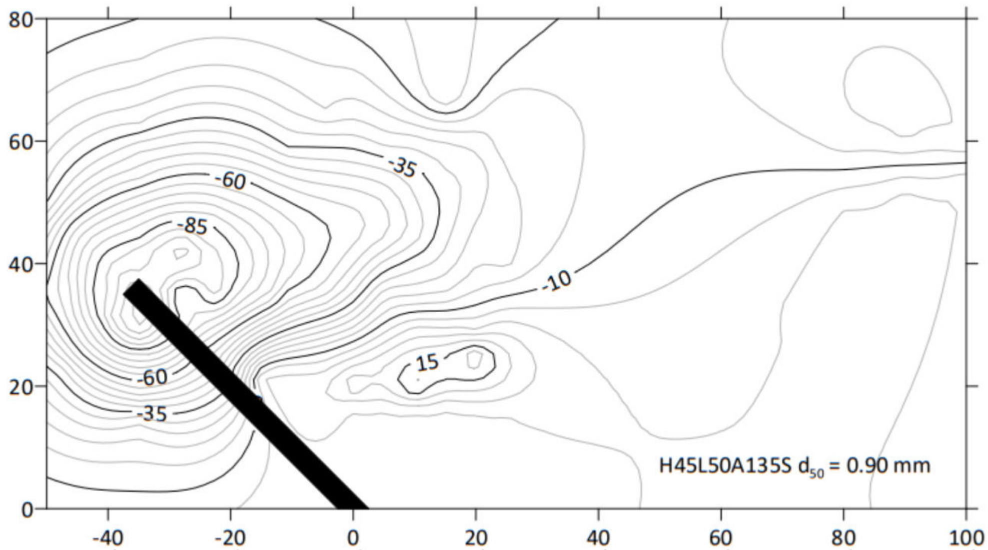

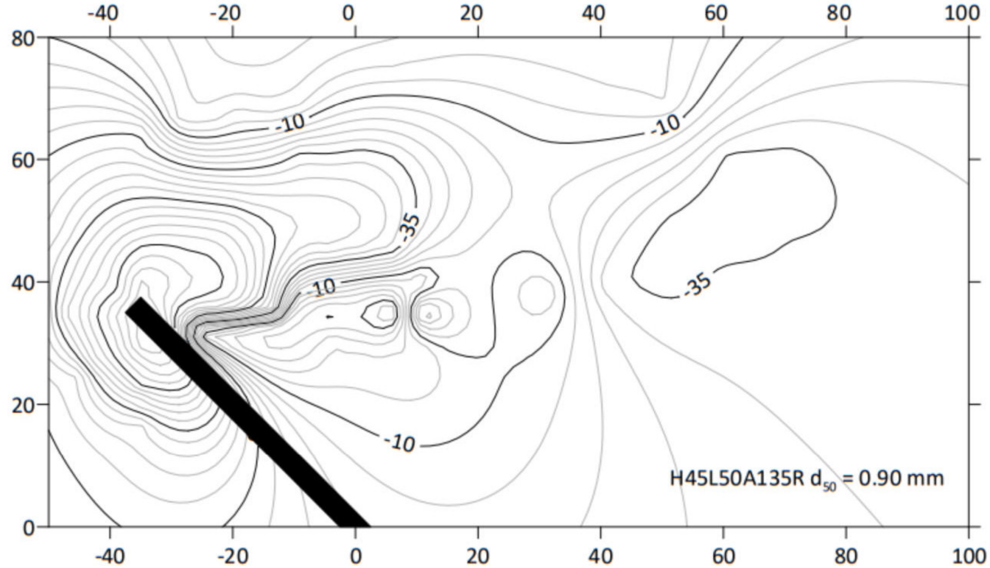

Note: In these contour maps, units for x and y axis are cm, whereas the contour unit is mm. In the experiment serial numbers, *H, L*, and *A* denotes the dike height (including buried in the sands, cm), design length (cm), and alignment angles (°). O, S, R indicate the cover conditions (open channel smooth cover, and rough cover respectively.

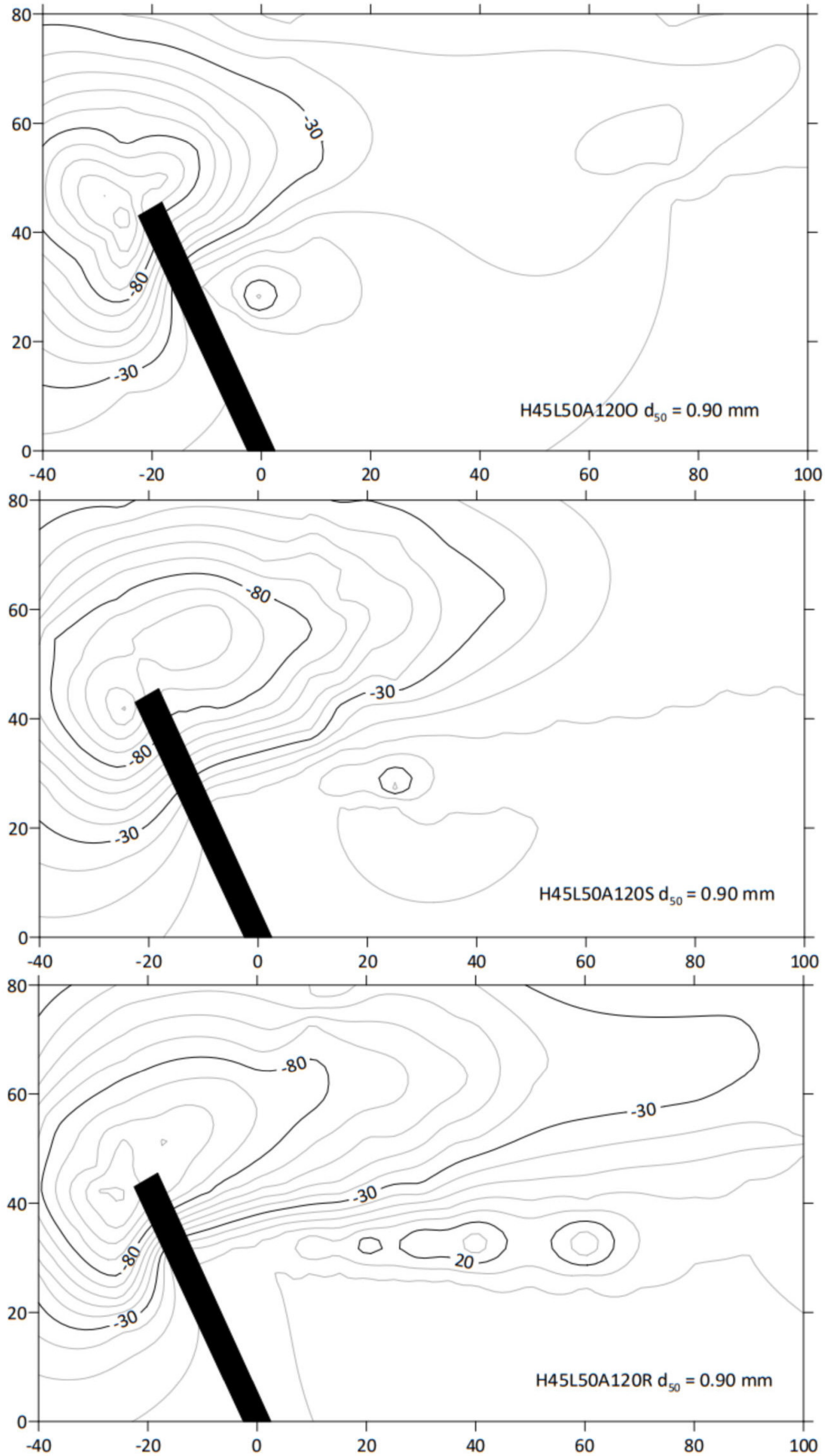

Note: In these contour maps, units for x and y axis are cm, whereas the contour unit is mm. In the experiment serial numbers, *H, L*, and *A* denotes the dike height (including buried in the sands, cm), design length (cm), and alignment angles (°). O, S, R indicate the cover conditions (open channel smooth cover, and rough cover respectively.

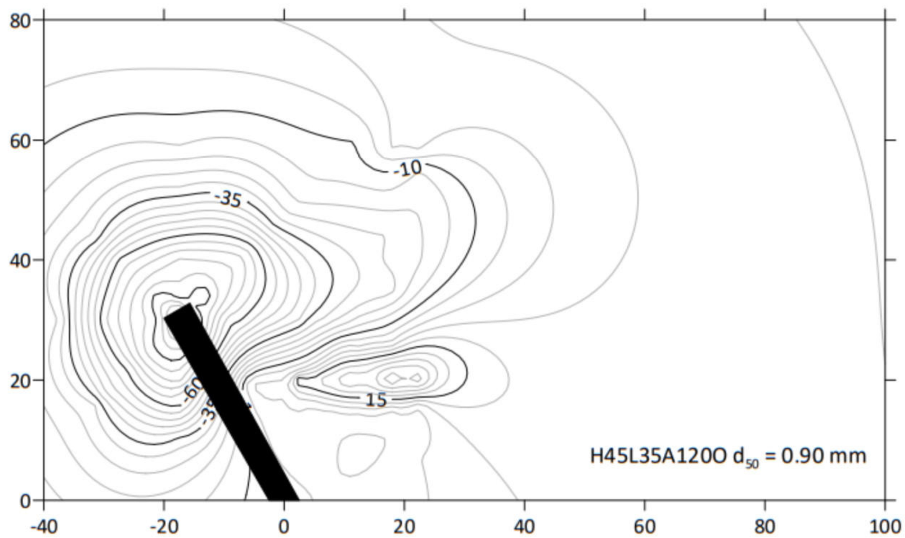

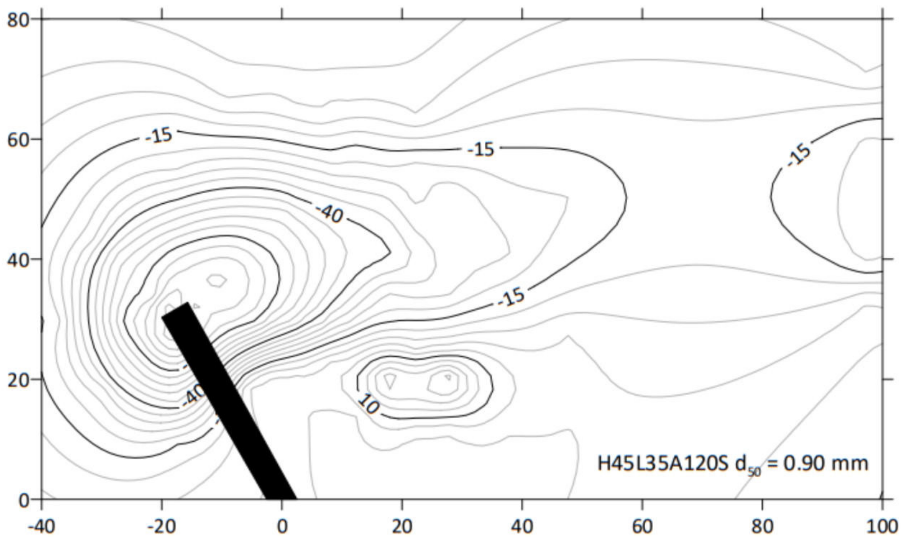

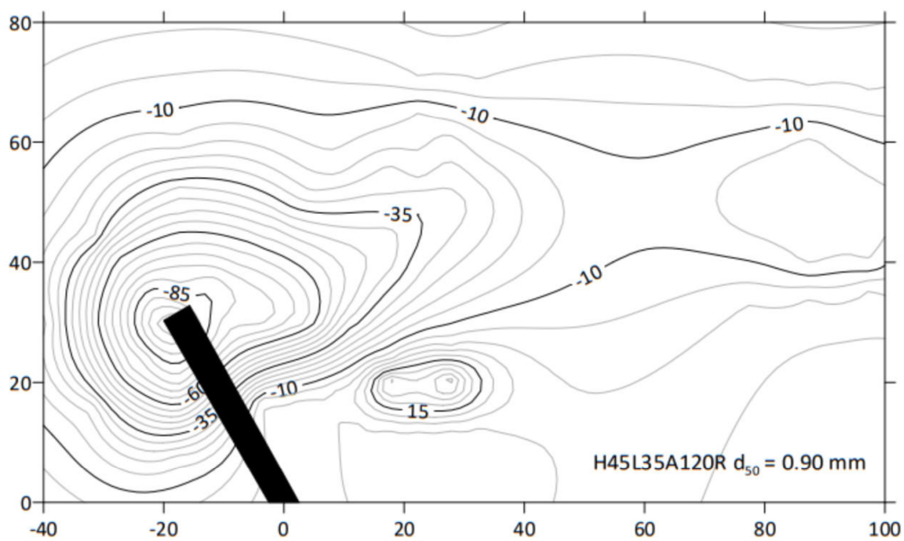

Note: In these contour maps, units for x and y axis are cm, whereas the contour unit is mm. In the experiment serial numbers, *H, L*, and *A* denotes the dike height (including buried in the sands, cm), design length (cm), and alignment angles (°). O, S, R indicate the cover conditions (open channel smooth cover, and rough cover respectively.

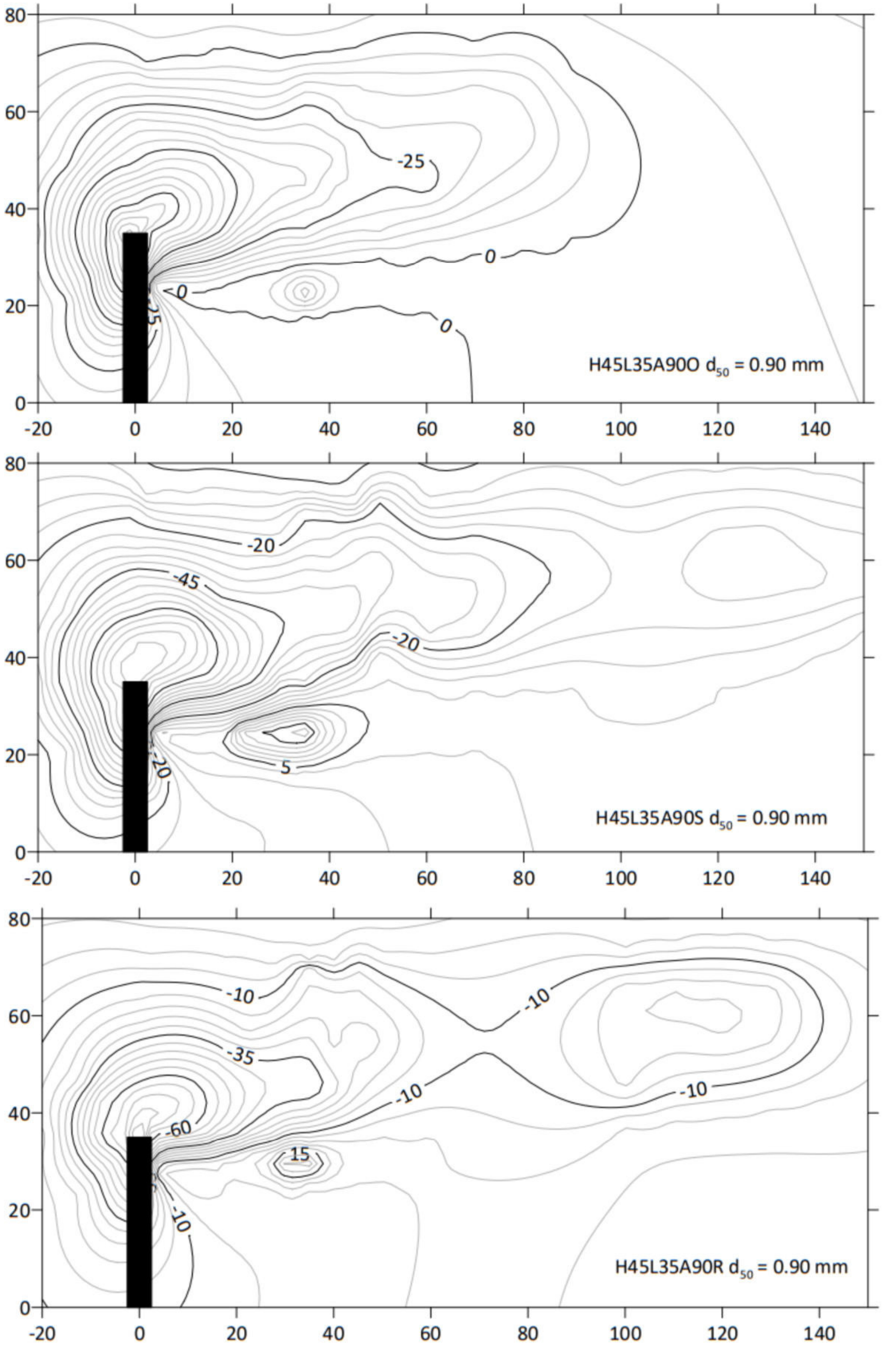

Note: In these contour maps, units for x and y axis are cm, whereas the contour unit is mm. In the experiment serial numbers, *H, L*, and *A* denotes the dike height (including buried in the sands, cm), design length (cm), and alignment angles (°). O, S, R indicate the cover conditions (open channel smooth cover, and rough cover respectively.

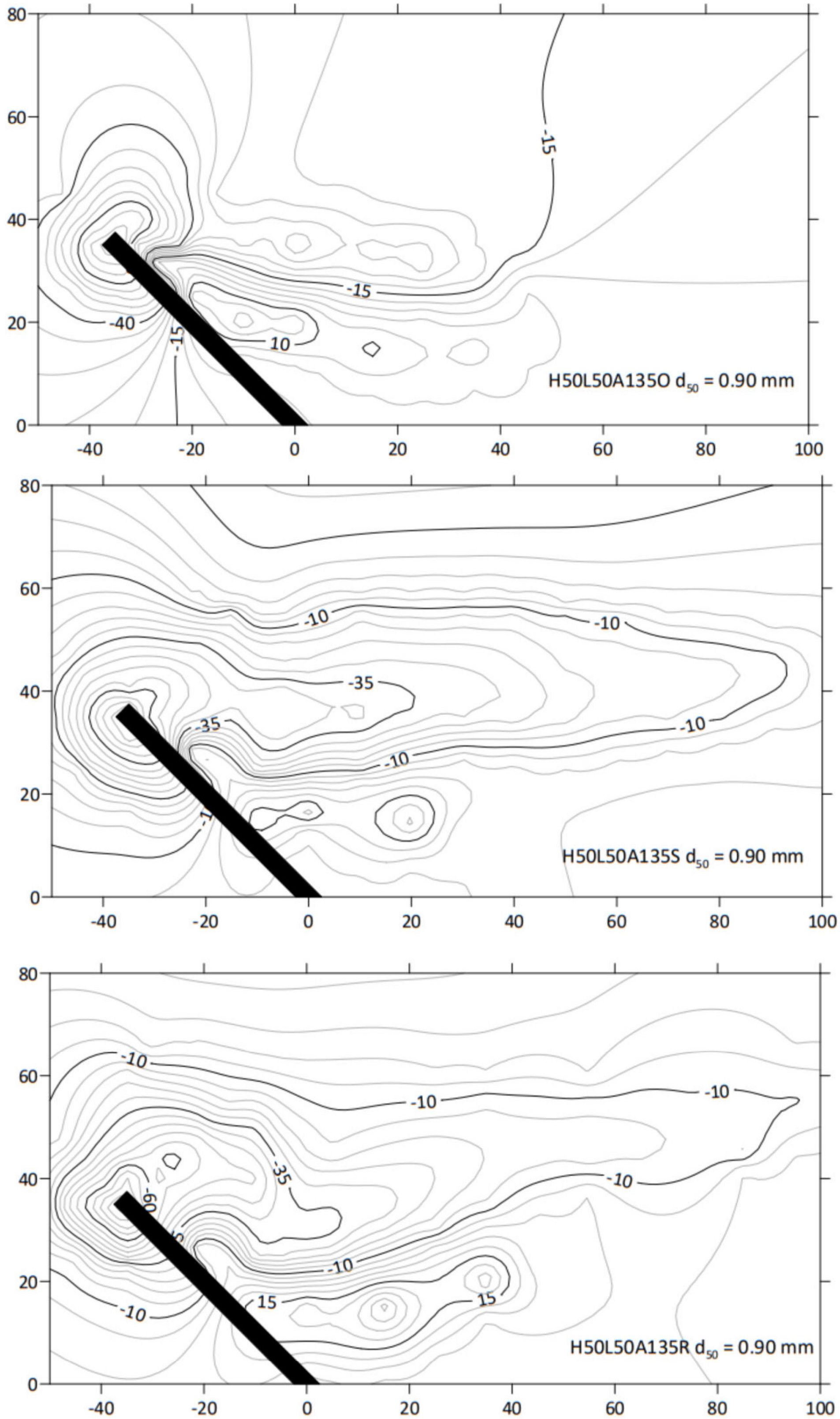

Note: In these contour maps, units for x and y axis are cm, whereas the contour unit is mm. In the experiment serial numbers, *H, L*, and *A* denotes the dike height (including buried in the sands, cm), design length (cm), and alignment angles (°). O, S, R indicate the cover conditions (open channel smooth cover, and rough cover respectively.

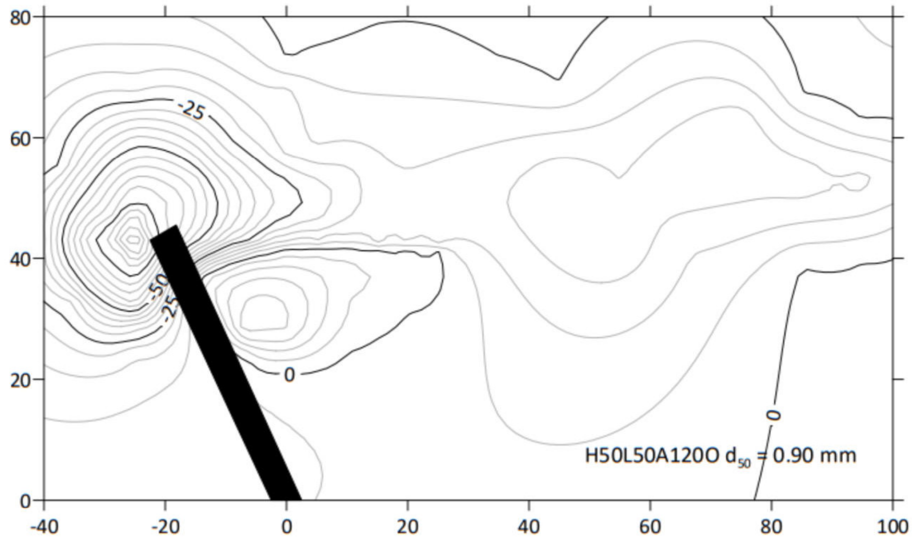

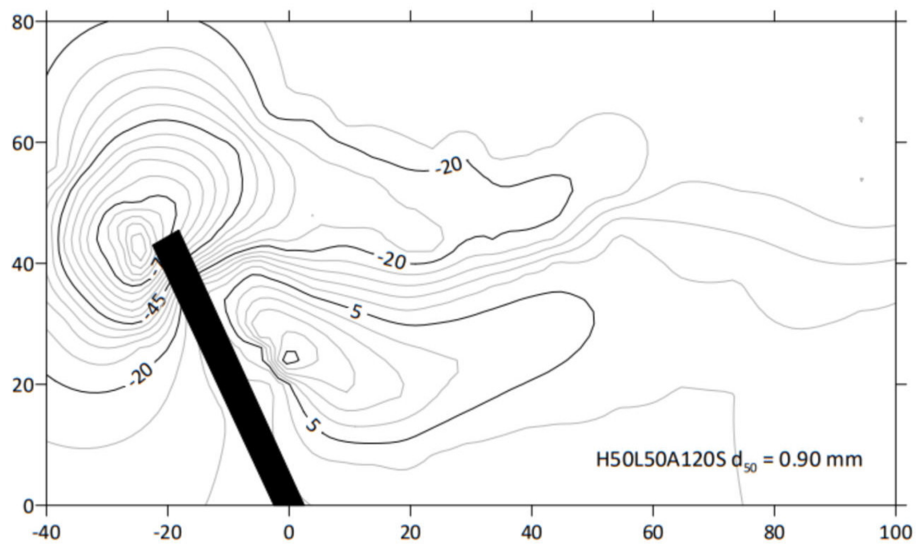

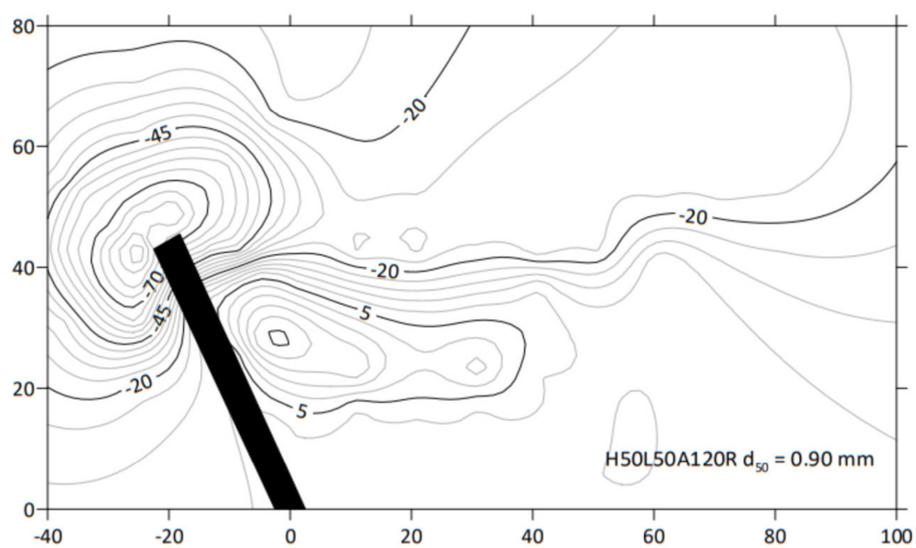

Note: In these contour maps, units for x and y axis are cm, whereas the contour unit is mm. In the experiment serial numbers, *H, L*, and *A* denotes the dike height (including buried in the sands, cm), design length (cm), and alignment angles (°). O, S, R indicate the cover conditions (open channel smooth cover, and rough cover respectively.

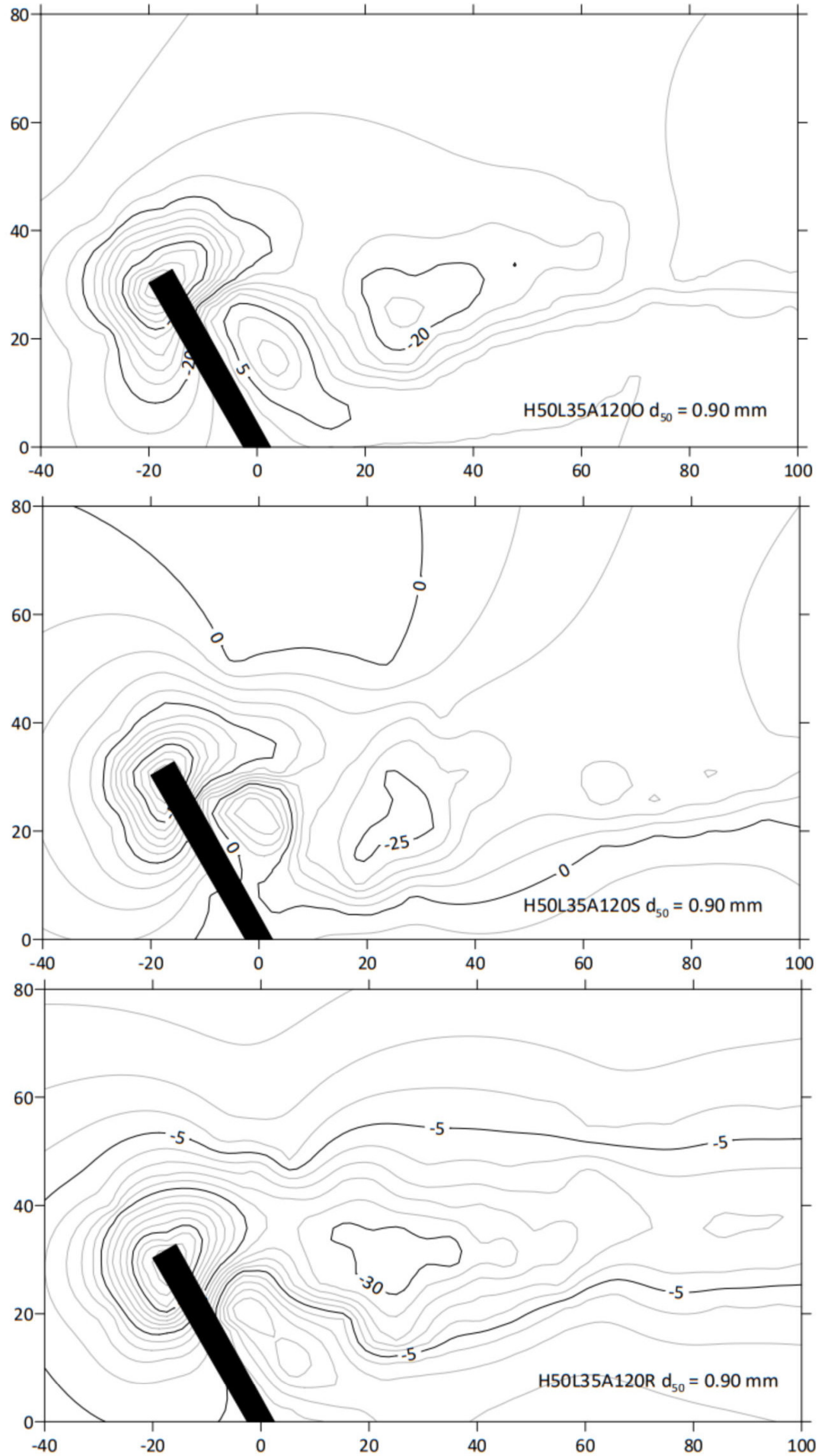

Note: In these contour maps, units for x and y axis are cm, whereas the contour unit is mm. In the experiment serial numbers, *H, L*, and *A* denotes the dike height (including buried in the sands, cm), design length (cm), and alignment angles (°). O, S, R indicate the cover conditions (open channel smooth cover, and rough cover respectively.

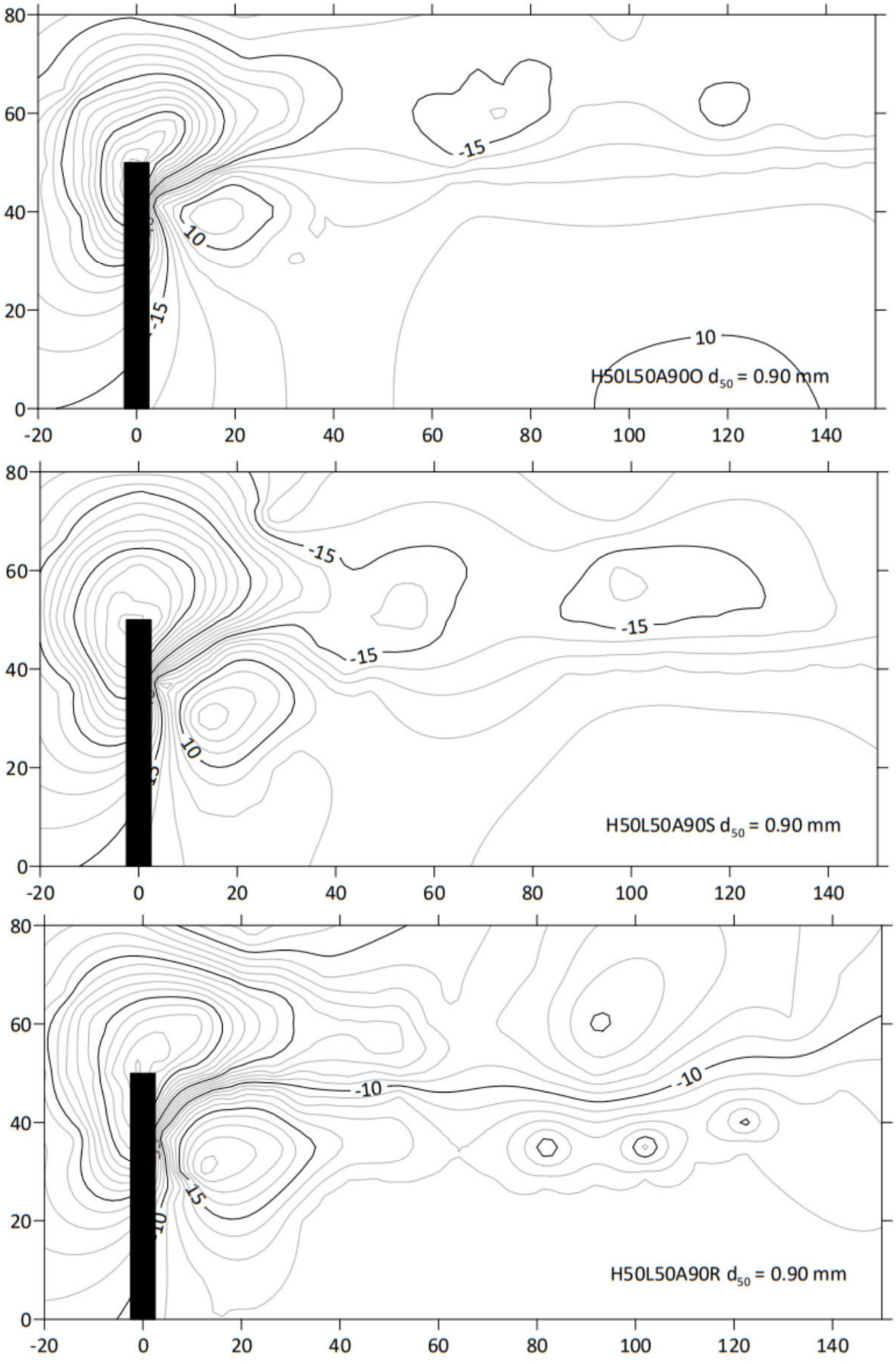

Note: In these contour maps, units for x and y axis are cm, whereas the contour unit is mm. In the experiment serial numbers, *H, L*, and *A* denotes the dike height (including buried in the sands, cm), design length (cm), and alignment angles (°). O, S, R indicate the cover conditions (open channel smooth cover, and rough cover respectively.

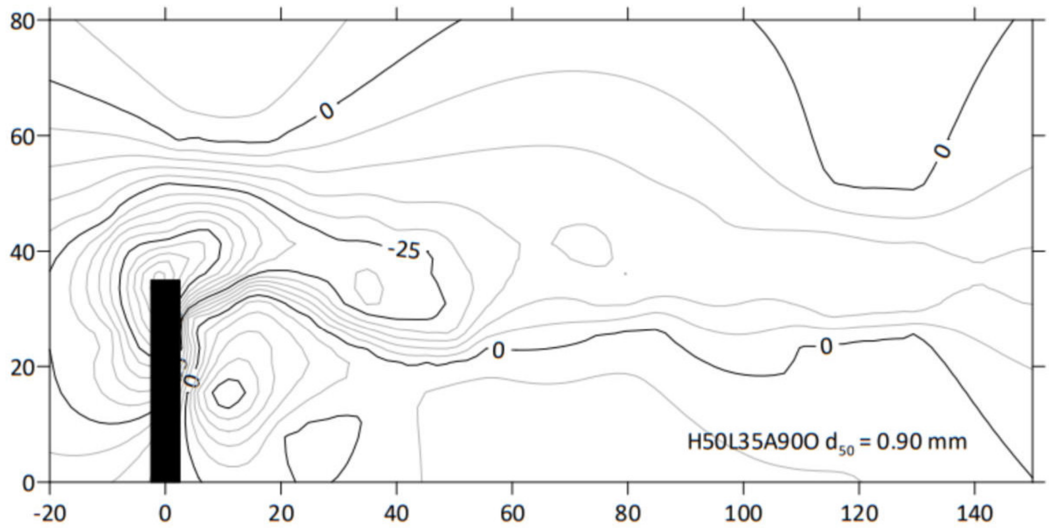

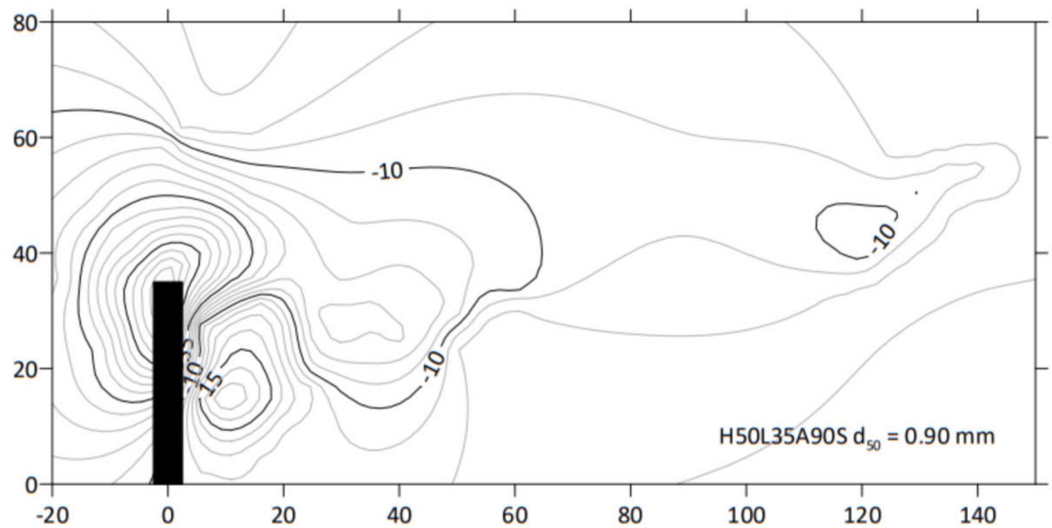

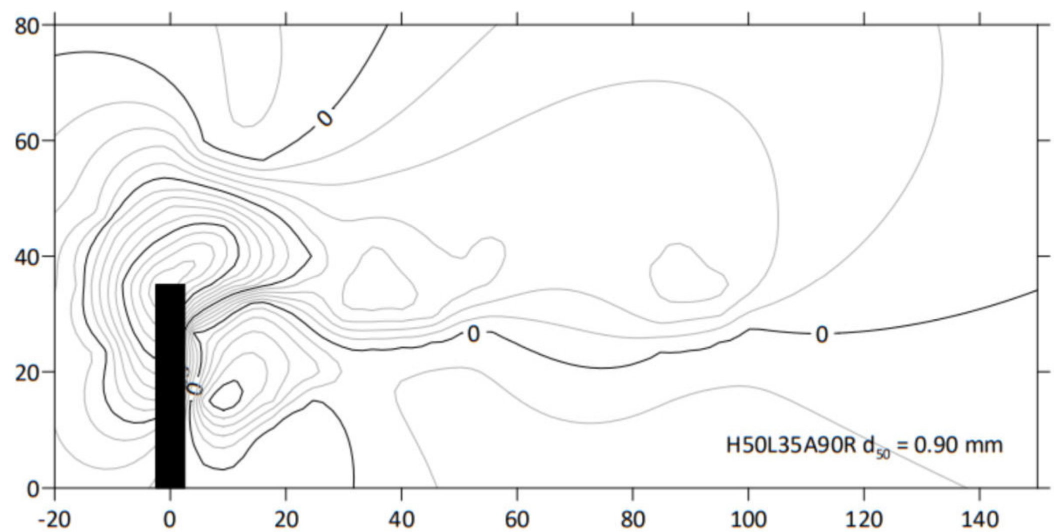

Note: In these contour maps, units for x and y axis are cm, whereas the contour unit is mm. In the experiment serial numbers, *H, L*, and *A* denotes the dike height (including buried in the sands, cm), design length (cm), and alignment angles (°). O, S, R indicate the cover conditions (open channel smooth cover, and rough cover respectively.

N.B.: The following few experimental conditions were to determine whether the width will influence the maximum scour depth. The widths in previous trials were 5 cm.

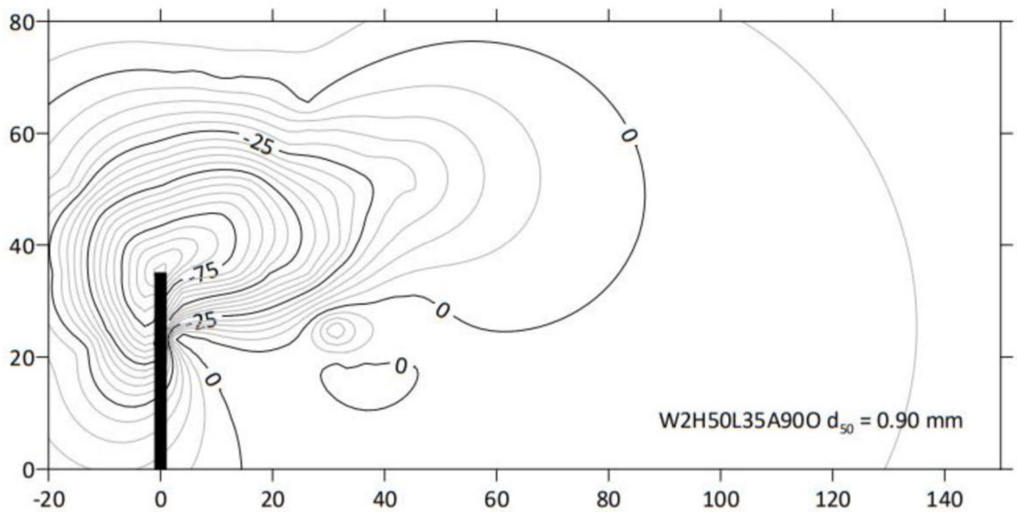

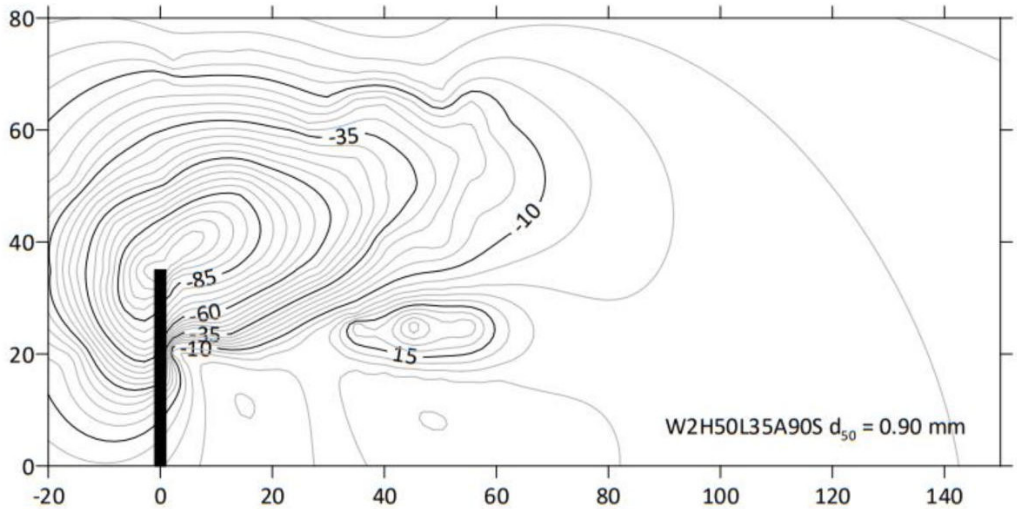

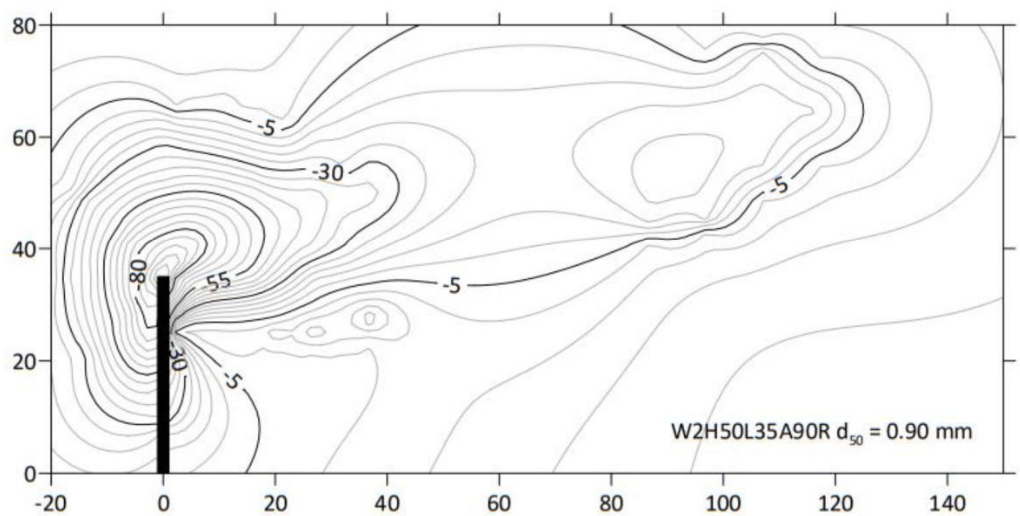

Note: In these contour maps, units for x and y axis are cm, whereas the contour unit is mm. In the experiment serial numbers, *H, L*, and *A* denotes the dike height (including buried in the sands, cm), design length (cm), and alignment angles (°). O, S, R indicate the cover conditions (open channel smooth cover, and rough cover respectively.

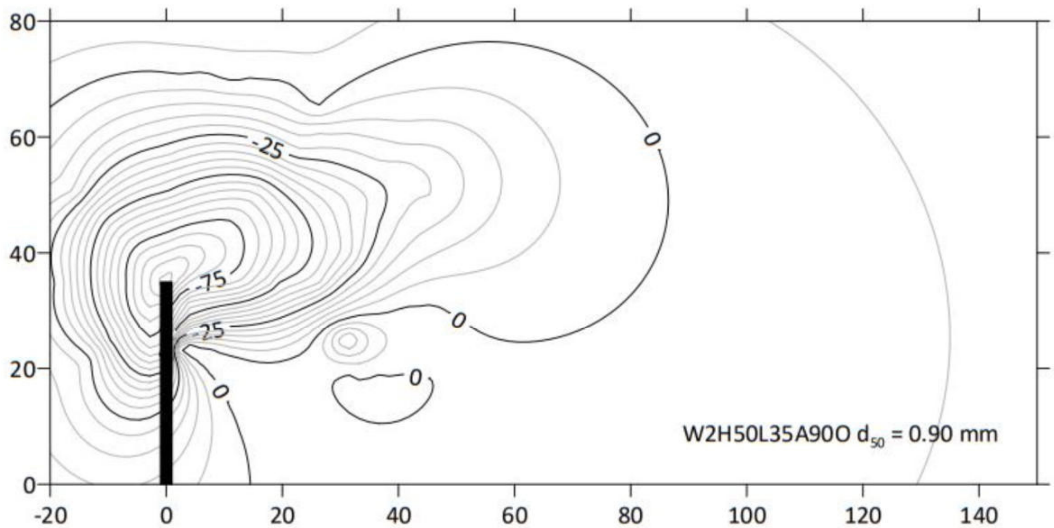

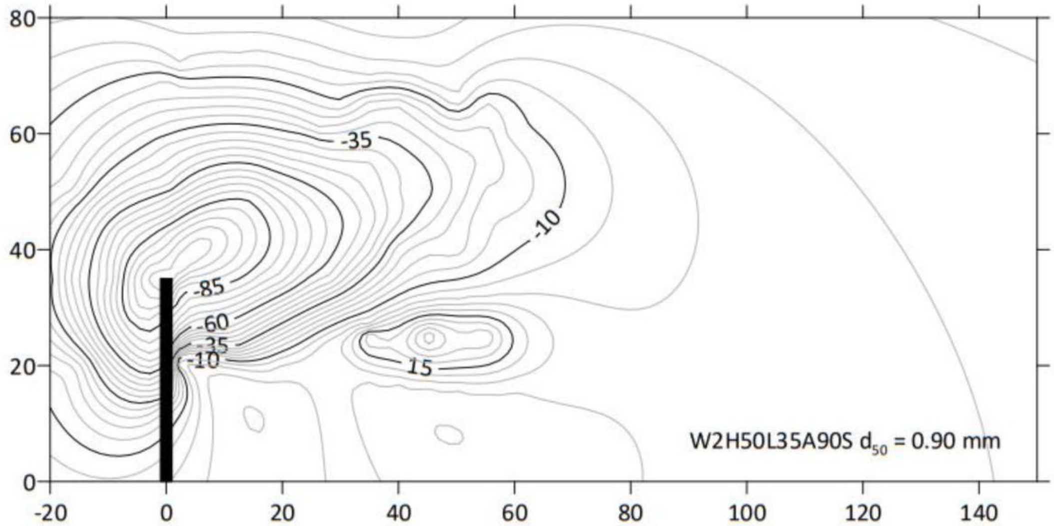

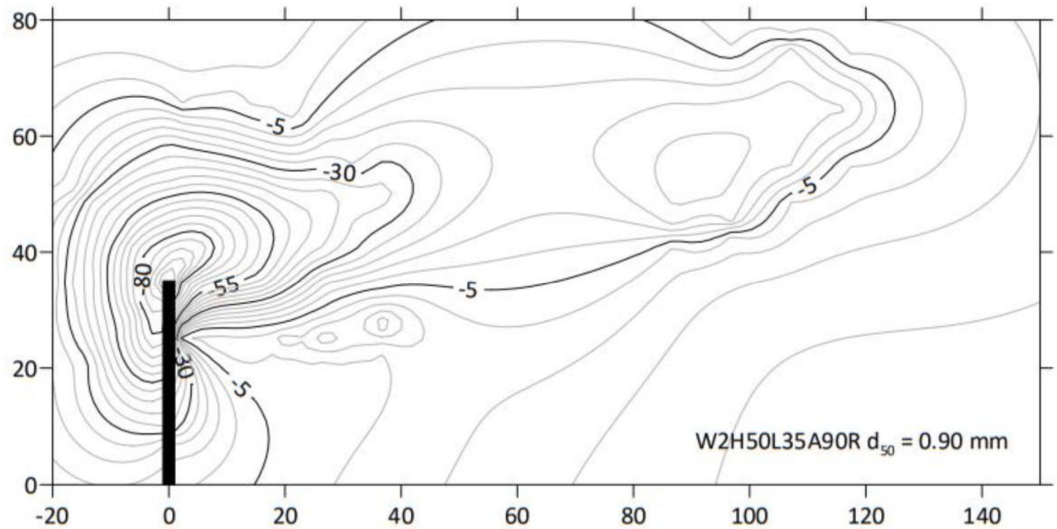

Note: In these contour maps, units for x and y axis are cm, whereas the contour unit is mm. In the experiment serial numbers, *H, L*, and *A* denotes the dike height (including buried in the sands, cm), design length (cm), and alignment angles (°). O, S, R indicate the cover conditions (open channel smooth cover, and rough cover respectively.

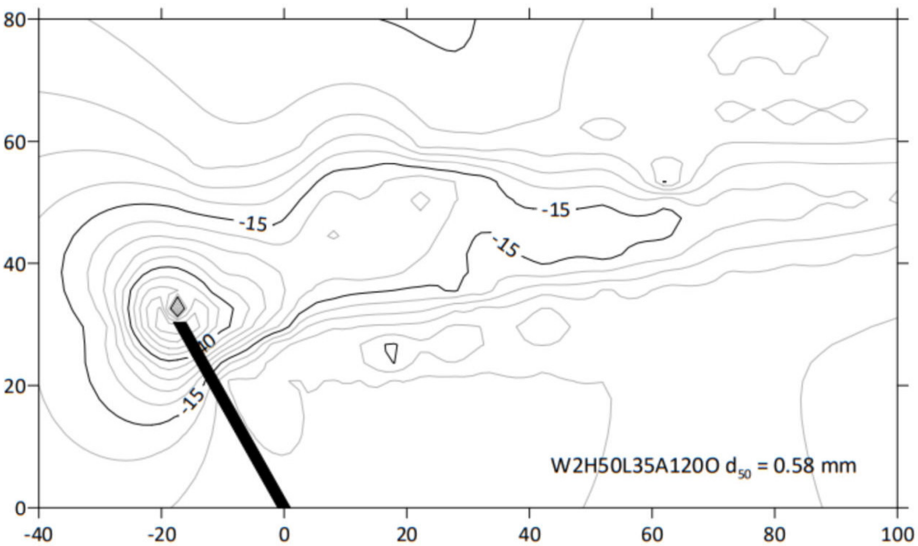

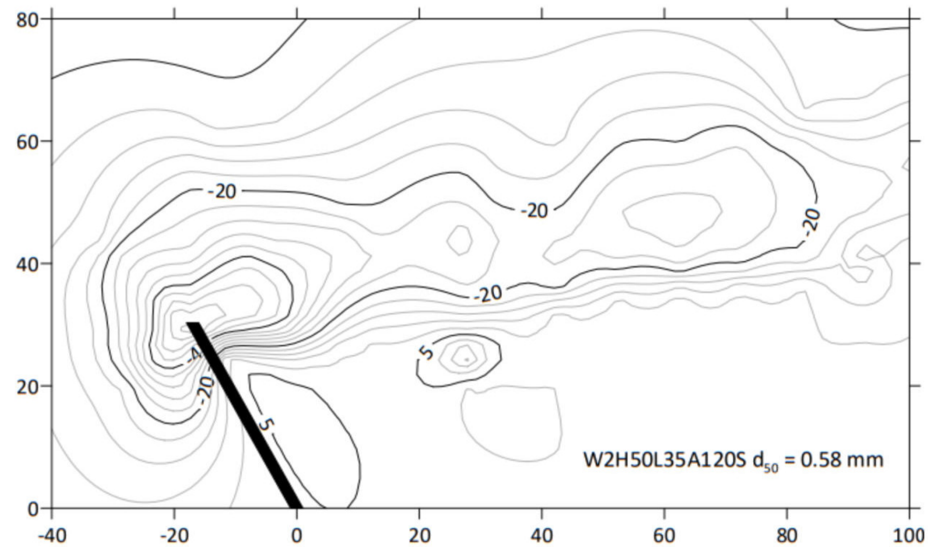

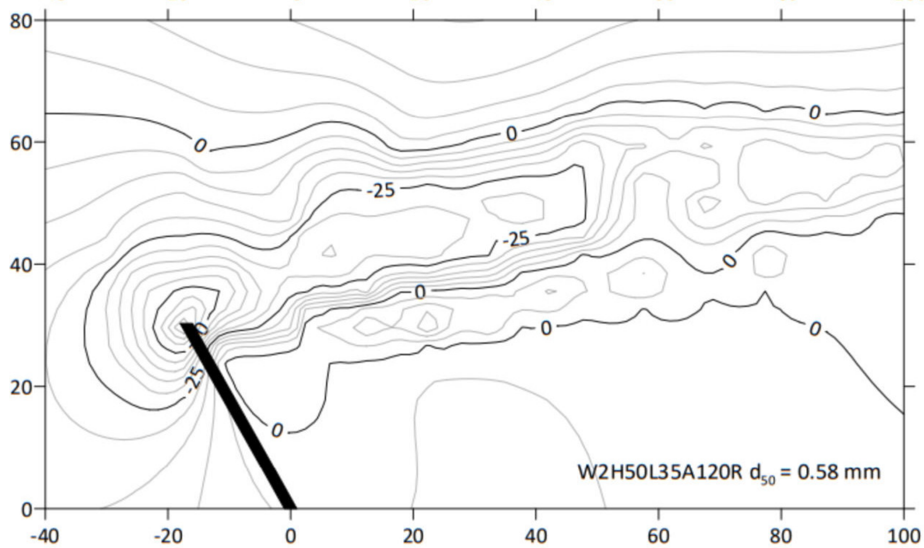

Note: In these contour maps, units for x and y axis are cm, whereas the contour unit is mm. In the experiment serial numbers, *H, L*, and *A* denotes the dike height (including buried in the sands, cm), design length (cm), and alignment angles (°). O, S, R indicate the cover conditions (open channel smooth cover, and rough cover respectively.

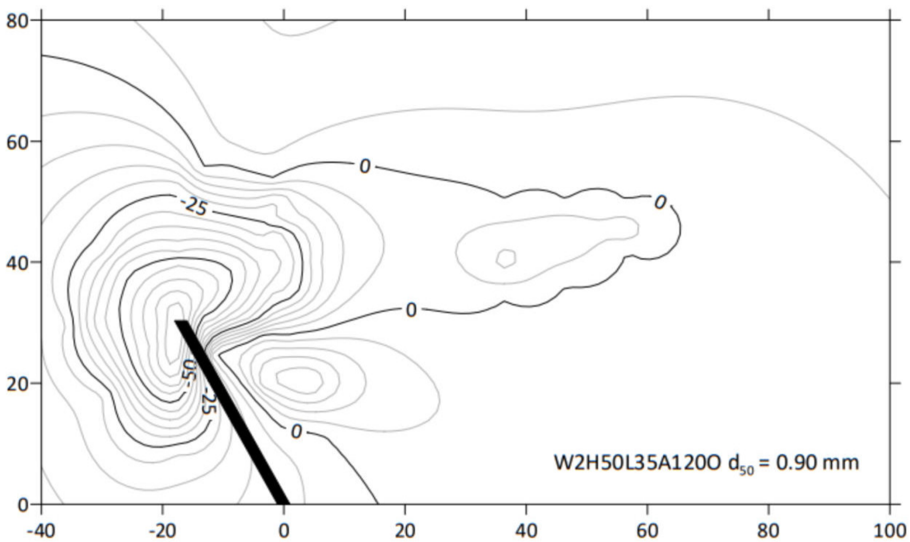

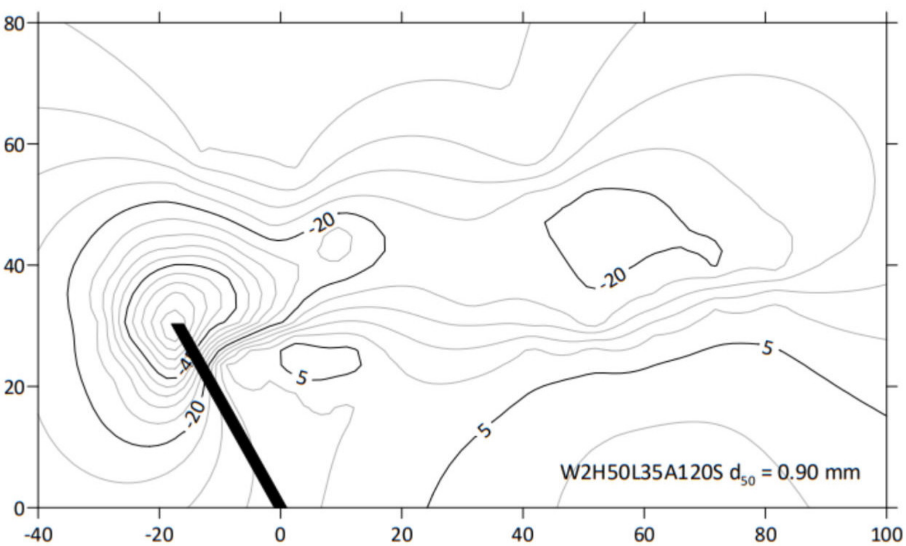

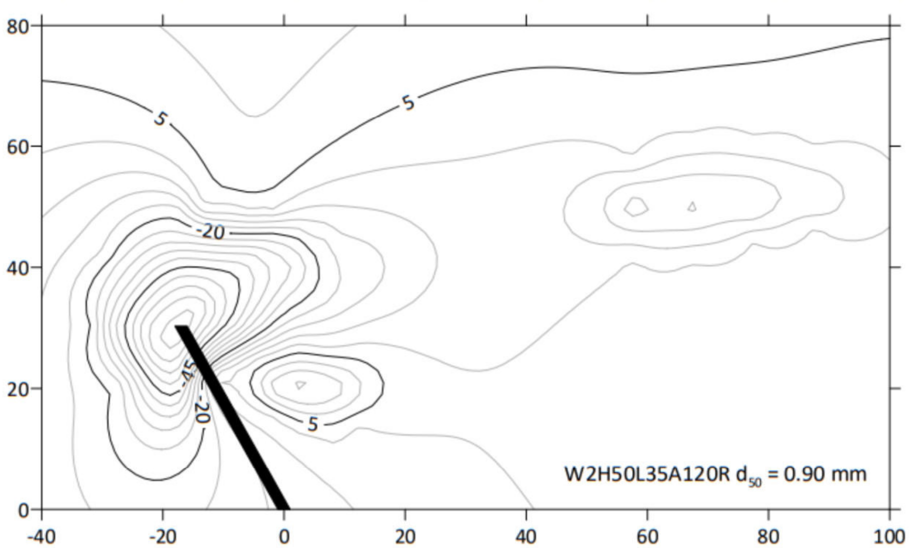

Note: In these contour maps, units for x and y axis are cm, whereas the contour unit is mm. In the experiment serial numbers, *H, L*, and *A* denotes the dike height (including buried in the sands, cm), design length (cm), and alignment angles (°). O, S, R indicate the cover conditions (open channel smooth cover, and rough cover respectively.

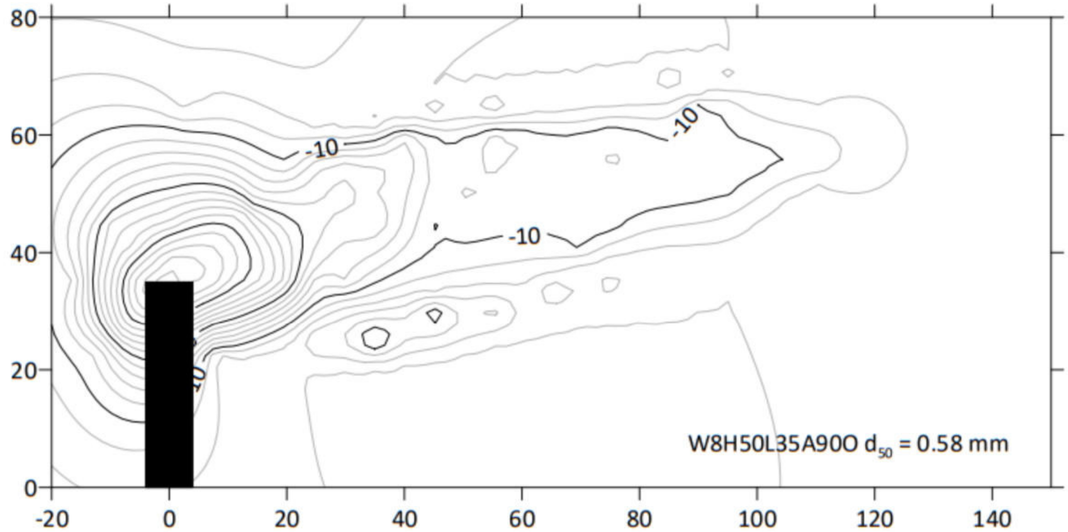

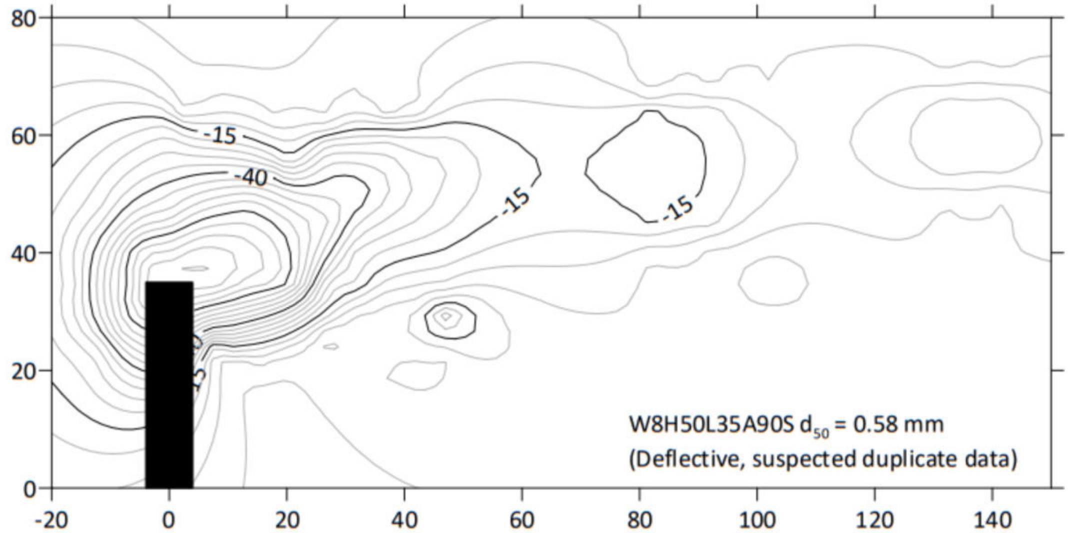

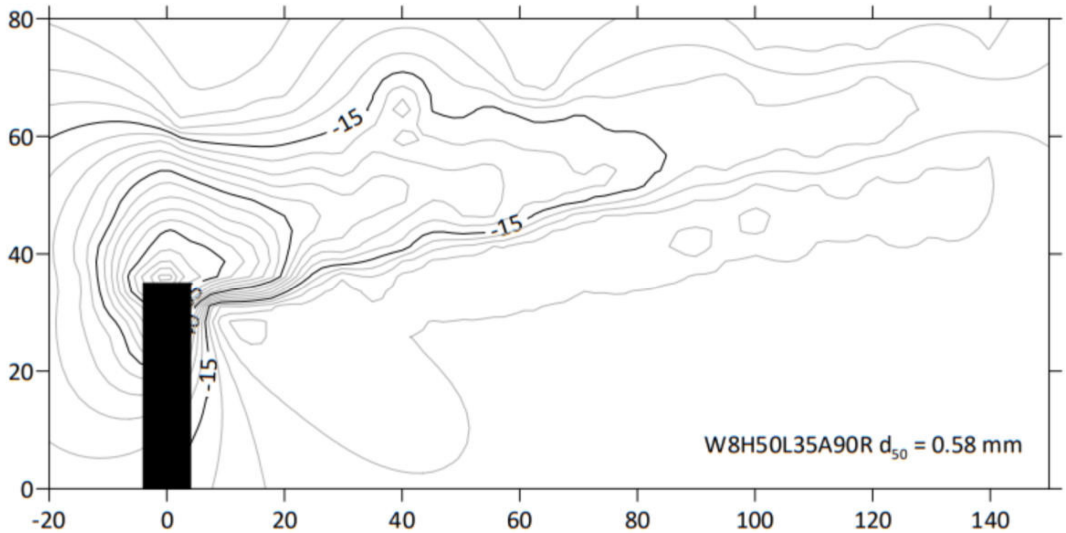

Note: In these contour maps, units for x and y axis are cm, whereas the contour unit is mm. In the experiment serial numbers, *H, L*, and *A* denotes the dike height (including buried in the sands, cm), design length (cm), and alignment angles (°). O, S, R indicate the cover conditions (open channel smooth cover, and rough cover respectively.

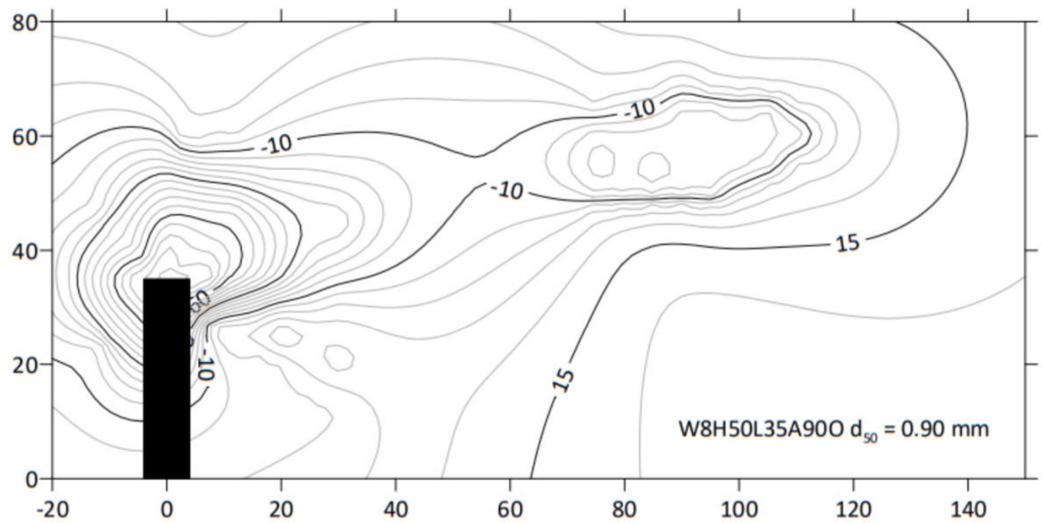

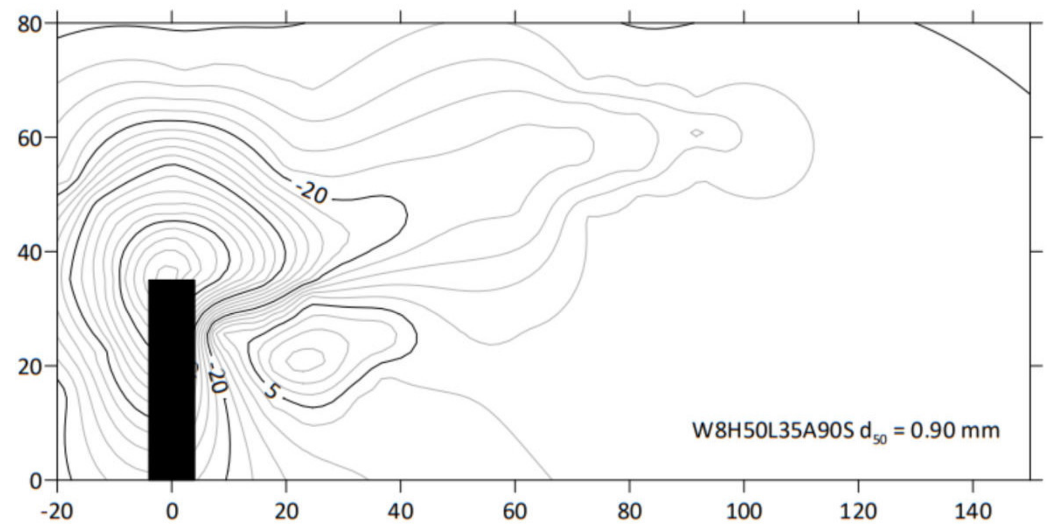

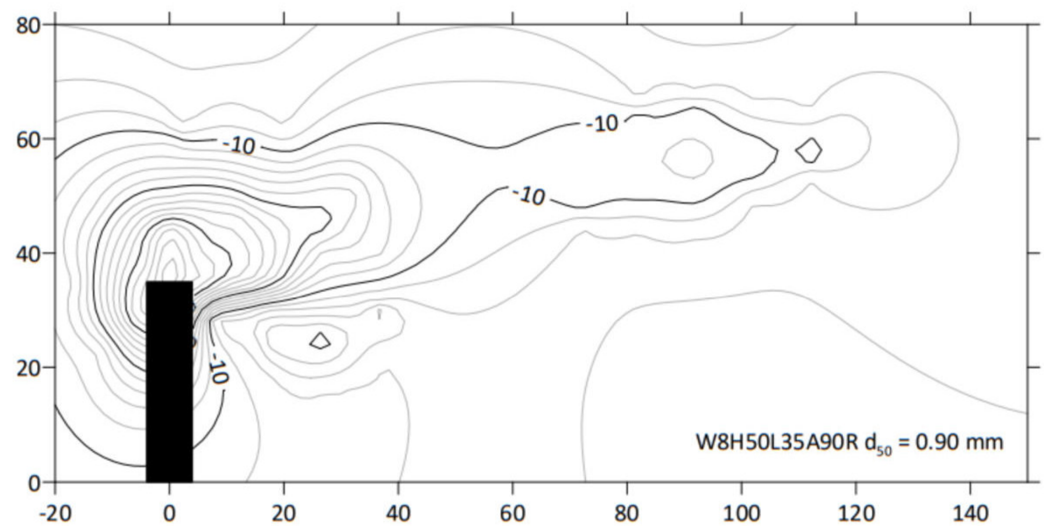

Note: In these contour maps, units for x and y axis are cm, whereas the contour unit is mm. In the experiment serial numbers, *H, L*, and *A* denotes the dike height (including buried in the sands, cm), design length (cm), and alignment angles (°). O, S, R indicate the cover conditions (open channel smooth cover, and rough cover respectively.

APPENDIX II. LINEAR REGRESSION DATA WORKSHEET

Table A.II.1 Linear regression data worksheet for the derivation of the empirical equation of local scour around the submerged spur dike (upstream sandbox)

d_s/h	L/h	Fr_d	S	$sin\ \alpha$	$n0$	Fr	$\ln(d_s/h)$	$\ln(L/h)$	$\ln(Fr_d)$	$\ln(S)$	$\ln(\sin\alpha)$	$\ln(n_0)$	$(B\text{-}L\sin a)/B$
0.410243	1.707317	4.822445	1.02	0.866025	0.018645	0.270659	-0.89101	0.534923	1.573281	0.019803	-0.14384	-3.98219	0.852142004
0.446387	1.715686	4.860219	1.045	1	0.018645	0.272779	-0.80657	0.539813	1.581083	0.044017	0	-3.98219	0.828431373
0.466346	2.439024	4.87281	1.025	0.707107	0.018645	0.273486	-0.76283	0.891598	1.583671	0.024693	-0.34657	-3.98219	0.827534931
0.55954	2.415459	4.986131	1.04	0.866025	0.018645	0.279846	-0.58064	0.881889	1.60666	0.039221	-0.14384	-3.98219	0.79081512
0.630833	2.45098	5.07427	1.065	1	0.018645	0.284793	-0.46071	0.896488	1.624183	0.062975	0	-3.98219	0.754901961
0.235725	2.439024	4.608394	1.4	1	0.018645	0.258645	-1.44509	0.891598	1.527879	0.336472	0	-3.98219	0.756097561
0.260693	2.475248	4.646168	1.366667	0.707107	0.018645	0.260766	-1.34441	0.90634	1.536043	0.312375	-0.34657	-3.98219	0.824973569
0.272307	1.732673	4.646168	1.346667	0.866025	0.018645	0.260766	-1.30083	0.549665	1.536043	0.297632	-0.14384	-3.98219	0.849946093
0.293819	2.45098	4.721715	1.386667	0.866025	0.018645	0.265006	-1.22479	0.896488	1.552172	0.326903	-0.14384	-3.98219	0.787738872
0.30931	1.724138	4.809854	1.36	1	0.018645	0.269952	-1.17341	0.544727	1.570667	0.307485	0	-3.98219	0.827586207
0.410665	1.707317	4.583212	1.065	0.866025	0.014649	0.257232	-0.88998	0.534923	1.5224	0.062975	-0.14384	-4.22342	0.852142004
0.43363	1.682692	4.608394	1.02	0.866025	0.014649	0.258645	-0.83556	0.520395	1.527879	0.019803	-0.14384	-4.22342	0.854274571
0.474587	1.690821	4.620985	1.06	1	0.014649	0.259352	-0.74531	0.525214	1.530608	0.058269	0	-4.22342	0.830917874
0.489567	2.403846	4.646168	1.035	0.707107	0.014649	0.260766	-0.71423	0.87707	1.536043	0.034401	-0.34657	-4.22342	0.830022408
0.595311	2.392344	4.721715	1.04	0.866025	0.014649	0.265006	-0.51867	0.872274	1.552172	0.039221	-0.14384	-4.22342	0.792816889
0.329387	2.439024	4.066971	1.366667	0.707107	0.014649	0.228258	-1.11052	0.891598	1.402898	0.312375	-0.34657	-4.22342	0.827534931
0.339142	1.707317	4.205474	1.366667	1	0.014649	0.236032	-1.08134	0.534923	1.436387	0.312375	0	-4.22342	0.829268293
0.394481	2.415459	4.293613	1.393333	0.866025	0.014649	0.240978	-0.93018	0.881889	1.457129	0.331699	-0.14384	-4.22342	0.79081512
0.450577	2.403846	4.432117	1.413333	1	0.014649	0.248752	-0.79723	0.87707	1.488877	0.345951	0	-4.22342	0.759615385
0.489698	2.403846	4.444708	1.346667	1	0.014649	0.249459	-0.71397	0.87707	1.491714	0.297632	0	-4.22342	0.759615385
0.483267	1.643192	3.966241	1.025	0.866025	0.01984	0.222605	-0.72719	0.496641	1.377819	0.024693	-0.14384	-3.92006	0.857695356
0.500467	1.650943	3.991423	1.065	1	0.01984	0.224018	-0.69221	0.501347	1.384148	0.062975	0	-3.92006	0.83490566
0.561006	2.347418	4.004015	1.035	0.707107	0.01984	0.224725	-0.57802	0.853316	1.387297	0.034401	-0.34657	-3.92006	0.834012493
0.641939	2.347418	4.230657	1.065	1	0.01984	0.237445	-0.44326	0.853316	1.442357	0.062975	0	-3.92006	0.765258216
0.656942	2.347418	4.268431	1.04	0.866025	0.01984	0.239565	-0.42016	0.853316	1.451246	0.039221	-0.14384	-3.92006	0.796707652
0.344072	1.666667	3.827737	1.353333	0.866025	0.01984	0.214831	-1.06691	0.510826	1.342274	0.302571	-0.14384	-3.92006	0.855662433
0.385559	1.674641	3.865511	1.38	1	0.01984	0.216951	-0.95306	0.515599	1.352094	0.322083	0	-3.92006	0.832535885

Table A.II.1 Cont'd

d_s/h	L/h	Fr_d	S	$sin\ \alpha$	$n0$	Fr	$\ln(d_s/h)$	$\ln(L/h)$	$\ln(Fr_d)$	$\ln(S)$	$\ln(\sin\alpha)$	$\ln(n_0)$	$(B\text{-}L\text{sina})/B$
0.398406	2.392344	3.890693	1.366667	0.707107	0.01984	0.218365	-0.92028	0.872274	1.358587	0.312375	-0.34657	-3.92006	0.830835698
0.458569	2.347418	3.915876	1.393333	0.866025	0.01984	0.219778	-0.77964	0.853316	1.365039	0.331699	-0.14384	-3.92006	0.796707652
0.488024	2.358491	3.928467	1.42	1	0.01984	0.220485	-0.71739	0.858022	1.368249	0.350657	0	-3.92006	0.764150943

Table A.II.2 Validation worksheet of the derived local scour around submerged angled spur dikes using data collected from the downstream sandbox.

$d_s(mm)$	L	α	h	$d_s/(L\sin\alpha)$	d/L	Fr_d	$S=h/T$	n_0	d_s/d	L/d	Fr	$Cal.\ ds/d$	$Mea.\ ds/d$
113.7	35	90	24.4	0.324857	0.697143	4.945625	0.976	0.016922	0.465984	1.434426	0.277573	0.426661	0.465984
93.04	35	120	24.6	0.306952	0.702857	4.82304	0.984	0.016922	0.378211	1.422764	0.270692	0.377947	0.378211
149.06	50	90	24.6	0.29812	0.492	4.378641	0.984	0.016922	0.605935	2.03252	0.245751	0.694935	0.605935
122.76	50	120	25.1	0.283502	0.502	4.251737	1.004	0.016922	0.489084	1.992032	0.238628	0.599348	0.489084
75.84	35	120	20.48	0.250207	0.585143	3.938633	1.024	0.016922	0.370313	1.708984	0.221055	0.567903	0.370313
88.19603	35	90	24.6	0.251989	0.702857	5.136734	1.23	0.016922	0.35852	1.422764	0.288298	0.256373	0.35852
81.65063	50	135	30.75	0.230943	0.615	5.062406	1.23	0.016922	0.265531	1.626016	0.284127	0.21199	0.265531
99.24108	50	120	24.7	0.229187	0.494	4.900173	1.235	0.016922	0.401786	2.024291	0.275022	0.327108	0.401786
108.8998	50	90	24.9	0.2178	0.498	4.849182	1.245	0.016922	0.437349	2.008032	0.27216	0.373202	0.437349
71.64406	50	135	25.7	0.20264	0.514	4.468853	1.285	0.016922	0.278771	1.945525	0.250814	0.278645	0.278771
115	35	90	24.7	0.328571	0.705714	4.918514	0.988	0.013683	0.465587	1.417004	0.276051	0.433068	0.465587
95.13	35	120	25	0.313848	0.714286	4.373226	1	0.013683	0.38052	1.4	0.245447	0.439005	0.38052
150.28	50	90	25.2	0.30056	0.504	4.31087	1.008	0.013683	0.596349	1.984127	0.241947	0.693219	0.596349
122.76	50	120	25.2	0.283502	0.504	4.235304	1.008	0.013683	0.487143	1.984127	0.237706	0.620986	0.487143
81.99	35	120	20.24	0.270497	0.578286	4.163101	1.012	0.013683	0.405089	1.729249	0.233653	0.560071	0.405089
92.04249	50	135	30.625	0.260335	0.6125	5.245543	1.225	0.013683	0.300547	1.632653	0.294405	0.211114	0.300547
84.03	35	90	24.6	0.240086	0.702857	4.995823	1.23	0.013683	0.341585	1.422764	0.28039	0.278951	0.341585
103.2582	50	120	24.7	0.238465	0.494	4.888393	1.235	0.013683	0.41805	2.024291	0.27436	0.341927	0.41805
113.3916	50	90	25	0.226783	0.5	4.616669	1.25	0.013683	0.453566	2	0.25911	0.415268	0.453566
76.58674	50	135	25.4	0.21662	0.508	4.061629	1.27	0.013683	0.301523	1.968504	0.227958	0.348681	0.301523
128.2872	35	90	24.8	0.366535	0.708571	4.686811	0.992	0.019016	0.517287	1.41129	0.263047	0.433959	0.517287
156.0143	50	120	24.8	0.3603	0.496	4.674036	0.992	0.019016	0.62909	2.016129	0.26233	0.522119	0.62909
95.09409	35	120	25.3	0.313729	0.722857	4.261541	1.012	0.019016	0.375866	1.383399	0.239178	0.415348	0.375866
153.6826	50	90	25.4	0.307365	0.508	4.070359	1.016	0.019016	0.60505	1.968504	0.228448	0.697154	0.60505
90.55	35	120	20.48	0.298738	0.585143	3.533704	1.024	0.019016	0.442139	1.708984	0.198329	0.659114	0.442139
93.23225	50	135	30.375	0.263701	0.6075	5.075488	1.215	0.019016	0.306937	1.646091	0.284861	0.213714	0.306937
87.38284	35	90	24.7	0.249665	0.705714	5.058859	1.235	0.019016	0.353777	1.417004	0.283928	0.253944	0.353777
101.127	50	120	24.9	0.233543	0.498	4.677437	1.245	0.019016	0.406133	2.008032	0.262521	0.336578	0.406133

Table A.II.2 Cont'd

$d_s(mm)$	L	α	h	$d_s/(L\sin\alpha)$	d/L	Fr_d	$S=h/T$	n_0	d_s/d	L/d	Fr	*Cal. ds/d*	*Mea. ds/d*
116.0705	50	90	25.7	0.232141	0.514	4.521583	1.285	0.019016	0.451636	1.945525	0.253773	0.372987	0.451636
78.19894	50	135	25.7	0.22118	0.514	4.271117	1.285	0.019016	0.304276	1.945525	0.239716	0.292688	0.304276

APPENDIX III. NUMERICAL SIMULATION RUNNING TIME OPTIMIZATION

```
 job name:     nwlw
 problem date: 07/30/2024
 problem time: 09:38:12

Simulation Template: Free Surface - TruVOF (Default)


 *** estimated uncompressed solver output file size (flsgrf):   62 gb  ***


 *** running solver on 1 rank and   8 cores ***

 ***
  restart and spatial data available at t= 0.00000E+00
 ***
 ----------------------  ---------------------  ---------------  ---------------------------      -------------------------------------
        progress                time step           pressure               fluid #1                           performance
   sim_time       cycle     delt   dt_stbl/code   iter  res/epsi     volume      %loss     frac      el_time  %PE   clk_time  est_rem_time
 ----------------------  ---------------------  ---------------  ---------------------------      -------------------------------------
 0.00000E+00          0  1.00E-02  1.50E-02/cx     12  6.01E-01   4.1616E+00  +0.00E+00  0.34      00:00:50   95  09:38:16           ...
 1.27843E+00        108  1.58E-02  1.59E-02/cx      4  4.76E-01   4.0331E+00  +5.05E-02  0.33      00:10:54  100  09:48:19  118:00:16:02
```

Figure A.III.1 FLOW-3D simulation log for running at the same time as experimental vegetated pool conditions (118 days, not realistic for multiple simulations)

```
7.20430E+02      80949   5.60E-03  5.60E-03/td       1  1.49E-03    4.1778E+00  +3.19E-02  0.34      13:09:37  100  23:20:15      07:54:30
7.26334E+02      82003   5.60E-03  5.60E-03/td       1  9.89E-04    4.1778E+00  +3.14E-02  0.34      13:19:38   99  23:30:16      07:44:13
7.32228E+02      83055   5.60E-03  5.60E-03/td       1  1.35E-03    4.1778E+00  +3.10E-02  0.34      13:29:38  100  23:40:16      07:34:40
7.38129E+02      84108   5.60E-03  5.60E-03/td       1  1.50E-03    4.1778E+00  +3.05E-02  0.34      13:39:38  100  23:50:16      07:24:03
7.44031E+02      85161   5.61E-03  5.61E-03/td       1  1.18E-03    4.1778E+00  +3.01E-02  0.34      13:49:39  100  00:00:17      07:13:52
7.49963E+02      86219   5.61E-03  5.61E-03/td       1  1.13E-03    4.1778E+00  +2.96E-02  0.34      13:59:39   98  00:10:17      07:01:33
7.55885E+02      87275   5.61E-03  5.61E-03/td       1  1.53E-03    4.1778E+00  +2.92E-02  0.34      14:09:39  100  00:20:17      06:51:21
7.61791E+02      88328   5.61E-03  5.61E-03/td       1  1.57E-03    4.1778E+00  +2.88E-02  0.34      14:19:40  100  00:30:18      06:43:36
7.67704E+02      89382   5.61E-03  5.61E-03/td       1  1.58E-03    4.1778E+00  +2.83E-02  0.34      14:29:40  100  00:40:18      06:32:59

================= tip ==================
      solution is nearly steady:
      variation from the mean is
 less than   2.0933E-01 %  at t=  7.72137E+02
========================================

================= tip ==================
      solution is nearly steady:
      variation from the mean is
 less than   2.0933E-01 %  at t=  7.72137E+02
========================================

7.73619E+02      90436   5.61E-03  5.61E-03/td       1  1.49E-03    4.1778E+00  +2.79E-02  0.34      14:39:40  100  00:50:18      06:23:02
```

Figure A.III.2 FLOW-3D tips on steady solution time (approximately 800 seconds). The simulation duration was set as 1000 seconds for each case to save computational time.

APPENDIX IV. SEDIMENT SIZE DISTRIBUTION IN NECHOKO RIVER

Date Sample Collected	Sample name	Northing (m)	Easting (m)	Transport rate (g/s/m)	Cumulative Per Cent Finer Than; Grain size class are in mm																				D50 (mm)	D84 (mm)	D16 (mm)
					45	32	23	16	11	8	5.7	4	2.8	2	1.4	1	0.71	0.5	0.35	0.25	0.18	0.13	0.09	0.06			
8/16/2013	FF-A	5991295	397197	1.8	100	100	100	100	100	100	100	100	100	100	100	98	96	88	70	23	2	0	0	0	0.31	0.46	0.22
8/16/2013	FF-B	5991297	397175	0.9	100	100	100	100	100	100	100	100	100	100	100	100	100	99	92	65	23	0	0	0	0.22	0.32	0.16
8/16/2013	FF-C	5991295	397160	41.8	100	100	100	100	100	100	100	100	100	100	100	98	95	80	45	8	1	0	0	0	0.37	0.55	0.27
8/16/2013	FF-D	5991295	397143	106.4	100	100	100	100	100	100	100	99	98	95	92	84	71	49	26	7	1	0	0	0	0.51	1.01	0.30
8/16/2013	FF-E2	5991296	397120	137.8	100	100	100	99	99	99	97	95	90	85	80	72	59	35	14	2	0	0	0	0	0.62	1.87	0.36
8/16/2013	FF-F	5991291	397098	1.2	100	100	100	100	82	47	31	24	15	10	9	8	7	4	2	1	0	0	0	0	8.23	11.77	2.95
8/15/2013	LP A	5986886	433772	6.0	100	100	100	82	70	63	50	39	30	25	23	20	16	12	7	2	1	0	0	0	5.72	16.72	0.68
8/15/2013	LP B	5986909	433766	5.6	100	100	100	58	35	27	20	16	12	10	8	7	6	4	2	1	0	0	0	0	14.19	19.82	4.02
8/15/2013	LP C	5986920	433766	6.2	100	100	100	89	56	35	29	22	17	15	12	9	6	4	2	1	0	0	0	0	10.28	15.22	2.40
8/15/2013	LP D	5986944	433767	25.2	100	100	92	82	53	43	36	33	30	28	27	25	24	21	15	4	0	0	0	0	10.24	17.16	0.37
8/15/2013	LP E2	5986959	433765	284.4	100	100	100	100	100	100	100	100	100	100	100	98	93	69	30	4	0	0	0	0	0.42	0.62	0.29
8/15/2013	LP F	5986980	433768	1.5	100	100	100	100	100	100	100	100	100	100	100	99	98	87	57	18	3	2	2	2	0.33	0.48	0.24
8/15/2013	LP G	5986992	433771	0.1	100	100	100	100	100	100	100	100	100	100	98	95	93	89	76	35	9	5	5	5	0.28	0.44	0.19
8/15/2013	LS A	5986800	434170	0.1	100	100	100	100	100	100	100	84	73	67	62	57	53	45	35	19	3	0	0	0	0.63	4.01	0.24
8/15/2013	LS B	5986787	434160	0.3	100	100	100	100	100	100	91	81	71	58	50	43	38	33	27	16	3	0	0	0	1.41	4.42	0.25
8/15/2013	LS C	5986765	434152	7.5	100	100	100	92	79	67	59	52	46	42	39	35	31	25	19	11	2	0	0	0	3.54	12.91	0.31
8/15/2013	LS D	5986745	434123	33.6	100	100	100	97	90	82	72	66	61	58	55	53	51	44	26	4	0	0	0	0	0.68	8.74	0.30
8/15/2013	LS E	5986732	434101	2.2	100	100	100	100	100	73	57	48	41	34	31	28	26	23	18	8	2	0	0	0	4.33	9.18	0.33
8/15/2013	LS F	5986760	434133	69.5	100	100	100	99	99	98	97	96	95	95	94	93	89	69	36	8	1	0	0	0	0.41	0.65	0.28
8/15/2013	MP-C	5986336	433324	10.2	100	100	100	94	83	80	74	69	60	39	18	7	5	5	4	3	1	0	0	0	2.40	11.60	1.31
8/15/2013	MP-D3	5986355	433311	3.1	100	100	60	43	26	17	17	16	15	14	13	12	11	10	8	3	0	0	0	0	18.51	27.82	4.30
8/15/2013	MP-E	5986372	433303	0.2	100	100	100	100	100	75	55	48	32	26	22	18	13	6	3	2	1	0	0	0	4.46	9.06	0.88
8/14/2013	US-1	5986116	431758	26.4	100	92	71	69	64	57	49	43	36	30	25	19	14	8	4	1	0	0	0	0	5.81	27.99	0.80
8/14/2013	US-2	5986151	431868	12.0	100	100	100	95	90	87	81	76	69	60	53	42	32	20	11	3	0	0	0	0	1.30	6.75	0.44
8/15/2013	U/S A	5986144	431750	6.1	100	100	100	100	100	100	100	100	100	100	100	100	99	86	47	11	1	1	1	1	0.36	0.49	0.26
8/15/2013	U/S B	5986128	431775	5.2	100	100	100	100	93	90	86	81	74	67	61	52	41	27	16	6	0	0	0	0	0.94	4.87	0.36
8/15/2013	U/S-C	5986109	431757	0.8	100	100	100	100	100	100	93	86	73	60	46	34	26	19	14	7	1	0	0	0	1.56	3.82	0.40
8/15/2013	U/S D	5986088	431756	0.6	100	100	100	100	84	55	45	37	33	32	29	25	20	15	12	7	1	0	0	0	6.67	11.43	0.55
8/15/2013	U/S E	5986113	431757	1.1	100	100	100	100	100	93	85	79	66	56	49	39	30	22	15	6	1	0	0	0	1.49	5.31	0.37
10/11/2013	Cumulative_US	Not Applicable		0.0	100	100	100	100	100	100	100	100	100	100	95	88	82	73	64	34	10	0	0	0	0.30	0.77	0.19
10/12/2013	LP-D	5986962	433780	0.0	100	100	100	100	100	100	100	100	100	100	100	93	85	78	66	36	13	2	2	2	0.29	0.66	0.18
10/12/2013	LP-E	5986975	433777	0.2	100	100	100	100	100	100	100	100	100	100	100	99	96	84	58	10	1	0	0	0	0.33	0.50	0.26
10/12/2013	LP-F	5986982	433771	0.2	100	100	100	100	100	100	100	100	95	93	91	88	84	79	73	37	10	0	0	0	0.28	0.71	0.19
10/12/2013	LS-B	5986787	434158	0.0	100	100	100	100	100	100	100	100	100	100	85	78	66	55	47	37	16	1	0	0	0.40	1.32	0.18
10/12/2013	LS-C	5986773	434148	11.6	100	100	100	100	100	100	98	97	96	96	95	91	77	49	25	5	1	0	0	0	0.51	0.84	0.30
10/12/2013	LS-D	5986763	434137	8.8	100	100	100	100	100	100	99	99	98	98	97	96	93	74	35	4	0	0	0	0	0.40	0.60	0.29
10/12/2013	LS-E	5986753	434127	0.1	100	100	100	100	100	100	100	100	100	100	94	91	87	76	52	13	5	1	0	0	0.35	0.64	0.26
10/10/2013	MP-D	5986336	433327	5.4	100	100	100	100	100	96	93	90	87	82	77	70	60	42	20	3	1	0	0	0	0.58	2.31	0.33